Kinetic Effects on Turbulence Driven by the Magnetorotational Instability in Black Hole Accretion

Prateek Sharma

A Dissertation
Presented to the Faculty
of Princeton University
in Candidacy for the Degree
of Doctor of Philosophy

Recommended for Acceptance
by the department of
Astrophysical sciences

September 2006

Abstract

Many astrophysical objects (e.g., spiral galaxies, the solar system, Saturn's rings, and luminous disks around compact objects) occur in the form of a disk. One of the important astrophysical problems is to understand how rotationally supported disks lose angular momentum, and accrete towards the bottom of the gravitational potential, converting gravitational energy into thermal (and radiation) energy.

The magnetorotational instability (MRI), an instability causing turbulent transport in ionized accretion disks, is studied in the kinetic regime. Kinetic effects are important because radiatively inefficient accretion flows (RIAFs), like the one around the supermassive black hole in the center of our Galaxy, are collisionless. The ion Larmor radius is tiny compared to the scale of MHD turbulence so that the drift kinetic equation (DKE), obtained by averaging the Vlasov equation over the fast gyromotion, is appropriate for evolving the distribution function. The kinetic MHD formalism, based on the moments of the DKE, is used for linear and nonlinear studies. A Landau fluid closure for parallel heat flux, which models kinetic effects like collisionless damping, is used to close the moment hierarchy.

We show that the kinetic MHD and drift kinetic formalisms give the same set of linear modes for a Keplerian disk. The BGK collision operator is used to study the transition of the MRI from kinetic to the MHD regime. The ZEUS MHD code

is modified to include the key kinetic MHD terms: anisotropic pressure tensor and anisotropic thermal conduction. The modified code is used to simulate the collisionless MRI in a local shearing box. As magnetic field is amplified by the MRI, pressure anisotropy ($p_\perp > p_\parallel$) is created because of the adiabatic invariance ($\mu \propto p_\perp/B$). Larmor radius scale instabilities—mirror, ion-cyclotron, and firehose—are excited even at small pressure anisotropies ($\Delta p/p \sim 1/\beta$). Pressure isotropization due to pitch angle scattering by these instabilities is included as a subgrid model. A key result of the kinetic MHD simulations is that the anisotropic stress can be as large as the Maxwell stress.

It is shown, with the help of simple tests, that the centered differencing of anisotropic thermal conduction can cause the heat to flow from lower to higher temperatures, giving negative temperatures in regions with large temperature gradients. A new method, based on limiting the transverse temperature gradient, allows heat to flow only from higher to lower temperatures. Several tests and convergence studies are presented to compare the different methods.

Acknowledgements

I foremost thank my adviser Greg Hammett, whose guidance made this thesis possible. His insight, quest for perfection, and passion for science has always inspired me. He was always patient, and ensured that I understood every subtle point. Thanks to Eliot Quataert, who is an inspiring mentor, and initiated me into the fascinating field of astrophysics. He was so accessible that I never felt that he was not in Princeton. I am thankful to Jim Stone for his constant encouragement, and help with numerical methods, especially ZEUS.

Finally, thanks to my loving and supporting family, and wonderful friends. Special thanks to my brother Rohit, sister Chubi, and cousins, who have always brought joy in my life. My wife Asha has been a loving and caring companion; her suggestion to keep it simple has significantly improved the thesis.

The thesis work was supported by U.S. DOE contract # DE-AC02-76CH03073, and NASA grants NAG5-12043 and NNH06AD01I. Many thanks to the NASA websites for amazing pictures, some of which I have used in this thesis.

To my parents and grandparents

Contents

List of Tables

List of Figures

Chapter 1

Introduction

Disks are ubiquitous in astrophysics. Many astrophysical objects, e.g., Saturn's rings, the solar system, and galaxies, are disk shaped. A disk is formed when the matter has sufficient angular momentum for the centrifugal force to balance the attractive gravitational force; this differs from other systems like stars and planets where gravitational attraction is balanced by pressure. Key astrophysical processes, like star and planet formation, and many sources in high energy astrophysics, are based on an accretion disk. Accretion refers to the accumulation of matter onto a central compact object or the center of mass of an extended system. Examples of accreting systems are: binaries where matter flows from a star to a compact object like a black hole, a neutron star, or a white dwarf (see Figure 1.1); Active Galactic Nuclei (AGN) powered by accretion onto a supermassive black hole in the center of galaxies (see Figure 1.2); and protostellar and protoplanetary disks, the predecessors of stars and planets.

To accrete, matter has to lose angular momentum. Gravitational binding energy released because of the infall of matter is a powerful source of luminosity. Quasars, one of the most luminous sources in the universe, are powered by accretion [120]. The central problem in accretion physics is, how does matter lose rotational support and

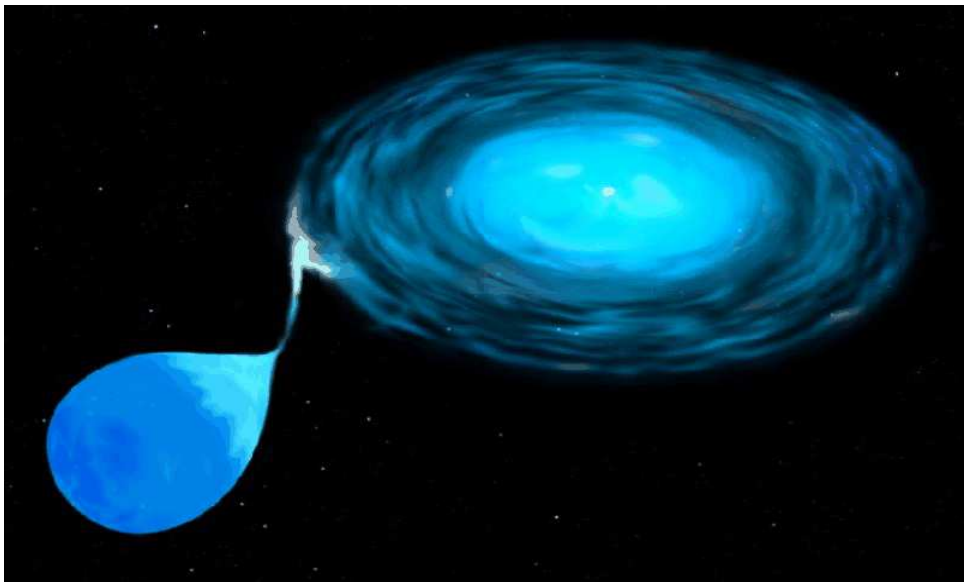

Figure 1.1: An artist's impression of a binary accretion disk. Plasma overflows from the stellar companion and forms an accretion disk around the compact object. Drawing Credit: ST ScI, NASA; http://antwrp.gsfc.nasa.gov/apod/ap991219.html.

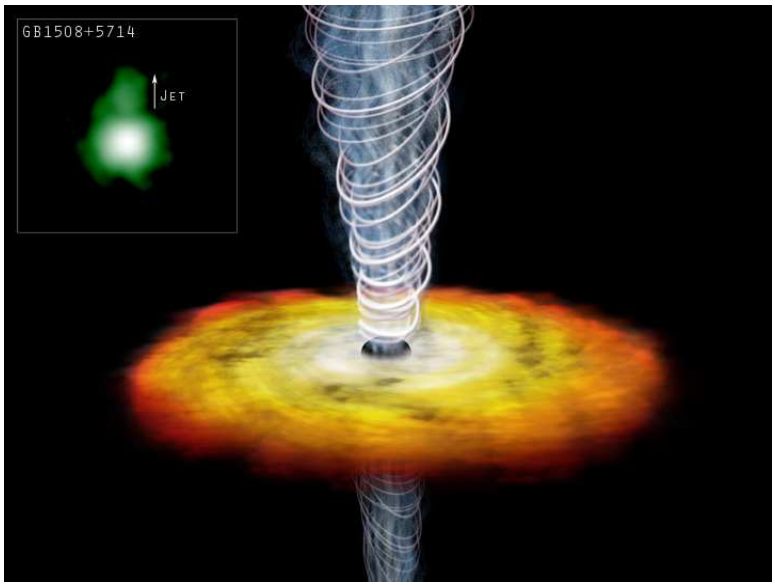

Figure 1.2: Inset at upper left shows X-ray emission from energetic particles in the jet of quasar GB1508+5714. Many accretion disks have jets associated with them. The illustration shows an accretion disk surrounding a supermassive black hole, which launches a collimated jet. Credit: A. Siemiginowska, Illustration by M.Weiss; http://antwrp.gsfc.nasa.gov/apod/ap031128.html.

fall in? In many disks the mass of the central object is much larger than the disk mass, resulting in a Keplerian rotation profile ($\Omega \sim R^{-3/2}$). In principle, the presence of a shear viscosity allows the transport of angular momentum from the faster inner fluid elements to the slower outer ones. However, the accretion rate obtained by putting in a typical number for microscopic (collisional) viscosity is several orders of magnitude smaller than needed to explain observations.

Turbulent stress due to interacting large scale ($\approx$ disk height) eddies is sufficient to provide the needed accretion rates. For turbulent stress one needs a source to sustain the turbulence; otherwise the nonlinear motions will be damped due to viscosity. Hydrodynamic disks with specific angular momentum (angular momentum per unit mass) increasing outwards (e.g., Keplerian disks) are linearly stable. A large Reynolds number is not sufficient to produce nonlinear turbulent motions from small perturbations. A source to produce and to sustain the turbulence is required. A linear instability, that can tap the free energy in differential rotation, can amplify small amplitude fluctuations into large scale nonlinear motions, and provide such a source. A big advance was made when Balbus and Hawley realized that the magnetorotational instability (MRI), an instability of magnetized, differentially rotating flows, can cause turbulent transport in accretion disks [14, 86].

Although, the identification of the MRI as the source of turbulence in accretion flows was a major step in understanding accretion, there are several unsolved problems. Although the MRI only requires a small amount of ionization to work [29], protostellar disks, from which stars and planets form, are very cold and may have such a low degree of ionization the MRI does not operate. Another topic of investigation is, whether the hydrodynamic Keplerian flow, like the planar shear flow [115], can become turbulent at large enough Reynolds numbers (discussed more in subsection 1.3.1). Another problem, a motivation for this thesis, is to understand why some black hole accretion disks are unusually dim [138]. Understanding of the microphysics

and the global structure of accretion flows, in important physical regimes, is still incomplete. The theoretical disk models have to be tested against the ever detailed observations.

1.1 Accretion as an energy source

Accretion is a very efficient source of energy. Disk models, based on accretion of matter from a stellar companion on to a compact object (first mentioned by [108]), were used to explain novae outbursts [50], and later compact X-ray sources [152]. The release of thermonuclear energy from stars is insufficient to account for the high luminosity, and significant X-ray (non-blackbody) luminosity. This section, including the subsections on the Eddington limit and the emitted spectrum, are based on Chapter 1 of [61].

To illustrate the enormous power of accretion consider the following example from [61]. For a body of mass M_* and radius R_*, the gravitational energy released by accretion of mass m on to its surface is $\Delta E_{acc} = GM_*m/R_*$, where G is the gravitational constant. This energy is expected to be released mainly in the form of electromagnetic radiation. Luminosity, the energy radiated per unit time, is proportional to the ratio M_*/R_* and $\dot{M}$, the mass accretion rate.

Writing in terms of the rest mass energy, $\Delta E_{acc} = 0.15(M_*/M_\odot)(10 \text{ km}/R_*)mc^2$, where $M_\odot$ is the solar mass. If the accreting body is a neutron star with $R_* \sim 10$ km and $M_* \sim M_\odot$, then the efficiency of accretion is 0.15. For comparison, the nuclear energy released on burning hydrogen to helium is $\Delta E_{nuc} = 0.007mc^2$, about one twentieth of the accretion yield. Thus, accretion is an even more efficient energy source than fusion (in fact by a factor of few tens)!

Since black holes have no surface, R_* refers to the radius beyond which matter does not radiate. This radius depends on black hole spin, which is difficult to measure.

Our ignorance of R_* can be parameterized by an efficiency η, with $\Delta E_{acc} = \eta mc^2$. Relativistic calculations give an efficiency of 6% for a non-rotating Schwarzchild black hole, and 42.3% for a maximally rotating Kerr black hole [133] (see Appendix A.1 for a discussion of the efficiency of black hole accretion).

For a white dwarf with $M_* \sim M_\odot$, $R_* \sim 10^9$ cm, nuclear burning is more efficient than accretion by factors $40-50$. Although the efficiency for nuclear burning for white dwarfs is much higher, in many cases the reaction tends to 'run away' to produce an event of great brightness but short duration, a nova outburst, in which available nuclear fuel is rapidly exhausted. For almost all of its lifetime no nuclear burning occurs, and the white dwarf may derive its entire luminosity from accretion. Whether accretion or nuclear fusion dominates depends on $\dot{M}$, the accretion rate.

1.1.1 The Eddington limit

At high luminosity, the accretion flow is affected by the outward momentum transferred from radiation to the accreting matter by scattering and absorption. We derive an upper limit on luminosity of an accretion disk by considering spherical, steady state accretion. Assume the accreting matter to be fully ionized hydrogen plasma. If S is radiant energy flux (erg cm^{-2} sec^{-1}), and $\sigma_T = 6.7 \times 10^{-25}$cm^2 is the electron Thomson scattering cross section, the outward radial force is $\sigma_T S/c$. The effective cross section can exceed σ_T if photons are absorbed by spectral lines. Because of the charge neutrality of plasma, radiative force on electrons couples to protons. If L is the luminosity of the accreting source, $S = L/4\pi r^2$, net inward force on proton is $(GM_* m_p - L\sigma_T/4\pi c)/r^2$. The limiting luminosity for which the radial force vanishes, the Eddington limit, is $L_{Edd} = 4\pi GM_* m_p c/\sigma_T \cong 1.38 \times 10^{38}(M_*/M_\odot)$ erg s^{-1}. At greater luminosities, the radiation pressure will halt accretion. The Eddington limit is a crude estimate of the upper limit on the steady state disk luminosity.

If all the kinetic energy of accretion is given up at the stellar surface, R_*, then

the luminosity is $L_{acc} = GM_*\dot{M}/R_*$. For accretion powered objects, the Eddington limit implies an upper limit on the accretion rate, $\dot{M} \lesssim \dot{M}_{Edd} = 4\pi R_* m_p c/\sigma_T = 9.5 \times 10^{11} R_*$ g s^{-1}. The Eddington limit applies only for uniform, steady accretion; e.g., photon bubble instability [6, 64, 30], a compressive instability of radiative disks that opens up optically thin "holes" through which radiation can escape, can allow for super-Eddington luminosity [193, 23].

1.1.2 The emitted spectrum

Order of magnitude estimates of spectral range of the emission from compact accreting objects can be made. The continuum spectrum can be characterized by a temperature $T_{rad} = h\overline{\nu}/k$ of emitted radiation, where $\overline{\nu}$ is the frequency of a typical photon. For an accretion disk with luminosity L_{acc}, one can define a blackbody temperature as $T_b = (L_{acc}/4\pi R_*^2\sigma)^{1/4}$, where σ is the Stefan-Boltzmann constant. Thermal temperature, T_{th}, is defined as the temperature material would reach if its gravitational potential energy is converted entirely into the thermal energy. For each proton-electron pair accreted, the potential energy released is $GM_*(m_p + m_e)/R_* \cong GM_* m_p/R_*$, and the thermal energy is $2 \times (3/2)kT$; therefore $T_{th} = GM_* m_p/3kR_*$. The virial temperature, $T_{vir} = T_{th}/2$, is also used frequently. If the accretion flow is optically thick, photons reach thermal equilibrium with the accreted material before leaking out to the observer and $T_{rad} = T_b$. Whereas, if accretion energy is converted directly into radiation which escapes without further interaction (i.e., the intervening material is optically thin), $T_{rad} = T_{th}$. In general, the observed radiation temperature is expected to lie between the two limits, $T_b \lesssim T_{rad} \lesssim T_{th}$.

Applying these limits to a solar mass neutron star radiating at the Eddington limit gives, 1 keV $\lesssim h\overline{\nu} \lesssim$ 50 MeV; similar results would hold for stellar mass black holes. Thus we can expect the most luminous accreting neutron star and black hole binary disks to appear as medium to hard X-ray emitters, and possibly as γ-ray sources.

Similarly for white dwarf accretion disks with $M_* = M_\odot$, $R_* = 10^9$ cm, we obtain 6 eV $\lesssim h\overline{\nu} \lesssim$ 100 keV. Consequently, accreting white dwarfs should be optical, UV, and possibly X-ray sources. Observations are mostly consistent with these estimates.

Nonthermal emission mechanisms also operate in disks. Examples are: synchrotron emission by relativistic electrons spiraling around magnetic field lines and inverse Compton up-scattering of photons by relativistic electrons. Line emission because of electronic transition between energy levels provides a useful diagnostic of density, temperature, and velocities in the emitting region.

Accretion disks, being efficient sources of energy, can be very luminous. Their spectra are also very rich, extending all the way from radio to X-ray and γ-ray frequencies. In order to interpret the radiative signatures, one needs to understand transport and radiation processes in accretion disks.

1.2 Accretion disk phenomenology

Much of the phenomenology of accretion disks was developed in mid-1970's when two influential papers, by Shakura and Sunyaev [174], and Lynden-Bell and Pringle [121], appeared. It was shown that in the presence of a shear viscosity, an infinitesimal mass can carry away all the angular momentum of the inner fluid elements, facilitating mass accretion [121, 153]. The structure (thick or thin) and radiation spectrum (luminous or radiatively inefficient) of a disk depends mainly on the rate of matter inflow, $\dot{M}$ [174]. Of course the overall luminosity and accretion time scale depends on M_*,the mass of the central object.

A binary system consisting of a star and a compact object (black hole, neutron star, or white dwarf) is likely to be very common in the Galaxy. The outflow of matter from the star's surface—the stellar wind—is significant ($\sim 10^{-5} M_\odot$ /yr) for massive O-stars and Wolf-Rayet stars ($M \gtrsim 20 M_\odot$). In binary systems, an additional strong

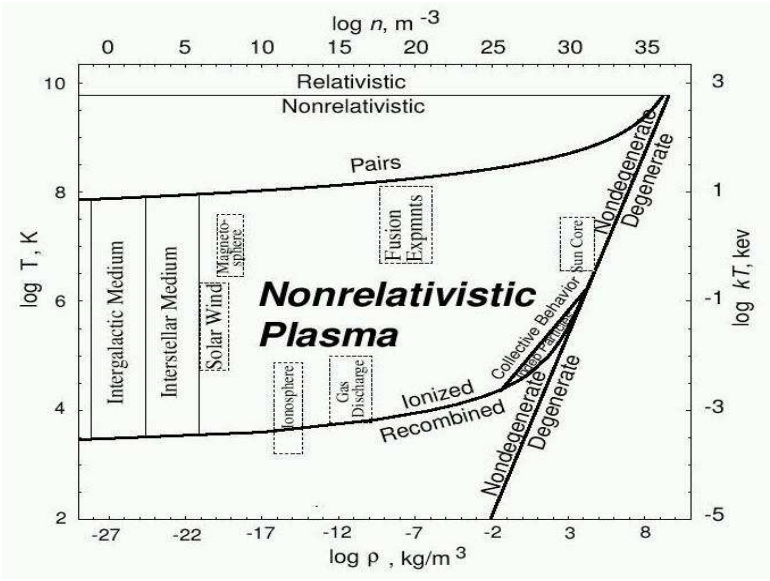

Figure 1.3: The density-temperature diagram for hydrogen in the regime where it behaves as a non-relativistic plasma. Many astrophysical systems including accretion disks are in the plasma state. The figure is taken from lecture notes by Niel Brandt, http://www.astro.psu.edu/users/niel/astro485/lectures/lecture08-overhead07.jpg

matter outflow connected with the Roche limiting surface is possible. The Roche surface is the surface around the star beyond which the gravitational influence of the compact object dominates. When a star leaves the main sequence at later stages of its evolution, it can increase in size and fill its Roche volume, giving rise to an intensive outflow of matter mostly through the inner Lagrangian point (an unstable equilibrium point between the star and compact object) [61]. Figure 1.1 shows an artist's impression of a binary accretion system, with a star filling its Roche lobe and accreting on to a compact object via a disk. Accretion in AGN is likely to be fed by the winds from nearby massive stars, or the infall of intergalactic gas. Once an accretion disk is formed around the compact object, the subsequent evolution does not depend on the source of matter.

Figure 1.3 shows the density-temperature phase diagram for hydrogen. This shows that the accretion disks with temperatures exceeding a few eV (and reasonable densities) are fully ionized. Most accretion disks, except possibly protostellar and proto-

planetary disks, are sufficiently ionized for the plasma description to be valid [29, 16]. Even relatively cold gas disks may have enough ionization by cosmic rays [63], X-rays [93], and radioactivity [168] to be sufficiently conducting for the MHD-like phenomena to occur.

Magnetohydrodynamics (MHD) is a good approximation for a magnetized plasma when the mean free path is much smaller than the scales of interest, e.g., in efficiently radiating, dense, thin disks. This is not always the case; the radiatively inefficient accretion flows (RIAFs), a motivation for this thesis, are believed to be collisionless with the mean free path comparable to (or even larger than) the disk size (see Table 1.2 for plasma parameters in the Galactic center disk). Ideal MHD, where resistive effects are negligible and the field is frozen into the plasma, is a good approximation for large scale dynamics of almost all astrophysical plasmas; as the dynamical scales are orders of magnitude larger than the resistive scale or the gyroradius scale. Even with a large separation between the dynamical and resistive/viscous scales, dissipation cannot be ignored—energy cascades from large scales to smaller scales, terminating at the dissipative scales, where it is dissipated in shocks and reconnection. In the inertial range of isotropic, homogeneous turbulence, energy dissipation rate balances the rate at which energy is injected, independent of resistivity and viscosity [62, 27].

In rest of the section we closely follow the review article by Balbus and Hawley to use the conservation of mass, energy, and angular momentum to derive the transport properties of disks. The widely used α model for turbulent stress is introduced [174].

1.2.1 Governing equations

Following [16], the conservation of total energy in magnetohydrodynamics (MHD), gives

$$\frac{\partial}{\partial t}\left(\frac{1}{2}\rho V^2 + \frac{3}{2}p + \rho\Phi + \frac{B^2}{8\pi}\right) + \nabla\cdot[\ ] = -\nabla\cdot\mathbf{F_{rad}}, \tag{1.1}$$

where ρ, $\mathbf{V}$, p, $\mathbf{B}$, and Φ are density, fluid velocity, pressure, magnetic field, and gravitational potential, respectively. The term on the right represents radiative losses. The conservative flux term $\nabla\cdot[\ ]$ consists of a dynamic contribution

$$\mathbf{v}\left(\frac{1}{2}\rho V^2+\frac{5}{2}p+\rho\Phi\right)+\frac{\mathbf{B}}{4\pi}\times(\mathbf{V}\times\mathbf{B}), \tag{1.2}$$

and a viscous contribution,

$$-\eta_V\left(\nabla\frac{V^2}{2}+\frac{\mathbf{V}}{3}\nabla\cdot\mathbf{V}\right)+\frac{\eta_B}{4\pi}(\nabla\times\mathbf{B})\times\mathbf{B}, \tag{1.3}$$

where, η_V is the microscopic kinematic shear viscosity, and η_B the microscopic resistivity. Here we use a uniform, isotropic viscosity for simplicity. The Braginskii viscosity is highly anisotropic as will be discussed later in the thesis. The dynamic flux in Eq. (1.2) consists of an advective flux of kinetic and thermal energy (the first term), and the Poynting flux of electromagnetic energy (the second term). The equation for angular momentum conservation in cylindrical, (R,ϕ,z), coordinate system is given by

$$\begin{aligned}\frac{\partial}{\partial t}(\rho R V_\phi) \quad &+ \quad \nabla\cdot R\left[\rho V_\phi\mathbf{V}-\frac{B_\phi}{4\pi}\mathbf{B_p}+\left(p+\frac{B^2}{8\pi}\right)\hat{\phi}\right]\\ &- \quad \nabla\cdot\left[\frac{R\eta_V}{3}(\nabla\cdot\mathbf{V})\hat{\phi}+\eta_V R^2\nabla\frac{V_\phi}{R}\right]=0,\end{aligned} \tag{1.4}$$

where $\hat{\phi}$ is the unit vector in the azimuthal direction, the subscript $\mathbf{p}$ refers to the poloidal magnetic field components (the R and z components). In an accretion disk, there is a net flux of energy and angular momentum in the radial direction, so the divergence terms in Eqs. (1.1) and (1.4) are dominated by the radial derivatives of radial fluxes.

1.2.2 Fluctuations

A fiducial disk system consists of a point mass potential situated at the center of the disk, with the gas going around in a Keplerian rotation, $\Omega^2 = GM_*/R^3$. The fluctuation velocity is given by V_R, $\delta V_\phi = V_\phi - R\Omega$, and V_z. When the azimuthal velocity $R\Omega$ much exceeds the isothermal sound speed $c_s = \sqrt{p/\rho}$, the disk is thin; the vertical structure is determined by hydrostatic balance, with the disk height scale $H = c_s/\Omega \ll R$. In this section we consider only thin disks because they are simpler, for the vertical dynamics and pressure forces do not play a significant role. For thick disks, where thermal forces are equally important and vertical motion is coupled to the motion in plane, there is no universally accepted standard model [141, 160, 31].

The radial flux of angular momentum from Eq. (1.4) is $R\left[\rho V_R(R\Omega + \delta V_\phi) - B_R B_\phi/4\pi\right]$. Taking an azimuthal average, integrating over height, and averaging over a narrow range ΔR in R, one obtains, $\Sigma R[R\Omega\langle V_R\rangle_\rho + \langle V_R\delta V_\phi - V_{AR}V_{A\phi}\rangle_\rho]$, where the surface density $\Sigma = \int \rho dz$, and for any X, $\langle X\rangle_\rho = 1/(2\pi\Sigma\Delta R)\int X\rho d\phi dR dz$. The notation V_{AR}, etc. denotes the Alfvén velocity, $\mathbf{V_A} = \mathbf{B}/\sqrt{4\pi\rho}$. The first term in the radial angular momentum flux is the direct inflow of angular momentum due to radially inward accretion of matter; the second term represents an outward component of flux due to turbulent transport because of statistical correlations in the velocity and magnetic stress tensors [191]. The $R\phi$ component of the stress, responsible for angular momentum transport (see Eq. 1.4), is $W_{R\phi} \equiv \langle V_R\delta V_\phi - V_{AR}V_{A\phi}\rangle_\rho$.

In steady state, the angular momentum flux must be divergence free, and thus vary as $1/R$, i.e., $\Sigma R^2(R\Omega\langle V_R\rangle_\rho + W_{R\phi})$ is independent of R. The condition of vanishing stress at the inner edge (R_*) gives, $\Sigma(\Omega R\langle V_r\rangle_\rho + W_{R\phi}) = \Sigma_*\Omega_* R_*\langle V_{r*}\rangle_\rho(R_*/R)^2$. Expressing in terms of the constant accretion rate, $\dot{M} = -2\pi R\Sigma\langle V_R\rangle_\rho$, leads to $-\dot{M}R\Omega/2\pi + \Sigma R W_{R\phi} = -\dot{M}R_*^2\Omega_*/2\pi R$. This gives an expression for the variation

of stress with radius as,

$$W_{R\phi} = \frac{\dot{M}\Omega}{2\pi\Sigma}\left[1 - \left(\frac{R_*}{R}\right)^{1/2}\right]. \tag{1.5}$$

Keeping only the second order terms in the energy flux in Eq. (1.2), one gets $\rho V_R(\Phi + R^2\Omega^2/2 + R\Omega\delta V_\phi) - (R\Omega/4\pi)B_R B_\phi$. Upon averaging, height integrating, and using the Keplerian potential $\Phi = -R^2\Omega^2$, energy flux becomes $F_E = \dot{M}R\Omega^2/4\pi + \Sigma R\Omega W_{R\phi}$. Substituting for Ω and using Eq. (1.5) for the stress tensor, this reduces to

$$F_E = \frac{3GM_*\dot{M}}{4\pi R^2}\left[1 - \frac{2}{3}\left(\frac{R_*}{R}\right)^{1/2}\right]. \tag{1.6}$$

The energy deposited by this flux is the source of disk's luminosity. Minus the divergence of the flux gives the disk surface emissivity (energy per unit area per unit time), Q. Dividing by a factor of two for each side of the disk gives

$$Q = \frac{3GM_*\dot{M}}{8\pi R^3}\left[1 - \left(\frac{R_*}{R}\right)^{1/2}\right]. \tag{1.7}$$

The $Q - \dot{M}$ relation depends on local energy conservation and is, as expected, independent of the form of the stress tensor (see [174, 153]). Eliminating $\dot{M}$ between Eqs. (1.5) and (1.7) yields

$$Q = \frac{3}{4}\Sigma\Omega W_{R\phi} = \frac{3}{4}\Sigma\Omega\langle V_R\delta V_\phi - V_{AR}V_{A\phi}\rangle_\rho, \tag{1.8}$$

a kind of fluctuation-dissipation relation for accretion disks [13]. From Eqs. (1.5) and (1.8), it is clear that the correlation of velocity (and magnetic field) fluctuation components is responsible for much of the disk transport and luminosity.

Above discussion is valid only for a cold, thin disk where pressure can be ignored. For a radiatively inefficient, hot, thick disk the pressure term $(5/2)pV_R$ should be

included in the radial energy flux; $\nabla \cdot F_E \approx 0$ in absence of radiation, and the gravitational energy released from accretion is converted into thermal and kinetic energies.

Total luminosity emitted from R_* to R is, $L(R_* < R) = 2\pi[R_* F_E(R_*) - R F_E(R)] = (GM_*\dot{M}/2R_*)[1 - 3R/R_* + (R_*/R)^{3/2}]$. In the limit $R \to \infty$, $L = GM_*\dot{M}/2R_*$, which shows that half the binding energy of the innermost orbit is converted to radiation. The other half is retained as kinetic energy. The fate of the residual energy depends on the nature of central accretor. If a stellar surface is present, remaining energy will be radiated in a boundary layer; if the central object is a black hole, the energy may be swallowed and lost.

1.2.3 α disk models

Although the relationship between disk's surface emissivity Q and the mass accretion rate $\dot{M}$ is independent of stress tensor, most other relations involve a dependence on $W_{R\phi}$. Recognizing the central importance of $W_{R\phi}$ and its computational inaccessibility, Shakura and Sunyaev [174] suggested a natural scaling for the stress tensor, $W_{R\phi} = \alpha c_s^2$, where $\alpha \lesssim 1$ is a parameter. The idea behind the α prescription is that the turbulent velocities, whose correlation determines $W_{R\phi}$, are limited by the sound speed c_s, as supersonic velocities will be quickly dissipated in shocks. The α formalism bypasses the thorny issue of disk turbulence, and can be thought as a closure for the stress tensor. The α formalism can be thought of as equivalent to a "turbulent viscosity"

$$\nu_t = \alpha c_s H \tag{1.9}$$

that is similar to microscopic viscosity in Navier Stokes equation. The role of random particle velocity is played by c_s, and the scale height H is the effective mean free path (eddy size). This is a closure based on plausibility arguments and is not rigorous like the Chapman-Enskog procedure [47]. The α formalism is the basis of much of

observationally driven disk phenomenology. The radial dependence of various physical quantities, like temperature, density, height, etc., can be obtained in terms of parameters $\dot{M}$ and α [61].

1.3 MRI: the source of disk turbulence

A breakthrough occurred when Balbus and Hawley proposed the magnetorotational instability (MRI), an instability of differentially rotating flows, as the source for turbulence and transport in accretion disks [14]. Before this, a robust mechanism to sustain turbulent angular momentum transport in accretion disks was unknown. Although the instability was described in its global form for magnetized Couette flow by Velikhov [197] and Chandrasekhar [44], its importance for accretion disks was not recognized. In his classic book [45], Chandrasekhar points out the essential feature of the MRI, "in the limit of zero magnetic field, a sufficient condition for stability is that the angular speed, $|\Omega|$, is a monotonic increasing function of r. At the same time, any adverse gradient of angular velocity can be stabilized by a magnetic field of sufficient strength."

Both local [86] and global [5, 81, 188] numerical simulations have confirmed that the MRI can amplify small perturbations to nonlinear turbulent motions. Correlations between the radial and azimuthal fields results in a sustained turbulent stress corresponding to $\alpha \equiv W_{R\phi}/p \sim 0.001 - 0.5$, enough to account for typical disk luminosities. Next, we discuss the inadequacy of the hydrodynamic models, followed by the linear and nonlinear characteristics of the MRI.

1.3.1 Insufficiency of hydrodynamics

In the Boussinesq approximation ($\nabla \cdot \mathbf{V} = 0$ in the equation of motion), if we ignore pressure, then a fluid element disturbed slightly from its Keplerian orbit will execute

retrograde epicycles at a frequency κ ($\kappa^2 \equiv \frac{1}{R^3}\frac{d(R^4\Omega^2)}{dR}$), as seen by an observer in an unperturbed Keplerian orbit. The criterion for local linear stability is simply $\kappa > 0$, i.e., specific angular momentum increases outwards, the Rayleigh criterion.[1] Therefore, a Keplerian disk with specific angular momentum $R^2\Omega \sim R^{1/2}$, increasing outwards is linearly stable, unable to produce (and sustain) nonlinear turbulent stress.

A rotating shear flow is different from a planar shear flow because of the coriolis force. Coriolis force is responsible for stable epicyclic oscillations in Keplerian flows, whereas planar shear flows are marginally stable in the linear regime. Nonlinear local shearing box simulations show that while planar shear flows can be nonlinearly unstable and become turbulent even at relatively small Reynolds numbers [21], $10^3 - 10^4$ (orders of magnitude smaller than the true Reynolds number for disks), Keplerian disks are nonlinearly stable and give no turbulence over the same range of Reynolds numbers [17, 85]. This is because stable epicycles prevent nonlinear instabilities to develop in Keplerian flows. Whether turbulence and transport can occur in hydrodynamic Keplerian flows, is still not universally agreed. There are experimental claims that the Keplerian disks are nonlinearly unstable [164], but recent experiments, with more carefully controlled boundary conditions (especially Eckman flows), which directly measure the Reynolds stress, show otherwise [39]. Also, there is some recent work on transient amplification in the linear regime, that can give rise to nonlinear amplitudes (and maybe turbulence) in hydrodynamic differentially rotating flows [42, 2, 195].

Convective turbulence was also proposed as a source of enhanced shear viscosity [118]. Convection is believed to arise from heating due to energy dissipated in the disk midplane. The hope was that somehow convective blobs can cause nonlinear correlations to produce non-vanishing stress. However, the linear analysis of convective instability in Keplerian flows gives a wrong sign of stress [166], with inward trans-

[1]The Rayleigh criterion applies only for axisymmetric disturbances.

port of angular momentum. Three dimensional simulations of convectively unstable disk show very small angular momentum transport ($\alpha \sim -10^{-4}$), and in the opposite direction [183]. None of the local hydrodynamic mechanisms to date are able to give sufficient angular momentum transport.[2] This launches us to the study of the dramatic effect of magnetic fields on accretion disk stability.

1.3.2 MHD accretion disks: Linear analysis

The ideal MHD equations are

$$\frac{\partial \rho}{\partial t} + \nabla \cdot (\rho \mathbf{V}) = 0, \tag{1.10}$$

$$\rho \frac{\partial \mathbf{V}}{\partial t} + \rho \left(\mathbf{V} \cdot \nabla\right) \mathbf{V} = \frac{(\nabla \times \mathbf{B}) \times \mathbf{B}}{4\pi} - \nabla p + \mathbf{F_g}, \tag{1.11}$$

$$\frac{\partial \mathbf{B}}{\partial t} = \nabla \times (\mathbf{V} \times \mathbf{B}), \tag{1.12}$$

$$\frac{\partial e}{\partial t} + \nabla \cdot (e\mathbf{V}) = -p \nabla \cdot \mathbf{V}, \tag{1.13}$$

where, $\mathbf{F_g}$ is the gravitational force, and $e = p/(\gamma - 1)$ relates internal energy density and pressure ($\gamma = 5/3$ in a 3-D non-relativistic plasma). Making $\mathbf{B} = 0$ in the MHD equations gives the hydrodynamic equations.

WKB analysis in a Keplerian disk

The linear response of a Keplerian hydrodynamic flow is stable epicyclic motion, however, addition of weak magnetic fields renders it unstable. Before considering Keplerian flows, it is useful to study waves in a homogeneous, non-rotating equilibrium. Linear waves in MHD and hydrodynamics are quite different. MHD is richer in waves with fast, Alfvén, and slow modes, compared to hydrodynamics with only an isotropically propagating sound wave [111]. As the name suggests, the fast mode

[2] Global modes like Papaloizou-Pringle instability [146, 72], and spiral shocks can in principle cause turbulence and transport, however, their role as a universal transport mechanism for Keplerian disks is not clear [16].

has the fastest phase speed and propagates isotropically. The Alfvén mode is intermediate with propagation along the field lines, and the slow mode with the smallest phase speed also propagates along the field lines. In addition to these, there is a non-propagating entropy mode with anticorrelated density and temperature fluctuations.

Consider a differentially rotating disk threaded by a magnetic field with a vertical component B_z and an azimuthal component B_ϕ. Consider WKB perturbations of the form $\exp i(\mathbf{k}\cdot\mathbf{r}-\omega t)$, $kR \gg 1$. Notation is the standard one: $\mathbf{k}$ is the wave vector, $\mathbf{r}$ the position vector, ω the angular frequency, and t the time. Linear perturbations are denoted by δ. Only a vertical wave number is considered, $\mathbf{k} = k\hat{\mathbf{z}}$. The local linear equations are

$$-\omega\frac{\delta\rho}{\rho} + k\delta V_z = 0, \tag{1.14}$$

$$-i\omega\delta V_R - 2\Omega\delta V_\phi - i\frac{kB_z}{4\pi\rho}\delta B_R = 0, \tag{1.15}$$

$$-i\omega\delta V_\phi + \frac{\kappa^2}{2\Omega}\delta V_R - i\frac{kB_z}{4\pi\rho}\delta B_\phi = 0, \tag{1.16}$$

$$-\omega\delta V_z + k\left(\frac{\delta p}{\rho} + \frac{B_\phi\delta B_\phi}{4\pi\rho}\right) = 0, \tag{1.17}$$

$$-\omega\delta B_R = kB_z\delta V_R, \tag{1.18}$$

$$-i\omega\delta B_\phi = \delta B_R\frac{d\Omega}{d\ln R} + ikB_z\delta V_\phi - B_\phi ik\delta V_z, \tag{1.19}$$

$$\delta B_z = 0, \tag{1.20}$$

$$\frac{\delta p}{p} = \frac{5}{3}\frac{\delta\rho}{\rho}. \tag{1.21}$$

The resulting dispersion relation is (Eq. (99) in [16])

$$\begin{aligned}[\omega^2 &- (\mathbf{k}\cdot\mathbf{V_A})^2][\omega^4 - k^2\omega^2(a^2+V_A^2) + (\mathbf{k}\cdot\mathbf{V_A})^2k^2a^2] \\ &- \left[\kappa^2\omega^4 - \omega^2\left(k^2\kappa^2(a^2+V_{A\phi}^2) + (\mathbf{k}\cdot\mathbf{V_A})^2\frac{d\Omega^2}{d\ln R}\right)\right] \\ &- k^2a^2(\mathbf{k}\cdot\mathbf{V_A})^2\frac{d\Omega^2}{d\ln R} = 0,\end{aligned} \tag{1.22}$$

where $a^2 = (5/3)P/\rho$, $\mathbf{V_A} = \mathbf{B}/\sqrt{4\pi\rho}$. Only the first term in the dispersion relation, Eq. (1.22), is non-zero in the non-rotating limit; the roots of the dispersion relation correspond to the fast, Alfvén, and slow modes.

The effect of Keplerian rotation on the three MHD modes is shown in Fig. (15) of Balbus and Hawley's review article [16], with ω^2 plotted as a function of Ω^2 (also see Figure 3.4). It shows that ω^2 becomes negative for the slow mode when $d\Omega^2/d\ln R > (\mathbf{k}\cdot\mathbf{V_A})^2$, i.e., slow modes becomes unstable. This destabilized MHD slow mode in differentially rotating flows is the MRI. For a fixed wave number there is an upper limit on the field strength for the MRI to exist, i.e., it is a weak field instability.

Spring model of the MRI

A simple physical description of the MRI, based on the spring model of Balbus and Hawley, is presented; the discussion closely follows [16]. It is useful to study the instability in the Boussinesq limit, where fast waves are eliminated. The simplest model to think is of axisymmetric perturbations on uniform vertical magnetic field in a Keplerian disk. If a fluid element is displaced from its circular orbit by ξ, with a spatial dependence e^{ikz}, induction equation leads to $\delta\mathbf{B} = ikB\xi$. Magnetic tension force is then $ikB\delta\mathbf{B}/4\pi\rho = -(\mathbf{k}\cdot\mathbf{V_A})^2\xi$. In an incompressible, pressure free limit, the equations of motion become

$$\ddot{\xi}_R - 2\Omega\dot{\xi}_\phi = -\left(\frac{d\Omega^2}{d\ln R} + (\mathbf{k}\cdot\mathbf{V_A})^2\right)\xi_R, \tag{1.23}$$

$$\ddot{\xi}_\phi + 2\Omega\dot{\xi}_R = -(\mathbf{k}\cdot\mathbf{V_A})^2\xi_\phi. \tag{1.24}$$

As before, 2Ω and $d\Omega^2/d\ln R$ terms represent coriolis and tidal forces, respectively. These equations also describe two orbiting point masses connected with a spring of spring constant $(\mathbf{k}\cdot\mathbf{V_A})^2$.

Consider two point masses, initially at the same orbital location, displaced slightly

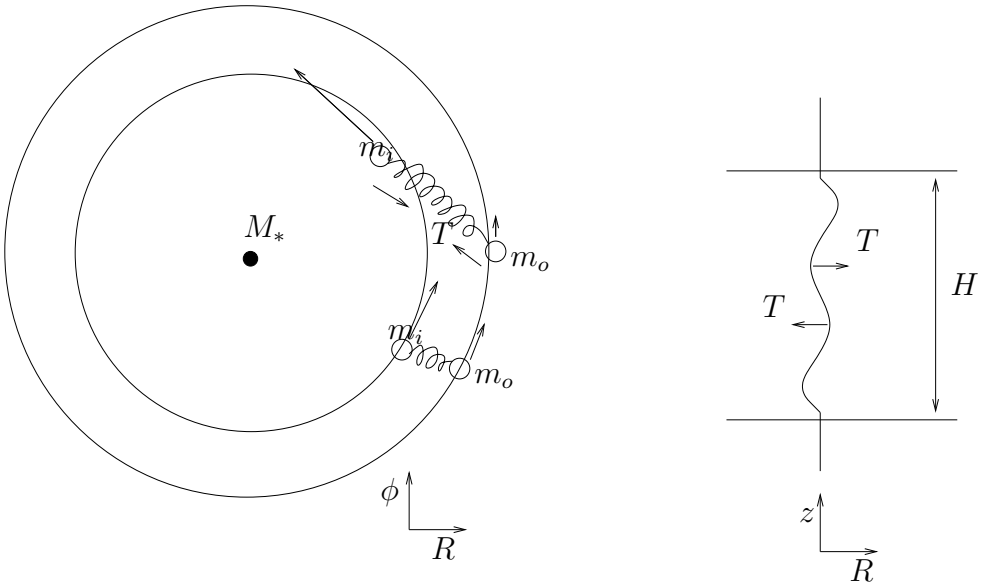

Figure 1.4: Spring model of the MRI. Left part shows a top view of inner and outer point masses m_i and m_o connected by a spring. Mass m_i is moving faster than m_o because velocity decreases outwards in a Keplerian flow. Spring force slows down m_i, and makes m_o go faster. Inner mass falls in as it loses angular momentum to the outer one, which moves out. Right part shows a side view of a perturbed field line that results in a restoring spring force. The field strength should be weak enough for an unstable mode to fit within a disk height scale, H.

in the radial direction, as shown in Figure 1.4. The inner mass m_i at radius R_i is connected via a spring to outer mass m_o at R_o. In a Keplerian disk, the inner mass rotates faster than the outer one. In the absence of a spring both execute stable epicycles. However, the spring stretches and builds up a tension T. T pulls backward on m_i and forward on m_o. Thus, m_i slows down and loses angular momentum to m_o which gains speed. This means that the slower m_i (compared to the local Keplerian velocity) cannot remain in orbit at R_i and must drop to a yet lower orbit. Similarly, m_o acquire too much angular momentum to stay at R_o and must move outwards. The separation widens, the spring stretches yet more, T goes up, and the process runs away. This is the essence of weak field instability in differentially rotating flows. The presence of other field components does not affect this picture, as by selecting $\mathbf{k} = k_z\hat{\mathbf{z}}$ we have ensured that only vertical field couples dynamically. It is very crucial that the spring be weak; if spring is very stiff, there are many stable vibrations in an orbital time and no net transport of angular momentum. The right side of Eq. (1.23) reproduces the stability criterion for the slow mode, $(\mathbf{k}\cdot\mathbf{V_A})^2 > -d\Omega^2/d\ln R$. One can always choose a small enough k to make a Keplerian disk unstable. Thus, the necessary and sufficient condition for the stability of a magnetized differentially rotating disk is $d\Omega^2/d\ln R > 0$.

Just how large a wavelength is permitted? In order for the WKB approximation to be valid, at least a half wavelength needs to fit in the box height H. The stability criterion for a Keplerian disk becomes $V_A^2 > \frac{H^2}{\pi^2}\frac{d\Omega^2}{d\ln R} \sim (6/\pi^2)c_s^2$, i.e., the Alfvén speed must significantly exceed the sound speed, if all the modes in a disk thickness are to be stable. The MRI is called a weak field instability because it requires pressure to exceed magnetic energy ($\beta = 8\pi p/B^2 \gtrsim 1$). It is interesting to note that there is no lower limit on the strength of the magnetic field for the instability to exist if dissipation scales are arbitrarily small [106].

The dispersion relation from Eqs. (1.23) and (1.24), on assuming $\xi \sim \exp(-i\omega t)$,

is

$$\omega^4 - \omega^2[\kappa^2 + 2(\mathbf{k}\cdot\mathbf{V_A})^2] + (\mathbf{k}\cdot\mathbf{V_A})^2\left((k\cdot V_A)^2 + \frac{d\Omega^2}{d\ln R}\right) = 0, \tag{1.25}$$

which is precisely the $a \to \infty$ Boussinesq limit of Eq. (1.22). Eq. (1.25) is a quadratic in ω^2 which can be solved easily. The fastest growth rate for a Keplerian disk is $\gamma_{max} = (3/4)\Omega$, and occurs at $(\mathbf{k}\cdot\mathbf{V_A})_{max} = (\sqrt{15}/4)\Omega$. This is a very fast instability that would cause amplification by $\sim 10^4$ in energy, per orbit. The instability is very robust, independent of the magnetic field orientation. In presence of a toroidal field the MRI is non-axisymmetric for the perturbations to couple to the field [15]. Nonlinear correlations resulting from this instability can provide a sizeable stress to explain fast angular momentum transport in disks, as we see in the next subsection.

1.3.3 MHD accretion disks: Nonlinear simulations

Tremendous progress has been made in the understanding of growth and saturation of the MRI. Numerical studies started with unstratified local shearing box simulations [82, 86] using the ZEUS MHD code [185, 186]. In the shearing box limit, equations are written in a frame rotating with the mean flow. There is shear in a Keplerian box with $d\Omega/d\ln R = -3/2$. Boundary conditions are periodic in y- (azimuthal) and $z-$ (vertical) directions, and shearing periodic in x- (radial direction).[3]

Shearing box simulations start with a random white noise imposed on an initial equilibrium. In simulations with a net vertical flux, magnetic energy increases exponentially until the channel solution (the nonlinear form of the fastest growing mode with $k_z V_{Az}/\Omega \sim 1$) becomes unstable to secondary Kelvin-Helmholtz type instabilities [75]. Magnetic energy increases by several orders of magnitude before secondary instabilities break the channel solutions into turbulence. Magnetic energy saturates at

[3]Shearing periodic means that periodic boundary conditions are applied after a time dependent remap in y- direction at the x- boundaries [86, 16]. There is a jump of $-(3/2)\Omega L_x$ in V_y between the inner and outer radial faces to take differential rotation into account. There are similarities between this and the boundary conditions used in fusion energy research to handle sheared magnetic fields in flux-tube simulations of turbulence [49, 77, 22].

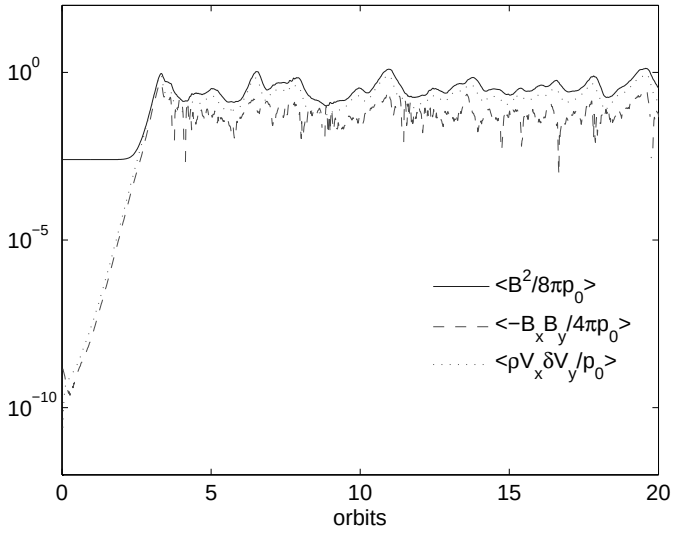

Figure 1.5: Volume averaged magnetic energy, Maxwell stress, and Reynolds stress normalized to the initial pressure, for an initial $\beta = 400$ vertical field. The Maxwell stress is ~ 3 larger than the Reynolds stress. Time and volume averaged values in the turbulent state are: $\alpha = 0.286$ and $\beta = 2.56$ (case ZMl in Table 4.1 from Chapter 4).

sub-equipartition ($\beta = 8\pi p_0/B^2 \sim 1 - 100$), with $\alpha = \langle\langle(\rho V_x \delta V_y - B_x B_y/4\pi)\rangle\rangle/p_0 \sim 0.001 - 0.5$, where "$\langle\langle\rangle\rangle$" represents a box and time average in the turbulent state. Figure 1.5 shows the time evolution of magnetic energy, and Maxwell and Reynolds stress for a simulation with an initial vertical field with $\beta = 400$. Magnetic energy is dominated by the toroidal component. All variables show large fluctuations from the mean in the turbulent state. Magnetic and kinetic energy power spectra are peaked at low wave numbers, indicating significant energy at scales comparable to the box size.

Nonlinear simulations of an initially toroidal field observe that the growth rates are smaller than the vertical field runs [86, 124]. The growth rate of the non-axisymmetric mode is fastest for largest vertical wave number k_z [15], but in simulations, these wave numbers are damped because of a finite resolution. In the saturated state dominated by large wave numbers $\alpha \sim 0.01$, smaller than the net vertical flux cases. Simulations

with no net flux, $\langle \mathbf{B} \rangle = 0$, also result in sustained MHD turbulence and transport at large scales. However, both magnetic energy and turbulent stress are smaller by a factor of $10 - 100$ compared with the net vertical field case [87]. Toroidal fields and the Maxwell stress dominate the other components, irrespective of the initial field configuration. Total stress is roughly proportional to the magnetic energy for all cases.

Stratified shearing boxes with vertical gravity were simulated to closely model a real accretion disk in the local limit [38, 184]. Vertical stratification allow the possibility of vertical motions driven by magnetic buoyancy. Stratified simulations are not very different from the unstratified ones because the Mach number (the ratio of fluid velocity and sound speed, V/c_s) is much less than unity for MRI turbulence. This ensures that the MRI timescale ($1/\Omega = H/c_s$) is much faster than the time scale for buoyant motions at large scales (H/V). Results are similar for the adiabatic and isothermal equations of state [184]. While the $R - \phi$ dynamics is dominated by the MRI, vertical stratification can result in significant mixing in the $z-$ direction. Stratified simulations show the eventual emergence of a magnetically dominated corona stable to the MRI because of buoyantly rising magnetic fields [132]. It is reassuring that irrespective of initial fields geometry, equation of state, boundary conditions, vertical stratification, numerical methods, etc., MHD turbulence and efficient transport of angular momentum always ensues. But the question of the exact saturation level and its dependence on physical and numerical parameters, such as net vertical flux, box size, or dissipation mechanisms, remain a topic of continued research [87, 167, 198, 28, 150].

Local shearing boxes have been used extensively to understand MRI turbulence in presence of other physical effects, e.g., resistivity [59], ambipolar diffusion [88], Hall effect [169], radiation and the photon bubble instability [194, 193], and the thermal instability [151].

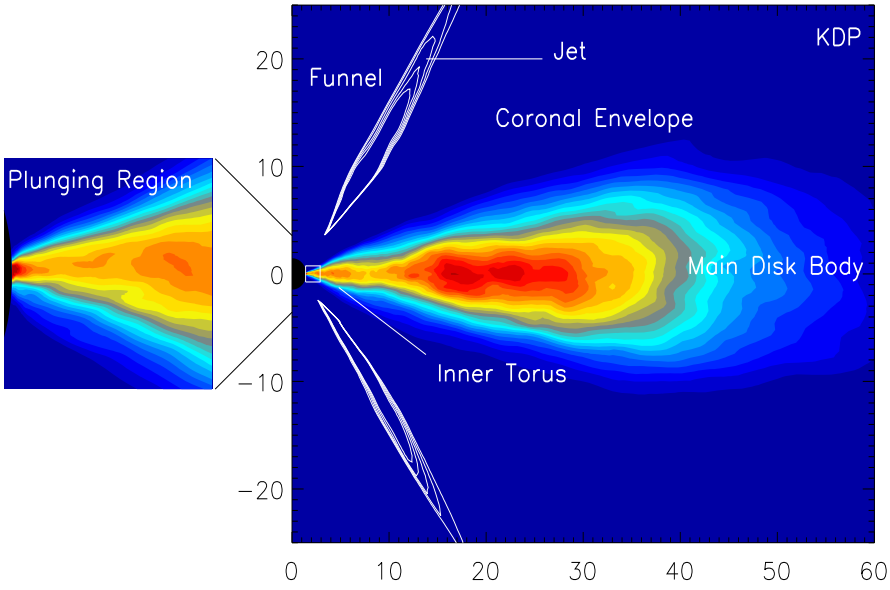

Figure 1.6: The inner regions of an accretion disk around a black hole calculated in a GRMHD simulation (Figure 3 of [199]). The black hole is at the origin with an event horizon of radius unity. The accretion disk rotates around the vertical direction. Color contours show the density distribution, with red representing highest density and dark blue the lowest. There is a hot magnetized corona above the disk, and between the corona and the rotation axis there is an ejection of mildly relativistic plasma. This example shows a non-radiating, thick disk.

The effect of MRI turbulence was first observed in global 2-D MHD simulations of Shibata and Uchida with a net vertical flux [178], but the reason for the disruption of the flow was not understood. Starting from the 2-D simulations [178, 187], tremendous progress in computer hardware and algorithms has made it possible to simulate realistic disks around rotating Kerr black holes with general relativistic MHD (GRMHD) in 3-D [199, 105]. Figure 1.6 shows the structure of a disk from a GRMHD simulation [199]. In addition to the efficient angular momentum transport in disks due to the MRI, global simulations allows one to study angular momentum extraction by global mechanisms such as magnetic braking and winds [33], and extraction of black hole spin energy in form of jets [34, 128, 102, 105]. Global simulations have also been used to understand the structure of thick disks in radiatively inefficient accretion flows (RIAFs, see Fig. 1.6), the subject of the next section [189, 188, 83, 155].

1.4 Radiatively inefficient accretion flows

This section borrows heavily from an unpublished document on the motivation for studying radiatively inefficient accretion flow (RIAF) regimes, by E. Quataert. There is growing observational evidence for the presence of supermassive black holes (SMBHs) in galactic nuclei. High resolution imaging of the stellar orbits around a dark object in the Galactic center, using adaptive optics, provides a compelling evidence for a $4.1 \pm 0.6 \times 10^6 M_\odot M_\odot$ SMBH [171, 71] (see Figure 1.7). Very large baseline interferometry (VLBI) observations of water masers in NGC 4258 show gas in a Keplerian orbit about a SMBH [134]. More generally, stellar motions and radiation from hot gas in the central regions of nearby galaxies have shown that SMBHs are present in nearly every galaxy with a bulge component [122, 70, 58]. [4]

One of the puzzles about many SMBHs is their extreme low luminosity, despite their gas rich environments. In contrast, the Active Galactic nuclei (e.g., quasars),

[4]The bulge component of a galaxy is the central roughly spherical region with old stars.

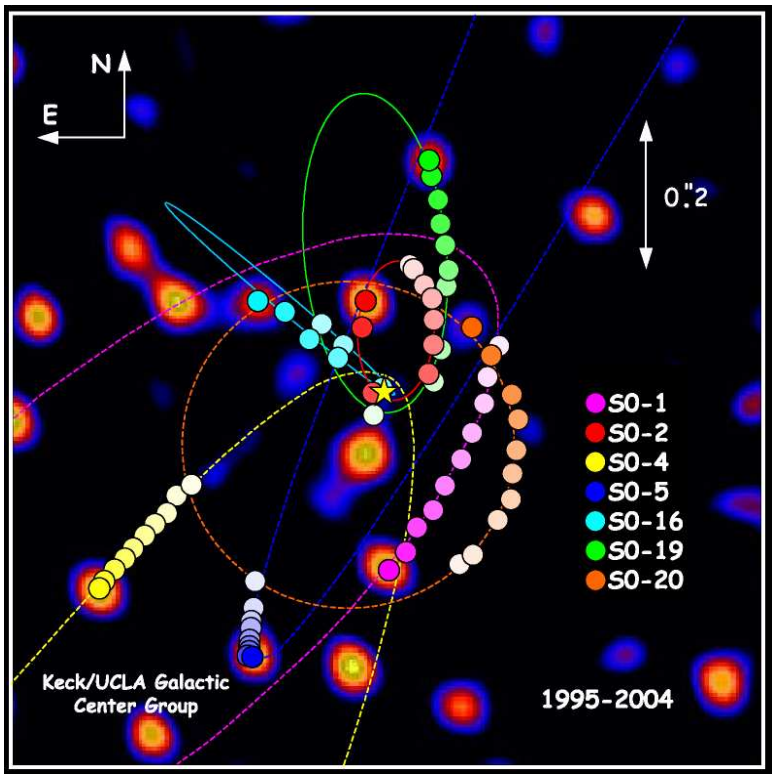

Figure 1.7: Keck observations of stellar orbits in the central 1×1 arcsecond (0.13 light years) of our Galaxy are shown. Stars show significant motion over a period of 9 years. Changing stellar locations with time, and best fitting Keplerian orbits are indicated. The orbital parameters confirm the presence of a $4.1 \pm 0.6 \times 10^6 M_\odot$ black hole in the center of our Galaxy. Source: http://www.astro.ucla.edu/~ghezgroup/gc/pictures/orbitsOverImage04.shtml

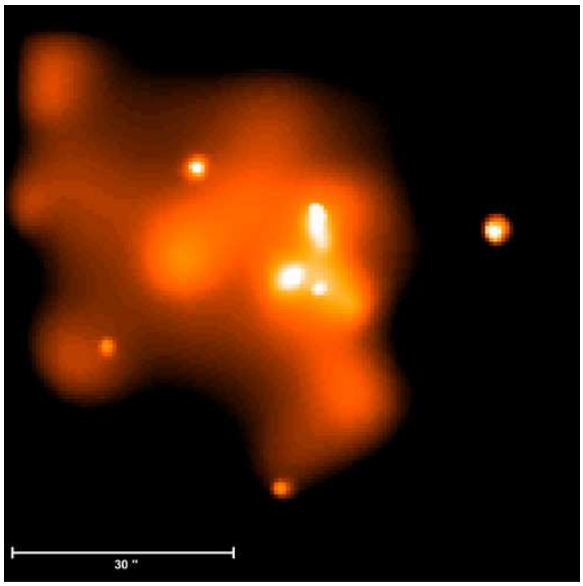

Figure 1.8: Chandra X-ray image of the innermost 10 light years (≈ 100 times larger than Figure 1.7) at the center of our Galaxy. The image shows an extended cloud of hot gas surrounding the supermassive black-hole Sagittarius A* (larger white dot at the very center of the image—a little to the left and above the smallest white dot). This gas glows in X-rays as it has been heated to a temperature of millions of degrees by shock waves produced by winds from young massive stars (and perhaps by supernova explosions). Source: http://chandra.harvard.edu/photo/2000/0204/index.html

which are also powered by accretion onto SMBHs, are luminous enough to outshine the rest of the galaxy. Our Galactic center (GC) is the canonical example of low luminosity accretion (see Figure 1.8) [139]. The winds from massive stars in the central ~ 0.1 pc of the Galactic center feed the black hole at an estimated Bondi accretion rate of $\dot{M}_{\rm Bondi} \approx 10^{-5} M_\odot$ /yr (see Appendix A.2 for Bondi accretion model) [8, 129, 157].[5] If this gas were to accrete onto the black hole with $\approx 10\%$ efficiency (typical of the Active Galactic Nuclei), the luminosity would be $\approx 10^{41}$ erg s^{-1}, five orders of magnitude larger than the observed luminosity (see Table 1.1) [156].

Table 1.1: Dim SMBHs in the Galactic center and nearby galaxies

Galaxy	$M_{\rm SMBH}$ 10^8 M$_\odot$	$\dot{M}_{\rm Bondi}$ M$_\odot$ yr^{-1}	$L_{\rm Bondi}{}^a$ erg s^{-1}	$L_{\rm X}{}^b$ erg s^{-1}	$L_X/L_{\rm Bondi}$
Milky Way[c]	0.03	10^{-5}	6×10^{40}	$2 \times 10^{33} - 10^{35}$	$3 \times 10^{-8} - 10^{-6}$
NGC 1399[d]	10.6	4×10^{-2}	2×10^{44}	$\lesssim 10^{39}$	$\lesssim 5 \times 10^{-6}$
NGC 4472[d]	5.6	8×10^{-3}	5×10^{43}	$\lesssim 10^{39}$	$\lesssim 2 \times 10^{-5}$
NGC 6166[e]	10	3×10^{-2}	2×10^{44}	10^{40}	5×10^{-5}
NGC 4636[d]	0.8	8×10^{-5}	5×10^{41}	$\lesssim 3 \times 10^{38}$	$\lesssim 6 \times 10^{-4}$

[a] $0.1 \dot{M}_{\rm Bondi} c^2$ [b] $2 - 10$ keV luminosity or an upper limit [c] [7, 8] [d] [119] [e] [125]
Sgr A* shows ≈ 100 times larger X-ray luminosity in the flaring state as compared to the quiescent state. The total RIAF luminosity ($L_{\rm Tot}$) is dominated by the radio emission, which is 2-3 orders of magnitude larger than the quiescent X-ray output in case of Sgr A*, so that $L_{\rm Tot}/L_{\rm Bondi} \sim 10^{-5}$ is still surprisingly small [156].

The Chandra X-ray Observatory, with its excellent spatial resolution (0.5 arcseconds), has put stringent constraints on the nuclear emission in a large number of nearby galaxies [90, 119, 125]. Table 1.1 gives some examples. In addition to the observed X-ray luminosity L_X and the mass of the SMBH, the table lists the observationally inferred Bondi accretion rate and "Bondi luminosity." Bondi rate is the accretion rate calculated from the density and temperature in the vicinity of the black hole (measured on $\sim 1''$ scales, which is $\sim 10^5 - 10^6$ Schwarzschild radii for the

[5] The hot wind from the X-ray source IRS 13E1 alone supplies $\approx 10^{-3} M_\odot$ yr^{-1} [137]; however, much of the hot gas in the GC is gravitationally unbound, leaving only a small fraction to be accreted by the central black hole.

systems in Table 1.1), and assuming spherical hydrodynamic accretion (see Appendix A.2). Bondi luminosity is the luminosity if the ambient gas accretes onto the SMBH at the Bondi rate and emits with $\approx 10\%$ efficiency. For all cases in Table 1.1, L_X is much less than the Bondi luminosity (which is orders of magnitude smaller than the Eddington limit for these systems). Thus, the observed luminosities are orders of magnitude smaller than simple theoretical predictions. Moreover, these discrepancies are not unique to X-ray observations, but are present in high resolution observations from the radio to the gamma-rays [89].

1.4.1 RIAF models

With compelling evidence for low luminosity SMBHs in the Galactic center and nearby galaxies, one needs to account for their extreme dimness. The explanation for their low luminosity must lie in how the surrounding gas accretes onto the central black hole. The standard accretion disk model is that of a geometrically thin, optically thick disk [174], applied extensively to luminous accreting sources in X-ray binaries and AGN [103, 56]. Low luminosity disks are fundamentally different; radiatively inefficient disks retain most of the accretion energy as thermal motion and puff up to become thick. Also, RIAFs show no significant black body component in their spectra in infrared-UV [114, 89, 161]; this emission is seen in luminous sources such as Seyferts and quasars [103]. Most low luminosity disk models have appealed to modes other than thin disks. Accretion disks where very little of the gravitational potential energy of the accreting gas is radiated away is referred to as radiatively inefficient accretion flows (RIAFs).

The plasma in RIAFs is hot and dilute because the gravitational energy released from accretion is stored as thermal energy. Because of the low densities and high temperatures, Coulomb collisions are inefficient at exchanging energy between the electrons and protons (see Table 1.2). If protons and electrons are heated to their

respective virial temperatures without exchanging energy, then protons will be hotter than electrons by their mass ratio $m_p/m_e \approx 2000$. But the temperatures depend on how energy released from accretion is dissipated into electrons and ions, which remains poorly understood. Most RIAF models assume that protons ($\sim 10^{12}$ K) are much hotter than the electrons ($\sim 10^{10} - 10^{12}$ K) [156]. The electron temperature is not well constrained but crucial as it determines the radiation that we see. The hot RIAFs are thus very different from the thin accretion disks, which are much cooler ($\sim 10^5 - 10^6$ K) and denser. In addition, because of the different physical conditions in the accretion flow, thin disk and RIAF models predict very different multiwavelength spectra (e.g., RIAFs are optically thin and do not produce blackbody emission).

Two ways to make a disk radiatively inefficient are: 1) energy released from accretion at Bondi rate is channeled preferentially into poorly radiating ions, which are eventually swallowed (with their energy) by the hole; and 2) instead of accreting all the available gas supply, processes like winds and outflows, and convection can constrict the net accretion ($\dot{M} \ll M_{\rm Bondi}$) onto the black hole.

The original RIAF models by Ichimaru (1977) and Rees et. al. (1982; the "ion torus" model) [92, 163] were based on the first approach. These models were revived in the 1990s, and extensively applied to observed systems, under the name advection-dominated accretion flows (ADAFs), by Narayan, Abramowicz, and others [141, 142, 1]. In ADAF models, the gas accretes at about the Bondi rate, but the radiative efficiency is $\ll 10\%$, providing a possible explanation for the very low luminosity of most galactic nuclei [163, 57]. The radiative efficiency is very low because it is assumed that the electrons, which produce the radiation we see, are much colder than the ions which are advected (with their thermal energy) on to the hole. Thus, instead of energy release in the form of radiation like in the cool, thin disks, energy is lost forever to the black hole in ADAF models.

The past few years have seen new steps in the theoretical understanding of RIAFs.

In particular, hydrodynamic and MHD numerical simulations of RIAFs have been performed [189, 94, 188, 84, 83, 95, 149, 154, 155]. The hydrodynamic simulations based on α model for stress (e.g., [189, 94, 154]) found that convection can stall accretion, with density varying like $\rho \sim r^{-1/2}$ with radius, as compared to a steeper $\sim r^{-3/2}$ dependence in ADAFs and Bondi accretion (see [141] and Appendix A.2). These simulations motivated analytical self-similar models known as convectively dominated accretion flows (CDAFs). The reason for a less steep dependence of density on radius is that the mass accretion rate in CDAFs decreases as we move in towards the black hole, $\dot{M}/\dot{M}_{\rm ADAF} \sim (r/r_{acc})$. The low luminosity in CDAFs is not because of low efficiency of accretion ($\eta \sim 0.1$), but because of the reduction of mass accretion due to convection. In global MHD simulations strong magnetic fields ($\beta \lesssim 10$) are generated by MHD turbulence driven by the MRI, and convection is unimportant [188, 84, 83, 95, 149, 155]. Numerical simulations by different groups (using different codes and boundary conditions) lead to the same conclusion—magnetically driven outflows prevent most of the mass supplied at outer regions to accrete. Outflows are natural outcome of hot RIAFs and have been incorporated in theoretical models to account for low accretion rates [141, 31, 32]; this adiabatic inflow-outflow solution (ADIOS) model also predicts a smaller accretion rate in the inner regions, ($\dot{M}/\dot{M}_{\rm ADAF} \sim (r/r_{acc})^p$, with $0 \leq p \leq 1$), and a gentle dependence of density on radius ($\rho \sim r^{-3/2+p}$) compared to an ADAF.

The ADIOS/CDAF models look very different from ADAF models; very little of the mass supplied at large radii actually accretes into the black holes. The accretion rate can be smaller than the Bondi estimate (e.g., Table 1.1) by a factor of $\sim R_{acc}/R_S \sim 10^5$, where R_S and R_{acc} are the inner ($\sim 2GM_*/c^2$, the Schwarzschild radius) and the outer ($\sim r_{acc} = 2GM_*/a^2$, the Bondi accretion radius) radii of the accretion flow. This very low accretion rate may explain the low luminosity of most galactic nuclei.

1.4.2 The Galactic center

Following Baganoff et al. [8], we apply the models discussed in the previous subsection to Sgr A*, the RIAF in the Galactic center (GC). The high resolution Chandra X-ray observations have enabled the detection of X-rays in the vicinity of Sgr A*, unpolluted by the emission from other X-ray sources in the region [8]. The X-rays arise because of thermal bremsstrahlung at larger radii, and synchrotron and Compton processes near the SMBH (these processes need very hot electrons). By assuming a thermal bremsstrahlung model for X-ray observations at $10''$, the ambient temperature is estimated to be $T(\infty) \approx 1.3$ keV and the plasma number density to be $n(\infty) \approx 26$ cm^{-3}. Quataert [157] has argued that the $10''$ observation probes the gas being driven out of the central star cluster, while the $1.''5$ observation probes the gas which is gravitationally captured by the black hole; we use $1.''5$ observations ($n \approx 130$ cm^{-3} and $T \approx 2$ keV) to estimate the accretion rate and to make Table 1.2.

We will use the ambient conditions and different RIAF models to estimate physical conditions in accretion flow of Sgr A*. The Bondi capture radius is given by $r_{acc} = 2GM/a^2 \approx 0.072$ pc ($1.''8$), where a is the sound speed (see Appendix A.2). The Bondi accretion rate is given by (see Eq. A.9)

$$\dot{M}_{\rm Bondi} \approx 3 \times 10^{-6} \left(\frac{n}{130 \text{ cm}^{-3}}\right) \left(\frac{kT}{2 \text{ keV}}\right)^{-3/2} M_\odot \text{ yr}^{-1}. \tag{1.26}$$

This is an order of magnitude smaller than what is estimated from the amount of gas available from stellar winds (see Table 1.1). The ADAF model gives $\dot{M}_{\rm ADAF} \sim \alpha \dot{M}_{\rm Bondi}$, where α is the Shakura-Sunyaev viscosity parameter [142]. The mass accretion rate as a function of radius for ADIOS/CDAF models is $\dot{M}_{\rm ADIOS/CDAF} \sim \alpha \dot{M}_{\rm Bondi} (R_S/r_{acc})^p$. Using $p = 1$ corresponding to a CDAF (or a CDAF-like ADIOS),

the accretion rate is

$$\dot{M}_{\rm CDAF/ADAF} \approx 1.2 \times 10^{-12} \left(\frac{\alpha}{0.1}\right) \left(\frac{n}{130\ {\rm cm}^{-3}}\right) \left(\frac{kT}{2\ {\rm keV}}\right)^{-3/2} M_\odot\ {\rm yr}^{-1}, \qquad (1.27)$$

much smaller than the Bondi estimate. Consistent with the CDAF/ADIOS models, the detection of linear polarization of radio emission from Sgr A* (see [4, 36]) implies a small Faraday rotation (indicating a small density and magnetic field) and places a stringent upper limit on $\dot{M} \lesssim 10^{-8} M_\odot\ {\rm yr}^{-1}$ [3, 159].

Table 1.2: Plasma parameters for Sgr A*

Parameter	$r = r_{acc}$ 2.2×10^{17} cm	$r = \sqrt{r_{acc} R_S}$ 4.2×10^{14} cm	$r = R_S$ 7.8×10^{11} cm
$\Omega_K = \sqrt{GM_*/r^3}$ (s^{-1})	1.84×10^{-10}	2.2×10^{-6}	0.028
$T \sim r^{-1}$ keV	2	1048	5.7×10^5
$n_{\rm ADAF} \sim r^{-3/2}$ (cm^{-3})	130	1.56×10^6	1.95×10^{10}
$n_{\rm CDAF} \sim r^{-3/2+p}$ (cm^{-3})	130	3000	7×10^4
$B^a_{\rm ADAF} \sim r^{-5/4}$ (G)	0.0012	2.93	7.6×10^3
$B^a_{\rm CDAF} \sim r^{-5/4+p/2}$ (G)	0.0012	0.13	14.4
$\nu_{i,{\rm ADAF}}/\Omega_K \sim r^{3/2}$	11.4	9.4×10^{-4}	7.6×10^{-8}
$\nu_{i,{\rm CDAF}}/\Omega_K \sim r^{3/2+p}$	11.4	1.81×10^{-6}	2.62×10^{-13}
$\rho_{i,{\rm ADAF}}/H \sim r^{-1/4}$	2×10^{-11}	9.94×10^{-11}	4.59×10^{-10}
$\rho_{i,{\rm CDAF}}/H \sim r^{-1/4-p/2}$	2×10^{-11}	2.23×10^{-9}	2.48×10^{-7}

[a] equipartition field, $H \approx 0.87r$, $p = 0$ for ADAF, $p = 1$ for ADIOS/CDAF,
ν_i is the ion collision frequency, ρ_i the ion gyroradius
$\nu_e = \nu_i (m_i/m_e)^{1/2} (T_e/T_i)^{-3/2}$, Coulomb logarithm ($\ln \Lambda$) chosen to be 30,
$\rho_e = \rho_i (T_e/T_i)^{1/2} (m_i/m_e)^{1/2}$

Table 1.2 shows different physical variables; the number density n, temperature T, equipartition magnetic field B, etc. at three radial locations (r_{acc}, $\sqrt{r_{acc} R_S}$, and R_S) using an ADAF (equivalent to the Bondi model for $\alpha \sim 1$) and CDAF/ADIOS model with $p = 1$. At radii smaller than r_{acc}, the mean free path is much larger than the disk height scale $H = c_s/\Omega \sim r$; the Larmor radius is many orders of magnitudes smaller than the disk height. This motivates us to investigate the role of plasma kinetic effects in the physics of RIAFs, as we discuss in the next section.

1.5 Motivation

As discussed in the previous section, there is ample evidence that RIAFs are collisionless, with the Coulomb collision time much longer than accretion time (see Table 1.2). However, most studies of the MRI have used ideal MHD equations, which are formally valid only for collisional, short mean free path plasmas. A collisionless analysis should use the Vlasov equation [104] which describes the time evolution of the distribution function of a collisionless plasma in a 6-D phase space. In cases when the scales of interest are much larger than the ion Larmor radius (e.g., in RIAFs ion Larmor radius is $\sim 10^8$ times smaller than the disk height scale, the scale of largest eddies in MRI turbulence), one can average over the fast gyromotion to obtain the drift kinetic equation (DKE) describing the distribution function in a 5-D phase space [110, 180]. Collisionless plasmas are different from the collisional MHD plasmas, in that the pressure is anisotropic with respect to the magnetic field, and rapid thermal conduction can occur along the field lines.

Quataert and coworkers [158], used the DKE to study the collisionless MRI in the linear regime. They found that with an equal vertical and azimuthal fields, the fastest growing mode is twice as fast as in MHD and occurs at a much larger length scale. The aim of the thesis is to follow up their work with numerical simulations of the MRI in the kinetic regime. A method based on the DKE that evolves the distribution function in a 5-D phase space is more expensive than the 3-D MHD simulations. A less expensive approach (and equivalent to the DKE in the linear regime) is to use the kinetic MHD (KMHD) equations with Landau fluid closure for parallel heat flux [180]. We started by showing the equivalence of linear modes in the drift kinetic and KMHD formalisms (the stable fast, Alfvén, slow, and entropy modes, and the unstable MRI) in a Keplerian disk [176]. This was followed up by nonlinear KMHD simulations in a local shearing box [177].

Transition of the MRI from collisionless to collisional regime was studied linearly,

using a BGK collision operator [176]. Transition from kinetic to the Braginskii regime occurs as the mean free path becomes short compared to the parallel wavelength, $\lambda_{\rm mfp} \ll \lambda_\parallel \equiv 2\pi/k_\parallel$; for the fastest growing mode this corresponds to $\nu \lesssim \Omega\sqrt{\beta}$, where ν is the collision frequency. As collision frequency is increased further ($\nu \gtrsim \Omega\beta$), anisotropic stress becomes negligible compared to the Maxwell stress, and transition to MHD occurs. Differences between the kinetic and MHD regimes is striking at large β's. A crucial difference from MHD is the presence of damped modes, indicating a possibility of wave-particle interactions in form of Landau and Barnes damping [113, 18, 182]. Balbus and Islam [12, 96] have studied MRI in the weakly collisional Braginskii regime and found agreement with our results.

The ZEUS MHD code [185, 186] is modified to include anisotropic pressure, and parallel thermal conduction based on Landau fluid closure [180]. Nonlinear KMHD simulations are done in a local shearing box limit [86]. The adiabatic invariant, $\mu = p_\perp/B$, is conserved in collisionless plasmas, as a result, pressure anisotropy ($p_\perp > p_\parallel$) is created as magnetic field is amplified by the MRI. Pressure anisotropy cannot become large ($p_\perp/p_\parallel - 1 \lesssim {\rm few}/\beta_\perp$), as mirror and ion-cyclotron instabilities will isotropize the pressure by pitch angle scattering. Subgrid models of pitch angle scattering by these instabilities at the Larmor radius scale have been included. Pressure anisotropy gives rise to a stress in addition to the usual Maxwell and Reynolds stress in MHD [177]. Pressure anisotropy driven instabilities are expected to arise in any collisionless plasma, when the field strength changes in a $\beta \gtrsim 1$ plasma, e.g., the solar wind [123, 98], magnetosphere [192, 66], and galaxy clusters [170].

The next step is to include collisionless effects in global MHD simulations [188]. Anisotropic thermal conduction is expected to change the convective stability criterion from an outward increasing entropy to an outward increasing temperature [10, 11, 148]. Self-similar solutions using saturated (isotropic) conduction have shown significant differences from standard non-conducting ADAF models [130, 190]. While

implementing anisotropic thermal conduction in global MHD simulations we discovered that the centered differencing of anisotropic thermal conduction can give rise to heat flowing from lower to higher temperatures, causing the temperature to become negative in regions with large temperature gradients, e.g., disk corona interface. We have developed a new numerical method that uses slope limiters to ensure that the temperature extrema are not amplified by anisotropic conduction [175]. Global numerical simulations with anisotropic thermal conduction can tell us about the global structure of RIAFs. These, combined with the insights on local energy dissipation in disks from the local KMHD simulations, can shed light on their low luminosity.

1.6 Overview

The main body of the thesis (chapters 3, 4, and 5) is based on three papers, the first on the transition of the MRI from collisionless to the collisional regime [176], the second on the shearing box simulations of the collisionless MRI [177], and the third on numerical implementation of anisotropic conduction in presence of large temperature gradients [175].

Chapter 2 introduces the kinetic MHD formalism. We begin with the Vlasov description of a collisionless plasma, and derive the drift kinetic equation (DKE) in the limit of length scales much larger than the Larmor radius, and frequencies much smaller than the gyrofrequency. Moments of the DKE with an anisotropic pressure tensor are called the kinetic MHD (KMHD) equations. The KMHD equations are closed by the '3+1' Landau fluid closure for heat flux along the field lines. Landau closure is equivalent to a Padé approximation to the drift kinetic linear response function. We discuss different ways to implement the nonlocal closure in a numerical simulation. We show that the moment equations with a BGK collision operator recover the Braginskii equations in the high collisionality regime.

Chapter 3, which is based on [176], describes the transition of the MRI from collisionless to the collisional regime. Linear modes of a magnetized, collisionless plasma in a Keplerian rotation are derived using both the DKE and the KMHD equations with Landau closure for the heat flux. The two methods agree very well for the real and imaginary parts for the frequency response; this motivates kinetic MHD simulations of the collisionless MRI. The presence of damped modes in the collisionless regime can cause waves to be damped by Landau/Barnes damping at large scales, instead of being damped only at small scales as in MHD with small resistivity and viscosity. A BGK collision operator is used to study the transition of the MRI from collisionless to the collisional (MHD) regime; the transition from kinetic to the Braginskii regime occurs when the mean free path becomes small compared to the wavelength, for the fastest growing mode this corresponds to $\nu \gtrsim \Omega\sqrt{\beta}$.

Chapter 4 presents results from the nonlinear shearing box simulations of the collisionless MRI. Pressure anisotropy ($p_\perp > p_\parallel$) is created because of adiabatic invariance ($\mu = p_\perp/B$), as magnetic field is amplified by the MRI. The effect of $p_\perp > p_\parallel$ is to make the field lines stiffer. If the pressure anisotropy is allowed to become arbitrarily large, the stiff field lines (because of $p_\perp > p_\parallel$) can result in the stabilization of all the MRI modes into small amplitude anisotropic Alfvén waves. However, at large pressure anisotropies ($p_\perp/p_\parallel - 1 >$ (a few)$/\beta$), mirror and ion-cyclotron instabilities are expected to arise. Although the mirror instability is present in the kinetic MHD approximation, the resolution (and hence the growth rate) is not enough to keep the pressure anisotropy within the marginal anisotropy. The ion-cyclotron instability is ordered out of the drift kinetic ordering. Therefore, subgrid models for pitch angle scattering due to these instabilities are included. Pitch angle scattering due to microinstabilities imposes an MHD-like dynamics on collisionless plasmas, this is the reason MHD provides a good approximation for many collisionless plasmas in astrophysics, e.g., the solar wind, the magnetosphere, and the interstellar medium.

Modifications to the ZEUS MHD code, to include the kinetic MHD terms, are described. The key result of the collisionless MRI simulations is that anisotropic stress, a qualitatively new mechanism to transport angular momentum, is as important as the dominant Maxwell stress in MHD. This can also affect the energetics; in particular the rate at which anisotropic pressure (collisionless damping is included in it) heats ions and electrons can be comparable. If electron heating is comparable to ion heating, it will be difficult to maintain $T_e \ll T_i$ as required by some RIAF models.

Chapter 5 is the result of our attempts to carry out global non-radiative disk simulations. The aim was to include the effect of anisotropic conduction on global MHD disk simulations [188]. The initial condition consists of a constant angular momentum torus surrounded by a hot, low density corona. We were running into numerical difficulties with this initial set up; the temperature was becoming negative at some grid points near the disk corona interface. This motivated us to investigate the effect of anisotropic conduction in regions of high temperature gradient. Chapter 5 describes simple tests where centered differencing of anisotropic thermal conduction results in heat flowing from lower to higher temperatures, resulting in negative temperature at large temperature gradients. We introduce a new numerical method based on limiting the transverse temperature gradient; this ensures that heat flows from higher to lower temperatures and the temperature extrema are not amplified. Many tests and convergence studies are described.

Chapter 6 concludes the thesis with an outline of possible future work. Future work include global disk simulations with anisotropic thermal conduction, local simulations with more sophisticated models for non-local anisotropic thermal conduction, and more accurate drift kinetic simulations evolving the distribution function in a 5-D phase space.

Appendix A describes the efficiency of black hole accretion based on a simple pseudo-Newtonian potential which captures key general relativistic effects [145]. Also

presented is the derivation of spherically symmetric, steady accretion.

Appendix B shows the derivation of closures for $p_\parallel$ and $p_\perp$, using the DKE with a BGK collision operator, in both high and low collisionality limit. These have been used in Chapter 2 to show the equivalence of the drift kinetic formalism and the kinetic MHD approximation with Landau closure for heat flux.

Appendix C describes the modifications to the ZEUS MHD code to include the kinetic MHD terms, anisotropic pressure and anisotropic thermal conduction based on Landau fluid closure. This also includes some tests of the collisionless aspects of the code, e.g., damping of a linear fast mode, mirror instability in an initially anisotropic plasma ($p_\perp > p_\perp$), shear generated pressure anisotropy and firehose instability driven by the anisotropy ($p_\parallel > p_\perp$).

Appendix D describes the error analysis of a time series where the sampling time is smaller than the correlation time. For such a data, all entries are not independent and the standard deviation is no a correct measure of uncertainty. This method based on [144] is used to put error bars on the time and volume averaged quantities derived from the shearing box simulations (in Chapter 4).

Chapter 2

Description of collisionless plasmas

Macroscopically collisionless plasmas, with collision mean free path comparable to the system size, are ubiquitous in astrophysics, e.g., the solar wind, earth's magnetotail, radiatively inefficient accretion flows (RIAFs), and X-ray clusters. Fluid theories, such as hydrodynamics and MHD, are applicable only when the mean free path is much smaller than the system size, but are routinely used even when the plasma is collisionless. While fluid theories are sometimes useful even outside of their rigorous regime of validity, collisionless plasmas can be quite different from MHD plasmas. For example, whereas, viscous and resistive dissipation at small scales are the only ways to dissipate kinetic and magnetic energies into thermal motion in MHD, collisionless damping at large scales is an important source of heating in collisionless plasmas. Although kinetic instabilities may enforce an MHD-like behavior, collisionless effects can be crucial, especially to understand energetics and particle acceleration.

In this chapter we discuss several descriptions of collisionless plasmas valid in different approximations. We start with the Vlasov equation, the most detailed description of a collisionless plasma, which describes the time evolution of the distribution function in a 6-D phase space. The drift kinetic equation (DKE) is obtained from the Vlasov equation, in the limit when length scales are much larger than the Larmor

radius and time scales much longer than the gyroperiod. Moments of the DKE result in kinetic MHD (KMHD) equations, where pressure is anisotropic with respect to the magnetic field direction. Landau fluid closure for heat flux along the field lines, which recovers the correct kinetic response in the linear regime, is described.

2.1 The Vlasov equation

A complete statistical description of the species 's' in a collisionless plasma involves a distribution function F_s in a $6N_s$ dimensional phase space, where N_s is the total number of particles of species 's'. The distribution function, F_s, satisfies the Liouville equation for an N-body system [74],

$$\frac{DF_s}{Dt} \equiv \frac{\partial F_s}{\partial t} + \sum_{i=1}^{N_s} \mathbf{v}_i \cdot \frac{\partial F_s}{\partial \mathbf{x}_i} + \sum_{i=1}^{N_s} \mathbf{a}_i \cdot \frac{\partial F_s}{\partial \mathbf{v}_i} = 0, \tag{2.1}$$

corresponding to the conservation of probability, where $\mathbf{x}$, $\mathbf{v}$, and $\mathbf{a}$ are position, velocity, and acceleration respectively, and D/Dt is the Lagrangian derivative in the $6N_s$ dimensional phase space [104]. Reduced distributions are obtained by integrating F_s over all but one, two, three, etc., particles.

Evolution for the single particle distribution function $f_s(\mathbf{x}, \mathbf{v}, t)$ is obtained by integrating Eq. 2.1 over all but one particle's phase space,

$$\frac{\partial f_s}{\partial t} + \mathbf{v} \cdot \nabla f_s + \left[\frac{q_s}{m_s}(\mathbf{E} + \mathbf{v} \times \mathbf{B}) + \frac{\mathbf{F_g}}{m_s} \right] \cdot \nabla_{\mathbf{v}} f_s = 0, \tag{2.2}$$

where all terms of order the plasma parameter, $g \equiv 1/n_s\lambda_D^3 \ll 1$ [135], are neglected. The plasma parameter is the inverse of the number of particles in a Debye sphere. The Debye length is the length scale over which plasma establishes quasineutrality, $\lambda_D = \sqrt{kT_s/4\pi n_s q_s^2}$, where n_s, T_s are number density and temperature [104]. For an ideal plasma, with effective shielding, $n_s\lambda_D^3 \gg 1$ or $g \ll 1$. The force of gravity is

denoted by $\mathbf{F_g}$, and the electromagnetic fields are governed by the Maxwell equations

$$\begin{aligned}
\nabla \cdot \mathbf{E} &= 4\pi \sum_s q_s \int f_s d\mathbf{v}, && (2.3)\\
\nabla \cdot \mathbf{B} &= 0, && (2.4)\\
\frac{\partial \mathbf{B}}{\partial t} &= -c\nabla \times \mathbf{E}, && (2.5)\\
\nabla \times \mathbf{B} &= 4\pi \sum_s \frac{q_s}{c} \int f_s \mathbf{v} d\mathbf{v} + \frac{1}{c}\frac{\partial \mathbf{E}}{\partial t}. && (2.6)
\end{aligned}$$

The higher order terms (in g) that we neglect in the derivation of Eq. 2.2–negligible compared to the collective force due to plasma–arise because of scattering due to microscopic fields of nearby particles. Eq. 2.2 is the Vlasov equation (also known as the collisionless Boltzmann equation) that describes the distribution function $f_s(\mathbf{x}, \mathbf{v}, t)$, the probability of finding a particle of species 's' in an interval $d\mathbf{x}d\mathbf{v}$ at $(\mathbf{x}, \mathbf{v})$ in phase space at time t. The Vlasov-Maxwell equations are more complicated than the fluid equations as they involve seven independent variables $t, \mathbf{x}, \mathbf{v}$ rather than four in MHD, $t, \mathbf{x}$. A collision operator, that takes into account the microscopic fields due to individual charges, can be added on the right side of Eq. 2.2 to obtain the Boltzmann equation. Going from $6N_s$ to 6 variables in phase space simplifies the description considerably for an ideal plasma with $g \ll 1$. Further simplifications can be made as we show in the following sections.

2.2 The drift kinetic equation

The Vlasov equation can be simplified further if the Larmor radius (ρ_s) is much smaller than the spatial scales ($\rho_s/L \ll 1$), and the gyroperiod ($2\pi/\Omega_s$) much smaller than the time scales ($\Omega_s \gg \omega$). An asymptotic expansion in $\rho_s/L = (m_s/q_s)(cv/BL) \ll 1$ can reduce the number of variables by two; the gyration phase is irrelevant, and the perpendicular velocity is governed by the adiabatic invariant, $\mu = v_\perp^2/2B$ [48].

To the lowest order, all particles drift with an $\mathbf{E} \times \mathbf{B}$ velocity perpendicular to the field lines, and a parallel motion along the field lines. The parallel electric field is small, $E_\parallel \sim O(1/q_s) \sim O(\epsilon)$, as charges streaming along the magnetic field lines will short it out. Lowest order term in the expansion of f_s, f_{0s}, is independent of the gyrophase. We avoid the messy details of the derivation [109, 110, 165, 107], and simply state the kinetic equation for the zeroth-order distribution function given by (we follow Kulsrud's derivation [109, 110])

$$\frac{\partial f_{0s}}{\partial t} + (\mathbf{V}_E + v_\parallel \hat{\mathbf{b}}) \cdot \nabla f_{0s} + \left(-\hat{\mathbf{b}} \cdot \frac{D\mathbf{V}_E}{Dt} - \mu \hat{\mathbf{b}} \cdot \nabla B + \frac{1}{m_s}(q_s E_\parallel + F_{g\parallel}) \right) \frac{\partial f_{0s}}{\partial v_\parallel} = 0, \tag{2.7}$$

where $\hat{\mathbf{b}} = \mathbf{B}/B$ is the unit vector in magnetic field direction, $\mathbf{V}_E = c(\mathbf{E} \times \mathbf{B})/B^2$ is the drift velocity independent of species, and $D/Dt \equiv \partial/\partial t + (\mathbf{V}_E + v_\parallel \hat{\mathbf{b}}) \cdot \nabla$ is the comoving derivative in phase space. The Maxwell equations to the lowest order gives the charge neutrality condition,

$$\sum_s \int q_s f_{0s} d\mathbf{v} = 0, \tag{2.8}$$

$$\sum_s \int q_s f_{0s} \mathbf{v} d\mathbf{v} = 0. \tag{2.9}$$

Some remarks on the drift kinetic equation (DKE) are in order. Eq. 2.7 can be interpreted as the conservation of probability in a 5-D phase space $(\mathbf{x}, \mu, v_\parallel)$ with characteristics, $d\mathbf{x}/dt = \mathbf{V}_E + v_\parallel \hat{\mathbf{b}}$, and $dv_\parallel/dt = -\hat{\mathbf{b}} \cdot \frac{D\mathbf{V}_E}{Dt} - \mu \hat{\mathbf{b}} \cdot \nabla B + \frac{1}{m_s}(q_s E_\parallel + F_{g\parallel})$. Only the $\mathbf{E} \times \mathbf{B}$ drift shows up in the perpendicular drift, other drifts–curvature, ∇B, etc., $\propto 1/q_s$–are higher order in ϵ in the drift-kinetic ordering. The force along the field lines consists of the fluid inertial force $(-\hat{\mathbf{b}} \cdot \frac{D\mathbf{V}_E}{Dt})$, the magnetic mirror force $(-\mu \hat{\mathbf{b}} \cdot \nabla B)$, the parallel electric force $(q_s E_\parallel)$, and the parallel gravitational force $(F_{g\parallel})$. Although $E_\parallel \ll E_\perp$ and can be dropped in the Ohm's law, it needs to be kept in the parallel particle dynamics where it ensures quasineutrality. The condition that

determines $E_\parallel$ will be given in Eq. 2.27. The DKE evolves the distribution function in a 5-D phase space $(\mathbf{x}, \mu, v_\parallel)$, with μ a parameter. A term with $\partial/\partial\mu$ does not appear in Eq. 2.7 as $d\mu/dt = 0$ along the characteristics.

2.3 Kinetic MHD equations

In the drift-kinetic approximation, particles free stream along the field lines, but move with the field lines in the perpendicular direction. This fluid-like behavior in the perpendicular plane restores the possibility of a fluid description of a $\rho_s/L \ll 1$ plasma.

Moments of the Vlasov equation combined with the Maxwell equations in the non-relativistic limit (ignoring the displacement current, $\partial E/\partial t$, in Eq. 2.6) yields the kinetic MHD equations [109, 110],

$$\frac{\partial \rho}{\partial t} + \nabla \cdot (\rho \mathbf{V}) = 0, \tag{2.10}$$

$$\rho \frac{\partial \mathbf{V}}{\partial t} + \rho \left(\mathbf{V} \cdot \nabla\right) \mathbf{V} = \frac{(\nabla \times \mathbf{B}) \times \mathbf{B}}{4\pi} - \nabla \cdot \mathbf{P}, \tag{2.11}$$

$$\frac{\partial \mathbf{B}}{\partial t} = \nabla \times (\mathbf{V} \times \mathbf{B}), \tag{2.12}$$

$$\mathbf{P} = p_\perp \mathbf{I} + \left(p_\parallel - p_\perp\right) \hat{\mathbf{b}}\hat{\mathbf{b}}, \tag{2.13}$$

$$p_\perp = \sum_s m_s \int f_{0s} \frac{v_\perp^2}{2} d\mathbf{v}, \tag{2.14}$$

$$p_\parallel = \sum_s m_s \int f_{0s} (v_\parallel - \mathbf{V} \cdot \hat{\mathbf{b}})^2 d\mathbf{v}, \tag{2.15}$$

where $\mathbf{V} = \mathbf{V}_E + V_\parallel \hat{\mathbf{b}}$ is the fluid velocity. Kinetic MHD, like MHD, is a single fluid description of plasma obtained by combining the moments of all species. Kinetic MHD appears similar to MHD, except the pressure is an anisotropic tensor unlike an isotropic pressure in MHD; the pressure tensor is determined by moments of the solution of the DKE, unlike the equation of state in MHD. The asymptotic ordering

in $1/q_s$ leads to the ideal Ohm's law [104]. In principle, equations for $p_\parallel$ and $p_\perp$ can be derived from the moments of the DKE. However, because of the inherent complexity of a phase space description, fluid approximations for closure are usually employed.

The simplest and the oldest approximation is the double adiabatic (CGL) approximation, where heat flux is assumed to vanish [48],

$$\frac{d}{dt}\left(\frac{p_\perp}{\rho B}\right) = 0, \tag{2.16}$$

$$\frac{d}{dt}\left(\frac{p_\parallel B^2}{\rho^3}\right) = 0. \tag{2.17}$$

The assumption that the heat flux vanishes is valid only if the phase speed, $\omega/k_\parallel$, is much larger than electron and ion thermal speeds, a cold plasma criterion almost never satisfied for slow and fast magnetoacoustic waves at high β.[1] Furthermore, the CGL equations are non-dissipative, incapable of modeling collisionless damping. The CGL closure is also known to give an incorrect marginal stability criterion for the mirror instability, an instability that regulates pressure anisotropy in collisionless plasmas [110, 180].

2.4 Landau fluid closure

In this section we describe a fluid closure that maintains the simplicity of the CGL model, while including kinetic effects like Landau damping [180]. We also include a simple BGK collision operator, which conserves number, momentum, and energy. Fluid closures that incorporated kinetic effects like collisionless damping were first derived in the electrostatic limit for nonlinear studies of drift-wave instabilities [79, 78, 54]. Snyder et al. [180] extended the closure to electromagnetic bi-Maxwellian (anisotropic) plasmas; similar closures were obtained by [46]. Fluid closures that

[1] This cold plasma criterion is also not satisfied for Alfvén waves, though the heat flux is zero for linear Alfvén waves in a uniform plasma.

capture kinetic effects are somewhat analogous to the flux limited diffusion methods used in radiation transport [117, 131].

2.4.1 The moment hierarchy

Multiplying Eq. 2.7 by B, and using Eq. 2.12 leads to the kinetic equation in a conservative form,

$$\frac{\partial}{\partial t} f_s B + \nabla \cdot [f_s B (v_\parallel \hat{\mathbf{b}} + \mathbf{V}_E)] + \frac{\partial}{\partial v_\parallel} \left[f_s B \left(-\hat{\mathbf{b}} \cdot \frac{D\mathbf{V}_E}{Dt} - \mu \hat{\mathbf{b}} \cdot \nabla B + \frac{q_s}{m_s} E_\parallel \right) \right] = BC(f_s), \tag{2.18}$$

where subscript '0' has been suppressed. The term on the right is a BGK collision operator [25]

$$C(f_j) = -\sum_k \nu_{jk} (f_j - F_{Mjk}), \tag{2.19}$$

where $\nu_{j,k}$ is the collision rate of species j with k. The collisions cause f_j to relax to a shifted Maxwellian with effective temperature of the species j and fluid velocity of the species k,

$$F_{Mjk} = \frac{n_j}{(2\pi T_j / m_j)^{3/2}} \exp \left[-\frac{-m_j (v_\parallel - V_{\parallel k})^2}{2T_j} - \frac{m_j \mu B}{T_j} \right], \tag{2.20}$$

where $T_j = (T_{\parallel j} + 2T_{\perp j})/3$.[2]

[2] A variant of this model is required to handle the large differences between energy and momentum relaxation rates that can occur in some cases, but this simpler model is sufficient for the case at hand, where $V_{\parallel,e} = V_{\parallel,i}$ to lowest order.

We define the velocity moments as:

$$
\begin{aligned}
n_s &= \int f_s d\mathbf{v}, \qquad n_s V_{\parallel s} = \int f_s v_\parallel d\mathbf{v}, \\
p_{\parallel s} &= m \int f_s (v_\parallel - V_\parallel)^2 d\mathbf{v}, \qquad p_{\perp s} = m \int f_s \mu B d\mathbf{v}, \\
q_{\parallel s} &= m \int f_s (v_\parallel - V_\parallel)^3 d\mathbf{v}, \qquad q_{\perp s} = m \int f_s \mu B (v_\parallel - V_\parallel) d\mathbf{v}, \\
r_{\parallel,\parallel s} &= m \int f_s (v_\parallel - V_\parallel)^4 d\mathbf{v}, \qquad r_{\parallel,\perp s} = m \int f_s \mu B (v_\parallel - V_\parallel)^2 d\mathbf{v}, \\
r_{\perp,\perp s} &= m \int f_s \mu^2 B^2 d\mathbf{v}.
\end{aligned}
$$

Specializing to the case of an electron-proton plasma, and using the charge neutrality condition (Eqs. 2.8 and 2.9), $n = n_e = n_i$ and $V_\parallel = V_{\parallel e} = V_{\parallel i}$. In this limit when electrons and protons drift at equal velocity, the only role of collisions is to isotropize

the distribution function. Taking appropriate moments of Eq. 2.18,

$$\frac{\partial n}{\partial t} + \nabla\cdot(n\mathbf{V}) = 0, \tag{2.21}$$

$$\frac{\partial V_\parallel}{\partial t} + \mathbf{V}\cdot\nabla V_\parallel + \hat{\mathbf{b}}\cdot\left(\frac{\partial \mathbf{V}_E}{\partial t} + \mathbf{V}\cdot\nabla\mathbf{V}_E\right) + \frac{\nabla\cdot(\hat{\mathbf{b}}p_{\parallel s})}{nm_s} - \frac{p_{\perp s}\nabla\cdot\hat{\mathbf{b}}}{nm_s} - \frac{q_s E_\parallel}{m_s} = 0, \tag{2.22}$$

$$\frac{\partial p_{\parallel s}}{\partial t} + \nabla\cdot(p_{\parallel s}\mathbf{V}) + \nabla\cdot\mathbf{q}_{\parallel\mathbf{s}} + 2p_{\parallel s}\hat{\mathbf{b}}\cdot\nabla\mathbf{V}\cdot\hat{\mathbf{b}} - 2q_{\perp s}\nabla\cdot\hat{\mathbf{b}} = -\frac{2}{3}\nu_s(p_{\parallel s} - p_{\perp s}), \tag{2.23}$$

$$\frac{\partial p_{\perp s}}{\partial t} + \nabla\cdot(p_{\perp s}\mathbf{V}) + \nabla\cdot\mathbf{q}_{\perp\mathbf{s}} + p_{\perp s}\nabla\cdot\mathbf{V} - p_{\perp s}\hat{\mathbf{b}}\cdot\nabla\mathbf{V}\cdot\hat{\mathbf{b}} + q_{\perp s}\nabla\cdot\hat{\mathbf{b}} = -\frac{1}{3}\nu_s(p_{\perp s} - p_{\parallel s}), \tag{2.24}$$

$$\frac{\partial q_{\parallel s}}{\partial t} + \nabla\cdot(\mathbf{V}q_{\parallel s}) + \nabla\cdot(\hat{\mathbf{b}}r_{\parallel,\parallel s}) + 3q_{\parallel s}\hat{\mathbf{b}}\cdot\nabla\mathbf{V}\cdot\hat{\mathbf{b}} - \frac{3p_{\parallel s}}{nm_s}\hat{\mathbf{b}}\cdot\nabla p_{\parallel s} + 3\left(\frac{p_{\perp s}p_{\parallel s}}{nm_s} - \frac{p_{\parallel s}^2}{nm_s} - r_{\parallel,\perp s}\right)\nabla\cdot\hat{\mathbf{b}} = -\nu_s q_{\parallel s}, \tag{2.25}$$

$$\frac{\partial q_{\perp s}}{\partial t} + \nabla\cdot(\mathbf{V}q_{\perp s}) + \nabla\cdot(\hat{\mathbf{b}}r_{\parallel,\perp s}) + q_{\perp s}\nabla\cdot(V_\parallel\hat{\mathbf{b}}) - \frac{p_{\perp s}}{nm_s}\hat{\mathbf{b}}\cdot\nabla p_{\parallel s} + \left(\frac{p_{\perp s}^2}{nm_s} - \frac{p_{\perp s}p_{\parallel s}}{nm_s} - r_{\perp,\perp s} + r_{\parallel,\perp s}\right)\nabla\cdot\hat{\mathbf{b}} = -\nu_s q_{\perp s}, \tag{2.26}$$

where $\rho = n(m_i + m_e)$, $\mathbf{V} = \mathbf{V}_E + V_\parallel\hat{\mathbf{b}}$, $\nu_i = \nu_{ii} + \nu_{ie}$ and $\nu_e = \nu_{ee} + \nu_{ei}$, and $\mathbf{q}_{\parallel\mathbf{s}} = \hat{\mathbf{b}}q_{\parallel s}$ and $\mathbf{q}_{\perp\mathbf{s}} = \hat{\mathbf{b}}q_{\perp s}$ are thermal fluxes of $p_{\parallel s}$ and $p_{\perp s}$ along the field lines; perpendicular heat flux vanishes as $\rho_s/L \ll 1$. The perpendicular equation of motion is given by the perpendicular component of Eq. 2.11, whose parallel component is equivalent to Eq. 2.22. The condition $V_{\parallel i} = V_{\parallel e}$, and Eq. 2.22 gives [110],

$$E_\parallel = \frac{\sum_s (q_s/m_s)\hat{\mathbf{b}}\cdot\nabla\cdot\mathbf{P}_\mathbf{s}}{\sum_s (n_s q_s^2/m_s)}. \tag{2.27}$$

Eqs. 2.21-2.24, like Eqs. 2.10-2.13, are not complete, and need a closure equation for $q_{\parallel s}$ and $q_{\perp s}$. In the next subsection we introduce Landau fluid closure for heat fluxes.

Conservation properties

The moment equations (Eqs. 2.10, 2.11, 2.23 and 2.24) conserve momentum and total energy irrespective of the closure for higher moments. Combining Eqs. 2.10 and 2.11 gives the momentum conservation equation,

$$\frac{\partial}{\partial t}(\rho \mathbf{V}) = -\nabla\cdot\left[\rho\mathbf{V}\mathbf{V} + \left(\frac{B^2}{8\pi}\mathbf{I} - \frac{\mathbf{B}\mathbf{B}}{4\pi}\right) + \mathbf{P}\right], \tag{2.28}$$

where $p_\parallel = p_{\parallel i} + p_{\parallel e}$ and $p_\perp = p_{\perp i} + p_{\perp e}$.

Total energy (the sum of kinetic, magnetic, and thermal energies), defined as $\Gamma = \rho V^2/2 + B^2/8\pi + p_\perp + p_\parallel/2$, is also conserved as

$$\frac{\partial \Gamma}{\partial t} = -\nabla\cdot\left[\left(\frac{1}{2}\rho V^2 + p_\perp + \frac{1}{2}p_\parallel\right)\mathbf{V}\right] - \nabla\cdot\left[\frac{\mathbf{B}\times(\mathbf{V}\times\mathbf{B})}{4\pi}\right] - \nabla\cdot(\mathbf{V}\cdot\mathbf{P}) - \nabla\cdot\mathbf{q}, \tag{2.29}$$

where $\mathbf{q} = (q_\perp + q_\parallel/2)\hat{\mathbf{b}}$, and $q_\parallel = q_{\parallel i} + q_{\parallel e}$ and $q_\parallel = q_{\parallel i} + q_{\parallel e}$.

2.4.2 The 3+1 Landau closure

A simple model which evolves $p_\parallel$ and $p_\perp$, and truncates the moment hierarchy with Eqs. 2.23 and 2.24, using closure approximations for $q_\parallel$ and $q_\perp$ is called a "3+1 model," as it evolves 3 parallel moments $(n, u_\parallel, p_\parallel)$ and 1 perpendicular moment $(p_\perp)$ [180].

The $3+1$ closure is derived by writing $q_\parallel$ and $q_\perp$ in terms of the lower moments and δB, and solving for coefficients by matching with the linear kinetic response. This gives [180]

$$q_{\parallel s} = -n\sqrt{\frac{8}{\pi}}v_{t\parallel s}\frac{ik_\parallel T_{\parallel s}}{|k_\parallel|}, \tag{2.30}$$

$$q_{\perp s} = -n\sqrt{\frac{2}{\pi}}v_{t\parallel s}\frac{ik_\parallel T_{\perp s}}{|k_\parallel|} + n\sqrt{\frac{2}{\pi}}v_{t\parallel s}T_{\perp s}\left(1 - \frac{T_{\perp s}}{T_{\parallel s}}\right)\frac{ik_\parallel \delta B}{|k_\parallel| B}, \tag{2.31}$$

where $v_{t\|s} = \sqrt{T_{\|s}/m_s}$, and $k_\|$ is the parallel wavenumber of small perturbation. The second term in the closure for $q_{\perp s}$ vanishes in the electrostatic limit or if pressure is isotropic, and is needed to conserve μ linearly [180].

Substituting the closures, Eqs. 2.30 and 2.31, into Eqs. 2.21-2.24 yields the density response

$$\delta n_s = \frac{in}{k_\| T_{\|s}} q_s E_\| R_3(\zeta_s) + n\frac{\delta B}{B}\left[1 - \frac{T_{\perp s}}{T_{\|s}} R_3(\zeta_s)\right], \tag{2.32}$$

and the perpendicular pressure response

$$p_{\perp s} = -\frac{ip_{\perp s}}{k_\| T_{\|s}} q_s E_\| R_3(\zeta_s) + 2p_{\perp s}\frac{\delta B}{B}\left[1 - \frac{T_{\perp s}}{T_{\|s}}\left(\frac{R_3(\zeta_s}{2} + \frac{R_1(\zeta_s}{2}\right)\right], \tag{2.33}$$

where $\zeta_s = \omega/\sqrt{2}|k_\||v_{t\|s}$, and $R_3(\zeta_s)$ is the three-pole Padé approximation of the electrostatic response function

$$R_3(\zeta_s) = \frac{2 - i\sqrt{\pi}\zeta_s}{2 - 3i\sqrt{\pi}\zeta_s - 4\zeta_s^2 + 2i\sqrt{\pi}\zeta_s^3}, \tag{2.34}$$

and $R_1(\zeta_s)$ is a one-pole model of $R(\zeta_s)$, $R_1(\zeta_s) = 1/(1 - i\sqrt{\pi}\zeta_s)$. The electrostatic response function, $R(\zeta_s) = 1 + \zeta_s Z(\zeta_s)$, where $Z(\zeta) = (1/\sqrt{\pi})\int dt \exp(-t^2)/(t - \zeta)$, arises frequently in linearized moments of the Vlasov equation (or the DKE). The $3 + 1$ model recovers the fully kinetic response function in both asymptotic limits, $\zeta_s \ll 1$ and $\zeta_s \gg 1$, and provides a good approximation in the intermediate regime. Figs. (1)-(4) in [180] show that Landau closure is a good approximation for the linear response function from the DKE. While the linear response function in CGL (and MHD) approximation shows no imaginary part in frequency, Landau closure gives collisionless damping rates consistent with the DKE.

The complete $3 + 1$ system of equations is given by Eqs. 2.10-2.13, and Eqs. 2.23 and 2.24, closed by the inverse Fourier transform of Eqs. 2.30 and 2.31. In Section 2.6 we discuss ways of computing the heat fluxes in coordinate space from the Fourier

space expressions.

2.5 Collisional effects

Collisions serve two roles, first they isotropize the pressure tensor, and second they reduce the heat fluxes. With the BGK collision operator, a pitch angle scattering term that isotropizes pressure appears in equations for $p_\parallel$ and $p_\perp$ (terms on the right side of Eqs. 2.23 and 2.24). Certain collisional effects, such as perpendicular diffusion, resistive effects, etc., are not included because of the drift kinetic ordering ($\Omega_s \gg \omega$, ν); also not included is the collisional heat transfer from one species to another.

To extend Landau closure to the collisional regime, it is useful to write Eqs. 2.23 and 2.24 in a form similar to Braginskii's equations [37]. This is done by defining an average pressure, $p_s = (p_{\parallel s} + 2p_{\perp s})/3$, a differential pressure, $\delta p_s = p_{\parallel s} - p_{\perp s}$, and a heat flux, $q_s = q_{\parallel s}/2 + q_{\perp s}$. The pressure tensor, $\mathbf{P}_s$, can be divided into an isotropic part, $p_s\mathbf{I}$, and an anisotropic stress, $\mathbf{\Pi_s} = -\delta p_s\mathbf{I}/3 + \delta p_s\hat{\mathbf{b}}\hat{\mathbf{b}}$, with $\delta p_s = (p_{\parallel s} - p_{\perp s})$. Combining Eqs. 2.23 and 2.24, then gives [180]

$$\frac{dp_s}{dt} + \frac{5}{3}p_s\nabla\cdot\mathbf{V} = -\frac{2}{3}\nabla\cdot(\hat{\mathbf{b}}q_s) - \frac{2}{3}\mathbf{\Pi_s}:\nabla\mathbf{V}, \tag{2.35}$$

$$\frac{d\delta p_s}{dt} + \frac{5}{3}\delta p_s\nabla\cdot\mathbf{V} + \mathbf{\Pi_s}:\nabla\mathbf{V} + 3p_s\hat{\mathbf{b}}\cdot\nabla\mathbf{V}\cdot\hat{\mathbf{b}} - p_s\nabla\cdot\mathbf{V} - 3q_\perp\nabla\cdot\mathbf{V} + \nabla\cdot[\hat{\mathbf{b}}(q_{\parallel s} - q_{\perp s})] = -\nu_s\delta p_s. \tag{2.36}$$

2.5.1 The high collisionality limit

In the high collisionality limit, $\nu \gg \omega$, the above equations yield approximation to the Braginskii transport equations in the $\nu \ll \Omega_s$ regime, as required by the initial ordering. An expansion in $1/\nu_s$ of Eqs. 2.25, 2.26, and 2.36 implies that

$q_{\parallel 0s} = q_{\perp 0s} = \delta p_{0s} = 0$. Combining this with Eq. 2.36 gives, to next order,

$$\delta p_{1s} = -\frac{p_{0s}}{\nu_s}(3\hat{\mathbf{b}} \cdot \nabla \mathbf{V} \cdot \hat{\mathbf{b}} - \nabla \cdot \mathbf{V}). \tag{2.37}$$

The expression for $\mathbf{\Pi_s}$ is the same as Braginskii's result, if ν_s is the inverse of Braginskii's collision time ($\nu_i^{-1} = 0.96\tau_{i,Brag}$ and $\nu_e^{-1} = 0.73\tau_{e,Brag}$; see [91]).

Similarly, a heat flux matching Braginskii's result can be obtained by taking the high collisionality limit of the equations evolving $q_\parallel$ and $q_\perp$ (Eqs. 2.25 and 2.26), which to the lowest order in $1/\nu_s$ gives

$$\nabla\cdot\left[\hat{\mathbf{b}}\left(\frac{r_{\parallel,\parallel 0s}}{2} + r_{\parallel,\perp 0s}\right)\right] - \frac{5}{2}\frac{p_{0s}}{n_0 m_s}\hat{\mathbf{b}}\cdot\nabla p_{0s} - \left(\frac{r_{\parallel,\perp 0s}}{2} + r_{\perp,\perp 0s}\right)\nabla\cdot\hat{\mathbf{b}} = -\nu_s q_s. \tag{2.38}$$

In the collisional limit r_0's will take their collisional values, $r_{\parallel,\parallel 0s} = 3p_{\parallel 0}^2/m_s n_0$, $r_{\parallel,\perp 0s} = p_{\parallel 0}^2/m_s n_0$, and $r_{\parallel,\parallel 0s} = 2p_{\parallel 0}^2/m_s n_0$. Substituting in the above equation gives

$$q_s = -\frac{5}{2}\frac{p_0}{\nu_s m_s}\nabla_\parallel T_{0s}, \tag{2.39}$$

which matches Braginskii's parallel heat flux (within factors of order unity).

2.5.2 3+1 closure with collisions

In principle, it is possible to use a kinetic response with the collision terms and to choose Landau closures that match the collisional linear response. Collisional heat fluxes can also be derived by using a higher moment model (e.g., a 4+1 model) and reducing the number of moments by taking a low frequency limit of the highest moment equations, with the collision terms included (see [180]). Without giving the details of derivation, we state the results for 3+1 closures that include the effects of

collisions,

$$q_{\parallel s} = -8nv_{t\parallel s}^2 \frac{ik_\parallel T_{\parallel s}}{(\sqrt{8\pi}|k_\parallel|v_{t\parallel s} + (3\pi - 8)\nu_s)}, \tag{2.40}$$

$$q_{\perp s} = -\frac{nv_{t\parallel s}^2 ik_\parallel T_{\perp s}}{\left(\sqrt{\frac{\pi}{2}}|k_\parallel|v_{t\parallel s} + \nu_s\right)} + \left(1 - \frac{T_{\perp s}}{T_{\parallel s}}\right) \frac{nv_{t\parallel s}^2 T_\perp ik_\parallel \delta B}{B\left(\sqrt{\frac{\pi}{2}}|k_\parallel|v_{t\parallel s} + \nu_s\right)}. \tag{2.41}$$

These closures allow a smooth transition from collisionless regime where collisionless damping is important, to the collisional regime with only viscous (collisional) damping. These closures give results similar to those derived from the DKE with a collision operator (in the linear regime), as shown for the case of MRI in Chapter 3. Thus, Landau models can be used to study collisionless and marginally collisional ($\omega \sim \nu$) regimes. However, accurate modeling of all the collisional effects, particularly those involving momentum exchange between species, requires a Braginskii formalism in highly collisional regime ($\nu \gg \omega$) or extension of the BGK model to use a velocity dependent collision frequency.

2.6 Nonlinear implementation of closure

Landau fluid closure for heat fluxes (Eqs. 2.30 and 2.31) involve terms containing $ik_\parallel/|k_\parallel|$. Numerical implementation of these in k-space is straightforward for electrostatic problems, as magnetic perturbations vanish and a simple Fourier transform along the magnetic field direction is needed. However, in more general problems, heat fluxes need to be calculated along the total (equilibrium+perturbation) magnetic field, and so $k_\parallel$ involves Fourier transforms along the perturbed field lines. Linear approximation of parallel heat flux, $q_\parallel \propto \hat{\mathbf{b_0}} \cdot \nabla \delta T_\parallel + \delta\hat{\mathbf{b}} \cdot \nabla T_\parallel$, has a contribution due to perturbed field lines. In an incompressible, ideally conducting plasma, temperature is constant along a field line ($q_\parallel = 0$), but temperature gradient along

the unperturbed field lines gives a nonzero result. Thus, the calculation of heat fluxes along the perturbed field lines is non-trivial.

For fully nonlinear, electromagnetic calculations one can use a Lagrangian coordinate system moving with the field lines, and coordinates aligned with the magnetic field. Then the standard fast Fourier transform (FFT) algorithm along the coordinate can be used to evaluate closures. While Lagrangian methods are useful for fusion plasma simulations where magnetic field fluctuations are small, in most astrophysical cases fields are turbulent with $B \lesssim \delta B$, making a grid aligned with field lines extremely difficult to implement. Alternatively, in an Eulerian grid, one needs to map $T_\parallel$ from the simulation grid to a field line following coordinate system, carry out the FFT, and then remap the result back to the simulation grid. FFTs can be avoided by working with the real space form of closures. This involves convolutions in one direction [$O(N^4)$ operations for N grid points in each direction], rather than the FFT algorithm [$O(N^3 \ln N)$ operations]. For example, the real-space form of the collisionless 3+1 closure for $q_{\parallel s}(z)$, Eq. 2.40, is the convolution

$$q_{\parallel s} = -n \left(\frac{2}{\pi}\right)^{3/2} v_{t\parallel s} \int_0^\infty dz' \frac{T_{\parallel s}(z+z') - T_{\parallel s}(z-z')}{z'} g(\frac{z'}{\lambda_{mfp}}), \tag{2.42}$$

where $g(z'/\lambda_{mfp}) = 1$ for z' small compared to the mean free path, but g falls off rapidly for z' large compared to the mean free path (see Eq. 51 of [180]). In a very low collisionality plasma, exact evaluation of the heat flux requires integrating a very long distance along a magnetic field line, but in practice the integral can be cut off at a few correlation lengths. Truncating the integral at $z' = L$ essentially means that Landau damping is applied to modes with $k_\parallel > 1/L$, while Landau damping is ignored for large scale $k_\parallel < 1/L$ modes. Choice of an appropriate L could be made by convergence studies.

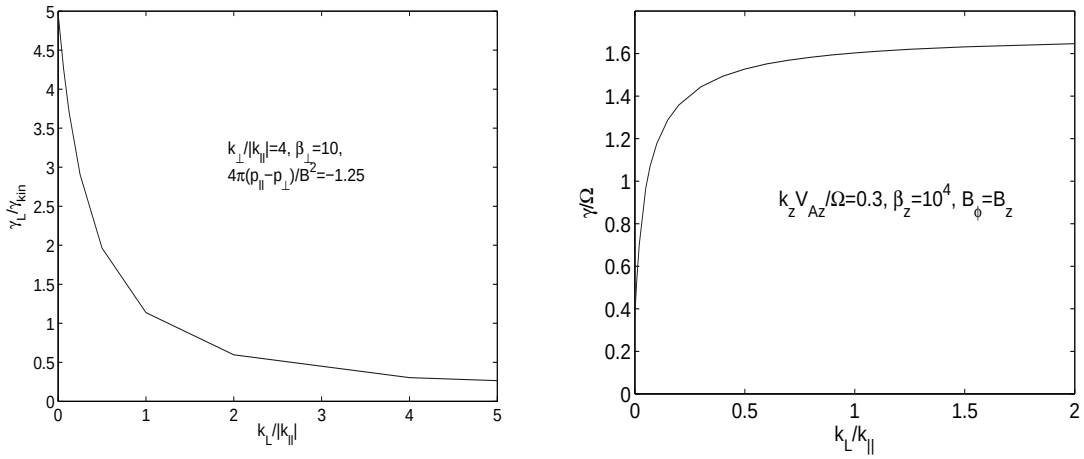

Figure 2.1: The dependence of the kinetic MHD growth rate, for a mirror mode and an MRI mode, on the assumed k_L Landau damping parameter in the heat fluxes. The optimal 3-pole approximation to the plasma Z function is recovered if $k_L/k_\parallel = 1$. The plot on the left shows that the growth rate of a mirror instability is fairly sensitive to the assumed k_L. On the other hand, the plot on the right shows that the growth rate of an MRI mode is not very sensitive to the assumed value of k_L (for these parameters). Note that $k_L = 0$ corresponds to an isothermal limit and $k_L \to \infty$ corresponds to a CGL limit where parallel heat fluxes are ignored. The existence of anomalous pitch-angle scattering by velocity-space microinstabilities may further reduce the sensitivity of the nonlinear MRI results to the assumed k_L parameter.

A crude closure for heat fluxes

A crude closure for parallel heat fluxes is obtained by using a local approximation where $|k_\parallel|$ in the denominator of Eqs. 2.40 and 2.41 is replaced by a parameter k_L, i.e.,

$$q_{\parallel s} = -8nv_{t\parallel s}^2 \frac{ik_\parallel T_{\parallel s}}{(\sqrt{8\pi}k_L v_{t\parallel s} + (3\pi - 8)\nu_s)}, \tag{2.43}$$

$$q_{\perp s} = -\frac{nv_{t\parallel s}^2 ik_\parallel T_{\perp s}}{\left(\sqrt{\frac{\pi}{2}}k_L v_{t\parallel s} + \nu_s\right)} + \left(1 - \frac{T_{\perp s}}{T_{\parallel s}}\right) \frac{nv_{t\parallel s}^2 T_\perp ik_\parallel \delta B}{B\left(\sqrt{\frac{\pi}{2}}k_L v_{t\parallel s} + \nu_s\right)}. \tag{2.44}$$

These are readily calculable local expressions for parallel heat fluxes that recovers the correct growth/damping rate for a mode with wavenumber k_L. Modes with $|k_\parallel| > k_L$ ($|k_\parallel| < k_L$) have a faster (slower) heat conduction rate than collisionless Landau

damping, but the final impact on the growth or damping rate of a mode depends on the type of mode (see Figure 2.1 for examples of mirror and MRI modes). Note that heat fluxes in Eqs. 2.43 and 2.44 with a constant k_L are diffusive, like Braginskii's heat fluxes. The shearing box simulations of the MRI in the collisionless regime use these local expressions [177]; the nonlinear results are not very sensitive to the choice of k_L, but do show some dependence (as shown in Chapter 4). However, there may be velocity-space microinstabilities that enhance the effective pitch-angle scattering rate, which may make the nonlinear results less sensitive to assumptions about k_L than one might at first think.

To improve on this in future work, there are several possible approaches that could be taken, such as a direct evaluation of the non-local heat flux expressions like Eq. 2.42, along field lines to some maximum length L. Another would be to use better Padé approximations to the k-space operator corresponding to the Landau-damping operator. For example, in Eqs. 2.30 and 2.31 the heat flux is proportional to $ik_\parallel/|k_\parallel|$, which at present we approximate as $ik_\parallel/k_L$ and then Fourier transform to real space to get the local operator $(1/k_L)\nabla_\parallel$. A next order Padé approximation to $ik_\parallel/|k_\parallel$ would be of the form $\alpha_0 ik_\parallel/(1+\beta_2 k_\parallel^2)$. Fourier transforming this gives the operator $(1-\beta_2\nabla_\parallel^2)^{-1}\alpha_0\nabla_\parallel$ [51]. If a fast iterative Krylov or Multigrid solver could be developed to invert the $(1-\beta_2\nabla_\parallel^2)$ operator (which would be non-trivial because it is an anisotropic operator corresponding to diffusion only along field lines), then this could be a faster way to approximate the non-local heat flux operator that would be relatively good over a range of $k_\parallel$ instead of only near $k_\parallel = k_L$. This procedure could be made more accurate by using higher order Padé approximations.

Another way to improve the calculation of the heat flux while retaining a local approximation could be by keeping more fluid moments before introducing a closure approximation, and modifying the closure approximations to correspond to hyper-collisions that selectively damp fine scales in velocity space. This would reduce the

number of fluid moments needed. Keeping higher order fluid moments before closing is related to a kinetic calculation that uses higher order Hermite polynomial basis functions in velocity space [77, 179]. While this is possible in principle, the rate of convergence as more terms are added and its computational cost relative to other options have not been evaluated.

Finally, another way to improve the calculation would be to do a direct 5-D calculation of the drift-kinetic equation. This would be computationally challenging, but would be feasible for a range of problems. It would be similar to 5-D gyrokinetic simulations recently developed in fusion energy research that have made significant contributions to understanding drift-wave turbulence in fusion devices [53, 97, 40].

2.6.1 The effects of small-scale anisotropy-driven instabilities

The MRI acts as a dynamo that amplifies the magnetic field. Conservation of the magnetic moment $\mu = v_\perp^2/(2B)$ means that as the magnetic field fluctuates, the perpendicular pressure $p_\perp$ will change, creating pressure anisotropies. As we will discuss in more detail in Chapter 4, if these pressure anisotropies exceed a certain threshold, they can drive velocity space instabilities (the mirror, cyclotron, and firehose instabilities) that have very fast growth rates at small scales. These instabilities can drive gyro-radius scale fluctuations that break adiabatic invariance and cause scattering to reduce the pressure anisotropy back to threshold.

To estimate the magnitude of this enhanced scattering rate, consider Eq. 2.36 in an incompressible limit, $\nabla \cdot \mathbf{V} = 0$ (as might be expected at high β for low Mach number MRI-driven flows):

$$d\delta p_s/dt + (3p_s + \delta p_s)\hat{\mathbf{b}} \cdot \nabla \mathbf{V} \cdot \hat{\mathbf{b}} + \nabla \cdot [\hat{\mathbf{b}}(q_{\parallel,s} - q_{\perp,s})] = -\nu \delta p_s.$$

Expanding the magnetic field evolution equation in the incompressible limit, $\partial \mathbf{B}/\partial t =$

$\nabla \times (\mathbf{V} \times \mathbf{B}) = \mathbf{B} \cdot \nabla \mathbf{V} - \mathbf{V} \cdot \mathbf{B}$, and dotting it with $\mathbf{B}$ gives

$$\frac{\partial}{\partial t}\left(\frac{1}{2}B^2\right) + \nabla \cdot \left(\mathbf{V}\frac{1}{2}B^2\right) = B^2 \hat{\mathbf{b}} \cdot \nabla \mathbf{V} \cdot \hat{\mathbf{b}}.$$

Substituting this in the pressure anisotropy equation, gives:

$$d\delta p_s/dt = -(3p_s + \delta p_s)\left[\frac{\partial \log B}{\partial t} + \nabla \cdot (\mathbf{V} \log B)\right] - \nabla \cdot [\hat{\mathbf{b}}(q_{\parallel,s} - q_{\perp,s})] - \nu \delta p_s.$$

The first term on the RHS represents the rate at which pressure anisotropies are driven due to adiabatic invariance in a changing magnetic field, which we will estimate as of order $3p_s \partial \log B/\partial t \sim 3p_s \gamma_{MRI}$, where γ_{MRI} is the growth rate for the dominant MRI modes in the simulation (this might be modified in the nonlinear state). In steady state, this will be balanced by the last term in this equation, which represents isotropization due to scattering at rate ν, due either to binary collisions (which are negligible for the regimes we focus on) or due to gyro-scale velocity-space instabilities. The growth rate of velocity-space instabilities is very rapid if the threshold for instability is exceeded, so a simple model for the effect of these instabilities is that they will cause just enough scattering ν_{eff} to keep the pressure anisotropy $\delta p_s/p_s = (p_{\parallel s} - p_{\perp s})/p_s$ close to the threshold value, which for the mirror instability is of order $7/\beta$ (further details of this will be discussed in Chapter 4). Thus, balancing the first and last terms on the RHS, we estimate the effective scattering rate by velocity-space instabilities to be of order

$$\nu_{eff} \sim 3p_s \gamma_{MRI}/\delta p_s \sim \gamma_{MRI}\beta. \tag{2.45}$$

The mean free path associated with this is

$$\lambda_{mfp,eff} \sim v_t/\nu_{eff} \sim L_{MRI}/\sqrt{\beta}, \tag{2.46}$$

assuming $\gamma_{MRI} \sim k_{MRI} V_{Alfvén} \sim V_{Alfvén}/L_{MRI}$, where L_{MRI} is of order the wavelength of a typical MRI mode in the system. There are factors of 2, π, etc. uncertainties in these estimates, but they suggest that, at very high β, the effective mean free path due to scattering by velocity-space instabilities might be short compared to the dominant MRI wavelength. This would reduce the sensitivity of the results to the assumed value of the k_L Landau damping parameter. However, there are intermittency issues that may complicate the picture, as we discuss next.

Intermittency of pitch angle scattering

Figure 2.2 shows that the fraction of the box where pitch angle scattering occurs is small ($\sim 0.01 - 0.1$) for both $\beta = 400$ and $\beta = 10^6$ simulations (runs $Zl4$ and $KZ4l$ in Chapter 4). The density of scattering regions (and hence the effective mean free path) is very similar for $\beta = 400$ and $\beta = 10^6$ simulations (see Figure 2.2). The volume averaged effective collision frequency ν_{eff} is also shown in Figure 2.2; at late times both initial $\beta = 400$ and initial $\beta = 10^6$ simulations give similar values for ν_{eff} because β at late times for the two simulations are comparable ($\beta \sim 500 - 1000$), roughly consistent with the β scaling of Eq. 2.45, but an order of magnitude smaller than the estimate of Eq. 2.45. Eqs. 2.45 and 2.46 assume that pitch angle scattering occurs roughly uniformly everywhere in the box. However, nonlinear simulations show that pitch angle scattering is not uniform but is concentrated in small volumes in the box. Because of the sparsity of scattering regions the true mean free path of most particles will be much longer than $H/\sqrt{\beta}$. The true mean free path will be some average measure of how far particles have to move along field lines before they find one of the isolated regions where rapid scattering is occurring; this may be comparable to the box size (or larger).

Further studies are required to understand the role of the distribution of intermittent scattering regions on thermal conduction and momentum transport, and to

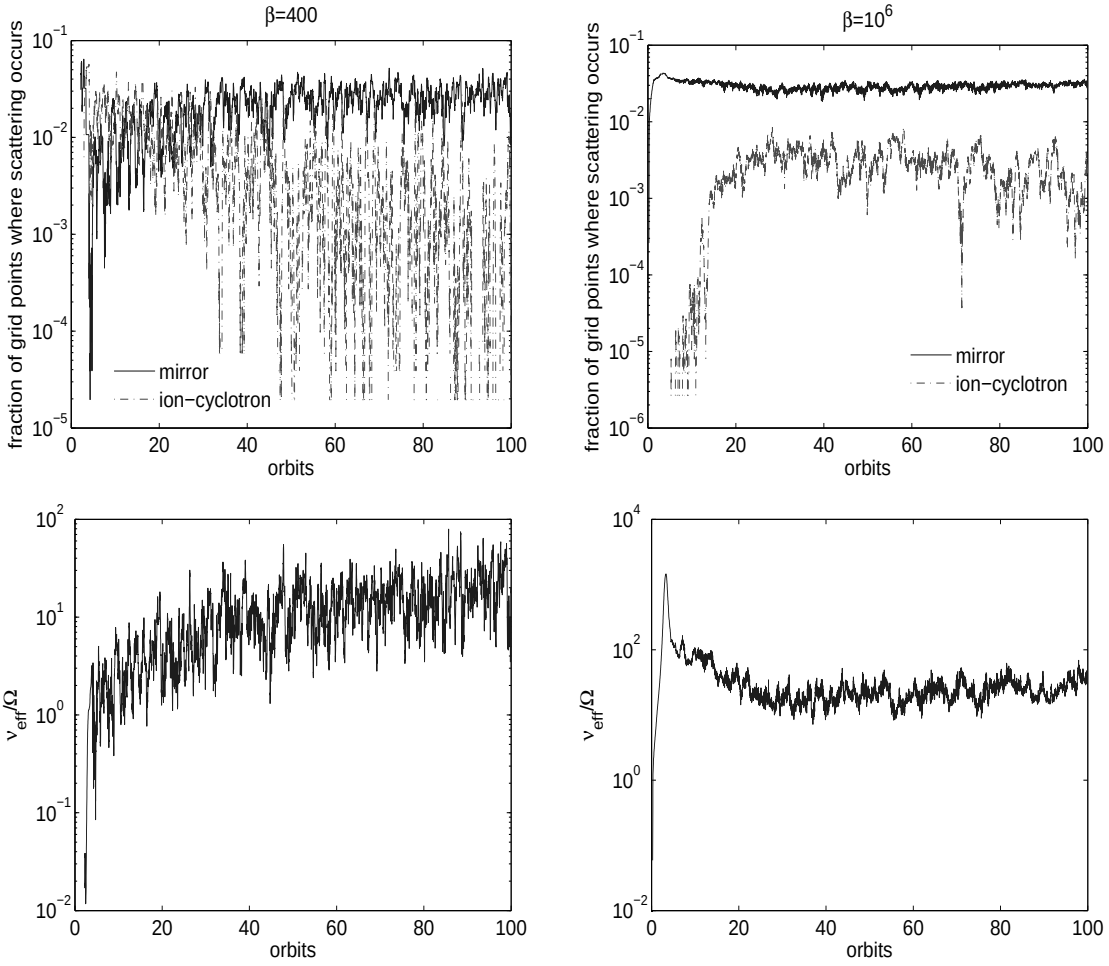

Figure 2.2: Top two plots show the fraction of grid points undergoing pitch angle scattering due to mirror (solid line) and ion-cyclotron (dot-dashed line) instabilities for $\beta = 400$ (left; low resolution run $Zl4$) and 10^6 (right; high resolution run $KZ4h$). Effective collision frequency due to pitch angle scattering (ν_{eff}/Ω) for $\beta = 400$ (left) and $\beta = 10^6$. Pitch angle scattering is not uniform in space, and occurs only in small volume-fraction of the box ($\sim 0.01 - 0.1$).

what extent does pitch angle scattering lead to MHD-like dynamics.

As we will find in Chapter 4, the limits on anisotropy provided by these velocity-space instabilities cause the nonlinear kinetic MHD simulations of the MRI to be qualitatively closer to regular MHD simulations of the MRI. However, even with these limits on anisotropy, the anisotropic pressure component of the angular momentum transport is found to be competitive with the usual Maxwell and Reynolds stress transport mechanisms. The enhanced scattering by these velocity-space instabilities may alter the relative electron/ion heating in MRI turbulence, a topic we leave for future research.

The enhanced scattering by velocity-space instabilities can also cause an increase in the effective Reynolds number (and thus a reduction of the effective magnetic Prandtl number, the ratio of viscosity and resistivity) of high β MHD turbulence in general. The possible implications of this are beyond the focus of this thesis, but they have been discussed in a recent paper [170], on which I was a co-author.

To summarize, in this chapter we began with the most detailed Vlasov description of collisionless plasmas, and motivated the drift kinetic equation (DKE) in the $k\rho_s \gg 1$, $\omega \ll \Omega_s$ regime. Further simplification was introduced in the form of fluid closures for parallel heat fluxes that reproduce correct kinetic behavior, and capture collisionless damping. Fourier space representation of the heat fluxes, and the nonlocal integral expression in coordinate space (and the ways to numerically compute it) were indicated. A generalization to include the collisional effects, which reduces to Braginskii's result in $\nu \gg \omega$ regime, was given. A crude, local approximation for the heat fluxes was presented, in which the parameter k_L represents a typical wavenumber of the mode. Only the local approximation has been used in the local shearing box simulations of the collisionless MRI, leaving sophisticated treatments for the future. Pitch-angle scattering by velocity space instabilities might provide a reduction of the effective mean-free-path, which may contribute to reducing the sensitivity of the re-

sults to the assumed k_L, but the scattering is found to be very intermittent spatially, so the reduction in the mean free path might be less than one might expect at first.

Chapter 3

Transition from collisionless to collisional MRI

This chapter is based on our paper on the transition of the MRI from the collisionless to the collisional regime [176]. Calculations by Quataert and coworkers [158] found that the growth rates of the magnetorotational instability (MRI) in a collisionless plasma can differ significantly from those calculated using MHD, particularly at long wavelengths. This can be important in hot accretion flows around compact objects (see Section 1.4 for a review). In this chapter we study the transition from the collisionless kinetic regime to the collisional MHD regime, mapping out the dependence of the MRI growth rate on collisionality. The Landau fluid closure for parallel heat flux, which recovers kinetic effects like Landau/Barnes damping, is used and the effect of collisions is included via a BGK operator. The kinetic MHD equation of motion has three forces: the isotropic pressure force, the magnetic force, and the anisotropic pressure force. For $\beta \gtrsim 1$ the transition from collisionless to Braginskii regime occurs as the anisotropic pressure becomes small compared to the isotropic pressure ($\nu \gtrsim \Omega\sqrt{\beta}$); and the transition from Braginskii to MHD occurs when anisotropic pressure force becomes negligible compared to the magnetic force ($\nu \gtrsim \Omega\beta$). In the

weak magnetic field regime where the Alfvén and MRI frequencies ω are small compared to the sound wave frequency $k_\parallel c_0$, the dynamics are still effectively collisionless even if $\omega \ll \nu$, so long as the collision frequency $\nu \lesssim k_\parallel c_0$ (i.e., so long as the mean free path is long compared to a wavelength); for an accretion flow this requires $\nu \lesssim \Omega\sqrt{\beta}$. The low collisionality regime not only modifies the MRI growth rate, but also introduces collisionless Landau or Barnes damping of long wavelength modes, which may be important for heating of electrons and protons. The fastest growth rate in the collisionless regime is $\approx$ twice faster than in MHD; moreover, the fastest growing mode occurs at large length scales compared to the fastest growing MHD mode.

3.1 Introduction

Balbus and Hawley [14] showed that the magnetorotational instability (MRI), a local instability of differentially rotating magnetized plasmas, is the most efficient source of angular momentum transport in many astrophysical accretion flows (see Section 1.3 for a review). The MRI may also be important for dynamo generation of galactic and stellar magnetic fields. Most studies of the MRI have employed standard MHD equations which are appropriate for collisional, short mean free path plasmas, but it is not obvious that this instability is relevant for collisionless, low luminosity accretion flows (see Section 1.4; Table 1.2 shows the collsion frequency is small compared to the rotation frequency). Quataert and coworkers ([158]; hereafter QDH) studied the MRI in the collisionless regime using the kinetic results of Snyder, Hammett & Dorland [180]. They showed that the MRI persists as a robust instability in a collisionless plasma, but that at high $\beta \gg 1$ (ratio of plasma pressure to magnetic pressure), the physics of the instability is quite different and the kinetic growth rates can differ significantly from the MHD growth rates.

One motivation for studying the MRI in the collisionless regime is to understand

radiatively inefficient accretion flows onto compact objects. An example of non-radiative accretion is the radio and x-ray source Sagittarius A*, which is powered by gas accreting onto a supermassive black hole at the center of our galaxy (see Subsection 1.4.2 for a review). In radiatively inefficient accretion flow models, the accreting gas is a hot, low density, plasma, with the proton temperature large compared to the electron temperature ($T_p \approx 10^{12}$ K $\gg T_e \approx 10^{10} - 10^{12}$ K). In order to maintain such a two-temperature configuration, the accretion flow must be collisionless in the sense that the timescale for electrons and protons to exchange energy by Coulomb collisions is longer than the inflow time of the gas (for models of Sagittarius A*, the collision time close to the black hole is ≈ 7 orders of magnitude longer than the inflow time, see Table 1.2).

In this chapter we extend the kinetic results of QDH to include collisions; we study the behavior of the MRI in the transition from the collisionless regime to the collisional MHD regime. Instead of using a more accurate (but very complicated) Landau or Balescu-Lenard collision operator, we use the simpler Bhatnagar-Gross-Krook (BGK) collision operator [25] that conserves number, momentum and energy.

There are several reasons for studying the MRI with a varying collision frequency: (1) to gain additional understanding of the qualitatively different physics in the MHD and kinetic regimes, (2) the key difference between the kinetic and MHD regimes is that the pressure is anisotropic (with respect to the local magnetic field) in a collisionless plasma (see Section 2.3). Even if particle collisions are negligible, high frequency waves with frequencies $\sim$ the proton cyclotron frequency can isotropize the proton distribution function (see Subsection 4.2.2). Our treatment of "collisions" can qualitatively describe this process as well; and (3) the transition from the collisional to the kinetic MRI could be dynamically interesting if accretion disks undergo transitions from thin disks to hot radiatively inefficient flows (as has been proposed to explain, e.g., state changes in X-ray binaries; [55]). There can be associated changes in the rate

of angular momentum transport (α), as disk transitions from collisional to collisionless state, and vice versa.

We begin with the linearized drift kinetic equation with a BGK collision operator and derive the exact closures for $\delta p_\parallel$ and $\delta p_\perp$; these are used to close the linearized kinetic MHD equations. We use Landau fluid closure for parallel heat fluxes, and show that they are equivalent to the kinetic closures in both low and high collisionality regimes; Landau fluids are considered because they are easier to implement computationally and we use them for local, nonlinear MHD disk simulations described in Chapter 4. The kinetic MHD linear analysis shows the presence of damped modes at all scales (see Figure 3.4), a feature absent in MHD.

3.2 Linearized kinetic MHD equations

The analysis is restricted to fluctuations that have wavelengths much larger than proton Larmor radius and frequencies well below the proton cyclotron frequency. In this limit, a plasma can be described by the following kinetic MHD equations (see Section 2.3):

$$\frac{\partial \rho}{\partial t} + \nabla \cdot (\rho \mathbf{V}) = 0, \tag{3.1}$$

$$\rho \frac{\partial \mathbf{V}}{\partial t} + \rho \left(\mathbf{V} \cdot \nabla\right) \mathbf{V} = \frac{\left(\nabla \times \mathbf{B}\right) \times \mathbf{B}}{4\pi} - \nabla \cdot \mathbf{P} + \mathbf{F_g}, \tag{3.2}$$

$$\frac{\partial \mathbf{B}}{\partial t} = \nabla \times \left(\mathbf{V} \times \mathbf{B}\right), \tag{3.3}$$

$$\mathbf{P} = p_\perp \mathbf{I} + \left(p_\parallel - p_\perp\right) \hat{\mathbf{b}}\hat{\mathbf{b}}, \tag{3.4}$$

where ρ is the mass density, $\mathbf{V}$ is the fluid velocity, $\mathbf{B}$ is the magnetic field, $\mathbf{F_g}$ is the gravitational force, $\hat{\mathbf{b}} = \mathbf{B}/|\mathbf{B}|$ is a unit vector in the direction of the magnetic field, and $\mathbf{I}$ is the unit tensor. In equation (3.3) an ideal Ohm's law is used, neglecting effects such as resistivity. $\mathbf{P}$ is the pressure tensor that has different perpendicular ($p_\perp$)

and parallel ($p_\parallel$) components with respect to the background magnetic field (unlike in MHD, where there is only a scalar pressure). The pressures are determined by solving the drift kinetic equation given below. $\mathbf{P}$ should in general be a sum over all species but in the limit where ion dynamics dominate and electrons just provide a neutralizing background, the pressure can be interpreted as the ion pressure. This is the case for hot accretion flows where $T_p \gg T_e$.

We assume that the background (unperturbed) plasma is described by a non-relativistic Maxwellian distribution function with equal parallel and perpendicular pressures (temperatures). Although the equilibrium pressure is assumed to be isotropic, the perturbed pressure is not. We take the plasma to be differentially rotating, but otherwise uniform (we neglect temperature and density gradients). Equilibrium state for equation (3.2) in presence of a subthermal magnetic field with vertical ($B_z = B_0 \sin\theta$) and azimuthal ($B_\phi = B_0 \cos\theta$) components gives a Keplerian rotation ($\Omega \propto R^{-3/2}$) profile.

In a differentially rotating plasma, a finite B_R is sheared to produce a time-dependent B_ϕ, which complicates the kinetic analysis (unlike in MHD, where a time-dependent B_ϕ does not couple to axisymmetric disturbances; [14]); we therefore set $B_R = 0$. For linearization we consider fluctuations of the form $\exp[-i\omega t + i\mathbf{k}\cdot\mathbf{x}]$, with $\mathbf{k} = k_R\hat{R} + k_z\hat{z}$, i.e., axisymmetric modes; we also restrict our analysis to local perturbations for which $|\mathbf{k}|R \gg 1$. Writing $\rho = \rho_0 + \delta\rho$, $\mathbf{B} = \mathbf{B_0} + \delta\mathbf{B}$, $p_\perp = p_0 + \delta p_\perp$, and $p_\parallel = p_0 + \delta p_\parallel$, $\mathbf{V} = \hat{\phi}\Omega R + \delta\mathbf{V}$ (with Keplerian rotation $\Omega(R)$), and working in cylindrical coordinates, the linearized versions of equations (3.1)-(3.3) become (see

QDH)

$$\omega\delta\rho = \rho_0 \mathbf{k}\cdot\delta\mathbf{V}, \tag{3.5}$$

$$-i\omega\rho_0\delta V_R - \rho_0 2\Omega\delta V_\phi = -\frac{ik_R}{4\pi}\left(B_z\delta B_z + B_\phi\delta B_\phi\right) + \frac{ik_z B_z\delta B_R}{4\pi} - ik_R\delta p_\perp, \tag{3.6}$$

$$-i\omega\rho_0\delta V_\phi + \rho_0\delta V_R\frac{\kappa^2}{2\Omega} = \frac{ik_z B_z\delta B_\phi}{4\pi} - ik_z\sin\theta\cos\theta[\delta p_\parallel - \delta p_\perp], \tag{3.7}$$

$$-i\omega\rho_0\delta V_z = -\frac{ik_z B_\phi\delta B_\phi}{4\pi} - ik_z[\sin^2\theta\delta p_\parallel + \cos^2\theta\delta p_\perp], \tag{3.8}$$

$$\omega\delta B_R = -k_z B_z\delta V_R, \tag{3.9}$$

$$\omega\delta B_\phi = -k_z B_z\delta V_\phi - \frac{ik_z B_z}{\omega}\frac{d\Omega}{d\ln R}\delta V_R + B_\phi\mathbf{k}\cdot\delta\mathbf{V}, \tag{3.10}$$

$$\omega\delta B_z = k_R B_z\delta V_R, \tag{3.11}$$

where $\kappa^2 = 4\Omega^2 + d\Omega^2/d\ln R$ is the epicyclic frequency. To complete this system of equations and derive the dispersion relation for linear perturbations, we need expressions for $\delta p_\perp$ and $\delta p_\parallel$ in terms of lower moments. These can be obtained by taking moments of the linearized and Fourier transformed drift-kinetic equation that includes a linearized BGK collision operator (see Section 2.2).

The drift-kinetic equation for the distribution function f, including the effects of gravity is (see Section 2.2 for details)

$$\frac{\partial f}{\partial t} + \left(v_\parallel\hat{\mathbf{b}} + \mathbf{V}_E\right)\cdot\nabla f + \left(-\hat{\mathbf{b}}\cdot\frac{D\mathbf{V}_E}{Dt} - \mu\hat{\mathbf{b}}\cdot\nabla B + \frac{e}{m}(E_\parallel + F_{g\parallel}/e)\right)\frac{\partial f}{\partial v_\parallel} = C\left(f\right), \tag{3.12}$$

where $\mathbf{V}_E = c\left(\mathbf{E}\times\mathbf{B}\right)/B^2$, $\mu = (\mathbf{v}_\perp - \mathbf{V}_E)^2/2B$ is the magnetic moment (conserved in our approximations in the absence of collisions), $F_{g\parallel} = GM_* m_p\hat{R}\cdot\hat{\mathbf{b}}/R^2$, and $D/Dt = \partial/\partial t + \left(v_\parallel\hat{\mathbf{b}} + \mathbf{V}_E\right)\cdot\nabla$. The fluid velocity $\mathbf{V} = \mathbf{V}_E + \hat{\mathbf{b}}V_\parallel$, where the $E\times B$ drift $\mathbf{V}_E$ is determined by the perpendicular component of equation (3.2). The parallel component of the gravitational force, $F_{g\parallel}$, is included as it is of the same order as the parallel electric force. Notice the addition of a collision operator on the right hand side to allow for generalization to collisional regimes. In the next

section we derive the linearly-exact kinetic expressions for $\delta p_{\parallel}$ and $\delta p_{\perp}$ using the BGK collision operator in equation (3.12). We then compare these with Landau closure approximations from Snyder et al. [180].

3.3 Kinetic closure including collisions

In this section we use a simple BGK collision operator [25] to calculate $\delta p_{\parallel}$ and $\delta p_{\perp}$ from equation (3.12). Since we consider only ion-ion collisions (see Subsection 2.4.1 for multiple species), the BGK operator is $C_K(f) = -\nu(f - F_M)$ where ν is the ion-ion collision frequency and F_M is a shifted Maxwellian with the same density, momentum, and energy as f (so that collisions conserve number, momentum, and energy). The integro-algebraic BGK operator greatly simplifies the calculations while adequately modeling many of the key properties of the full integro-differential collision operator. In some situations, the effects of weak collisions can be enhanced in a more complete collision operator due to sharp velocity gradients in the distribution function; we ignore such effects in the present analysis.

In this section, we calculate the linearization of the drift-kinetic equation around an accretion disk equilibrium, including equilibrium flows and gravity. A number of complicated intermediate terms end up canceling, and the final forms of the closures used (from equations (3.26-3.27) onwards) are identical to what one would get from perturbing around a slab equilibrium with no flows. We carried out the more detailed calculation to verify that there were no missing terms in the final closures.

The equilibrium distribution function f_0 is given by

$$f_0 = \frac{n_0}{(2\pi T_0/m)^{3/2}} \exp\left(-\frac{m}{2T_0}|\mathbf{v} - \mathbf{V}_0|^2\right), \tag{3.13}$$

where $\mathbf{V}_0 = \mathbf{V}_{E0} + V_{\parallel 0}\hat{\mathbf{b}}_0$ is the Keplerian rotation velocity in the $\hat{\phi}$ direction. Since

$|\mathbf{v}-\mathbf{V}_0|^2 = (v_\parallel - V_{\parallel 0})^2 + 2\mu B_0$, f_0 can be expressed in terms of $\left(\mu, v_\parallel\right)$ as

$$f_0 = \frac{n_0}{\left(2\pi T_0/m\right)^{3/2}} \exp\left(-\frac{m}{2T_0}\left((v_\parallel - V_{\parallel 0})^2 + 2\mu B_0\right)\right). \tag{3.14}$$

We shall linearize the drift-kinetic equation and the BGK collision operator. The distribution function is given as $f = f_0 + \delta f$ where δf is the perturbation in the distribution function. The shifted Maxwellian that appears in the BGK collision operator is given by

$$F_M = \frac{N_M}{\left(2\pi T_M/m\right)^{3/2}} \exp\left\{-\frac{m}{2T_M}\left(\left(v_\parallel - V_{\parallel M}\right)^2 + 2\mu B\right)\right\}. \tag{3.15}$$

F_M has three free parameters (N_M, $V_{\parallel M}$, T_M) which are to be chosen so as to conserve number, parallel momentum, and energy. When taking moments of the BGK operator, it is important to note that $\int d^3v = \int 2\pi \left(B_0 + \delta B\right) d\mu dv_\parallel$. From equation (3.15) and conservation of number, momentum, and energy it follows that

$$\begin{aligned}
N_M &= n_0 + \delta n \approx n_0\left(1 + \frac{\delta B}{B_0}\right) + 2\pi B_0 \int d\mu dv_\parallel \delta f, && (3.16)\\
N_M V_{\parallel M} &= N_M(V_{\parallel 0} + \delta V) \approx n_0 V_{\parallel 0}\left(1 + \frac{\delta B}{B_0}\right) + 2\pi B_0 \int d\mu dv_\parallel \delta f v_\parallel, && (3.17)\\
N_M T_M &= p_0 + \delta p = p_0 + (\delta p_\parallel + 2\delta p_\perp)/3, && (3.18)\\
\delta p_\parallel &\approx p_0 \delta B/B_0 + 2\pi B_0 \int d\mu dv_\parallel \delta f m (v_\parallel - V_{\parallel 0})^2, && (3.19)\\
\delta p_\perp &\approx 2p_0 \delta B/B_0 + 2\pi B_0 \int d\mu dv_\parallel \delta f \mu m B_0, && (3.20)
\end{aligned}$$

where the approximate expressions retain only linear terms in perturbed quantities. Linearizing the expression for the relaxed Maxwellian in equation (3.15) about f_0,

the drift-kinetic BGK collision operator is given by

$$\begin{aligned} C_K\left(\delta f\right) &= -\nu\delta f + \nu f_0 \times \left\{ \left(\frac{\delta n}{n_0} - \frac{3\delta T}{2T_0} \right) \right. \\ &+ \left. \frac{m}{T_0} \left(\left(v_\parallel - V_{\parallel 0}\right) \delta u + \left(v_\parallel - V_{\parallel 0}\right)^2 \frac{\delta T}{2T_0} \right) - \frac{m\mu B_0}{T_0} \left(\frac{\delta B}{B_0} - \frac{\delta T}{T_0} \right) \right\} \quad (3.21) \end{aligned}$$

The drift-kinetic equation including the BGK operator can be linearized to obtain the following equation for δf

$$\begin{aligned} \delta f &= V_{\phi 0}(v_\parallel - V_{\parallel 0}) f_0 \sin\theta \frac{(\delta B_\phi \sin\theta - \delta B_z \cos\theta)\, m}{T_0 B_0} + \frac{m\left(v_\parallel - V_{\parallel 0}\right) f_0}{T_0\left(-i\omega + ik_\parallel\left(v_\parallel - V_{\parallel 0}\right) + \nu\right)} \times \\ &\left(-ik_\parallel \mu \delta B + \frac{\left(eE_\parallel + F_{g\parallel}\right)}{m} \right) + \frac{\nu f_0}{\left(-i\omega + ik_\parallel\left(v_\parallel - V_{\parallel 0}\right) + \nu\right)} \times \\ &\left(\frac{\delta n}{n_0} - \frac{3}{2}\frac{\delta T}{T_0} + \frac{m(v_\parallel - V_{\parallel 0})\delta u}{T_0} + \frac{m(v_\parallel - V_{\parallel 0})^2}{2T_0}\frac{\delta T}{T_0} + \frac{m\mu B_0}{T_0}\frac{\delta T}{T_0} - \frac{m\mu\delta B}{T_0} \right), \quad (3.22) \end{aligned}$$

where $F_{g\parallel} = GM_* m_p \delta B_R / B_0 R^2$ is the component of gravitational force in the direction of magnetic field. Choosing a compact notation where $-i\omega \sin\theta(\delta B_\phi \sin\theta - \delta B_z \cos\theta) m V_{\phi 0}/eB_0 + F_{g\parallel}/e + E_\parallel \rightarrow E_\parallel$, the moments of the perturbed distribution function δf in drift coordinates $(v_\parallel, \mu)$, $\int \left(1, 2\mu B_0, (v_\parallel - V_{\parallel 0})^2\right) \delta f 2\pi B_0 d\mu dv_\parallel$ give

$$\begin{aligned} \frac{\delta n}{n_0} &= \frac{\delta B}{B_0}(1-R) + \frac{eE_\parallel}{ik_\parallel T_0} R - \zeta_2 \left\{ \left(\frac{\delta n}{n_0} - \frac{3}{2}\frac{\delta T}{T_0} \right) Z + \left(\frac{\delta T}{T_0} - \frac{\delta B}{B_0} \right) Z \right. \\ &+ \left. \sqrt{2}\frac{\delta V}{c_0} R + \left(\frac{\delta T}{T_0} + 2i\sin\theta \frac{k_\parallel V_{\phi 0}}{\nu} \frac{(\delta B_\phi \sin\theta - \delta B_z \cos\theta)}{B_0} \right) \zeta R \right\}, \quad (3.23) \\ \frac{\delta p_\perp}{p_0} &= 2\frac{\delta B}{B_0}(1-R) + \frac{eE_\parallel}{ik_\parallel T_0} R - \zeta_2 \left\{ \left(\frac{\delta n}{n_0} - \frac{3}{2}\frac{\delta T}{T_0} \right) Z + 2\left(\frac{\delta T}{T_0} - \frac{\delta B}{B_0} \right) Z \right. \\ &+ \left. \sqrt{2}\frac{\delta V}{c_0} R + \left(\frac{\delta T}{T_0} + 2i\sin\theta \frac{k_\parallel V_{\phi 0}}{\nu} \frac{(\delta B_\phi \sin\theta - \delta B_z \cos\theta)}{B_0} \right) \zeta R \right\}, \quad (3.24) \\ \frac{\delta p_\parallel}{p_0} &= -2\frac{\delta B}{B_0}\zeta^2 R + \frac{eE_\parallel}{ik_\parallel T_0}\left(1 + 2\zeta^2 R\right) - \zeta_2 \left\{ 2\left(\frac{\delta n}{n_0} - \frac{3}{2}\frac{\delta T}{T_0} \right) \zeta R \right. \\ &+ 2\left(\frac{\delta T}{T_0} - \frac{\delta B}{B_0} \right) \zeta R + \sqrt{2}\frac{\delta V}{c_0}\left(1 + 2\zeta^2 R\right) \\ &+ \left. \left(\frac{\delta T}{T_0} + 2i\sin\theta \frac{k_\parallel V_{\phi 0}}{\nu} \frac{(\delta B_\phi \sin\theta - \delta B_z \cos\theta)}{B_0} \right) \zeta \left(1 + 2\zeta^2 R\right) \right\}. \quad (3.25) \end{aligned}$$

The parallel electric field, $E_\parallel$, can be eliminated by taking appropriate combinations of these three equations, giving

$$\frac{\delta\rho}{\rho_0} - \frac{\delta p_\perp}{p_0} = -\frac{\delta B}{B_0}(1-R) + \zeta_2 Z\left(\frac{\delta T}{T_0} - \frac{\delta B}{B_0}\right), \tag{3.26}$$

and

$$\left(1+2\zeta^2 R\right)\frac{\delta\rho}{\rho_0} - R\frac{\delta p_\parallel}{p_0} = \frac{\delta B}{B_0}\left(1+2\zeta^2 R - R\right) - \zeta_2\left(Z - 2\zeta R\right)\left(\frac{\delta\rho}{\rho_0} - \frac{\delta T}{2T_0} - \frac{\delta B}{B_0}\right), \tag{3.27}$$

where $\delta T = \left(2\delta T_\perp + \delta T_\parallel\right)/3$, $\delta B = \hat{\mathbf{b}}_\mathbf{0}\cdot\delta\mathbf{B}$, $\zeta = (\omega + i\nu)/\sqrt{2}|k_\parallel|c_0$, $\zeta_2 = i\nu/\sqrt{2}|k_\parallel|c_0$, $k_\parallel = \hat{\mathbf{b}}_\mathbf{0}\cdot\mathbf{k}$, $T_{\parallel,\perp} = mp_{\parallel,\perp}/\rho$, and $c_0 = \sqrt{T_0/m}$ is the isothermal sound speed of the ions. In equations (3.26) and (3.27), $R = 1 + \zeta Z$ is the plasma response function, where

$$Z(\zeta) = \frac{1}{\sqrt{\pi}}\int dx \frac{\exp[-x^2]}{x-\zeta} \tag{3.28}$$

is the plasma dispersion function [91]. Equations (3.26) and (3.27) can be substituted into the linearized fluid equations 3.5-3.11 to derive the dispersion relation for the plasma. The full closures are, however, very complicated, so it is useful to consider several simplifying limits that isolate much of the relevant physics. In addition, the solution of linearized kinetic MHD equations fully kinetic closures will give an implicit equation for the growth rate (involving the Z function) that has to be solved numerically.

The closure equations can be simplified in two limits, $|\zeta| \ll 1$, the collisionless limit, and $|\zeta| \gg 1$, the high collisionality limit. The derivation of the asymptotic solution for the closure equations in these two limits is given in Appendix B. In the high collisionality limit,

$$\frac{\delta p_\perp}{p_0} = \frac{5}{3}\frac{\delta\rho}{\rho_0} + \frac{\zeta_1}{\zeta_2}\left(\frac{4}{3} + \frac{5}{9\zeta_1^2}\right)\frac{\delta\rho}{\rho_0} - 2\frac{\zeta_1}{\zeta_2}\frac{\delta B}{B_0}, \tag{3.29}$$

and

$$\frac{\delta p_\parallel}{p_0} = \frac{5}{3}\frac{\delta\rho}{\rho_0} + \frac{\zeta_1}{\zeta_2}\left(-\frac{2}{3} + \frac{5}{9\zeta_1^2}\right)\frac{\delta\rho}{\rho_0} + \frac{\zeta_1}{\zeta_2}\frac{\delta B}{B_0}, \tag{3.30}$$

where $\zeta_1 = \omega/\sqrt{2}|k_\parallel|c_0$. Notice that in the limit that the collision frequency is very high, $\zeta_2 \to \infty$, one recovers the MHD result that the perturbations are adiabatic and isotropic: $\delta p_\parallel/p_0 = \delta p_\perp/p_0 = 5\delta\rho/3\rho_0$.

For low collisionality, $|\zeta| \ll 1$, to second order in ζ,

$$\frac{\delta p_\perp}{p_0} = \frac{\delta\rho}{\rho_0} - i\sqrt{\pi}\zeta_1\frac{\delta B}{B_0} - \frac{\pi\zeta_1\zeta_2}{3}\frac{\delta\rho}{\rho_0} + \zeta_1\zeta_2\left(2 - \frac{\pi}{3}\right)\frac{\delta B}{B_0}, \tag{3.31}$$

and

$$\begin{aligned}\frac{\delta p_\parallel}{p_0} &= \frac{\delta\rho}{\rho_0} - i\sqrt{\pi}\zeta_1\left(\frac{\delta\rho}{\rho_0} - \frac{\delta B}{B_0}\right) + \frac{\delta\rho}{\rho_0}\left(4\zeta_1\zeta_2 - \pi\zeta_1^2 - \frac{7\pi\zeta_1\zeta_2}{6}\right) + \\ &\quad \frac{\delta B}{B_0}\left(\sqrt{\pi}\zeta_1\zeta_2 - \frac{\pi\zeta_1\zeta_2}{6} - 2\zeta^2 - 4\zeta_2\zeta\right).\end{aligned} \tag{3.32}$$

To first order, there is no effect of collisions on the growth rate of the MRI; the results above are then exactly same as equations (20) and (21) in QDH (who neglected collisions entirely). Collisional effects modify the closure only at order ζ^2, though one has to go to this order to find the first order dependence of ω on ν in the dispersion relation.

3.4 Comparison with Landau fluid closure

The results from last section provide expressions for $\delta p_\perp$ and $\delta p_\parallel$ in both low and high collisionality regimes, $|\zeta| \ll 1$ and $|\zeta| \gg 1$, but it would be convenient to have a single set of equations that can provide a robust transition between these two regimes. The Landau fluid closure [180], which we discuss in Section 2.4, can do this.

The second order moments of the drift kinetic equation (Eq. 3.12) yield evolution

equations for $\delta p_\perp$ and $\delta p_\parallel$ (see, e.g., Eqs. 2.23 and 2.24). The linearized versions of these equations, including a BGK collision operator, are given by [1]

$$-i\omega\delta p_\parallel + p_0 i\mathbf{k}\cdot\delta\mathbf{v} + ik_\parallel q_\parallel + 2p_0 ik_\parallel \delta v_\parallel - 3p_0\Omega\cos\theta\frac{\delta B_R}{B_0} = -\frac{2}{3}\nu\left(\delta p_\parallel - \delta p_\perp\right), \quad (3.33)$$

and

$$-i\omega\delta p_\perp + 2p_0 i\mathbf{k}\cdot\delta\mathbf{v} + ik_\parallel q_\perp - p_0 ik_\parallel \delta v_\parallel + \frac{3}{2}p_0\Omega\cos\theta\frac{\delta B_R}{B_0} = -\frac{1}{3}\nu\left(\delta p_\perp - \delta p_\parallel\right). \quad (3.34)$$

As is usual with moment hierarchies, the above equations for $\delta p_{\parallel,\perp}$ depend on third moments of the distribution function, $q_\parallel$ and $q_\perp$, the parallel and perpendicular heat fluxes.[2] Snyder et al. [180] introduced closure approximations for $q_\parallel$ and $q_\perp$ that determine $\delta p_\perp$ and $\delta p_\parallel$ without solving the full kinetic equation of the previous section (see Section 2.4 for a review). These Landau-fluid approximations "close" equations (3.1)-(3.4) and allow one to solve for the linear response of the plasma.

The linearized heat fluxes of parallel and perpendicular pressures are given by

$$q_\perp = -p_0 c_0^2 \frac{ik_\parallel\left(\delta p_\perp/p_0 - \delta\rho/\rho_0\right)}{\left(\sqrt{\pi/2}|k_\parallel|c_0 + \nu\right)} \quad (3.35)$$

and

$$q_\parallel = -8p_0 c_0^2 \frac{ik_\parallel\left(\delta p_\parallel/p_0 - \delta\rho/\rho_0\right)}{\left(\sqrt{8\pi}|k_\parallel|c_0 + (3\pi - 8)\,\nu\right)}. \quad (3.36)$$

As discussed in earlier work [180, 78, 77, 179], Landau-fluid closure approximations provide n-pole Padé approximations to the exact plasma dispersion function $Z(\zeta)$ that appears in the kinetic plasma response (see Section 2.4). These Padé approximations

[1] A comparison of our equations (3.33) and (3.34) with equations (30) and (31) in Snyder et al. (linearized version of Eqs. 2.23 and 2.24) shows that our equations have an extra term proportional to the Keplerian rotation frequency; this is because [180] did not include gravitational effects and Keplerian rotation in their linearized equations.

[2] It is important to note that $q_\parallel$ and $q_\perp$ are the fluxes of $p_\parallel$ and $p_\perp$ along the field lines; thermal conduction perpendicular to field lines vanishes as the Larmor radius is tiny.

are thus able to provide robust results that capture kinetic effects such as Landau damping, and that can also smoothly transition between the high and low ζ regimes.[3] We have found, not surprisingly, that the fluid approximations remain robust when collisions are included. That is, in all of the numerical tests we have carried out, we have found good agreement between the results from equations (3.33)-(3.36) and the asymptotic kinetic results from the previous section for the low and high collisionality regimes. All plots in this chapter are calculated with the Landau-fluid closure equations (3.33)-(3.36).

The Landau-Fluid closure approximations provide a useful way to extend existing non-linear MHD codes to study key kinetic effects (see Chapter 4). The closure approximations are independent of the frequency (or the Z function), so are straightforward to implement in a nonlinear initial value code (though, as discussed in Chapter 2 they do require FFT's or non-local heat flux integrals to evaluate some terms[180, 78]; however, in nonlinear simulations discussed in Chapter 4 we use a simple local form for heat flux). But one should remember that they are approximations and so do not accurately model all kinetic effects in all regimes, particularly near marginal stability ([126, 179, 52]), though it is generally found that they work fairly well in strong turbulence regimes ([77, 147, 179, 52]).

As an aside, we note that the double adiabatic (CGL) closure [48], which is a simpler closure approximation that sets $q_\parallel = q_\perp = 0$ in equations (3.33) and (3.34), generally does a poor job of reproducing the full kinetic calculations. This is because the perturbations of interest have $\omega \ll |k_\parallel| c_0$ and are thus far from adiabatic (see also QDH); moreover, the CGL approximation excludes kinetic effects like Landau damping.

[3]The approximations are fairly good near or above the real ζ axis, though they will have only a finite number of damped roots, corresponding to the finite number of poles in the lower half of the complex plane, while the full transcendental $Z(\zeta)$ function has an infinite number of damped roots.

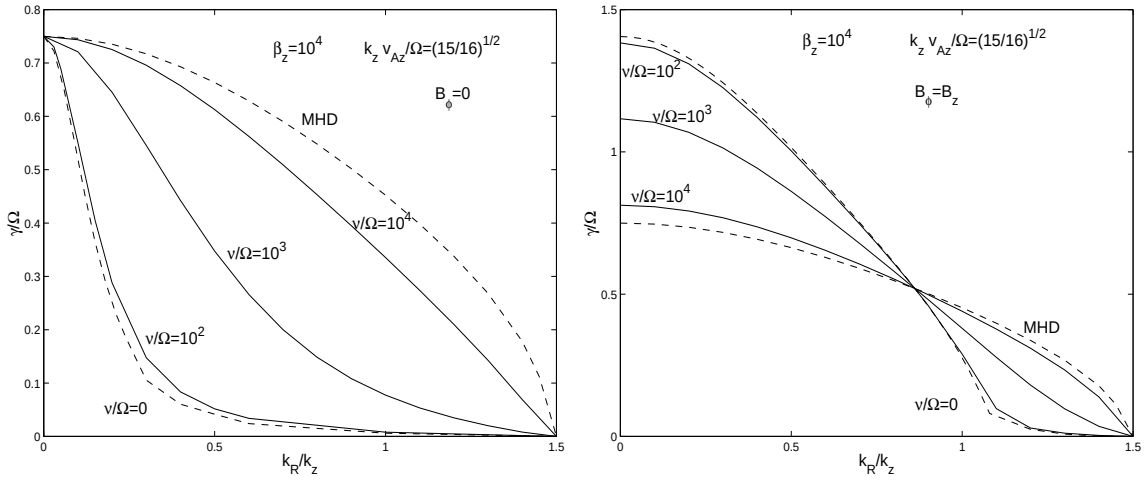

Figure 3.1: Growth rates of the MRI as a function of k_R/k_z for different collision frequencies; $\beta_z = 10^4$, $B_\phi = 0$ for the plot on the left, and $B_\phi = B_z$ for the plot on right. For $\nu/\Omega \geq 10^4$ ($=\beta$; this is the transition to MHD) the growth rates are very close to the MHD values, while for $\nu/\Omega \leq 10^2$ ($=\sqrt{\beta}$; this is the transition to Braginskii regime) they are quite similar to the collisionless limit. The enhancement of the growth rate in the collisionless regime for small k_R is the result of pressure anisotropy.

3.5 Collisionality dependence of the MRI growth rate

Figures 3.1 and 3.2 show the growth rate of the MRI for intermediate values of collisionality, in addition to the limits of zero and infinite collision frequency (the MHD limit; the latter two cases were shown in QDH). To produce these plots, we have used equations (3.5)-(3.11) and (3.33)-(3.36). These equations were solved both with a linear initial value code to find the fastest growing eigenmode, and with MATHEMATICA to find the complete set of eigenvalues ω.

Figures 3.1 and 3.2 show that the transition from the MHD to the collisionless regime is fairly smooth and occurs, for these particular parameters, in the vicinity of $\nu/\Omega \sim 10^3$, which corresponds to $\nu \sim \beta^{1/4} k c_0$, or $k\lambda_{mfp} \sim \beta^{-1/4}$, where $\lambda_{mfp} = c_0/\nu$ is the mean free path. Figure 3.3 shows the growth rate versus collisionality for

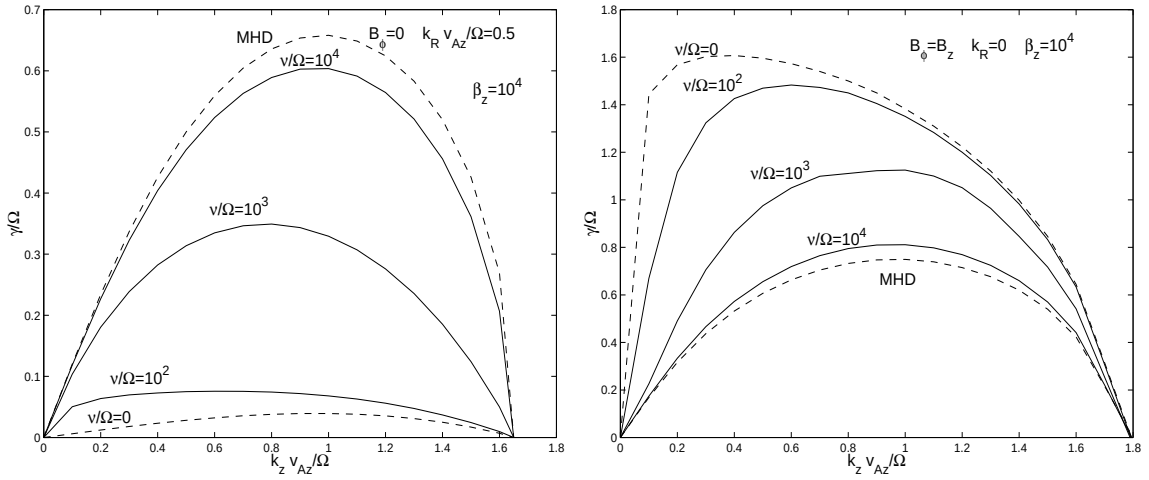

Figure 3.2: Growth rates of the MRI as a function of $k_z V_{Az}/\Omega$ for different collision frequencies; $\beta_z = 10^4$, $B_\phi = 0$ for the plot on left, and $B_\phi = B_z$ for the plot on right. For $\nu/\Omega \geq \beta$ the growth rates are very close to the MHD values, while for $\nu/\Omega \leq \sqrt{\beta}$ they are quite similar to the collisionless limit. Notice that the fastest growing mode in the collisionless regime is $\approx$ twice faster than the fastest growing mode in MHD, and also occurs at a much larger length scale.

$\beta_z = 100$ and $\beta_z = 10^4$, and for $B_\phi = B_z$, $k_R = 0$ and $B_\phi = 0$, $k_R/k_z = 0.5$.

It is clear from these figures that the transition from the collisionless to the collisional MRI takes place at far higher collision rates than $\nu \sim \Omega \sim \omega$. That is, $\nu > \omega$ is not a sufficient criterion to be in the collisional regime. The transition from collisionless to collisional regime can be understood in terms of the forces in equation of motion: the isotropic pressure force ($\sim \rho c_0^2$), the anisotropic pressure force ($\sim \frac{\hat{\mathbf{b}}\hat{\mathbf{b}}:\nabla V}{\nu}\rho c_0^2$), and the magnetic force ($\sim \rho V_A^2$). For $\nu = 0$ and $\beta \gg 1$, the anisotropic pressure force is comparable to the isotropic pressure and is much larger than the magnetic force. As ν is increased, the anisotropic pressure is reduced in comparison to the isotropic pressure and the transition to the Braginskii regime occurs when $\nu \gtrsim k_\parallel c_0$. Transition to MHD occurs on further increasing the collisionality, as anisotropic pressure becomes negligible compared to the magnetic force $\nu \gtrsim \beta k_\parallel V_A = k_\parallel \sqrt{\beta} c_0$. Using $k_\parallel V_A \sim \Omega$ for the MRI, these transitions are given in terms of the rotation frequency and β; collisionless to Braginskii when $\nu \gtrsim \Omega\sqrt{\beta}$, and Braginskii to MHD when $\nu \gtrsim \Omega\beta$. Figure

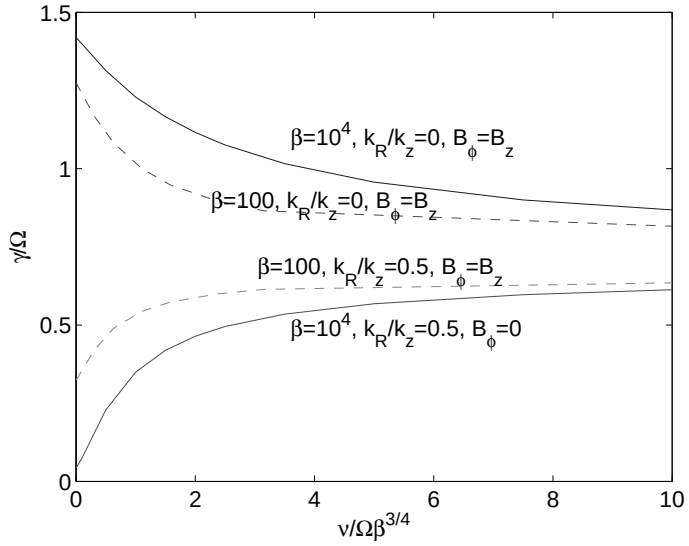

Figure 3.3: Variation of the MRI growth rate with collisionality for $k_R = 0$, $B_\phi = B_z$ (top curves) and $k_R/k_z = 0.5$, $B_\phi = 0$ (bottom curves). Collisions isotropize the distribution function and can increase the growth rate in some regimes and decrease it in others. Solid lines correspond to $\beta = 10^4$ and dotted lines to $\beta = 10^2$.

3.3 clearly shows that the transition from collisionless to MHD regime occurs roughly when $\nu \gtrsim \Omega\beta^{3/4}$, the geometric mean of the two transition collision frequencies.

At high $\beta(\gg 1)$, the Alfvén and MRI frequencies are small compared to the sound wave frequency, and there exists a regime $\omega \ll \nu \lesssim k_\parallel c_0$ where the collisionless results still hold, despite the collision time being shorter than the growth rate of the mode. Physically, this is because in order to wipe out the pressure anisotropy, that is crucial to the MRI in a collisionless plasma (see QDH), the collision frequency must be greater than the sound wave frequency, rather than the (much slower) growth rate of the mode. This can also be seen by comparing Figures 3.1 and 3.2 with the corresponding figures in QDH: the effect of increasing collisions (decreasing pressure anisotropy) is similar to that of decreasing β_z (decreasing pressure force relative to magnetic forces). From the point of view of Snyder et al.'s fluid approach, the weak dependence of growth rate on collisionality, even if ν is as large as ω, is because the terms proportional to ω and ν in Eqs. (3.33) and (3.34) are both much smaller than

the dominant terms involving convection, heat conduction, and magnetic forces. So the relative magnitudes of ω and ν are not that important, and it is not until ν is large enough to be relevant in Eqs. 3.33-3.36, that collisional effects become noticeable.

Figure 3.4 shows the complete spectrum of eigenmode frequencies as k_z is varied, including the propagating and damped modes, in addition to the unstable MRI branch. We show all the waves present in collisionless Landau fluid and MHD calculations for a general choice of wavenumbers and a moderate $\beta_z(= 10)$. The MRI is operational at lower k_z, while at high k_z the eigenfrequencies eventually approach the uniform plasma limit.

Focusing first on the MHD solutions at high k_z, we see the standard set of 3 MHD waves: in order of descending frequency these are the fast magnetosonic wave, the shear Alfvén wave, and the slow wave. Eqs. 3.5-3.11 with an MHD adiabatic pressure equation $\omega\delta p = p_0\mathbf{k}\cdot\delta\mathbf{v}$ is a set of 8 equations with 8 eigenvalues for ω. The standard 3 MHD waves provide 6 of the eigenvalues ($\pm\omega$ for oppositely propagating waves). The remaining roots are zero frequency modes (not shown in the plot). One is an entropy mode, corresponding to $\delta\rho/\rho_0 = -\delta T/T_0$ so that $\delta p = 0$. The other solution corresponds to an unphysical fluctuation that violates $\nabla\cdot\mathbf{B} = 0$, which is eliminated by imposing the proper initial condition $\nabla\cdot\mathbf{B} = 0$. At lower k_z in the MHD plots in Figure 3.4, the slow mode is destabilized to become the MRI, as discussed in [16].

Turning next to the collisionless limit in Figure 3.4, there are two roots plotted in addition to the three "MHD-like" modes; this is because the single pressure equation of MHD is replaced by separate equations for the parallel and perpendicular pressure, so that there are now two entropy-like modes, both of which have non-zero frequencies but which are also strongly damped by collisionless heat conduction (which is neglected in MHD).[4]

[4]We should point out that while our equations using the 3+1 Landau-fluid closure approximations have 8 eigenfrequencies, the equations using the more accurate 4+2 Landau-fluid closure approximations have 10 eigenfrequencies, with 2 additional strongly damped roots. If the exact kinetic response were used, one would find an infinite number of strongly damped eigenmodes because the

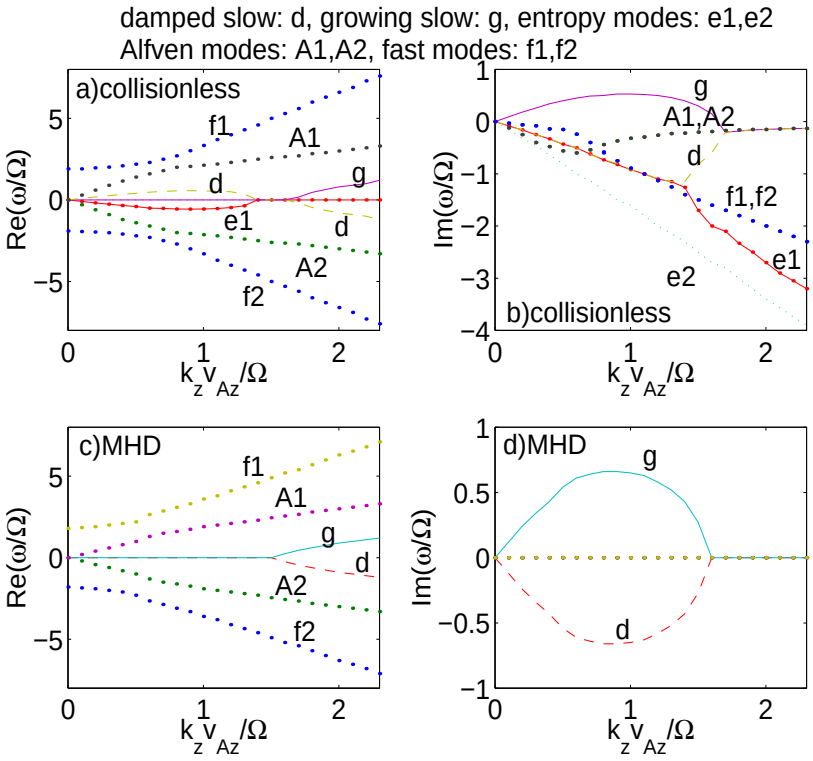

Figure 3.4: The real and imaginary parts of the mode frequency as a function of k_z, using collisionless Landau fluid closures (a,b) and MHD (c,d), are shown ($\nu = 0$, $k_R v_{Az}/\Omega = 0.5$, $\beta_z = 10$, $B_\phi = 0$).

The fast, Alfvén, and slow waves in the collisionless calculation can again be identified in order of decreasing (real) frequency at high k_z. At lower k_z, one of the slow modes becomes destabilized to become the MRI, as in MHD. Unlike in MHD, however, the fast magnetosonic waves are strongly Landau damped since the resonance condition $\omega \sim k_\parallel c_0$ is easily satisfied. In addition, it is interesting to note that both the shear Alfvén and slow waves have some collisionless damping at the highest k_z used in this plot, though the damping will approach zero for very high k_z. In a uniform plasma the shear Alfvén wave is undamped unless its wavelength is comparable to the proton Larmor radius or its frequency is comparable to the proton cyclotron frequency (neither of which is true for the modes considered here). By contrast, the slow mode is strongly damped unless $k_\perp \ll k_\parallel$ (because $\delta v_\parallel \propto (k_\perp/k_\parallel) \ll c_0$ in this regime; e.g., [18, 60]). The damping of small k_z shear Alfvén waves in Figure 3.4 is because our background plasma is rotating so the uniform-plasma modes are mixed together. Thus the well-known dissipation of the slow mode by transit-time damping also leads to damping of what we identify as the shear Alfvén wave (based on its high k_z properties).

3.6 Summary and Discussion

In this chapter we have extended the linear, axisymmetric, kinetic magnetorotational instability (MRI) calculation of QDH to include the effect of collisions. As the collision frequency is increased, the MRI transitions from collisionless to Braginskii regime ($\nu \gtrsim \Omega\sqrt{\beta}$), and eventually to the MHD regime ($\nu \gtrsim \Omega\beta$). Interestingly, the collisionless MRI results hold not only if $\nu \ll \omega$, but even when $\omega \ll \nu \ll k_\parallel c_0$. This intermediate regime can exist in $\beta \gtrsim 1$ plasmas because the MRI growth rate is slow compared to the sound wave frequency, $\omega \sim k_\parallel V_A = k_\parallel c_0 \sqrt{2/\beta} \ll k_\parallel c_0$. The fastest growing

$Z(\zeta)$ function is transcendental. These strongly damped modes are related to "ballistic modes" and transients in the standard analysis of Landau damping.

collisionless MRI mode is $\approx$ twice faster than the fastest growing MHD mode, and occurs at a much larger length scale; thus, MRI in the collisionless regime can result in fast MHD dynamo at large scales (not much smaller than the disk height scale).

If we consider the application of our results to accretion flows, the collisionless limit will be applicable so long as $\nu/\Omega \lesssim \sqrt{\beta}$. This condition is amply satisfied for proton-proton and proton-electron collisions in all hot radiatively inefficient accretion flow models (see Table 1.2), suggesting that the collisionless limit is always appropriate. However, high frequency waves such as ion-cyclotron waves can isotropize the proton distribution function and thus provide an effective "collision" term crudely analogous to the one considered here (see Subsection 4.2.2). In the drift kinetic limit, when the Larmor radius is small compared to the dynamical length scales, the adiabatic invariant $\mu = p_\perp/B$ is conserved. Nonlinear simulations described in Chapter 4 show that the MRI results in fast growth of magnetic fields resulting in an anisotropic plasma ($p_\perp > p_\perp$). Fairly large pressure anisotropies ($\Delta p/p \sim$ (a few)$/\beta$) are created at the dynamical timescales and small scale instabilities—mirror and ion-cyclotron—are excited. Pressure isotropization due to these instabilities imposes an MHD like dynamics on a formally collisionless plasma. However, selective heating of resonant electrons and ions may result in different electron and ion temperatures, and spectral signatures different from MHD.

One might anticipate that the linear differences between the collisionless and collisional MRI highlighted here and in QDH will imply differences in the nonlinear turbulent state in hot accretion flows (see, e.g., [83, 95] for global MHD simulations of such flows). Not only are there differences in the linear growth rates of the instability that drives turbulence, but the spectrum of damped modes is also very different. In particular, in the kinetic regime there exist modes at all scales in $|\mathbf{k}|$ that are subject to Landau/Barnes collisionless damping, while in the MHD regime the only sink for turbulent energy is due to viscosity/resistivity at very small scales

(very high $|\mathbf{k}|$). Indeed, as we have shown, even long wavelength Alfvén waves can be damped by collisionless effects because of the mixture of uniform-plasma modes in the differentially rotating accretion flow (Figure 3.4). Whether these differences are important or not may depend on how efficiently nonlinearities couple energy into the damped modes. These could modify the nonlinear saturated turbulent spectrum (e.g., the efficiency of angular momentum transport) or the fraction of electron vs. ion heating (the heating may also be anisotropic), which in turn determines the basic observational signatures of hot accretion flows (the accretion rate and the radiative efficiency). One approach for investigating nonlinear collisionless effects would be to extend existing MHD codes to include anisotropic pressure, the fluid closure approximations for kinetic effects [180], and the BGK collision operator considered here. By varying the collision frequency, one can then scan from the collisionless kinetic to the collisional MHD regime, and assess any differences in the nonlinear turbulent state. The nonlinear simulations of the collisionless MRI, based on Landau fluid closure for heat fluxes, are described in the next chapter.

Chapter 4

Nonlinear Simulations of kinetic MRI

In this chapter we describe local shearing box simulations of turbulence driven by the magnetorotational instability (MRI) in a collisionless plasma. Collisionless effects may be important in radiatively inefficient accretion flows, such as near the black hole in the Galactic center (see Section 1.4). The ZEUS MHD code is modified to evolve an anisotropic pressure tensor. A Landau-fluid closure approximation is used to calculate heat conduction along magnetic field lines. The anisotropic pressure tensor provides a qualitatively new mechanism for transporting angular momentum in accretion flows (in addition to the Maxwell and Reynolds stresses). We estimate limits on the pressure anisotropy due to pitch angle scattering by kinetic instabilities. Such instabilities provide an effective "collision" rate in a collisionless plasma and lead to more MHD-like dynamics. We find that the MRI leads to efficient growth of the magnetic field in a collisionless plasma, with saturation amplitudes comparable to those in MHD. In the saturated state, the anisotropic stress is comparable to the Maxwell stress, implying that the rate of angular momentum transport may be moderately enhanced in a collisionless plasma. More importantly, heating due to

anisotropic stress is comparable to the numerical energy loss in updating magnetic fields; this can have important consequences for electron and ion heating.

4.1 Introduction

Following the seminal work of Balbus and Hawley [14], numerical simulations have demonstrated that magnetohydrodynamic (MHD) turbulence initiated by the magnetorotational instability (MRI) is an efficient mechanism for transporting angular momentum in accretion disks (see Section 1.3 for a review). For a broad class of astrophysical accretion flows, however, the MHD assumption is not directly applicable. In particular, in radiatively inefficient accretion flow (RIAF) models for accretion onto compact objects, the accretion proceeds via a hot, low density, collisionless plasma with the proton temperature larger than the electron temperature [140, 156] (see Section 1.4 for a review). In order to maintain such a two-temperature flow the plasma must be collisionless, with the Coulomb mean-free path many orders of magnitude larger than the system size (see Table 1.2 for plasma parameters in Sgr A*). Motivated by the application to RIAFs, this chapter studies the nonlinear evolution of the collisionless MRI in the local shearing box limit.

Quataert, Dorland, & Hammett (2001; hereafter QDH) and Sharma, Hammett, & Quataert (2003; hereafter SHQ) showed that the linear dynamics of the MRI in a collisionless plasma can be quite different from that in MHD (see Chapter 3). The maximum growth rate is a factor of ≈ 2 larger and, perhaps more importantly, the fastest growing modes can shift to much longer wavelengths, giving direct amplification of long wavelength modes. Dynamical instability exists even when the magnetic tension forces are negligible because of the anisotropic pressure response in a collisionless plasma. In related work using Braginskii's anisotropic viscosity, the collisionless MRI is studied as the "magnetoviscous" instability [12, 96].

We are interested in simulating the dynamics of a collisionless plasma on length-scales ($\sim$ disk height) and time-scales ($\sim$ orbital period) that are very large compared to the microscopic plasma scales (such as the Larmor radius and the cyclotron period). Since the ratio of the size of the accretion flow to the proton Larmor radius is $\sim 10^8$ for typical RIAF models (see Table 1.2), direct particle methods such as PIC (particle in a cell), which need to resolve both of these scales, are computationally challenging and require simulating a reduced range of scales. Instead, we use a fluid-based method to describe the large-scale dynamics of a collisionless plasma ("kinetic MHD," described in Section 2.3). The key differences with respect to MHD are that the pressure is a tensor rather than a scalar, anisotropic with respect to the direction of the local magnetic field, and that there are heat fluxes along magnetic field lines (related to Landau damping and wave-particle interactions). The drawback of our fluid-based method is, of course, that there is no exact expression for the heat fluxes if only a few fluid moments are retained in a weakly collisional plasma (the "closure problem"). We use results from Snyder, Hammett, & Dorland (1997; hereafter SHD) who have derived approximations for the heat fluxes in terms of nonlocal parallel temperature and magnetic field gradients. These heat flux expressions can be shown to be equivalent to multi-pole Padé approximations to the Z-function involved in Landau damping (see Section 2.4). This approach can be shown to converge as more fluid moments of the distribution function are kept [77], just as an Eulerian kinetic algorithm converges as more grid points in velocity space are kept. These fluid-based methods have been applied with reasonable success to modeling collisionless turbulence in fusion plasmas, generally coming within a factor of 2 of more complicated kinetic calculations in strong turbulence regimes [52, 147, 77, 173], though there can be larger differences in weak turbulence regimes [77, 52]. The simulations we report here use an even simpler local approximation to the heat flux closures than those derived in [180] (see "the crude closure" in Section 2.4). While not exact, these clo-

sure approximations allow one to begin to investigate kinetic effects with relatively fast modifications of fluid codes; whereas, solving the full drift kinetic equation (see Section 2.2) is considerably slower and requires code development and testing from scratch.

In a collisionless plasma the magnetic moment, $\mu = v_\perp^2/2B$, is an adiabatic invariant. Averaged over velocity space, this leads to conservation of $\langle\mu\rangle = p_\perp/(\rho B)$. As a result, pressure anisotropy with $p_\perp > p_\parallel$ is created as the MRI amplifies the magnetic field in the accretion flow. This pressure anisotropy creates an anisotropic stress (like a viscosity!) which can be as important for angular momentum transport as the magnetic stress. It is interesting to note that for cold disks, the mean free path is negligible compared to the disk height resulting in a viscosity insufficient to account for efficient transport; but hot, thick accretion flows are collisionless with large viscosity, and viscous stress is quite efficient in transporting angular momentum. However, it is important to emphasize that an anisotropic viscosity in a collisionless, magnetized plasma is very different from an isotropic viscosity (since viscosity perpendicular to the field lines is vanishingly small). Although, the Reynolds number ($Re \equiv VL/\eta_V$) based on parallel viscosity is small, $O(1)$, the plasma is turbulent; this would not be true if the Reynolds number based on an isotropic viscosity is so small.

The pressure anisotropy cannot, however, grow without bound because high frequency waves and kinetic microinstabilities feed on the free energy in the pressure anisotropy, effectively providing an enhanced rate of collisions that limit the pressure tensor anisotropy (leading to more MHD-like dynamics in a collisionless plasma). We capture this physics by using a subgrid model to restrict the allowed amplitude of the pressure anisotropy. This subgrid model (described in §2.3) is based on existing linear and nonlinear studies of instabilities driven by pressure anisotropy [80, 69].

The remainder of this paper is organized as follows. We begin with Kulsrud's formulation of kinetic MHD (KMHD) and our closure model for the heat fluxes in

a collisionless plasma. We also include a linear analysis of the MRI in the presence of a background pressure anisotropy and describe limits on the pressure anisotropy set by kinetic instabilities. Next, we describe our modifications to the ZEUS code to model kinetic effects. We present our primary results on the nonlinear evolution of the MRI in a collisionless plasma. At the end we discuss these results, their astrophysical implications, and future work required to understand the global dynamics of collisionless accretion disks.

4.2 Governing equations

In the limit that all fluctuations of interest are at scales larger than the proton Larmor radius and have frequencies much smaller than the proton cyclotron frequency, a collisionless plasma can be described by the following magnetofluid equations [110, 180] (see Section 2.3 for details):

$$\frac{\partial \rho}{\partial t} + \nabla \cdot (\rho \mathbf{V}) = 0, \tag{4.1}$$

$$\rho \frac{\partial \mathbf{V}}{\partial t} + \rho \left(\mathbf{V} \cdot \nabla \right) \mathbf{V} = \frac{(\nabla \times \mathbf{B}) \times \mathbf{B}}{4\pi} - \nabla \cdot \mathbf{P} + \mathbf{F_g}, \tag{4.2}$$

$$\frac{\partial \mathbf{B}}{\partial t} = \nabla \times (\mathbf{V} \times \mathbf{B}), \tag{4.3}$$

$$\mathbf{P} = p_\perp \mathbf{I} + \left(p_\parallel - p_\perp \right) \hat{\mathbf{b}} \hat{\mathbf{b}} = p_\perp \mathbf{I} + \mathbf{\Pi}, \tag{4.4}$$

where ρ is the mass density, $\mathbf{V}$ is the fluid velocity, $\mathbf{B}$ is the magnetic field, $\mathbf{F_g}$ is the gravitational force, $\hat{\mathbf{b}} = \mathbf{B}/|\mathbf{B}|$ is a unit vector in the direction of the magnetic field, and $\mathbf{I}$ is the unit tensor. In equation (4.3) an ideal Ohm's law is used, neglecting resistivity. In equation (4.4), $\mathbf{P}$ is the pressure tensor with different perpendicular ($p_\perp$) and parallel ($p_\parallel$) components with respect to the background magnetic field, and $\mathbf{\Pi} = \hat{\mathbf{b}}\hat{\mathbf{b}}(p_\parallel - p_\perp)$ is the anisotropic stress tensor. (Note that $\mathbf{\Pi}$ is not traceless in the convention used here.) $\mathbf{P}$ should in general be a sum over all species but in the limit

where ion dynamics dominate and electrons just provide a neutralizing background, the pressure can be interpreted as the ion pressure. This is the case for hot accretion flows in which $T_p \gg T_e$.

The exact pressures $p_\parallel$ and $p_\perp$ can be rigorously determined by taking moments of the drift kinetic equation (see Section 2.2),

$$\frac{\partial f_s}{\partial t} + (v_\parallel \hat{\mathbf{b}} + \mathbf{V_E}) \cdot \nabla f_s + \left[-\hat{\mathbf{b}} \cdot \frac{D\mathbf{V_E}}{Dt} - \mu \hat{\mathbf{b}} \cdot \nabla B + \frac{e_s}{m_s} \left(E_\parallel + \frac{F_{g\parallel}}{e_s} \right) \right] \frac{\partial f_s}{\partial v_\parallel} = C(f_s), \tag{4.5}$$

which is the asymptotic expansion of the Vlasov equation for the distribution function $f_s(\mathbf{x}, \mu, v_\parallel, t)$ for species 's' with mass m_s and charge e_s in the limit $\rho_s/L \ll 1$, $\omega/\Omega_s \ll 1$, where ρ_s and Ω_s are the gyroradius and gyrofrequency, respectively. In equation (4.5), $\mathbf{V_E} = c(\mathbf{E} \times \mathbf{B})/B^2$ is the perpendicular drift velocity, $\mu = (\mathbf{v}_\perp - \mathbf{V_E})^2/2B$ is the magnetic moment (a conserved quantity in the absence of collisions), $F_{g\parallel}$ is the component of the gravitational force parallel to the direction of the magnetic field, and $D/Dt = \partial/\partial t + (v_\parallel \hat{\mathbf{b}} + \mathbf{V_E}) \cdot \nabla$ is the particle Lagrangian derivative in the phase space. The fluid velocity $\mathbf{V} = \mathbf{V_E} + \hat{\mathbf{b}} V_\parallel$, so the $\mathbf{E} \times \mathbf{B}$ drift is determined by the perpendicular component of equation (4.2). Other drifts such as grad B, curvature, and gravity $\times\mathbf{B}$ drifts are higher order in the drift kinetic ordering and do not appear in this equation. In equation (4.5), $C(f_s)$ is the collision operator to allow for generalization to collisional regimes. Collisions can also be used to mimic rapid pitch angle scattering due to high frequency waves that break μ invariance. The parallel electric field is determined by $E_\parallel = \sum_s (e_s/m_s) \hat{\mathbf{b}} \cdot \nabla \cdot \mathbf{P}_s / \sum_s (n_s e_s^2/m_s)$, which insures quasineutrality (see Subsection 2.4.1).

Separate equations of state for the parallel and perpendicular pressures can be obtained from the moments of the drift kinetic equation [48]. Neglecting the collision

term these are:

$$\rho B \frac{D}{Dt}\left(\frac{p_\perp}{\rho B}\right) = -\nabla\cdot\mathbf{q}_\perp - q_\perp \nabla\cdot\hat{\mathbf{b}}, \tag{4.6}$$

$$\frac{\rho^3}{B^2}\frac{D}{Dt}\left(\frac{p_\parallel B^2}{\rho^3}\right) = -\nabla\cdot\mathbf{q}_\parallel + 2q_\perp \nabla\cdot\hat{\mathbf{b}}, \tag{4.7}$$

where $D/Dt = \partial/\partial t + \mathbf{V}\cdot\nabla$ is the fluid Lagrangian derivative and $\mathbf{q}_{\parallel,\perp} = q_{\parallel,\perp}\hat{\mathbf{b}}$ are the heat fluxes (flux of $p_\parallel$ and $p_\perp$) parallel to the magnetic field. The equation for the magnetic moment density $\rho\langle\mu\rangle = p_\perp/B$ can be written in a conservative form:

$$\frac{\partial}{\partial t}\left(\frac{p_\perp}{B}\right) + \nabla\cdot\left(\frac{p_\perp}{B}\mathbf{V}\right) = -\nabla\cdot\left(\frac{q_\perp}{B}\hat{\mathbf{b}}\right), \tag{4.8}$$

If the heat fluxes are neglected (called the CGL or double adiabatic limit), as the magnetic field strength (B) increases, $p_\perp$ increases ($p_\perp \propto \rho B$), and $p_\parallel$ decreases ($p_\parallel \propto \rho^3/B^2$). Integrating equation (4.8) over a finite periodic (even a shearing periodic) box shows that $\langle p_\perp/B\rangle$ is conserved, where $\langle\rangle$ denotes a volume average. This implies that even when $q_{\parallel,\perp} \neq 0$, $p_\perp$ increases in a volume averaged sense as the magnetic energy in the box increases. This means that that for a collisionless plasma, pressure anisotropy $p_\perp > (<)\, p_\parallel$ is created as a natural consequence of processes that amplify (reduce) B. This pressure anisotropy is crucial for understanding magnetic field amplification in collisionless dynamos.

To solve the set of equations (4.1-4.4), (4.6-4.7) in a simple fluid based formalism, we require expressions for $q_\parallel$ and $q_\perp$ in terms of lower order moments. No simple, exact expressions for $q_\parallel$ and $q_\perp$ exist for nonlinear collisionless plasmas. Although simple, the double adiabatic or CGL approximation (where $q_\parallel = q_\perp = 0$) does not capture key kinetic effects such as Landau damping. In the moderately collisional limit ($\rho_i <$ mean free path $<$ system size), where the distribution function is not very different from a local Maxwellian, one can use the Braginskii equations to describe

anisotropic transport ([37]; see [10, 12] for astrophysical applications). However, in the hot RIAF regime, the mean free path is often much larger than the system size and the Braginskii equations are not formally applicable, though they are still useful as a qualitative indication of the importance of kinetic effects. The collisional limit of the kinetic MHD equations can be shown to recover the dominant anisotropic heat flux and viscosity tensor of Braginskii (see Subsection 2.5.1). The local approximation to kinetic MHD that we use here leads to equations that are similar in form to Braginskii MHD, but with separate dynamical equations for parallel and perpendicular pressures. We also add models for enhanced pitch angle scattering by microinstabilities, which occur at very small scales and high frequencies beyond the range of validity of standard kinetic MHD. [1]

Hammett and collaborators have developed approximate fluid closures (called Landau fluid closure) for collisionless plasmas [79, 78, 180] that capture kinetic effects such Landau damping. SHD [180] give the resulting expressions for parallel heat fluxes ($q_\parallel$, $q_\perp$) to be used in equations (4.6) and (4.7). Landau closures are based on Padé approximations to the full kinetic plasma dispersion function that reproduce the correct asymptotic behavior in both the adiabatic ($\omega/k_\parallel c_\parallel \gg 1$) and isothermal ($\omega/k_\parallel c_\parallel \ll 1$) regimes (and provide a good approximation in between), where ω is the angular frequency, $k_\parallel$ is the wavenumber parallel to the magnetic field, and $c_\parallel = \sqrt{p_\parallel/\rho}$ is the parallel thermal velocity of the particles. In Fourier space, the linearized heat fluxes can be written as equations (39) & (40) in SHD,

$$q_\parallel = -\sqrt{\frac{8}{\pi}}\rho_0 c_{\parallel 0}\frac{ik_\parallel \left(p_\parallel/\rho\right)}{|k_\parallel|}, \tag{4.9}$$

$$q_\perp = -\sqrt{\frac{2}{\pi}}\rho_0 c_{\parallel 0}\frac{ik_\parallel \left(p_\perp/\rho\right)}{|k_\parallel|} + \sqrt{\frac{2}{\pi}}c_{\parallel 0}\frac{p_{\perp 0}}{B_0}\left(1-\frac{p_{\perp 0}}{p_{\parallel 0}}\right)\frac{ik_\parallel B}{|k_\parallel|}, \tag{4.10}$$

[1] This would also be needed when using Braginskii equations, because they are not necessarily well posed in situations where the anisotropic stress tensor can drive arbitrarily small scale instabilities[170].

where '0′ subscripts indicate equilibrium quantities. Real space expressions are somewhat more cumbersome and are given by convolution integrals (see Section 2.4)

$$q_{\parallel} = -\left(\frac{2}{\pi}\right)^{3/2} n_0 c_{\parallel 0} \int_0^\infty \delta z' \frac{T_\parallel(z+z') - T_\parallel(z-z')}{z'}, \tag{4.11}$$

$$q_{\perp} = -\left(\frac{2}{\pi^3}\right)^{1/2} n_0 c_{\parallel 0} \int_0^\infty \delta z' \frac{T_\perp(z+z') - T_\perp(z-z')}{z'} + \left(\frac{2}{\pi^3}\right)^{1/2} c_{\parallel 0} \left(1 - \frac{p_{\perp 0}}{p_{\parallel 0}}\right) \frac{p_{\perp 0}}{B_0} \times \int_0^\infty \delta z' \frac{B(z+z') - B(z-z')}{z'}, \tag{4.12}$$

where n_0 is the number density, $T_\parallel = p_\parallel/n$, and $T_\perp = p_\perp/n$ are the parallel and perpendicular temperatures, and z' is the spatial variable along the magnetic field line. In the previous chapter (based on [176]) we have shown that these fluid closures for the heat fluxes accurately reproduce the kinetic linear Landau damping rate for all MHD modes (slow, Alfv́en, fast and entropy modes). The growth rate of the MRI using the Landau closure model is also very similar to that obtained from full kinetic theory. As noted in the introduction, in addition to reproducing linear modes/instabilities, Landau fluid closures have also been used to model turbulence in fusion plasmas with reasonable success.

These closure approximations were originally developed for turbulence problems in fusion energy devices with a strong guide magnetic field, where the parallel dynamics is essentially linear and FFTs could be easily used to quickly evaluate the Fourier expressions above. In astrophysical problems with larger amplitude fluctuations and tangled magnetic fields, evaluation of the heat fluxes become somewhat more complicated. One could evaluate the convolution expressions, equations (4.11) and (4.12) (with some modest complexity involved in writing a subroutine to integrate along magnetic field lines), leading to a code with a computational time $T_{cpu} \propto N_x^3 N_\parallel$, where N_x^3 is the number of spatial grid points and $N_\parallel$ is the number of points kept in the integrals along field lines. (In some cases, it may be feasible to map the fluid

quantities to and from a field-line following coordinate system so that FFTs can reduce this to $T_{cpu} \propto N_x^3 \log N_\parallel$.) While this is more expensive than simple MHD where $T_{cpu} \propto N_x^3$, it could still represent a savings over a direct solution of the drift kinetic equation, which would require $T_{cpu} \propto N_x^3 N_{v_\parallel} N_{v_\perp}$, where $N_{v_\parallel} N_{v_\perp}$ is the number of grid points for velocity space.[2]

As a first step for studying kinetic effects, in this paper we pick out a characteristic wavenumber k_L that represents the scale of collisionless damping and use a local approximation for the heat fluxes in Fourier space (see the "crude closure for thermal conduction" in Section 2.4), with a straightforward assumption about the nonlinear generalization:

$$q_\parallel = -\sqrt{\frac{8}{\pi}} \rho c_\parallel \frac{\nabla_\parallel \left(p_\parallel / \rho \right)}{k_L}, \tag{4.13}$$

$$q_\perp = -\sqrt{\frac{2}{\pi}} \rho c_\parallel \frac{\nabla_\parallel \left(p_\perp / \rho \right)}{k_L} + \sqrt{\frac{2}{\pi}} c_\parallel p_\perp \left(1 - \frac{p_\perp}{p_\parallel} \right) \frac{\nabla_\parallel B}{k_L B}. \tag{4.14}$$

Note that this formulation of the heat flux is analogous to a Braginskii heat conduction along magnetic field lines. For linear modes with $|k_\parallel| \sim k_L$, these approximations will of course agree with kinetic theory as well as the Padé approximations shown in SHD. One can think of k_L as approximately controlling the heat conduction rate, though this does not necessarily affect the resulting Landau damping rate of a mode in a monotonic way, since this sometimes exhibits impedance matching behavior,i.e., some modes are weakly damped in both the small and large (isothermal) heat conduction limits. We vary k_L to investigate the sensitivity of our results to this parameter.

[2]On the other hand, an effective hyperdiffusion operator in velocity space may reduce the velocity resolution requirements, and recent direct kinetic simulations of turbulence in fusion devices have found that often one does not need very high velocity resolution. This may make a direct solution of the drift kinetic equation tractable for some astrophysical kinetic MHD problems. Furthermore, a direct solution of the drift kinetic equation involves only local operations, and thus is somewhat easier to parallelize than the convolution integrals.

4.2.1 Linear modes

Since pressure anisotropy arises as a consequence of magnetic field amplification in a collisionless plasma, it is of interest to repeat the linear analysis of the collisionless MRI done in Chapter 3, but with a background pressure anisotropy ($p_{\parallel 0} \neq p_{\perp 0}$). We consider the simple case of a vertical magnetic field. This analysis provides a useful guide to understanding some of our numerical results.

We linearize equations (4.1)-(4.4) for a differentially rotating disk ($\mathbf{V_0} = R\Omega(R)\hat{\phi}$) with an anisotropic pressure about a uniform subthermal vertical magnetic field ($\mathbf{B_0} = B_z\hat{\mathbf{z}}$). We assume that the background (unperturbed) plasma is described by a bi-Maxwellian distribution ($p_{\parallel 0} \neq p_{\perp 0}$). We also assume that the perturbations are axisymmetric, of the form $\exp[-i\omega t + i\mathbf{k}\cdot\mathbf{x}]$ with $\mathbf{k} = k_R\hat{\mathbf{R}} + k_z\hat{\mathbf{z}}$. Writing $\rho = \rho_0 + \delta\rho$, $\mathbf{B} = \mathbf{B_0} + \delta\mathbf{B}$, $p_\perp = p_{\perp 0} + \delta p_\perp$, $p_\parallel = p_{\parallel 0} + \delta p_\parallel$, working in cylindrical coordinates and making a $|k|R \gg 1$ assumption, the linearized versions of equations (4.1)-(4.3) become:

$$\omega\delta\rho = \rho_0\mathbf{k}\cdot\delta\mathbf{v}, \tag{4.15}$$

$$-i\omega\rho_0\delta v_R - \rho_0 2\Omega\delta v_\phi = -\frac{ik_R}{4\pi}B_z\delta B_z + ik_z\left(\frac{B_z}{4\pi} - \frac{(p_{\parallel 0} - p_{\perp 0})}{B_z}\right)\delta B_R - ik_R\delta p_\perp, \tag{4.16}$$

$$-i\omega\rho_0\delta v_\phi + \rho_0\delta v_R\frac{\kappa^2}{2\Omega} = ik_z\left(\frac{B_z}{4\pi} - \frac{(p_{\parallel 0} - p_{\perp 0})}{B_z}\right)\delta B_\phi, \tag{4.17}$$

$$-i\omega\rho_0\delta v_z = -ik_R\left(p_{\parallel 0} - p_{\perp 0}\right)\frac{\delta B_R}{B_z} - ik_z\delta p_\parallel, \tag{4.18}$$

$$\omega\delta B_R = -k_z B_z\delta v_R, \tag{4.19}$$

$$\omega\delta B_\phi = -k_z B_z\delta v_\phi - \frac{ik_z B_z}{\omega}\frac{d\Omega}{d\ln R}\delta v_R, \tag{4.20}$$

$$\omega\delta B_z = k_R B_z\delta v_R, \tag{4.21}$$

where $\kappa^2 = 4\Omega^2 + d\Omega^2/d\ln R$ is the epicyclic frequency. Equations (4.15)-(4.21) describe the linear modes of a collisionless disk with an initial pressure anisotropy

about a vertical magnetic field. This corresponds to the $\theta = \pi/2$ case of Chapter 3, but with an anisotropic initial pressure. Equations (4.16) & (4.17) show that an initial anisotropic pressure modifies the Alfvén wave characteristics, so we expect a background pressure anisotropy to have an important effect on the MRI. One way of interpreting equations (4.16) & (4.17) is that $p_\perp > p_\parallel$ ($p_\parallel > p_\perp$) makes the magnetic fields more (less) stiff; as a result, this will shift the fastest growing MRI mode to larger (smaller) scales.

The linearized equations for the parallel and perpendicular pressure response are given by Eqs. 3.33 and 3.34 from Chapter 3. We present them here for the sake of completeness.

$$-i\omega\delta p_\parallel \quad + \quad p_{\parallel 0} i\mathbf{k}\cdot\delta\mathbf{v} + ik_z q_\parallel + 2p_{\parallel 0} ik_z \delta v_z = 0, \tag{4.22}$$

$$-i\omega\delta p_\perp \quad + \quad 2p_{\perp 0} i\mathbf{k}\cdot\delta\mathbf{v} + ik_z q_\perp - p_{\perp 0} ik_z \delta v_z = 0, \tag{4.23}$$

where the heat fluxes can be expressed in terms of lower moments using

$$q_\perp = -\sqrt{\frac{2}{\pi}} c_{\parallel 0} \frac{ik_z}{|k_z|}(\delta p_\perp - c_{\parallel 0}^2 \delta\rho) + \sqrt{\frac{2}{\pi}} c_{\parallel 0} p_{\perp 0} \left(1 - \frac{p_{\perp 0}}{p_{\parallel 0}}\right) \frac{ik_z}{|k_z|} \frac{\delta B}{B_z}, \tag{4.24}$$

$$q_\parallel = -\sqrt{\frac{8}{\pi}} c_{\parallel 0} \frac{ik_z}{|k_z|}(\delta p_\parallel - c_{\parallel 0}^2 \delta\rho), \tag{4.25}$$

where $c_{\parallel 0} = \sqrt{p_{\parallel 0}/\rho_0}$ and $\delta B = |\delta\mathbf{B}|$.

Figure 4.1 shows the MRI growth rate as a function of pressure anisotropy for two values of k_R for $\beta = 100$. This figure shows that the fastest growing MHD mode ($k_R = 0$) is stabilized for $(p_{\perp 0} - p_{\parallel 0})/p_{\parallel 0} \sim 4/\beta$; modes with $k_R \neq 0$ modes require larger anisotropy for stabilization. For $\beta \gg 1$, these results highlight that only a very small pressure anisotropy is required to stabilize the fastest growing MRI modes. Growth at large pressure anisotropies in Figure 4.1 for $k_R \neq 0$ mode is because of the mirror instability that is discussed below. The physical interpretation of the

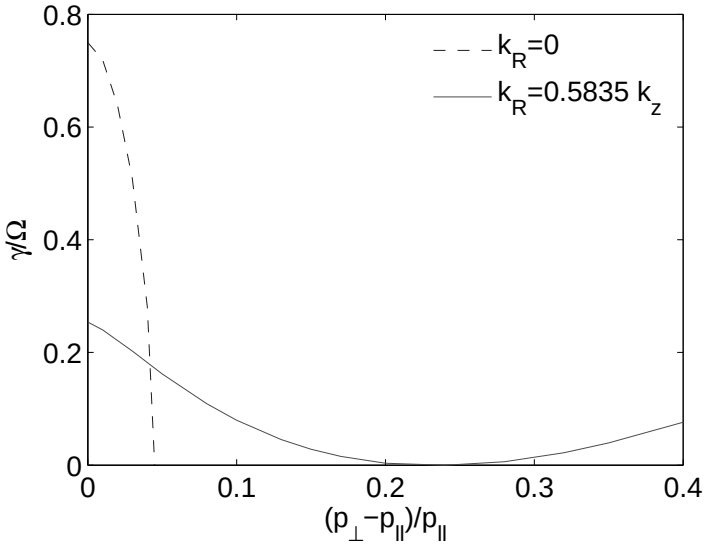

Figure 4.1: Normalized growth rate (γ/Ω) of the MRI versus normalized pressure anisotropy, $(p_\perp - p_\perp)/p_\parallel$ for $\beta = 100$, $k_z V_{Az}/\Omega = \sqrt{15/16}$, and two different k_R's. Note that even a small anisotropy can stabilize the fastest growing MRI mode. The growth at large pressure anisotropy for $k_R \neq 0$ is due to the mirror mode.

stabilization of the MRI in Figure 4.1 is that as the pressure anisotropy increases ($p_{\perp 0} > p_{\parallel 0}$), the field lines effectively become stiffer and modes of a given k can be stabilized (though longer wavelength modes will still be unstable). In a numerical simulation in which the pressure anisotropy is allowed (unphysically, as we see in Subsection 4.2.2) to grow without bound as the magnetic field grows, this effect is capable of stabilizing all of the MRI modes in the computational domain at very small amplitudes (see Figure 4.6).

4.2.2 Isotropization of the pressure tensor in collisionless plasmas

Pressure anisotropy ($p_\perp \neq p_\parallel$) is a source of free energy that can drive instabilities which act to isotropize the pressure, effectively providing an enhanced "collision" rate in a collisionless plasma [69]. In order to do so, the instabilities must break

magnetic moment conservation, and thus must have frequencies comparable to the cyclotron frequency and/or parallel wavelengths comparable to the Larmor radius. Because of the large disparity in timescales between μ-breaking microinstabilities and the MRI ($\omega_{micro}/\Omega \sim 10^8$), one can envision the microinstabilities as providing a "hard wall" limit on the pressure anisotropy; once the pressure anisotropy exceeds the threshold value where microinstabilities are driven and cause rapid pitch angle scattering, the pressure anisotropy nearly instantaneously reduces the anisotropy to its threshold value (from the point of view of the global disk dynamics). In this section we review the relevant instabilities that limit the pressure anisotropy in high β collisionless plasmas—these are the firehose, mirror, and ion cyclotron instabilities. We then discuss how we have implemented these estimated upper bounds on the pressure anisotropy in our numerical simulations.

Maximum anisotropy for $p_\parallel > p_\perp$

Plasmas with $p_\parallel > p_\perp$ can be unstable to the firehose instability, whose dispersion relation for parallel propagation is given by equation (2.12) of [100]:

$$\omega^2 - \omega\Omega_i k_\parallel^2 \rho_i^2 + \Omega_i^2 k_\parallel^2 \rho_i^2 \left(1 - \frac{p_\perp}{p_\parallel} - \frac{2}{\beta_\parallel}\right) = 0, \tag{4.26}$$

where $\beta_\parallel = 8\pi p_\parallel / B^2$, ρ_i is the ion Larmor radius, Ω_i is the ion cyclotron frequency, and $k_\parallel$ is the wavenumber parallel to the local magnetic field direction. Solving for ω gives

$$\omega = k_\parallel^2 \rho_i^2 \frac{\Omega_i}{2} \pm i k_\parallel c_{\parallel 0} \left(1 - \frac{p_\perp}{p_\parallel} - \frac{2}{\beta_\parallel} - \frac{k_\parallel^2 \rho_i^2}{4}\right)^{1/2} \tag{4.27}$$

For long wavelengths, the firehose instability requires $p_\parallel > p_\perp + B^2/4\pi$, and is essentially an Alfvén wave destabilized by the pressure anisotropy. The maximum growth rate occurs when $k_\parallel^2 \rho_i^2 = 2(1 - p_\perp/p_\parallel - 2/\beta_\parallel)$ and is given by $\Omega_i(1 - p_\perp/p_\parallel - 2/\beta_\parallel)$. We use an upper limit on $p_\parallel > p_\perp$ corresponding to $1 - p_\perp/p_\parallel - 2/\beta_\parallel < 1/2$, which

is an approximate condition for the growth of modes that will violate μ conservation and produce rapid pitch angle scattering (when $\omega \sim \Omega_i$ and $k_\parallel \rho_i \sim 1$).

Maximum anisotropy for $p_\perp > p_\parallel$

For $p_\perp > p_\parallel$ there are two instabilities that act to isotropize the pressure, the mirror instability and the ion cyclotron instability [69]. A plasma is unstable to the mirror instability when $p_\perp/p_\parallel - 1 > 1/\beta_\perp$, although as discussed below only for somewhat larger anisotropies is magnetic moment conservation violated. Formally, a plasma with any nonzero pressure anisotropy can be unstable to the ion cyclotron instability [182]. However, there is an effective threshold given by the requirement that the unstable modes grow on a timescale comparable to the disk rotation period.

The growth rate of the mirror instability is given by (Eq. (36) of [80])

$$\gamma = \left(\frac{2}{\pi}\right)^{1/2} \left(\frac{T_\perp}{T_\parallel}\right)^{3/2} k_\parallel c_{\perp 0} \left[\frac{T_\perp}{T_\parallel} - 1 - \frac{1}{\beta_\perp}\left(1 + \frac{k_\parallel^2}{k_\perp^2}\right) \frac{\exp(\lambda)}{I_0(\lambda) - I_1(\lambda)}\right], \tag{4.28}$$

where $c_{\perp 0} = \sqrt{p_\perp/\rho}$, $\lambda = (k_\parallel c_{\perp 0}/\Omega_i)^2$, and I_0 and I_1 are modified Bessel functions of order 0 and 1. Minimizing the growth rate with respect to $k_\parallel$ and $k_\perp$ gives equations (43′) & (44′) of [80], which give the wavenumber for the fastest growing mirror mode,

$$\frac{k_\parallel}{k_\perp} = \sqrt{\frac{(D-1)}{4}}, \tag{4.29}$$

$$k_\perp \rho_i = \sqrt{\frac{(D-1)}{6}}, \tag{4.30}$$

where $D = \beta_\perp(p_\perp/p_\parallel - 1)$, $\beta_\perp = 8\pi p_\perp/B^2$. To estimate the pressure anisotropy at which μ conservation is broken and thus pitch angle scattering is efficient, we calculate D for which $k_\parallel \rho_i \sim k_\perp \rho_i \sim 1$. This implies $D \approx 7$, or that μ conservation fails (and

pitch angle scattering occurs) if the pressure anisotropy satisfies

$$\frac{p_\perp}{p_\parallel} - 1 > \frac{7}{\beta_\perp}. \tag{4.31}$$

The ion cyclotron instability can be also be excited when $p_\perp > p_\parallel$. Gary and collaborators have analyzed the ion cyclotron instability in detail through linear analysis and numerical simulations [69, 67]. They calculate the pressure anisotropy required for a given growth rate γ relative to the ion cyclotron frequency Ω_i

$$\frac{p_\perp}{p_\parallel} - 1 > \frac{S'}{\beta_\parallel^p} \tag{4.32}$$

where $S' = 0.35$ and $p = 0.42$ are fitting parameters quoted in equation (2) of [67] for $\gamma/\Omega_i = 10^{-4}$. Moreover, for $\gamma \ll \Omega_i$ the threshold anisotropy depends only very weakly on the growth rate γ. As a result, equation (4.32) provides a reasonable estimate of the pressure anisotropy required for pitch angle scattering by the ion cyclotron instability to be important on a timescale comparable to the disk rotation period.

4.2.3 Pressure anisotropy limits

Motivated by the above considerations, we require that the pressure anisotropy satisfy the following inequalities in our simulations (at each grid point and at all times):

$$\frac{p_\perp}{p_\parallel} - 1 + \frac{2}{\beta_\parallel} > \frac{1}{2}, \tag{4.33}$$

$$\frac{p_\perp}{p_\parallel} - 1 < \frac{2\xi}{\beta_\perp}, \tag{4.34}$$

$$\frac{p_\perp}{p_\parallel} - 1 < S\left(\frac{2}{\beta_\parallel}\right)^{1/2}, \tag{4.35}$$

where S and ξ are constants described below. It is important to note that the fluid-based kinetic theory utilized in this paper can correctly reproduce the existence and growth rates of the firehose and mirror instabilities (though not the ion cyclotron instability).[3] However, it can only do so for long wavelength perturbations that conserve μ. The relevant modes for pitch angle scattering occur at the Larmor radius scale, which is very small in typical accretion flows and is unresolved in our simulations. For this reason we must impose limits on the pressure anisotropy and cannot simultaneously simulate the MRI and the relevant instabilities that limit the pressure anisotropy. The algorithm to impose the pressure anisotropy limits is explained in Appendix C.2.

In Eq. 4.34, the parameter ξ determines the threshold anisotropy above which the mirror instability leads to pitch angle scattering. A value of $\xi = 3.5$ was estimated in Section 4.2.2. We take this as our fiducial value, but for comparison also describe calculations with $\xi = 0.5$, which corresponds to the marginal state for the mirror instability. We compare both models because the saturation of the mirror instability is not well understood, particularly under the conditions appropriate to a turbulent accretion disk. Eq. 4.35 is based on the pitch angle scattering model used by [26] for simulations of magnetic reconnection in collisionless plasmas; following them we choose $S = 0.3$. Eq. 4.35 with $S = 0.3$ gives results which are nearly identical (for the typical range of β studied here) to the pressure anisotropy threshold for the ion cyclotron instability discussed in Section 4.2.2 (Eq. 4.32).

In our simulations we find that for typical calculations, if $\xi = 0.5$ then Eq. 4.34 (the "mirror instability") dominates the isotropization of the pressure tensor, while if $\xi = 3.5$ then Eq. 4.35 (the "ion cyclotron instability") dominates. We also find that our results are insensitive to the form of the $p_\parallel > p_\perp$ threshold (Eq. 4.33); e.g.,

[3]The double adiabatic limit ($q_\perp = q_\parallel = 0$) predicts an incorrect threshold and incorrect growth rates for the mirror instability [180]. Thus it is important to use the heat flux models described in §2 to capture the physics of the mirror instability.

simulations with $1-p_\perp/p_\parallel < 2/\beta_\parallel$ (the marginal state of the firehose mode) instead of equation (4.33) give nearly identical results. Fully kinetic simulations of the mirror, firehose, and ion cyclotron instabilities will be useful for calibrating the pitch angle scattering models used here.

4.3 Kinetic MHD simulations in shearing box

In this section we discuss the shearing box equations that we solve numerically, and the modifications made to ZEUS to include kinetic effects.

4.3.1 Shearing box

The shearing box is based on a local expansion of the tidal forces in a reference frame rotating with the disk (see HGB for details). A fiducial radius R_0 in the disk is picked out and the analysis is restricted to a local Cartesian patch such that $L_x, L_y, L_z \ll R_0$ (where $x = r - R_0$, $y = \phi$ and $z = z$). In this paper only the radial component of gravity is considered, and vertical gravity and buoyancy effects are ignored. We also assume a Keplerian rotation profile. With these approximations, the equations of Landau MHD (kinetic MHD combined with Landau closure for parallel heat fluxes)

in the shearing box are:

$$\frac{\partial \rho}{\partial t} + \nabla \cdot (\rho \mathbf{V}) = 0, \tag{4.36}$$

$$\frac{\partial \mathbf{V}}{\partial t} + \mathbf{V} \cdot \nabla \mathbf{V} = -\frac{1}{\rho} \nabla \left(p_\perp + \frac{B^2}{8\pi} \right) + \frac{\mathbf{B} \cdot \nabla \mathbf{B}}{4\pi\rho} - \frac{1}{\rho} \nabla \cdot \mathbf{\Pi} - 2\mathbf{\Omega} \times \mathbf{V} + 3\Omega^2 x \hat{\mathbf{x}}, \tag{4.37}$$

$$\frac{\partial \mathbf{B}}{\partial t} = \nabla \times (\mathbf{V} \times \mathbf{B}), \tag{4.38}$$

$$\frac{\partial p_\parallel}{\partial t} + \nabla \cdot (p_\parallel \mathbf{V}) + \nabla \cdot \mathbf{q}_\parallel + 2p_\parallel \hat{\mathbf{b}} \cdot \nabla \mathbf{V} \cdot \hat{\mathbf{b}} - 2q_\perp \nabla \cdot \hat{\mathbf{b}} = -\frac{2}{3} \nu_{eff} (p_\parallel - p_\perp), \tag{4.39}$$

$$\frac{\partial p_\perp}{\partial t} + \nabla \cdot (p_\perp \mathbf{V}) + \nabla \cdot \mathbf{q}_\perp + p_\perp \nabla \cdot \mathbf{V} - p_\perp \hat{\mathbf{b}} \cdot \nabla \mathbf{V} \cdot \hat{\mathbf{b}} + q_\perp \nabla \cdot \hat{\mathbf{b}} = -\frac{1}{3} \nu_{eff} (p_\perp - p_\parallel), \tag{4.40}$$

$$q_\parallel = -\rho \kappa_\parallel \nabla_\parallel \left(\frac{p_\parallel}{\rho} \right), \tag{4.41}$$

$$q_\perp = -\rho \kappa_\perp \nabla_\parallel \left(\frac{p_\perp}{\rho} \right) + \kappa_m \mathbf{B} \cdot \nabla B, \tag{4.42}$$

where $\mathbf{q}_\parallel = q_\parallel \hat{\mathbf{b}}$ and $\mathbf{q}_\perp = q_\perp \hat{\mathbf{b}}$ are the heat fluxes parallel to the magnetic field, ν_{eff} is the effective pitch-angle scattering rate (includes microinstabilities, see Subsection 4.2.2 and Appendix C.2), $\kappa_\parallel$ and $\kappa_\perp$ are the coefficients of heat conduction, and κ_m is the coefficient in $q_\perp$ due to parallel gradients in the strength of magnetic field [180]. The κ_m component of $q_\perp$ that arises because of parallel magnetic field gradients is important for correctly recovering the saturated state for the mirror instability in the fluid limit, where (in steady state) $q_{\parallel,\perp} \approx 0$ implies that $T_\parallel$ is constant along the field line, and $T_\perp$ and magnetic pressure are anticorrelated.

Given our closure models, the coefficients for the heat fluxes are given by

$$\kappa_{\parallel} = \frac{8p_{\parallel}}{\rho}\frac{1}{\sqrt{8\pi\frac{p_{\parallel}}{\rho}}k_L + (3\pi-8)\nu_{eff}}, \tag{4.43}$$

$$\kappa_{\perp} = \frac{p_{\parallel}}{\rho}\frac{1}{\sqrt{\frac{\pi}{2}\frac{p_{\parallel}}{\rho}}k_L + \nu_{eff}}, \tag{4.44}$$

$$\kappa_m = \left(1-\frac{p_{\perp}}{p_{\parallel}}\right)\frac{p_{\perp}}{B^2}\kappa_{\perp}, \tag{4.45}$$

where k_L is the parameter that corresponds to a typical wavenumber characterizing Landau damping (see "crude model of Landau damping" in Section 2.4). We consider several values of k_L to study the effect of Landau damping on different scales. In particular, we consider $k_L = 0.5/\delta z$, $0.25/\delta z$, and $0.125/\delta z$ which correspond to correctly capturing Landau damping on scales of $12\delta z$, $24\delta z$, $48\delta z$, respectively, where $\delta z = L_z/N_z$, $L_z = 1$ for all our runs, and N_z is the number of grid points in the z-direction (taken be 27 and 54 for low and high resolution calculations, respectively). Thus, $k_L = 0.25/\delta z$ corresponds to correctly capturing Landau damping for modes with wavelengths comparable to the size of the box in the low resolution runs.

The term ν_{eff} in Eqs. 4.43 and 4.44 is an effective collision frequency which is equal to the real collision frequency ν, as long as μ conservation is satisfied. However, when the pressure anisotropy is large enough to drive microinstabilities that break μ invariance , and enhance pitch angle scattering, then there is an increase in the effective collision frequency that decreases the associated conductivities. The expressions for ν_{eff} are given in Eqs. C.12, C.15, and C.18 in Appendix C.2.

Shearing periodic boundary conditions appropriate to the shearing box are described in [86]. Excluding V_y, all variables at the inner x- boundary are mapped to sheared ghost zones at the outer boundary; a similar procedure applies for the inner ghost zones. V_y has a jump of $(3/2)\Omega L_x$ across the box while applying the x- shearing boundary conditions, to account for the background shear in V_y.

4.3.2 Numerical methods

We have used the shearing box version of the ZEUS MHD code [185, 186], and modified it to include kinetic effects. The ZEUS code is a time explicit, operator split, finite difference algorithm on a staggered mesh, i.e., scalars and the diagonal components of second rank tensors are zone centered, while vectors are located at zone faces, and pseudovectors and offdiagonal components of second rank tensors are located at the edges. The location of different variables on the grid is described in detail in Appendix C.1. Appendix C.1.1 describes how we choose the time step δt to satisfy the Courant condition (which is modified by pressure anisotropy and heat conduction). We also require that the choice of δt maintain positivity of $p_\parallel$ and $p_\perp$.

Implementation of the shearing box boundary conditions is described in [86]. One can either apply boundary conditions on the components of $\mathbf{B}$ or the EMFs (whose derivatives give $\mathbf{B}$). We apply shearing periodic boundary conditions on the EMFs to preserve the net vertical flux in the box, although applying boundary conditions directly on $\mathbf{B}$ gives similar results.

Eqs. 4.39 and 4.40 are split into transport and source steps, analogous to the energy equation in the original ZEUS MHD. The transport step is advanced conservatively, and the source step uses centered differences in space. It should be noted that in Eq. 4.40 the $\nabla \cdot \mathbf{q}_\perp$ term is not purely diffusive, and it is necessary to carefully treat the magnetic gradient part of $q_\perp$ in the transport step for robustness of the code (Appendix C.2.1).

We have tested the newly added subroutines for evolving anisotropic pressure and parallel heat conduction. We tested the anisotropic conduction routine by initializing a "hot" patch in circular magnetic field lines and assessing the extent to which heat remains confined along the field. This is the same test described in [148], and we find good agreement with their results. The method we use for the simulations in this chapter is the "asymmetric method," described in Chapter 5 which contains

different tests we carried out. Additional tests include linear (damped and undamped) waves and instabilities in non-rotating anisotropic plasmas, the Alfvén wave, and the firehose and mirror instabilities (see Appendix C). For mirror simulations we observe the formation of stationary anticorrelated density and magnetic structures as seen in the hybrid simulations of [127]. For firehose we see the instability with magnetic perturbations developing at small scales but during saturation the perturbations are at larger scales (as seen in [162]); a 2-D test for firehose instability, where pressure anisotropy is caused by the shearing of plasma, is presented in Appendix C.

Finally, the numerical growth rates of the kinetic MRI were compared to the analytic results for different pressure anisotropies, (k_x, k_z), collision frequencies, and angles between the magnetic field and $\hat{\mathbf{z}}$; we find good agreement with the results of [158] and [176] (described in Chapter 3). When $k_L = k_\parallel$, the growth rate of the fastest growing mode is within $\sim 3\%$ of the theoretical prediction. The simulations with $B_\phi = B_z$ show $\approx$ twice faster growth as compared to $B_z = 0$, as predicted by linear theory.

4.3.3 Shearing box and kinetic MHD

Certain analytic constraints on the properties and energetics of shearing box simulations have been described in [86]. These constraints serve as a useful check on the numerical simulations. Here we mention the modifications to these constraints in KMHD. Conservation of total energy in the shearing box gives

$$\frac{\partial}{\partial t}\Gamma = \frac{3}{2}\Omega L_x \int_x dA \left[\rho V_x \delta V_y - \left(1 - \frac{4\pi(p_\parallel - p_\perp)}{B^2}\right)\frac{B_x B_y}{4\pi}\right], \tag{4.46}$$

where $\delta V_y = V_y + (3/2)\Omega x$, and Γ is the total energy given by,

$$\Gamma = \int d^3x \left[\rho\left(\frac{V^2}{2} + \phi\right) + \frac{p_\parallel}{2} + p_\perp + \frac{B^2}{8\pi}\right] \tag{4.47}$$

where $\phi = -(3/2)\Omega^2 x^2$ is the tidal effective potential about R_0. Eq. (4.46) states that the change in the total energy of the shearing box is due to work done on the box by the boundaries. Notice that there is an anisotropic pressure contribution to the work done on the box. Eq. (29) in [16] for conservation of angular momentum in cylindrical geometry (same as Eq. 1.4) is also modified because of the anisotropic pressure and is given by

$$\frac{\partial}{\partial t}(\rho R V_\phi) + \nabla \cdot \left[\rho V_\phi \mathbf{V} R - \frac{B_\phi}{4\pi} \left(1 - \frac{4\pi(p_\parallel - p_\perp)}{B^2} \right) \mathbf{B_p} R + \left(p_\perp + \frac{B_p^2}{8\pi} \right) \hat{\phi} R \right] = 0, \tag{4.48}$$

where $\mathbf{B_p} = B_R \hat{\mathbf{R}} + B_z \hat{\mathbf{z}}$ is the poloidal field. We can calculate the level of angular momentum transport (and corresponding heating) in our simulations by measuring the stress tensor given by

$$W_{xy} = \rho V_x \delta V_y - \frac{B_x B_y}{4\pi} + \frac{(p_\parallel - p_\perp)}{B^2} B_x B_y \tag{4.49}$$

Note that the stress tensor has an additional contribution due to pressure anisotropy. One can define a dimensionless stress via Shakura and Sunyaev's α parameter by

$$\alpha \equiv \frac{W_{xy}}{P_0} = \alpha_R + \alpha_M + \alpha_A \tag{4.50}$$

where α_R, α_M, α_A are the Reynolds, Maxwell and anisotropic stress parameters, respectively. As in [86], we normalize the stress using the initial pressure to define an α parameter.

4.3.4 Shearing box parameters and initial conditions

The parameters for our baseline case have been chosen to match the fiducial run Z4 of [86]. The simulation box has a radial size $L_x = 1$, azimuthal size $L_y = 2\pi$, and vertical size $L_z = 1$. The sound speed $V_s = \sqrt{p/\rho} = L_z \Omega$, so that the vertical size is

about a disk scale height (though it is an unstratified box). The pressure is assumed to be isotropic initially, with $p_0 = \rho_0 V_s^2 = 10^{-6}$ and $\rho_0 = 1$. All of our simulations start with a vertical field with $\beta = 8\pi p_0/B_0^2 = 400$. The fastest growing MRI mode for this choice of parameters is well resolved. We consider two different numerical resolutions: $27 \times 59 \times 27$ and $54 \times 118 \times 54$. Perturbations are introduced as initially uncorrelated velocity fluctuations. These fluctuations are randomly and uniformly distributed throughout the box. They have a mean amplitude of $|\delta V| = 10^{-3} V_s$.

4.4 Results

The important parameters for our simulations are listed in Table 4.1. Each simulation is labeled by Z (for the initial B_z field), and l and h represent low ($27 \times 59 \times 27$) and high ($54 \times 118 \times 54$) resolution runs, respectively. We also include low and high resolution MHD runs for comparison with kinetic calculations (labeled by ZM). Our models for heat conduction and pressure isotropization have several parameters: k_L, the typical wavenumber for Landau damping used in the heat flux (Eqs. 4.13 and 4.14), and ξ, the parameter that forces the pressure anisotropy to be limited by $p_\perp/p_\parallel - 1 < 2\xi/\beta_\perp$ (representing pitch angle scattering due to small scale mirror modes; Eq. 4.34). All calculations except $Zl8$, $Zl1$, and $Zh1$ also use the ion cyclotron scattering "hard wall" from Eq. 4.35. In addition to these model parameters, Table 4.1 also lists the results of the simulations, including the volume and time averaged magnetic and kinetic energies, and Maxwell, Reynolds, and anisotropic stresses. As Table 4.1 indicates, the results of our simulations depend quantitatively—though generally not qualitatively—on the microphysics associated with heat conduction and pressure isotropization. Throughout this section we use single brackets $\langle f \rangle$ to denote a volume average of quantity f; we use double brackets $\langle\langle f \rangle\rangle$ to denote a volume and time average in the saturated turbulent state, from orbit 5 onwards.

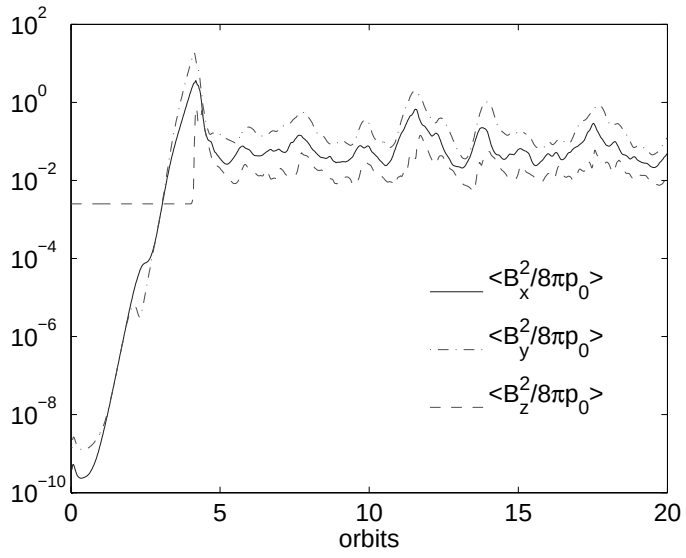

Figure 4.2: Time evolution of volume-averaged magnetic energy for the fiducial run $Zl4$. Time is given in number of orbits. There is a small decrease in the magnetic energy at ≈ 2 orbits when the pressure anisotropy is sufficient to stabilize the fastest growing mode. However, small-scale kinetic instabilities limit the magnitude of the pressure anisotropy, allowing the magnetic field to continue to amplify. As in MHD, there is a channel phase which breaks down into turbulence at ≈ 4 orbits.

4.4.1 Fiducial run

We have selected run $Zl4$ as our fiducial model to describe in detail. This model includes isotropization by ion cyclotron instabilities and mirror modes, with the former dominating (for $\xi = 3.5$; see Section 4.2.2) except at early times. The conductivity is determined by $k_L = 0.5/\delta z$ which implies that modes with wavelengths $\sim 12\delta z \sim L_z/2$ are damped at a rate consistent with linear theory.

Figures 4.2-4.4 show the time evolution of various physical quantities for run $Zl4$. The early linear development of the instability is similar to that in MHD, with the field growing exponentially in time. The key new feature is the simultaneous exponential growth of pressure anisotropy ($p_\perp > p_\parallel$) as a result of μ conservation (up to 2 orbits in Fig. 4.4). As described in Section 4.2.1, this pressure anisotropy tends to stabilize the MRI modes and shut off the growth of the magnetic field. Indeed, in simulations that

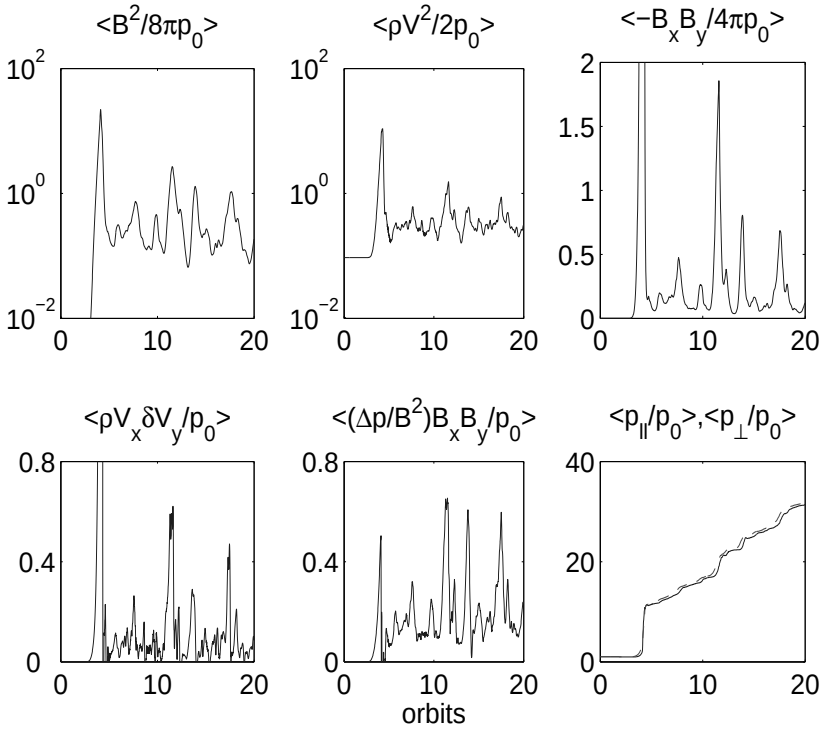

Figure 4.3: Time evolution of volume-averaged magnetic and kinetic energies, Maxwell, Reynolds, and anisotropic stress, and pressure ($p_\parallel$: solid line, $p_\perp$: dashed line) for the fiducial model $Zl4$. Time is given in orbits and all quantities are normalized to the initial pressure p_0. $\delta V_y = V_y + (3/2)\Omega x$ and $\Delta p = (p_\parallel - p_\perp)$.

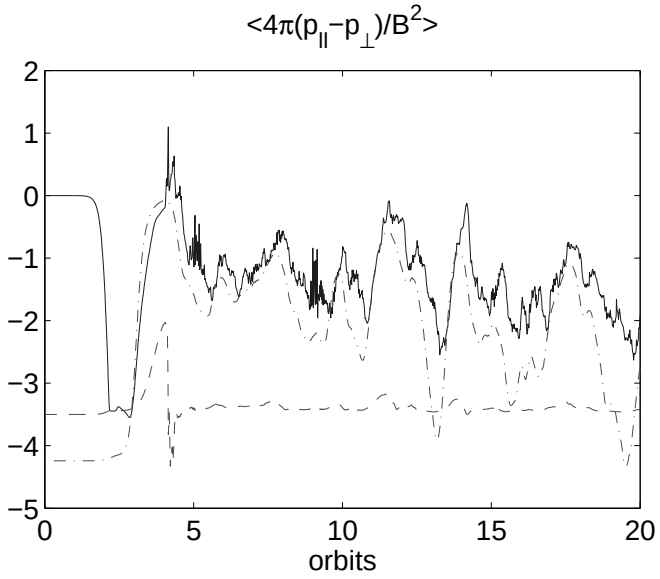

Figure 4.4: Time evolution of volume-averaged pressure anisotropy ($4\pi(p_{\|} - p_{\perp})/B^2$: solid line) for model $Zl4$. Also plotted are the "hard wall" limits on the pressure anisotropy due to the ion cyclotron (dot dashed line) and mirror instabilities (dashed line). Ion cyclotron scattering is generally more efficient in the steady state. The limits on pressure anisotropy are applied at each grid point while this figure is based on volume averaged quantities.

do not include any isotropization of the pressure tensor, we find that all MRI modes in the box are stabilized by the pressure anisotropy and the simulation saturates with the box filled with small amplitude anisotropic Alfvén waves (see Figure 4.6). This highlights the fact that, unlike in MHD, the MRI is not an exact nonlinear solution in kinetic theory. However, the pressure anisotropy required to stabilize all MRI modes exceeds the pressure anisotropy at which pitch angle scattering due to mirror and ion cyclotron instabilities become important. This takes place at about orbit 2 in run *Zl*4 (see the small 'dip' in the growth of magnetic energies in Figure 4.2), at which point the pressure anisotropy is significantly reduced and the magnetic field is able to grow to nonlinear amplitudes.

The nonlinear saturation at orbit ~ 5 appears qualitatively similar to that in MHD, and may occur via analogues of the parasitic instabilities described by [75]. The channel solution is, however, much more extreme in KMHD than MHD (the maximum B^2 in Figure 4.2 is approximately an order of magnitude larger than in analogous MHD runs). After saturation, the magnetic and kinetic energies in the saturated state are comparable in KMHD and MHD (see Table 4.1). This is essentially because the pitch angle scattering induced by the kinetic microinstabilities acts to isotropize the pressure, enforcing a degree of MHD-like dynamics on the collisionless plasma.

Figure 4.3 and Table 4.1 show the various contributions to the total stress. As in MHD, the Reynolds stress is significantly smaller than the Maxwell stress. In kinetic theory, however, there is an additional component to the stress due to the anisotropic pressure (Eq. 4.48). In the saturated state, we find that the Maxwell stress is similar in KMHD and MHD, but that the anisotropic stress itself is comparable to the Maxwell stress. Expressed in terms of an α normalized to the initial pressure, our fiducial run *Zl*4 has $\alpha_M = 0.23$, $\alpha_R = 0.097$, and $\alpha_A = 0.2$, indicating that stress due to pressure anisotropy is dynamically important.

Nearly all physical quantities in Figures 4.2-4.4 reach an approximate statistical steady state. The exceptions are $p_\parallel$ and $p_\perp$, which increase steadily in time because the momentum flux on the boundaries does work on the system (Eq. 4.46), which is eventually converted to heat in the plasma by artificial viscosity; there is no cooling for internal energy to reach a steady state (the same is true in HGB's MHD simulations). Because of the steadily increasing internal energy and approximately fixed B^2 (although with large fluctuations), the plasma β shows a small secular increase from orbits 5-20 (a factor of ≈ 3 increase, though with very large fluctuations due to the large fluctuations in magnetic energy).

Figure 4.4 shows the pressure anisotropy thresholds due to the ion cyclotron and mirror instabilities, in addition to the volume averaged pressure anisotropy in run $Zl4$. From Eq. 4.35, the ion cyclotron threshold ($4\pi\Delta p/B^2$) is expected to scale as $\sqrt{\beta_\parallel}$, which is fairly consistent with the trend in Figure 4.4. The actual pressure anisotropy in the simulation shows a small increase in time as well, although less than that of the ion cyclotron threshold. These secular changes in β and Δp are a consequence of the increasing internal energy in the shearing box, and are probably not realistic. In a global disk, we expect that—except perhaps near the inner and outer boundaries—β will not undergo significant secular changes in time. In a small region of a real disk in statistical equilibrium, the heating would be balanced by radiation (for thin disks) or by cooler plasma entering at large R and hotter plasma leaving at small R (in low luminosity, thick disks).

It is interesting to note that in Figure 4.4, the pressure anisotropy ($4\pi\Delta p/B^2$) is closely tied to the ion cyclotron threshold at times when B^2 is rising (which corresponds to the channel solution reemerging). Increasing B leads to a pressure anisotropy with $p_\perp > p_\parallel$ by μ conservation. At the same time, the ion cyclotron threshold ($\sim \sqrt{\beta}$) decreases, eventually the pressure limiting threshold is encountered. When B is decreasing, however, we do not find the same tight relationship

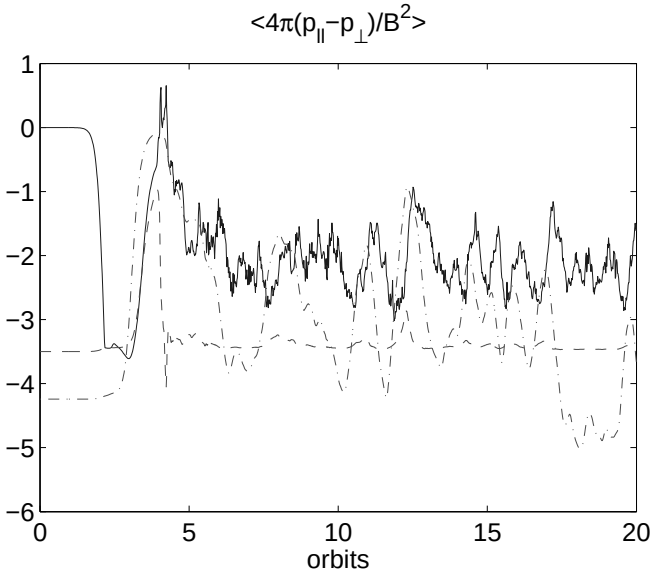

Figure 4.5: Time evolution of volume-averaged pressure anisotropy ($4\pi(p_\parallel - p_\perp)/B^2$: solid line) for model $Zl8$. Also plotted are the "hard wall" limits on the pressure anisotropy due to the ion cyclotron (dot dashed line) and mirror instabilities (dashed line), although the ion cyclotron scattering limit is not applied in this simulation. The volume averaged pressure anisotropy saturates at smaller anisotropy than the mirror threshold at $\xi = 3.5$, which is the only limit on pressure anisotropy used.

between the pressure anisotropy and the imposed threshold. Figure 4.4 clearly indicates that in our fiducial simulation pitch angle scattering is dominated by the ion cyclotron threshold. For comparison, Figure 4.5 shows the pressure anisotropy and thresholds for run *Zl*8 which is identical to the fiducial run, except that the ion cyclotron threshold is not used and the only scattering is due to the mirror threshold. In this case, the saturated pressure anisotropy is somewhat larger than in the fiducial run, but the pressure anisotropy is not tied to the mirror threshold.

Table 4.2 gives the mean, standard deviation, and standard error in the mean, for various quantities in the saturated portion of the fiducial simulation. The standard errors are estimated by taking into account the finite correlation time for the physical quantities in the simulation, as described in Appendix D. In many cases, the deviations are significantly larger than the mean. As in MHD, we find that the magnetic energy is dominated by the y- component, which is about a factor of 3 larger than the x- component; the vertical component is smaller yet. The radial and azimuthal kinetic energy fluctuations are comparable, while the vertical component is smaller. We also find that, as in MHD, the perturbed kinetic and magnetic energies are not in exact equipartition: the magnetic energy is consistently larger. Table 4.2 also shows the mean and deviations for $\langle p_\perp/B\rangle$ and $\langle p_\parallel B^2/\rho^2\rangle$. Because of pitch angle scattering $\mu = \langle p_\perp/B\rangle$ is no longer conserved. $\langle p_\parallel B^2/\rho^2\rangle$ varies because of both, heat conduction and pitch angle scattering.

The pressure anisotropy in our fiducial run saturates at $4\pi(p_\perp - p_\parallel)/B^2 \approx 1.5$. By contrast, the threshold for the mirror instability is $4\pi(p_\perp - p_\parallel)/B^2 = 0.5$. This implies that the model is unstable to generating mirror modes. However, the mirror modes that can be excited at this level of anisotropy do not violate μ conservation and thus do not contribute to pitch angle scattering (see Section 4.2.2). They can in principle isotropize the plasma in a volume averaged sense by spatially redistributing plasma into magnetic wells [101]. This saturation mechanism is simulated using our

kinetic MHD code for a uniform, anisotropic plasma (see Appendix C.3.3). It does not appear to be fully efficient in the saturated state of our turbulent disk simulations, even at the highest resolution; strong MRI turbulence dominates over everything else for these parameters.

In the next few sections we compare the fiducial simulation described above with variations in the pitch angle scattering model and the parallel conductivity. A comparison of the total stress in all of our simulations is shown in Figure 4.7.

4.4.2 The double adiabatic limit

Simulations $Zl1$ and $Zh1$ are simulations in the double adiabatic limit (no heat conduction), with no limit on the pressure anisotropy imposed. In this limit both $\mu = \langle p_\perp/B \rangle$ and $\langle p_\parallel B^2/\rho^2 \rangle$ are conserved. Figure 4.6 shows volume averages of various quantities as a function of time for the run $Zl1$. These calculations are very different from the rest of our results and show saturation at very low amplitudes ($\delta B^2/B^2 \approx 0.04$). In the saturated state, the box is filled with shear modified anisotropic Alfvén waves and all physical quantities are oscillating in time. The total stress is also oscillatory with a vanishing mean, resulting in negligible transport. In these calculations, the pressure anisotropy grows to such a large value that it shuts off the growth of all of the resolved MRI modes in the box. Table 4.1 shows that $\langle\langle 4\pi(p_\parallel - p_\perp)/B^2 \rangle\rangle$ saturates at -11.96 and -10.2 for the low and high resolution runs, respectively (although the normalized pressure anisotropy $\langle\langle (p_\parallel - p_\perp)/p_\parallel \rangle\rangle \approx -0.07$ is quite small). This is much larger than the anisotropy thresholds for pitch angle scattering described in Subsection 4.2.2. As a result, we do not expect these cases to be representative of the actual physics of collisionless disks. These cases are of interest, however, in supporting the predictions of the linear theory with anisotropic initial conditions considered in Section 4.2.1, and in providing a simple test for the simulations. They also highlight the central role of pressure isotropization in collisionless

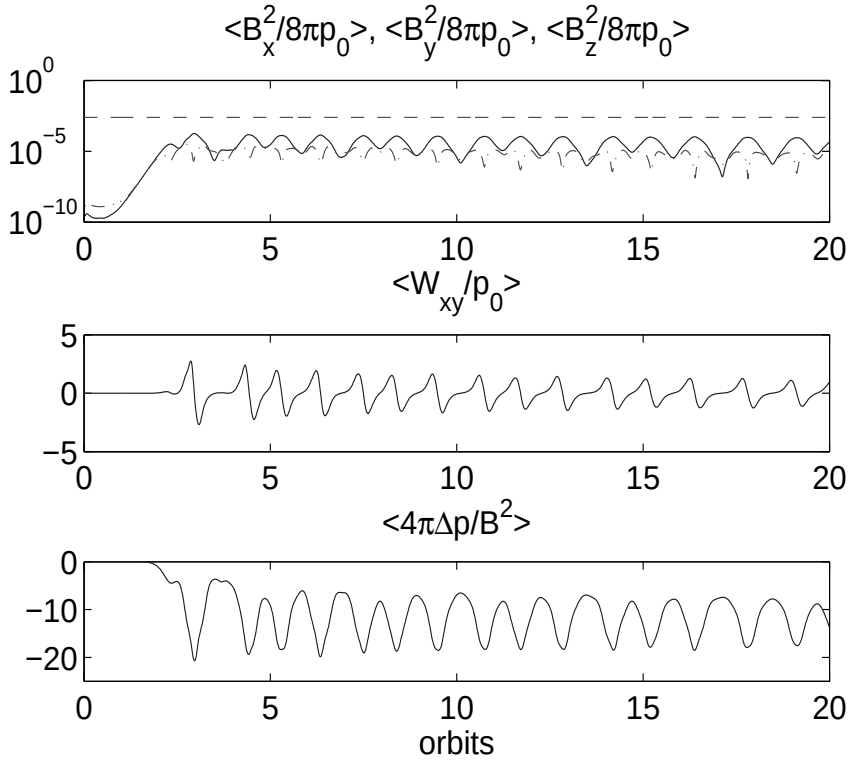

Figure 4.6: Time evolution of volume-averaged magnetic energy (dashed line: $B_z^2/8\pi p_0$, solid line: $B_x^2/8\pi p_0$, dot dashed line: $B_y^2/8\pi p_0$), total stress (W_{xy}/p_0) in units of 10^{-3}, and pressure anisotropy for model $Zl1$. Time is given in orbits and all quantities are normalized to the initial pressure p_0. $\delta V_y = V_y + (3/2)\Omega x$ and $\Delta p = (p_\parallel - p_\perp)$. In this calculation there is no heat conduction and no isotropization of the pressure tensor. All resolved MRI modes are thus stabilized by pressure anisotropy and the 'saturated' state is linear anisotropic Alfvén waves with no net angular momentum transport.

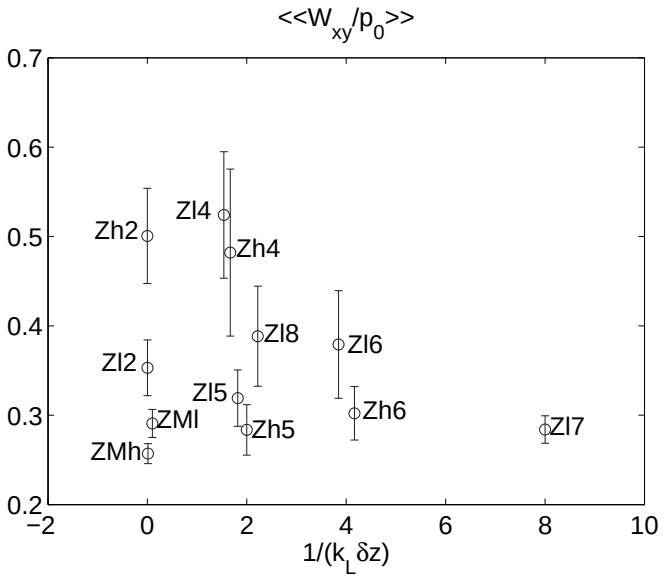

Figure 4.7: Space and time average of the total stress $\langle\langle W_{xy}/p_0\rangle\rangle$ versus $1/(k_L\delta z)$ for different runs. Error bars shown are based on estimates of the correlation time of the fluctuations described in [144].

dynamos [170].

4.4.3 Varying conductivity

We have carried out a series of simulations with different conductivities defined by the parameter k_L. Simulations $Zl2$ and $Zh2$ are in the CGL limit with vanishing parallel heat conduction, but with the same limits on pressure anisotropy as the fiducial model. Simulations $Z6$ use $k_L\delta z = 0.25$ while run $Zl7$ uses $k_L = 0.125/\delta z$. Both of these are smaller than the value of $k_L\delta z = 0.5$ in the fiducial run, which implies a larger conductivity. Figure 4.7 shows that the total stress varies by about a factor of 2 depending on the conductivity and resolution. Simulations with larger conductivity tend to have smaller saturation amplitudes and stresses. This could be because larger conductivity implies more rapid Landau damping of slow and fast magnetosonic waves. In all cases, however, the anisotropic stress is comparable to the Maxwell stress, as in the fiducial run. Until a more accurate evaluation is available of

the heat fluxes for modes of all wavelengths in the simulation simultaneously (either by a more complete evaluation of the nonlocal heat fluxes, Eqs. 4.11-4.12, or even by a fully kinetic MHD code that directly solves the DKE, Eq. 4.5), it is difficult to ascertain which value of the conductivity best reflects the true physics of collisionless disks.

4.4.4 Different pitch angle scattering models

In this section we consider variations in our model for pitch angle scattering by high frequency waves. All of these calculations use $k_L = 0.5/\delta z$. We note again that the appropriate pitch angle scattering model remains somewhat uncertain, primarily because of uncertainties in the nonlinear saturation of long-wavelength, μ-conserving mirror modes. The calculations reported here cover what, we believe, is a plausible range of models.

Models $Zl5$ and $Zh5$ place a more stringent limit on the allowed pressure anisotropy, taking $\xi = 0.5$ in Eq. 4.34. This corresponds to the threshold of the mirror instability. Not surprisingly, this simulation is the most "MHD-like" of our calculations, with magnetic and kinetic energies, and Maxwell stresses that are quite similar to those in MHD. Even with this stringent limit, however, the anisotropic stress is $\approx 1/3$ of the Maxwell stress. It is also interesting to note that although the dimensionless pressure anisotropy is quite small $\langle\langle 4\pi(p_\parallel - p_\perp)/B^2\rangle\rangle \approx -0.02$, the dimensionless anisotropic stress $\langle\langle 4\pi(p_\parallel - p_\perp)/B^2 \times B_x B_y/p_0\rangle\rangle \approx -0.07$ is significantly larger (and larger than Reynolds stress) because of correlations between the pressure anisotropy and field strength.

As a test of how large a collisionality is needed for the results of our kinetic simulations to rigorously approach the MHD limit, we have carried out a series of simulations including an explicit collisionality ν and varying its magnitude relative to the disk frequency Ω. Our results are summarized in Table 4.3 and Figure 4.8. In these

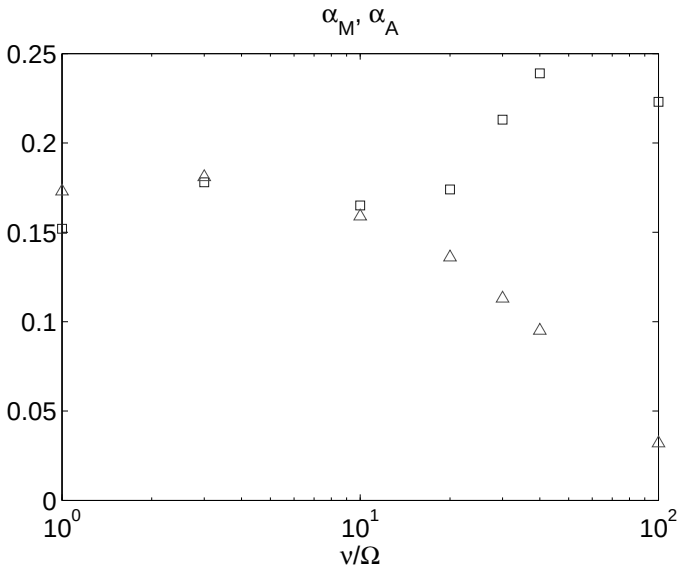

Figure 4.8: Maxwell (α_M: squares) and anisotropic stress (α_A: triangles) plotted against the collision frequency normalized to rotation frequency (ν/Ω). Transition to MHD occurs for $\nu/\Omega \gtrsim 30$ (see Table 4.3).

simulations we start with initial conditions determined by the saturated turbulent state of our fiducial run *Zl*4, but with an explicit collision frequency (in addition to the scattering models described in Section 4.2.3). Figure 4.8 shows that for $\nu/\Omega \lesssim 20$, the results are very similar to the collisionless limit. For larger collision frequencies the anisotropic stress is reduced and the simulations quantitatively approach the MHD limit. These results are similar to those obtained in Chapter 3 (see Figure 3.3), where linear calculations indicate that the MHD limit for modes with $k \sim \Omega/V_A$ is approached when $\nu \gtrsim \beta^{3/4}\Omega$.

To consider the opposite limit of low collisionality (because of pitch angle scattering), run *Zl*8 places a less stringent limit on the allowed pressure anisotropy, taking $\xi = 3.5$ in Eq. 4.34, and ignoring the limit set by the ion cyclotron instability in Eq. 4.35. The results of this calculation are not physical but are useful for further clarifying the relative importance of the Maxwell and anisotropic stresses as a function of the pitch angle scattering rate. In *Zl*8, the saturated magnetic energy and Maxwell

stress are lower than in all of our other calculations (excluding the double adiabatic models described in Section 4.4.2). Interestingly, however, the total stress is comparable to that in the other calculations (Figure 4.7) because the anisotropic stress is ≈ 2.4 times larger than the Maxwell stress (Table 4.1). As discussed briefly in Section 4.4.1, the pressure anisotropy in this simulation is not simply set by the applied mirror pitch angle scattering threshold (its quite smaller than the mirror "hard wall;" see Figure 4.5). It is possible that resolved mirror modes contribute to decreasing the volume averaged pressure anisotropy (but see below).

Finally, in models $Z3$ we include parallel heat conduction but do not limit the pressure anisotropy. In these calculations, we expect to be able to resolve the long-wavelength μ-conserving mirror modes that reduce the pressure anisotropy by forming magnetic wells [101].[4] In our test problems with uniform anisotropic plasmas, this is precisely what we find (see Appendix C.3.3). In the shearing box calculations, however, even at the highest resolutions, we find that the pressure anisotropy becomes so large that Eqs. 4.34) and 4.35 are violated, so that pitch angle scattering due to high frequency microinstabilities would become important. The resolved mirror modes are thus not able to isotropize the pressure sufficiently fast at all places in the box.[5] However, it is hard to draw any firm conclusions from these simulations because they stop at around 4 orbits (for both resolutions $Zl3$ and $Zh3$) during the initial nonlinear transient stage. At this time the pressure becomes highly anisotropic and becomes very small at some grid points, and the time step limit causes $\delta t \to 0$.

Pitch angle scattering centers are not uniformly distributed in space and show intermittency. Subsection 2.6.1 gives simple estimates for effective collision frequency and mean free path assuming a uniform distribution of scattering centers. Also dis-

[4] At the resolution of $Zl3$, the fastest growing mirror mode in the computational domain has a linear growth comparable to that of the MRI.

[5] In higher resolution simulations, one can resolve smaller-scale and faster growing mirror modes, and thus the effects of isotropization by resolved mirror modes could become increasingly important. We see no such indications, however, for the range of resolutions we have been able to simulate.

cussed are simulation results which show that only a very small fraction of the box undergoes pitch angle scattering (see Figure 2.2). Figure 2.2 also shows that pitch angle scattering due to mirror instability dominates ion-cyclotron instability for $\beta \gtrsim 100$. Intermittency of pitch angle scattering can be crucial for thermal conduction and viscous transport in collisionless high-β plasmas.

4.5 Additional simulations

Our paper, [177], describes simulations with an initial $\beta = 400$ and an initial vertical field ($B_\phi = 0$). The linear theory predicts that the fastest growing mode for $B_\phi = B_z$ in the kinetic regime is $\approx$ twice faster than MHD, and at a much larger scale. The scale separation between the fastest growing kinetic MHD and MHD modes for $B_\phi = B_z$ is greatest for large β (see [158]). In this section we describe simulations not described in [177]—initial conditions with $B_\phi = B_z$ and only B_ϕ, and the high β regime. One of the motivations is to see whether a faster growth rate for $B_\phi = B_z$ in the kinetic regime results in a nonlinear saturation different from MHD. The fastest growing MRI mode in MHD occurs at a scale $H/\sqrt{\beta}$, much smaller than the disk height scale $H = c_s/\Omega$ for large initial β. Thus, we vary the box size and resolution to study the effect of these parameters on nonlinear saturation.

4.5.1 High β simulations

Figure 4.9 shows the growth rate of the MRI in the kinetic and MHD regimes for $\beta = 10^6$—the fastest growing kinetic MRI is at a much larger length scale. Because of a large separation of scales between the fastest growing modes in the kinetic and MHD regimes, it is difficult to resolve both the scales in a numerical simulation. The figure also marks, by arrows, the minimum and maximum wavenumber corresponding to the chosen box size for the low resolution runs ($KYZl$ and $MYZl$); for these

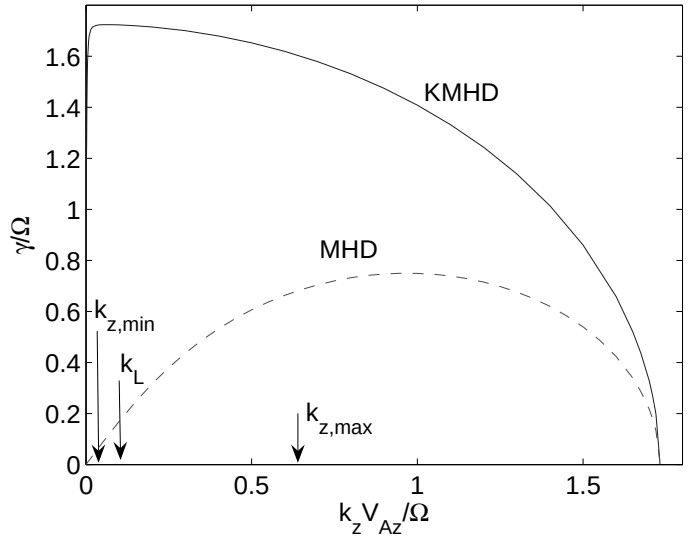

Figure 4.9: The MRI growth rate in kinetic (using $k_L = 0.5/\delta z$) and MHD regimes for $\beta = 10^6$. Arrows $k_{z,min} = 2\pi/L_z$ and $k_{z,max} = \pi/\delta z$ mark the minimum and maximum wavenumbers in the low resolution ($27 \times 59 \times 27$) runs. For a higher resolution ($54 \times 118 \times 54$) simulation both k_L and $k_{z,max}$ double as δz is reduced by half.

runs both these scales are not resolved. We carry out low ($27 \times 59 \times 27$) and high ($54 \times 118 \times 58$) resolution kinetic and MHD simulations, with different box sizes. The arrows in Figure 4.9 correspond to the low resolution runs with the smallest boxes that we have considered—increasing the box size resolves the fastest growing kinetic modes at large scales, while increasing the number of grid points resolves the fastest MHD modes at small scales.

Figure 4.10 shows the magnetic energy in the x- component of the magnetic field, $\langle\langle B_x^2/8\pi\rangle\rangle$, for runs initialized with an MRI eigenmode (runs $KYZlin$ and $MYZlin$ in Table 4.4); the kinetic growth rate is indeed faster than in MHD, as predicted by linear theory. The MHD growth rate for $MYZlin$ calculated from the slope of $B_x^2/8\pi$ is $\gamma/\Omega = 0.29$, consistent with linear theory for this particular mode (Figure 4.9 shows a similar growth rate for $k_z = 4k_{z,min}$, the mode initialized in $MYZlin$). For the same run, Table 4.4 shows that the magnetic energy and stresses in the saturated state are

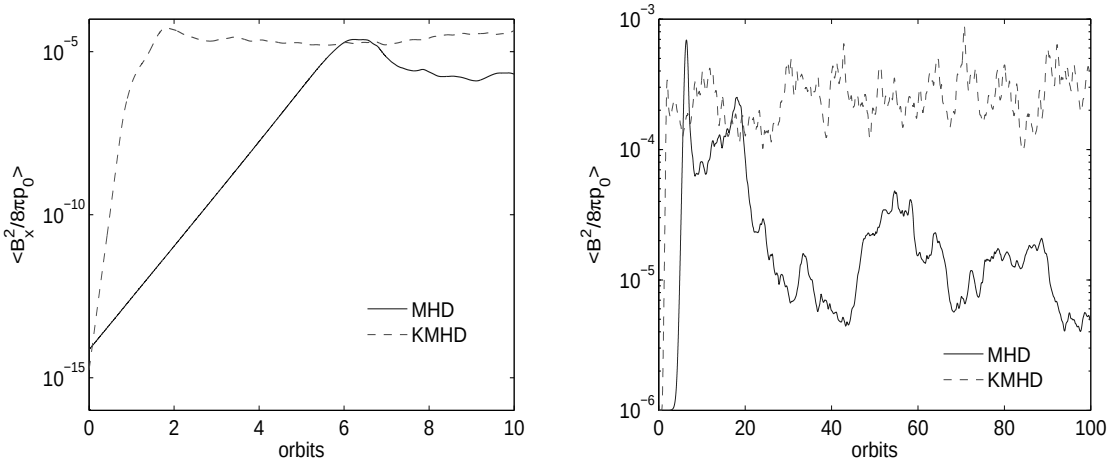

Figure 4.10: Figure on left shows magnetic energy in the x- component, $\langle B_x^2/8\pi p_0\rangle$, plotted as a function of number of orbits for runs $MYZlin$ and $KYZlin$. The initial disturbance is a linear eigenmode with an amplitude of 10^{-9} and vertical wavenumber $k_z = 8\pi/L_z = 4k_{z,min}$. Resolution for both cases is $27 \times 59 \times 27$. As expected, the MRI growth rate is much faster in kinetic regime than in MHD. The growth rates deduced from the slope are for MHD: $\gamma/\Omega = 0.29$, and for KMHD: $\gamma/\Omega = 1.78$. Figure on right shows the total magnetic energy for 100 orbits. Saturated magnetic energy in MHD is much smaller than KMHD at late times.

much smaller than all other runs unlike the kinetic run $KYZlin$, the presence of a single mode somehow affects the saturation in MHD! In comparison, similar case initialized with random noise ($MYZl$) saturates at large amplitude as shown in Table 4.4. It seems that nonlinear saturation in MHD shows a bifurcation depending on the initial conditions; somehow the memory of initial conditions is retained even at late times.

Apart from verifying the linear growth, we also study the differences between the nonlinear saturation of the kinetic and MHD simulations; all the runs described in this section use pitch angle scattering models and conduction parameter (k_L) similar to the fiducial run $Zl4$. We use a range of box sizes, starting from the smallest boxes ($KYZl$, $KYZh$ and $MYZl$, $MYZh$) to the boxes with vertical height equal to the disk height scale ($KYZ8l$, $KYZ8h$ and $MYZ8l$, $MYZ8h$). The nonlinear simulations are done at low ($27 \times 59 \times 27$) and high ($54 \times 118 \times 54$) resolutions.

Both MHD and kinetic simulations show that the magnetic and kinetic energies, and stresses scale with the box size, provided that the resolution is good enough (see Figure 4.13); this is similar to what was observed by [86] for MHD simulations. The magnetic energy is ≈ 5 times smaller for the kinetic simulations, however, the total stress (dominated by the anisotropic stress for kinetic simulations) is comparable for kinetic and MHD simulations. Although the MRI growth in the kinetic regime is double that in MHD, the kinetic simulations saturate at a smaller magnetic energy compared to MHD.

Figure 4.11 shows the spectra of magnetic and kinetic energies for runs $KYZh$ and $Zh4$; a $k^{-11/3}$ Kolmogorov spectrum is a good fit for the kinetic and magnetic energies. The spectra as a function of k_y look slightly steeper for high β simulations. This may be because fluctuation energy is small compared to the energy in the radial shear of V_ϕ, which elongates the eddies in the azimuthal direction. The spectra for MHD $B_\phi = B_z$ runs are similar (see Figure 4.12) to the kinetic runs. Although the spectra are similar to the Kolmogorov spectrum for isotropic, homogeneous turbulence, MRI turbulence is anisotropic with non-zero correlations between radial and azimuthal fields, resulting in sustained Maxwell and Reynolds stresses.

We have carried out vertical field simulation with $\beta = 10^6$ to compare with high β $B_\phi = B_z$ simulations. For an initial vertical field, the growth rate for the fastest growing mode is the same in MHD and kinetic regimes (see Figure 3.1). The parameters for these simulations are similar to the $B_\phi = B_z$ simulations; the volume and time averaged quantities are listed in Table 4.5. Although the growth rates for $B_\phi = B_z$ cases are larger than for a vertical field, Figure 4.13 shows that the saturation energies and stresses are $\approx$ 1-2 times larger for the vertical field cases. Similarly, MHD simulations show slightly larger stresses and energies for pure vertical field cases. Also, as in $B_\phi = B_z$ simulations, pure vertical field simulations show that the saturated magnetic energy is $\approx 3 - 5$ times smaller for the kinetic regime compared to MHD,

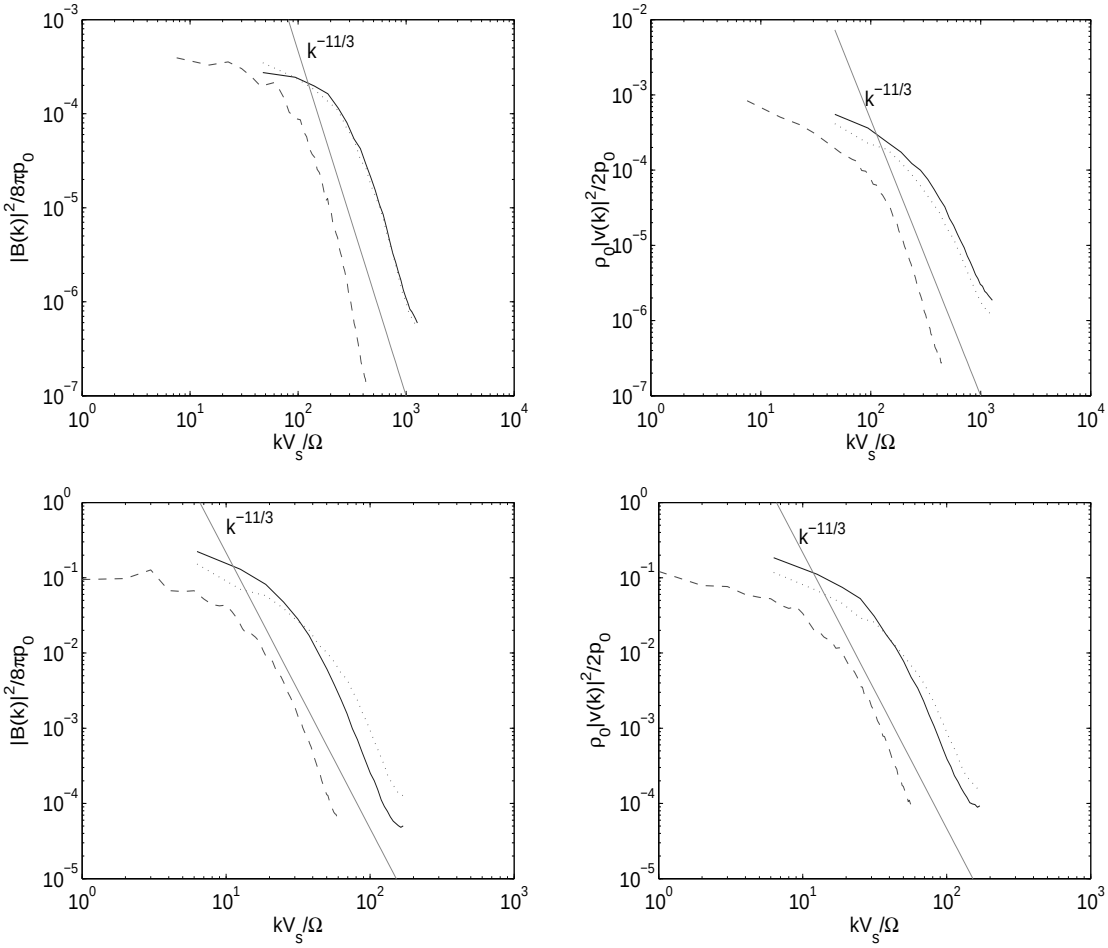

Figure 4.11: Turbulent magnetic ($|B(k)|^2/8\pi p_0$) and kinetic energy ($\rho_0|V(k)|^2/2p_0$) spectra for kinetic MHD: the $\beta = 10^6$ run $KYZh$ (top), and the $\beta = 400$ initial vertical field case (bottom, run $Zh4$ in [177]; see Table 4.1). Spectra with respect to k_x (solid line), k_y (dashed line) and k_z (dotted line) are shown. Also shown is the $k^{-11/3}$ Kolmogorov spectrum. The magnetic and kinetic energies for $KYZh$ are much smaller than for $Zh4$. For top figures, spectra with respect to k_y are steeper, because for $\beta = 10^6$ cases shear in velocity V_y dominates the fluctuations, causing the eddies to be elongated in the y- direction, with a steeper spectrum. The spectra are averaged in the other two directions in k- space; e.g., for a spectrum with respect to k_x, $|\mathbf{B}|^2(k_x) = \int dk_y dk_z \mathbf{B}(k_x, k_y, k_z)\mathbf{B}^*(k_x, k_y, k_z)$.

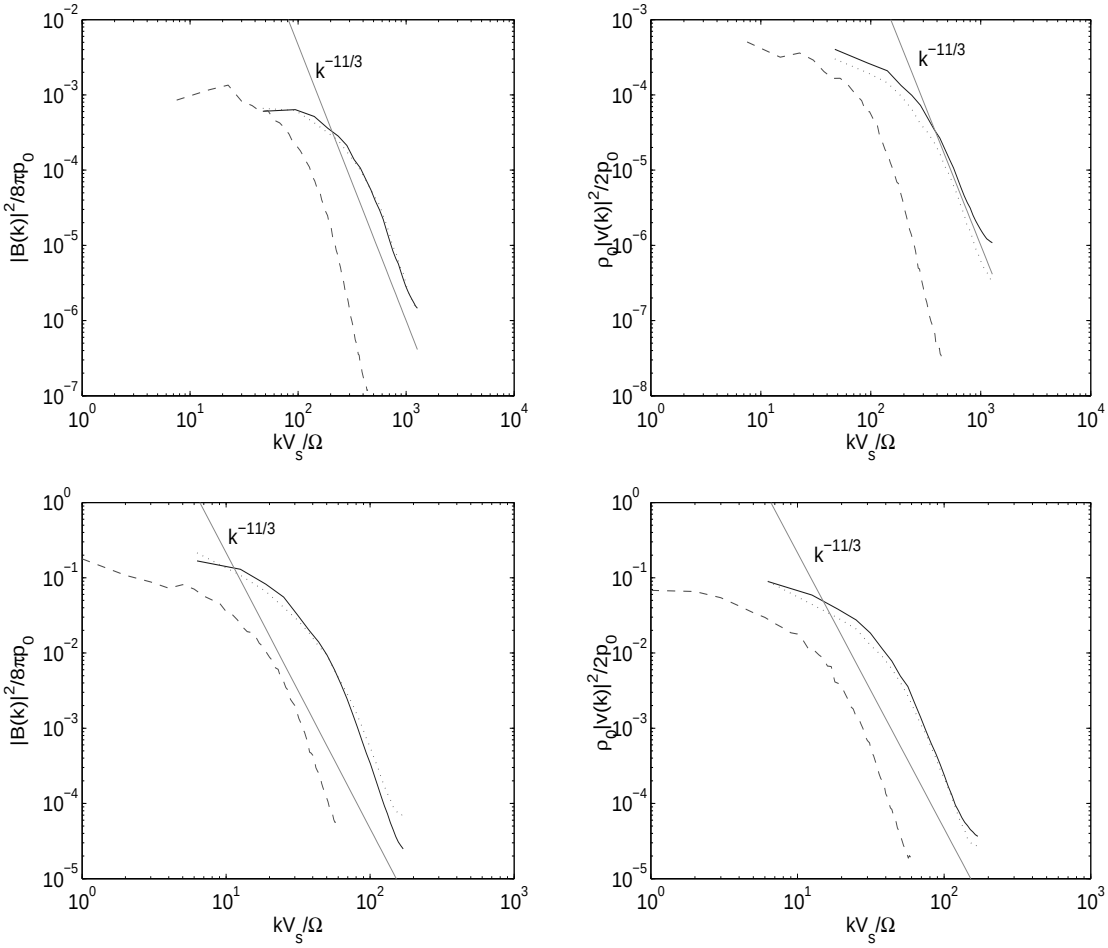

Figure 4.12: Turbulent magnetic ($|B(k)|^2/8\pi p_0$) and kinetic energy ($\rho_0|V(k)|^2/2p_0$) spectra for MHD: the $\beta = 10^6$ run $MYZh$ (top), and the $\beta = 400$ initial vertical field case (bottom, run ZMh in [177]; see Table 4.1). Spectra with respect to k_x (solid line), k_y (dashed line) and k_z (dotted line) are shown. Also shown is the $k^{-11/3}$ Kolmogorov spectrum. The magnetic and kinetic energies for $MYZh$ are much smaller than for MZh. For top figures, spectra with respect to k_y are steeper, because for $\beta = 10^6$ cases shear in velocity V_y dominates the fluctuations, causing the eddies to be elongated in the y- direction, with a steeper spectrum. The spectra are averaged in the other two directions in k- space; e.g., for a spectrum with respect to, $|\mathbf{B}|^2(k_x) = \int dk_y dk_z \mathbf{B}(k_x, k_y, k_z)\mathbf{B}^*(k_x, k_y, k_z)$.

whereas, the total stress (dominated by the anisotropic stress in the kinetic regime) is comparable. This demonstrates that $B_\phi = B_z$ simulations are not very different from the pure vertical field simulations in the kinetic regime. Although the magnetic energy in MHD regime is larger, anisotropic stress results in a comparable total stress in the kinetic and MHD regimes.

4.5.2 Runs with $\beta = 400$

We also carried runs with $\beta = 400$ to compare different field geometries. Figure 4.14 shows that kinetic and magnetic energies, and stresses are largest for the pure vertical field cases (similar to $\beta = 10^6$ simulations), followed by $B_\phi = B_z$, and azimuthal field cases, for both MHD and kinetic regime. Another point to be taken from Figure 4.14 is that in the kinetic regime, unlike MHD, the total stress is larger than the magnetic energy. For azimuthal field simulations in both kinetic and MHD regimes, the fluctuation energy is smaller than the energy in the shear flow; smaller fluctuations correspond to lower level of turbulence and transport. For $B_\phi = B_z$ simulations, the magnetic energy is ($\approx$ twice) larger in the MHD than in kinetic regime; reminiscent of $\beta = 10^6$ results where magnetic energy in MHD is even larger. Comparing simulations where the initial $\beta = 10^6$ with simulations where the initial $\beta = 400$ suggest that magnetic and kinetic energies and stresses increase as we reduce the initial β. This behavior is not fully understood but is similar to that observed in MHD simulations with a net flux (see Figure 8 in [87]). MHD simulations with no net flux result in a saturated β independent of the initial β [87, 167], we expect the same to be true in the kinetic regime.

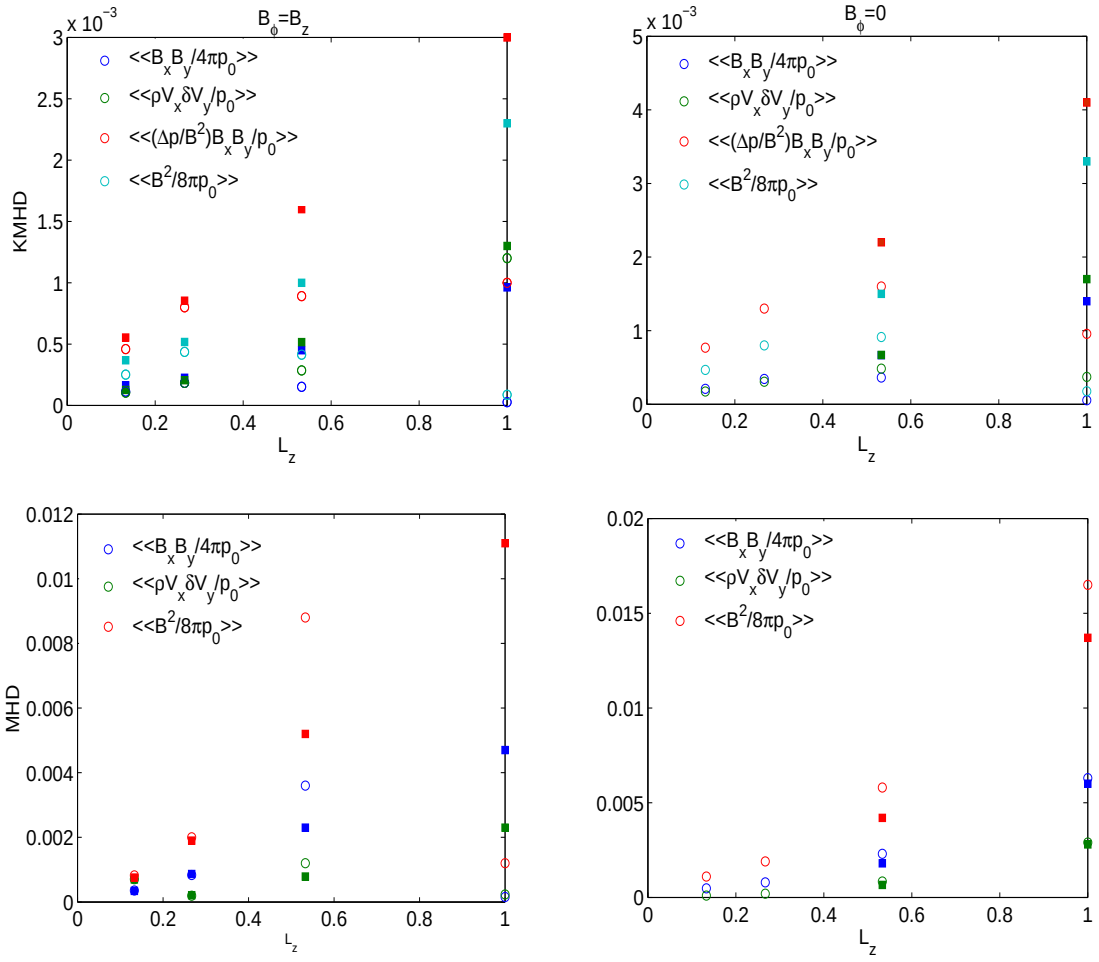

Figure 4.13: The top plots shows the Maxwell, Reynolds, and anisotropic stresses, and magnetic energy for $\beta = 10^6$ runs in the kinetic regime; the left one with $B_\phi = B_z$ and the right one with only B_z. The bottom plots show the Maxwell and Reynolds stresses, and magnetic energy for MHD runs; the left one with $B_\phi = B_z$ and the right one with only B_z. Open circles represent low resolution runs ($27 \times 59 \times 27$), while filled squares represent high resolution runs ($54 \times 118 \times 54$). The magnetic energy in the saturated state is $\approx 3 - 5$ times larger in the MHD regime, while the total stress is comparable in the two regimes. The stresses and magnetic energy increases with the box size, except for the low resolution kinetic and $B_\phi = B_z$ MHD runs with the vertical box size equal to the box height scale (runs labeled by '$8l$').

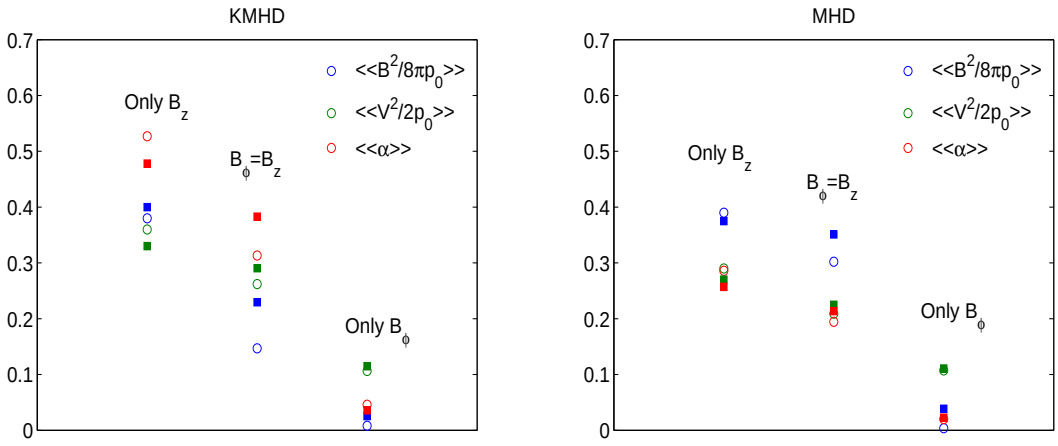

Figure 4.14: The magnetic and kinetic energies, and the total stress for kinetic (left) and MHD (right) simulations for $\beta = 10^6$. For both cases, energies and stresses are the largest for vertical field simulations, followed by the $B_\phi = B_z$ runs, and the pure azimuthal field runs. The total stress is $\approx$ twice larger for the kinetic runs, whereas the magnetic energy is comparable with MHD (smaller for the case of $B_\phi = B_z$). The kinetic and MHD simulations with an azimuthal field give similar results. The fluctuating kinetic energy is small compared to the energy in the velocity shear for azimuthal field simulations; this is the reason kinetic energy is larger than other quantities for azimuthal simulations.

4.6 Summary and Discussion

In this chapter we have described our local shearing box simulations of the magnetorotational instability in a collisionless plasma [177]. We are motivated by the application to hot radiatively inefficient flows which are believed to be present in many low-luminosity accreting systems (see Section 1.4). Our method for simulating the dynamics of a collisionless plasma is fluid-based, and relies on evolving a pressure tensor with closure models for the heat flux along magnetic field lines. These heat flux models can be thought of as approximating the collisionless (Landau) damping of linear modes in the simulation.

By adiabatic invariance, a slow increase (decrease) in the magnetic field strength tends to give rise to a pressure anisotropy with $p_\perp > p_\parallel$ ($p_\parallel > p_\perp$), where the sign of anisotropy is defined by the local magnetic field. Such a pressure anisotropy can, however, give rise to small scale kinetic instabilities (firehose, mirror, and ion cyclotron) which act to isotropize the pressure tensor, effectively providing an enhanced rate of pitch angle scattering ("collisions"). We have included the effects of this isotropization via a subgrid model which restricts the allowed magnitude of the pressure anisotropy (see Section 4.2.3).

We find that the nonlinear evolution of the MRI in a collisionless plasma is qualitatively similar to that in MHD, with comparable saturation magnetic field strengths and magnetic stresses. The primary new effect in kinetic theory is the existence of angular momentum transport due to the anisotropic pressure stress (Eq. 4.48). For the allowed pressure anisotropies estimated in Section 4.2.3, the anisotropic stress is dynamically important and is as large as the Maxwell stress (Table 4.1). The high β $B_\phi = B_z$ simulations, although showing the expected faster growth rate than in MHD, show a smaller magnetic energy (factor of ~ 5) in the kinetic regime, but the total stress is comparable to MHD. Although the MRI in kinetic and MHD regimes is different linearly (with the fastest growing mode in the kinetic regime twice faster

than in MHD), they are qualitatively similar in the nonlinear regime.

The precise rate of transport in the present simulations is difficult to quantify accurately and depends—at the factor of ~ 2 level—on some of the uncertain microphysics in our kinetic analysis (e.g., the rate of heat conduction along magnetic field lines and the exact threshold for pitch angle scattering by small-scale instabilities; see Figure 4.7). For better results, it would be interesting to extend these calculations with a more accurate evaluation of the actual nonlocal heat fluxes, Eqs. 4.11-4.12, or even to directly solve the drift kinetic equation, Eq. 4.5, for the particle distribution function. Further kinetic studies in the local shearing box, including studies of the small-scale instabilities that limit pressure anisotropy, would be helpful in developing appropriate fluid closures for global simulations.

It is interesting to note that two-temperature RIAFs can only be maintained below a critical luminosity $\sim \alpha^2 L_{\rm EDD}$ [163]. Thus enhanced transport in kinetic theory due to the anisotropic pressure stress would extend upward in luminosity the range of systems to which RIAFs could be applicable. This is important for understanding, e.g., state transitions in X-ray binaries [55].

In addition to angular momentum transport by anisotropic pressure stresses, Landau damping of long-wavelength modes can be important in heating collisionless accretion flows. Because the version of ZEUS MHD code we use is non-conservative, we cannot carry out a rigorous calculation of heating by different mechanisms such as Landau damping and reconnection. Following the total energy-conserving scheme of [194], however, we estimate that the energy dissipated by collisionless damping (present in the form of work done by anisotropic stress) is comparable to or larger than that due to numerical magnetic energy loss (which is the major source of heating in MHD simulations), which represents both energy lost due to reconnection and the energy cascading beyond the scales at the resolution limit. One caveat to studying energetics in a local shearing box is that in local simulations, the pressure increases

in time due to heating, while $B^2 \sim$ constant. Thus β increases in time and the turbulence becomes more and more incompressible. This will artificially decrease the importance of compressible channels of heating. Clearly it is of significant interest to better understand heating and energy dissipation in RIAFs, particularly for the electrons. The one fluid simulations provide some indications of electron heating in RIAFs; electrons will also be anisotropic because of magnetic energy fluctuations. The pressure anisotropy in electrons is also limited due to microinstabilities, e.g., the electron whistler instability considered by [68]. The heating rate of electrons due to anisotropic stress ($d \ln p/dt$) is comparable to that of ions because pressure anisotropy is comparable for electrons and ions. For RIAFs, it may mean that electrons cannot be kept too cool compared to the ion; but systematic 2-fluid simulations that account for all sources of heating are needed to draw firm conclusions.

In all of our calculations, we have assumed that the dominant source of pitch angle scattering is high frequency microinstabilities generated during the growth and nonlinear evolution of the MRI. We cannot, however, rule out that there are other sources of high frequency waves that pitch angle scatter and effectively decrease the mean free path of particles relative to that calculated here (e.g., shocks and reconnection). As shown in Table 4.3 and Figure 4.8, this would decrease the magnitude of the anisotropic stress; we find that for $\nu \gtrsim 30\,\Omega$, the results of our kinetic simulations quantitatively approach the MHD limit. In this context it is important to note that the incompressible part of the MHD cascade launched by the MRI is expected to be highly anisotropic with $k_\perp \gg k_\parallel$ [73]. As a result, there is very little power in high frequency waves that could break μ conservation. It is also interesting to note that satellites have observed that the pressure anisotropy in the solar wind near 1 AU is approximately marginally stable to the firehose instability [98], consistent with our assumption that microinstabilities dominate the isotropization of the plasma. There is evidence for pressure anisotropy in other collisionless plasmas, e.g., the solar wind

[123, 98] and magnetosphere [192, 66].

In this chapter we have focused on kinetic modifications to angular momentum transport via anisotropic pressure stresses and parallel heat conduction. In addition, kinetic effects substantially modify the stability of thermally stratified low collisionality plasmas such as those expected in RIAFs. Balbus [10] showed that in the presence of anisotropic heat conduction, thermally stratified plasmas are unstable when the temperature decreases outwards, rather than when the entropy decreases outwards (the usual Schwarzschild criterion). This has been called the magnetothermal instability (MTI). Parrish and Stone [148] show that in non-rotating atmospheres the MTI leads to magnetic field amplification and efficient heat transport. In future global simulations of RIAFs, it will be interesting to explore the combined dynamics of the MTI, the MRI, and angular momentum transport via anisotropic pressure stresses. Apart from affecting the local dynamics and energetics, collisionless effects can affect the global structure of hot, collisionless disks.

Table 4.1: Vertical field simulations with $\beta = 400$

Label	k_L^a	ξ^b	$\langle\langle \frac{B^2}{8\pi p_0} \rangle\rangle^c$	$\langle\langle \frac{V^2}{2p_0} \rangle\rangle$	$\langle\langle \frac{B_x B_y}{4\pi p_0} \rangle\rangle$	$\langle\langle \frac{\rho V_x \delta V_y}{p_0} \rangle\rangle$	$\langle\langle \frac{\Delta p^*}{B^2} \frac{B_x B_y}{p_0} \rangle\rangle$	$\langle\langle \frac{4\pi \Delta p}{B^2} \rangle\rangle$
$Zl1$	∞	∞	0.0026	0.094	0.0	0.0	0.0	-11.96
$Zl2$	∞	3.5	0.25	0.28	0.15	0.067	0.14	-0.96
$Zl3^\dagger$	$0.5/\delta z$	∞	–	–	–	–	–	–
$Zl4$	$0.5/\delta z$	3.5	0.38	0.36	0.23	0.097	0.20	-1.37
$Zl5$	$0.5/\delta z$	0.5	0.35	0.27	0.197	0.054	0.069	-0.02
$Zl6$	$0.25/\delta z$	3.5	0.27	0.30	0.16	0.070	0.15	-1.39
$Zl7$	$0.125/\delta z$	3.5	0.21	0.26	0.124	0.051	0.117	-1.44
$Zl8$	$0.5/\delta z$	3.5	0.157	0.315	0.094	0.069	0.225	-2.11
ZMl	–	–	0.39	0.29	0.22	0.066	–	–
$Zh1$	∞	∞	0.0026	0.095	0.0	0.0	0.0	-10.2
$Zh2$	∞	3.5	0.41	0.32	0.24	0.083	0.18	-1.09
$Zh3^\dagger$	$0.5/\delta z$	∞	–	–	–	–	–	–
$Zh4$	$0.5/\delta z$	3.5	0.40	0.33	0.22	0.078	0.18	-1.20
$Zh5$	$0.5/\delta z$	0.5	0.349	0.253	0.186	0.042	0.055	-0.02
$Zh6$	$0.25/\delta z$	3.5	0.24	0.26	0.13	0.044	0.13	-1.42
ZMh	–	–	0.375	0.27	0.204	0.0531	–	–

Vertical field simulation with initial $\beta = 400$. Z indicates that all simulations start with a vertical field, 'l', 'h' indicate low ($27 \times 59 \times 27$) and high ($54 \times 118 \times 54$) resolution runs respectively. $Zl4$ is the fiducial run. $Zl1$, $Zh1$ are the runs in CGL limit. ZMl andZMh are the MHD runs.

[a] Wavenumber parameter used in Landau closure for parallel heat conduction (Eqs. 4.13 and 4.14).

[b] Imposed limit on pressure anisotropy for pitch angle scattering due to mirror instability (Eq. 4.34). Excluding $Zl1$, $Zh1$, and $Zl8$ all of these calculations also use a pressure anisotropy limit due to the ion cyclotron instability (Eq. 4.35).

[c] $\langle\langle\rangle\rangle$ denotes a time and space average taken from 5 to 20 orbits.

[*] $\Delta p = (p_\parallel - p_\perp)$

[†] These cases run for only ≈ 4 orbits at which point the time step becomes very small because regions of large pressure anisotropy are created (see Section 4.4.4).

Table 4.2: Statistics for Model $Zl4$

Quantity f	$\langle\langle f\rangle\rangle$	$\langle\langle \delta f^2\rangle\rangle^{1/2}$	$(\frac{\tau_{int}}{T})^{1/2}\langle\langle \delta f^2\rangle\rangle^{1/2}$	$\min(f)$	$\max(f)$
$\frac{B_x^2}{8\pi p_0}$	0.083	0.092	0.016	0.021	0.662
$\frac{B_y^2}{8\pi p_0}$	0.276	0.318	0.048	0.036	1.987
$\frac{B_z^2}{8\pi p_0}$	0.021	0.017	0.0025	0.0032	0.144
$\frac{\rho V_x^2}{2p_0}$	0.102	0.094	0.014	0.0184	0.63
$\frac{\rho \delta V_y^2}{2p_0}$	0.125	0.079	0.0127	0.715	0.0264
$\frac{\rho V_z^2}{2p_0}$	0.037	0.034	0.0032	0.008	0.348
$\frac{-B_x B_y}{4\pi p_0}$	0.229	0.277	0.0434	0.037	1.856
$\frac{\rho V_x \delta V_y}{p_0}$	0.097	0.113	0.0147	-0.072	0.6211
$\frac{(p_\parallel - p_\perp)}{p_0}\frac{B_x B_y}{B^2}$	0.198	0.129	0.0178	0.017	0.654
$\frac{4\pi(p_\parallel - p_\perp)}{B^2}$	-1.366	0.51	0.098	-2.632	-0.083
$\frac{-B_x B_y}{(B^2/2)}$	0.5895	0.1043	0.0067	0.3744	0.8611
$\frac{\rho V_x \delta V_y}{(B^2/8\pi)}$	0.3323	0.2725	0.017	-0.5307	1.2704
$\frac{4\pi(p_\parallel - p_\perp)}{B^2}\frac{B_x B_y}{(B^2/2)}$	0.7356	0.3718	0.0714	0.032	1.807
$\frac{W_{xy}}{(B^2/8\pi)}$	1.6574	0.6598	0.084	0.4364	3.7159
$\frac{\alpha_R}{\alpha_M}$	0.5357	0.3975	0.024	-0.9105	2.084
$\frac{\alpha_A}{\alpha_M}$	1.2287	0.5504	0.119	0.0854	2.7243
$\frac{\rho}{\rho_0}$	0.99935	2.3×10^{-5}	1.1×10^{-5}	0.9993	0.9994
$\frac{p_\perp B_0}{B p_0}$	3.557	1.665	$-^a$	1.1178	7.929
$\frac{p_\parallel B^2 \rho_0^2}{\rho^2 B_0^2 p_0}$	3.144×10^3	3.49×10^3	$-$	585.4	1.993×10^4

[a] We calculate the error using the autocorrelation time only for quantities that saturate to a steady state after 5 orbits. Estimate for correlation time τ_{int} is based on the discussion in [144]. $p_\perp$ and $p_\parallel$ show a secular growth with time, so this way of expressing them as an average and an error is not applicable.

Table 4.3: Simulations with an explicit collision term

ν/Ω	$\langle\langle 4\pi\Delta p/B^2\rangle\rangle$	$\langle\langle -\frac{B_x B_y}{4\pi p_0}\rangle\rangle$	$\langle\langle \frac{\rho V_x \delta V_y}{p_0}\rangle\rangle$	$\langle\langle \frac{\Delta p^*}{B^2}\frac{B_x B_y}{p_0}\rangle\rangle$	α_A/α_M	$\alpha_A/\alpha_A(\nu=0)$
0	-1.41	0.18	0.082	0.196	1.09	1
1	-1.47	0.152	0.072	0.173	1.14	0.88
3	-1.43	0.178	0.08	0.181	1.02	0.92
10	-1.35	0.165	0.071	0.159	0.96	0.81
20	-1.24	0.174	0.070	0.136	0.78	0.69
30	-1.01	0.213	0.070	0.113	0.53	0.58
40	-0.87	0.239	0.070	0.095	0.4	0.48
100	-0.43	0.223	0.06	0.032	0.14	0.16

* $\Delta p = (p_\parallel - p_\perp)$

Table 4.4: $B_\phi = B_z$, $\beta = 10^6$ simulations

Label	L_x	L_y	L_z	$\langle\langle \frac{B^2}{8\pi p_0} \rangle\rangle$	$\langle\langle \frac{V^2}{2p_0} \rangle\rangle$	$\langle\langle \frac{B_x B_y}{4\pi p_0} \rangle\rangle$	$\langle\langle \frac{\rho V_x \delta V_y}{p_0} \rangle\rangle$	$\langle\langle \frac{\Delta p^*}{B^2} \frac{B_x B_y}{p_0} \rangle\rangle$	$\langle\langle \alpha \rangle\rangle$
$KYZl$	0.133	0.837	0.133	2.51×10^{-4}	0.0021	1.12×10^{-4}	1.04×10^{-4}	4.59×10^{-4}	7.75×10^{-4}
$KYZlin$	0.133	0.837	0.133	2.84×10^{-4}	0.0021	1.24×10^{-4}	1.11×10^{-4}	5.00×10^{-4}	7.34×10^{-4}
$KYZh$	0.133	0.837	0.133	3.68×10^{-4}	0.0021	1.63×10^{-4}	1.26×10^{-4}	5.53×10^{-4}	8.42×10^{-4}
$KYZ2l$	0.267	1.675	0.267	4.36×10^{-4}	0.0073	1.84×10^{-4}	1.84×10^{-4}	8.00×10^{-4}	0.0012
$KYZ2h$	0.267	1.675	0.267	5.17×10^{-4}	0.0074	2.25×10^{-4}	2.05×10^{-4}	8.54×10^{-4}	0.0013
$KYZ4l$	0.533	3.350	0.533	4.14×10^{-4}	0.0273	1.52×10^{-4}	2.85×10^{-4}	8.91×10^{-4}	0.0013
$KYZ4h$	0.533	3.350	0.533	0.001	0.0277	4.5×10^{-4}	5.16×10^{-4}	0.0016	0.0026
$KYZ8l$	1.0	6.283	1.0	8.63×10^{-5}	0.1024	2.63×10^{-5}	0.0012	0.0010	0.0022
$KYZ8h$	1.0	6.283	1.0	0.0023	0.0948	9.62×10^{-4}	0.0013	0.0030	0.0053
$MYZl$	0.133	0.837	0.133	8.21×10^{-4}	0.0019	3.56×10^{-4}	7.05×10^{-4}	–	0.0011
$MYZlin$	0.133	0.837	0.133	1.40×10^{-5}	0.0015	2.66×10^{-6}	1.69×10^{-6}	–	4.35×10^{-6}
$MYZh$	0.133	0.837	0.133	7.57×10^{-4}	0.0019	3.43×10^{-4}	6.96×10^{-5}	–	0.0010
$MYZ2l$	0.267	1.675	0.267	0.0020	0.0071	8.35×10^{-4}	1.96×10^{-4}	–	0.0010
$MYZ2h$	0.267	1.675	0.267	0.0019	0.0072	8.68×10^{-4}	2.10×10^{-4}	–	0.0011
$MYZ4l$	0.533	3.350	0.533	0.0088	0.0297	0.0036	0.0012	–	0.0048
$MYZ4h$	0.533	3.350	0.533	0.0052	0.0282	0.0023	7.88×10^{-4}	–	0.0031
$MYZ8l$	1.0	6.283	1.0	0.0012	0.0959	1.56×10^{-4}	2.32×10^{-4}	–	3.88×10^{-4}
$MYZ8h$	1.0	6.283	1.0	0.0111	0.0967	0.0047	0.0023	–	0.007

'YZ' represents both Y an Z fields. 'l' and 'h' stand for low ($27 \times 59 \times 27$) and high resolution ($54 \times 118 \times 54$) runs. 'lin' stands for an initial linear eigenmode with $k_z = 8\pi/L_z$. 'K' and 'M' stand for kinetic and MHD respectively.

*$\Delta p = (p_\parallel - p_\perp)$

Table 4.5: Only B_z, $\beta = 10^6$ simulations

Label	L_x	L_y	L_z	$\langle\langle\frac{B^2}{8\pi p_0}\rangle\rangle$	$\langle\langle\frac{V^2}{2p_0}\rangle\rangle$	$\langle\langle\frac{B_xB_y}{4\pi p_0}\rangle\rangle$	$\langle\langle\frac{\rho V_x\delta V_y}{p_0}\rangle\rangle$	$\langle\langle\frac{\Delta p^*}{B^2}\frac{B_xB_y}{p_0}\rangle\rangle$	$\langle\langle\alpha\rangle\rangle$
KZl	0.133	0.837	0.133	4.66×10^{-4}	0.0023	2.09×10^{-4}	1.74×10^{-4}	7.68×10^{-4}	0.0012
$KZ2l$	0.267	1.675	0.267	7.99×10^{-4}	0.0077	3.45×10^{-4}	3.07×10^{-4}	0.0013	0.0019
$KZ4l$	0.533	3.350	0.533	9.14×10^{-4}	0.0278	3.63×10^{-4}	4.84×10^{-4}	0.0016	0.0024
$KZ4h$	0.533	3.350	0.533	0.0015	0.0282	6.66×10^{-4}	6.71×10^{-4}	0.0022	0.0035
$KZ8l$	1.0	6.283	1.0	1.77×10^{-4}	0.0992	5.35×10^{-5}	3.72×10^{-4}	9.57×10^{-4}	0.0014
$KZ8h$	1.0	6.283	1.0	0.0033	0.0946	0.0014	0.0017	0.0041	0.0072
MZl	0.133	0.837	0.133	0.0011	0.0020	4.79×10^{-4}	9.41×10^{-5}	–	5.73×10^{-4}
$MZ2l$	0.267	1.675	0.267	0.0019	0.0072	7.93×10^{-4}	1.96×10^{-4}	–	9.89×10^{-4}
$MZ4l$	0.533	3.350	0.533	0.0058	0.0283	0.0023	8.44×10^{-4}	–	0.0031
$MZ4h$	0.533	3.350	0.533	0.0042	0.0276	0.0018	6.59×10^{-4}	–	0.0025
$MZ8l$	1.0	6.283	1.0	0.0165	0.0978	0.0063	0.0029	–	0.0092
$MZ8h$	1.0	6.283	1.0	0.0137	0.0986	0.006	0.0028	–	0.0089

'Z' represents a vertical field. 'l' and 'h' stand for low ($27\times59\times27$) and high resolution ($54\times118\times54$) runs. 'K' and 'M' stand for kinetic and MHD respectively.

$^*\Delta p = (p_\parallel - p_\perp)$

Table 4.6: $\beta = 400$ simulations with different field orientations

Label	L_x	L_y	L_z	$\langle\langle \frac{B^2}{8\pi p_0} \rangle\rangle$	$\langle\langle \frac{V^2}{2p_0} \rangle\rangle$	$\langle\langle \frac{B_x B_y}{4\pi p_0} \rangle\rangle$	$\langle\langle \frac{\rho V_x \delta V_y}{p_0} \rangle\rangle$	$\langle\langle \frac{\Delta p^*}{B^2} \frac{B_x B_y}{p_0} \rangle\rangle$	$\langle\langle \alpha \rangle\rangle$
$Zl4^\dagger$	1.0	6.283	1.0	0.38	0.36	0.23	0.097	0.20	0.527
$KYZl400$	1.0	6.283	1.0	0.147	0.262	0.0838	0.0537	0.1757	0.3132
$KYl400$	1.0	6.283	1.0	0.008	0.1063	0.032	0.0032	0.0106	0.0169
$Zh4^\dagger$	1.0	6.283	1.0	0.40	0.33	0.22	0.078	0.18	0.478
$KYZh400$	1.0	6.283	1.0	0.2294	0.2904	0.1211	0.0571	0.2046	0.3828
$KYh400$	1.0	6.283	1.0	0.0253	0.1148	0.0108	0.0067	0.0183	0.0358
$MZl^\dagger$	1.0	6.283	1.0	0.39	0.29	0.22	0.066	–	0.286
$MYZl400$	1.0	6.283	1.0	0.302	0.209	0.1595	0.0350	–	0.1945
$MYl400$	1.0	6.283	1.0	0.0372	0.1073	0.015	0.0051	–	0.0201
$MZh^\dagger$	1.0	6.283	1.0	0.375	0.27	0.204	0.0531	–	0.257
$MYZh400$	1.0	6.283	1.0	0.351	0.225	0.1793	0.0342	–	0.2135
$MYh400$	1.0	6.283	1.0	0.0385	0.1107	0.017	0.0057	–	0.0227

'Z' and Y represent vertical and azimuthal initial field. 'l' and 'h' stand for low and high resolution runs. 'K' and 'M' stand for kinetic and MHD respectively.

† These runs are from [177]; see Table 4.1

$^*\Delta p = (p_\parallel - p_\perp)$

Chapter 5

Anisotropic conduction with large temperature gradients

A natural step, after local studies of the MRI in the collisionless regime, is to investigate the effects of collisionless plasma processes on the global structure of collisionless disks in radiatively inefficient accretion flows (RIAFs). Instead of including both anisotropic pressure and anisotropic conduction, as in the local studies described in Chapters 3 and 4, we began by looking at just the effects of anisotropic thermal conduction. Anisotropic conduction is important for global disk structure because an anisotropically conducting plasma is convectively stable if the temperature increases outwards ($dT/dr \geq 0$; see [16, 10]). Whereas, convective stability in collisional fluids require the entropy ($s = p/\rho^{\gamma}$) to increase outwards. Local, 2-D, vertically stratified MHD simulations of Parrish and Stone [148] have confirmed that the convective instability in plasma with anisotropic thermal conduction, christened the magnetothermal instability (MTI), is driven by temperature gradients. If convection is important, as in hydrodynamic disks [189, 160], anisotropic conduction can modify the global structure (and hence the luminosity) of RIAFs.

Our aim was to include anisotropic thermal conduction in global, 2-D MHD sim-

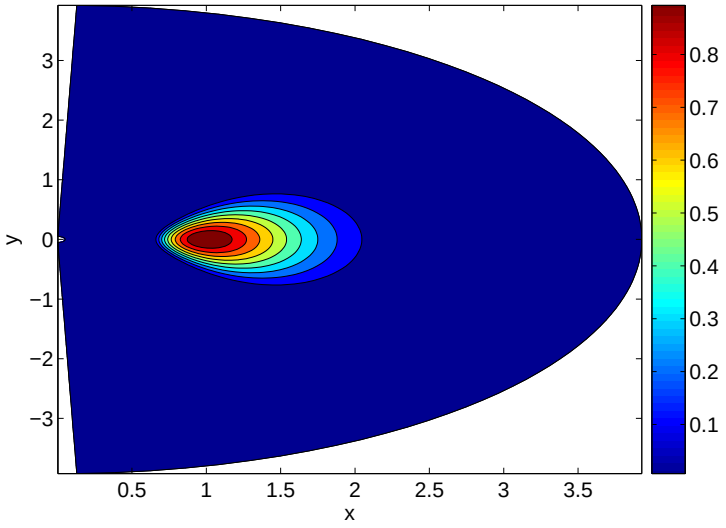

Figure 5.1: The initial density for a typical global MHD disk simulation (e.g., [188, 83]). A high density, constant angular momentum torus is surrounded by a non-rotating, low density corona. Temperature (and density) jumps by ~ 100 at the torus-corona interface. Magnetic field vanishes in the corona, while it is along the density contours in the torus ($\beta \sim 100$).

ulations of RIAFs, and to see if the structure of turbulent, quasi-steady disk changes. We began by adding an anisotropic conduction routine, based on centered differencing, to the global ZEUS MHD code used by Stone and Pringle [188]. The initial condition for most global MHD disk simulations [83, 188] is a constant angular momentum, high density torus surrounded by a low density, non-rotating corona (see Figure 5.1 for a typical example). Pressure balance at the torus-corona interface requires a big jump in temperature across it (ratio of temperatures = inverse ratio of densities ~ 100).

The implementation of anisotropic thermal conduction in presence of large temperature gradients was far from trivial. The simulations with anisotropic conduction and MHD-disk initial conditions (with a large temperature gradient; see Figure 5.1) did not run for long, eventually becoming numerically unstable, even though we were using a Courant stable time step. We found that, unlike isotropic conduc-

tion, the centered differencing of anisotropic conduction allowed for heat to flow from higher to lower temperatures. The heat flow in the "wrong" direction can lead to negative temperatures in regions with large temperature gradients. An implementation of anisotropic thermal conduction that does not give rise to negative temperatures required considerable time and effort. Thus, global MHD disk simulations with anisotropic thermal conduction have been left for the future.

Anisotropic diffusion, in which the rate of diffusion of some quantity is faster in some directions than others, occurs in many different physical systems and applications. Examples include diffusion in geological formations, thermal properties of structural materials and crystals, image processing [41, 136], biological systems, and plasma physics. Diffusion Tensor Magnetic Resonance Imaging makes use of anisotropic diffusion to distinguish different types of tissue as a medical diagnostic [19]. In plasma physics, the collision operator gives rise to anisotropic diffusion in velocity space, as does the quasilinear operator describing the interaction of particles with waves [182]. In magnetized plasmas, thermal conduction can be much more rapid along a field line than across it; this will be the main application in mind for this chapter.

In this chapter we show that anisotropic thermal conduction based on centered differences is not always consistent with the second law of thermodynamics. Test problems that result in negative temperature with centered "asymmetric" and "symmetric" differencing are presented. This happens because heat can flow from lower to higher temperature in regions with large temperature gradient. Temperature gradients in anisotropic heat fluxes need to be limited to ensure that temperature extrema are not accentuated. We tried several different approaches, and eventually developed slope-limited methods that successfully avoid the negative temperature problem, by using limiters analogous to those used in numerical solution of hyperbolic equations [116]. Perpendicular numerical diffusion ($\chi_{\perp,num}$) scales as $\sim \chi_{\parallel}\Delta x^2$ in case of the

least diffusive slope limited schemes. The limited methods are more diffusive than the "symmetric" method, but comparable to the "asymmetric" method. Also, like the "asymmetric" method, the limited methods lack the desirable property of "symmetric" method that the perpendicular numerical diffusion ($\chi_{\perp,num}$) is independent of the parallel conduction $\chi_{\parallel}$. The main advantage of slope limited methods is that they do not give rise to negative temperatures in presence of large temperature gradients. Thus, limited methods will be useful to simulate hot, dilute astrophysical plasmas where conduction is anisotropic and temperature gradients are enormous, e.g., disk-corona boundary, energetic reconnection events, and collisionless shocks.

5.1 Introduction

When the plasma collision frequency, ν ($\propto nT^{-3/2}$, n is the number density and T is the temperature), is small compared to the cyclotron frequency $\Omega_c = qB/mc$, key transport quantities like stress and thermal conduction become anisotropic with respect to the magnetic field direction (the ratio of parallel to perpendicular transport coefficients is $\sim (\Omega_c/\nu)^2$); heat and momentum transport parallel to the field is much larger than in the cross-field direction [37]. In a plasma with comparable electron and proton temperatures, heat transport is dominated by electrons, which are faster than ions by the ratio $\sqrt{m_i/m_e}$, and momentum transport is dominated by the protons. Anisotropic plasmas are abundant in nature (e.g., solar corona, solar wind, magnetosphere, and radiatively inefficient accretion flows) as well as high temperature laboratory devices like tokamaks. In order to simulate dilute, anisotropic plasmas, accurate and robust numerical methods are needed.

Numerical methods based on finite differences [76] and higher order finite elements [181] have been useful in simulating highly anisotropic conduction ($\chi_{\parallel}/\chi_{\perp} \sim 10^9$, where $\chi_{\parallel}$ and $\chi_{\perp}$ are parallel and perpendicular conduction coefficients) in lab-

oratory plasmas. "Symmetric" differencing introduced in [76] is particularly simple and has some desirable properties—perpendicular numerical diffusion independent of $\chi_\parallel$, and self adjointness of the numerical heat flux operator. The scheme based on asymmetric centered differences, with components of the heat flux vector located at the cell faces, have been used to study convection in anisotropically conducting plasmas [148] and for local simulations of collisionless accretion disks [177]. Anisotropic thermal conduction plays a crucial role in the convective stability of dilute plasmas; Parrish and Stone [148] have confirmed the prediction that convection in stratified anisotropic plasmas is governed, not by the entropy gradient (the classic Schwarzchild criterion, $ds/dr > 0$ for convective stability of fluids), but by the temperature gradient ($dT/dr > 0$ for convective stability of plasmas with anisotropic conduction; see [10, 11]).

An important fact that has not been discussed before (to our knowledge) is that the methods based on centered differences can give rise to heat fluxes inconsistent with the second law of thermodynamics, i.e., heat can flow from lower to higher temperatures! Temperature extrema can be accentuated unphysically, and negative temperatures can arise if centered differencing is used. We show, using simple numerical test problems, that both symmetric and asymmetric centered methods can give rise to negative temperatures at some grid points. Negative temperature results in numerical instability because the sound speed becomes imaginary.

We show that the symmetric and asymmetric methods can be modified so that the temperature extrema are not accentuated. The components of anisotropic heat flux, e.g., q_x, consist of two contributions: the normal term, $q_{xx} = -n\chi b_x^2 \partial T/\partial x$, and the transverse term, $q_{xy} = -n\chi b_x b_y \partial T/\partial y$. The normal term for the asymmetric method, like isotropic conduction, is from higher to lower temperatures, but the transverse term can be of any sign. The transverse term needs to be "limited" to ensure that temperature extrema are not accentuated. We use slope limiters, analogous

to those used in second order methods for hyperbolic problems [196, 116], to limit the transverse heat fluxes. However, for the symmetric method where primary heat fluxes are located at cell corners, $q_{xx,i+1/2,j}$ need not be the same sign as $\partial T/\partial x|_{i+1/2,j}$. Thus, both the normal and transverse terms have to be limited for the symmetric method. Methods based on the entropy-like function ($\dot{s}^* \equiv -\mathbf{q} \cdot \nabla T \geq 0$; see Appendix E to see how this is different from the entropy function), which limit the transverse component of the heat flux, are also discussed.

Limiting introduces numerical diffusion in the perpendicular direction, and the desirable property of the symmetric method that perpendicular pollution is independent of $\chi_\parallel$ no longer holds. The ratio of perpendicular numerical diffusion and the physical parallel conductivity with a Monotonized Central (MC; see [116] for discussion of slope limiters) limiter is $\chi_{\perp,num}/\chi_\parallel \sim 10^{-3}$ for a modest number of grid points ($\sim$ 100 in each direction). This clearly is not adequate for simulating laboratory plasmas which require $\chi_\parallel/\chi_\perp \sim 10^9$, as perpendicular numerical diffusion will swamp the true perpendicular diffusion. For laboratory plasmas, the temperature profile is relatively smooth and the negative temperature problem does not arise, so symmetric differencing [76] or higher order finite elements [181] will be adequate.

However, astrophysical plasmas can have sharp gradients in temperature (e.g., the transition region of the sun separating the hot corona and the much cooler chromosphere, the disk-corona interface in accretion flows), and centered differencing can give rise to negative temperatures. Thus, symmetric and asymmetric centered methods cannot be used (the sound speed becomes imaginary with negative temperature and can give rise to spurious instabilities). The slope limited methods will introduce somewhat larger perpendicular numerical diffusion ($\chi_{\perp,num}/\chi_\parallel \sim 10^{-3}$) but will always ensure the correct direction of heat fluxes, and hence the positivity of the temperature. Even a modest anisotropy in conduction ($\chi_\parallel/\chi_\perp \sim 10^3$) should be useful to study the qualitatively new effects of anisotropic conduction on dilute as-

trophysical plasmas, but the positivity condition on temperature is a must for robust numerical simulations (ruling out the use of centered differencing for plasmas with large temperature gradients). Figure 3 in [148] shows that the linear growth rate of the magnetothermal instability (the convective instability of stratified anisotropic plasmas discussed in [16, 10]) is not much different for $\chi_\perp/\chi_\parallel \to 0$ and $\chi_\perp/\chi_\parallel \lesssim 0.1$, and a numerical method that gives rise to slightly larger (compared to the symmetric method, but still $\chi_{\perp,num}/\chi_\parallel < 0.1$) pollution of perpendicular conduction looks acceptable. We have tested our slope-limited methods on the magnetothermal instability and get results similar to [148], both linearly and nonlinearly.

The chapter is organized as follows. We begin with the equation for anisotropic conduction and its numerical implementation using asymmetric and symmetric centered differencing. We present simple 2-D test problems for which asymmetric and symmetric centered differencing give rise to negative temperatures. The slope limited methods for anisotropic heat conduction are introduced, followed by the limiting of the symmetric method based on the entropy-like condition. We discuss some mathematical properties of the slope limited methods. We present further test problems comparing different methods and study their convergence properties. In the end we conclude and discuss the applications of the methods that we have developed.

5.2 Anisotropic thermal conduction

Anisotropic thermal conduction can be important in a magnetized plasmas if the mean free path (much larger than the gyroradius) is comparable to the dynamical length scales. In such cases, a divergence of anisotropic heat flux has to be added to the energy equation. Such a term can modify the characteristic structure of the MHD equations and can be evolved separately by using operator splitting, as done in [148]. In operator splitting, MHD evolution operator and anisotropic thermal conduction

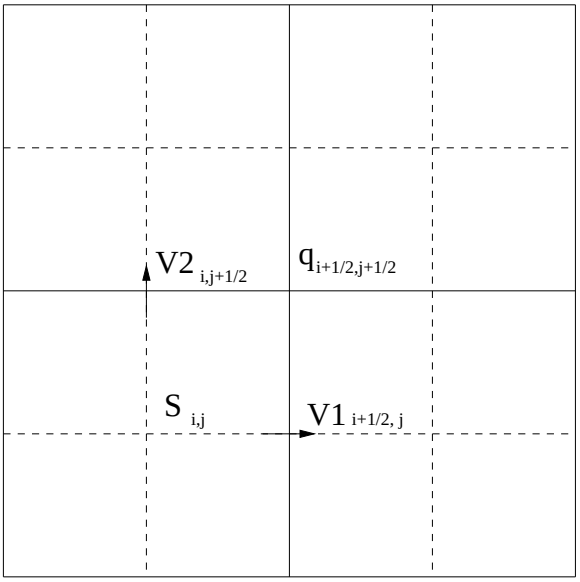

Figure 5.2: A staggered grid with scalars $S_{i,j}$ (such as n, e, and T) located at cell centers. The components of vectors, e.g., $\hat{\mathbf{b}}$ and $\mathbf{q}$ are located at cell faces. However, for the symmetric centered scheme the primary heat fluxes are located at cell corners [76], and the face centered flux is obtained by interpolation.

are applied alternately, and their numerical implementations are independent. The equation for the evolution of internal energy due to anisotropic conduction is

$$\frac{\partial e}{\partial t} = -\nabla \cdot \mathbf{q}, \tag{5.1}$$

$$\mathbf{q} = -\hat{\mathbf{b}} n(\chi_{\parallel} - \chi_{\perp})\nabla_{\parallel} T - n\chi_{\perp}\nabla T \tag{5.2}$$

where e is the internal energy per unit volume, $\mathbf{q}$ is the heat flux, $\chi_{\parallel}$ and $\chi_{\perp}$ are the coefficients of parallel and perpendicular conduction with respect to the local field direction (with dimensions L^2T^{-1}), n is the number density, $T = (\gamma - 1)e/n$ is the temperature, $\gamma = 5/3$ is the ratio of the specific heats for an ideal gas, $\hat{\mathbf{b}}$ is the unit vector along the field line, and $\nabla_{\parallel} = \hat{\mathbf{b}} \cdot \nabla$ represents the derivative along the direction of the magnetic field. In the test problems that we present, $\gamma = 2$ is chosen to avoid factors of 2/3 and 5/3; qualitative features are independent of γ.

On a staggered grid, scalars like n, e, and T are located at the cell centers whereas

the components of vectors like $\hat{\mathbf{b}}$ and $\mathbf{q}$ are located at cell faces, as shown in Figure 5.2. The face centered components of vectors naturally represent the flux of scalars out of a cell. Notice however, as we describe later, that in Günter et al.'s symmetric method [76], primary heat fluxes are located at cell corners which are averaged to get the face centered heat fluxes.

All the schemes presented here are conservative and fully explicit. It should be possible to take longer time steps with an implicit generalization of these schemes, but the construction of a fast implicit scheme for anisotropic conduction is non-trivial. In two dimensions the internal energy density is updated as follows,

$$e_{i,j}^{n+1} = e_{i,j}^{n} - \Delta t \left[\frac{q_{x,i+1/2,j}^{n} - q_{x,i-1/2,j}^{n}}{\Delta x} + \frac{q_{y,i,j+1/2}^{n} - q_{y,i,j-1/2}^{n}}{\Delta y} \right], \tag{5.3}$$

where the time step, Δt, satisfies the stability condition (ignoring density variations)

$$\Delta t \leq \frac{\min[\Delta x^2, \Delta y^2]}{4(\chi_{\parallel} + \chi_{\perp})}, \tag{5.4}$$

Δx and Δy are grid sizes in the two directions. The generalization to three dimensions is straightforward.

The methods we discuss differ in the way heat fluxes are calculated at the faces. In rest of the section we discuss the methods based on asymmetric and symmetric centered differencing, as discussed in [76]. The asymmetric method was used by [148] and [177] for simulations of hot, dilute, anisotropic astrophysical plasmas. We show in Section 5.3 that both symmetric and asymmetric methods can give rise to negative temperatures in regions with large temperature gradients. From here on χ will represent parallel conduction coefficient in cases where an explicit perpendicular diffusion is not considered (i.e., the only perpendicular diffusion is due to numerical effects).

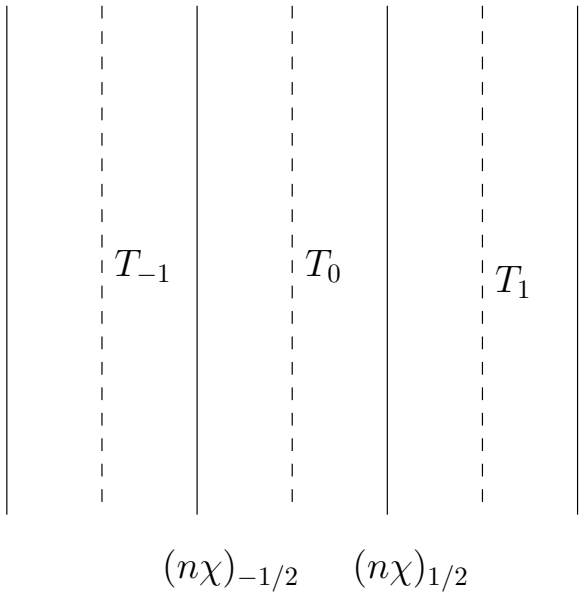

Figure 5.3: This figure provides a motivation for using a harmonic average for $\overline{n\chi}$. Consider a 1-D case with the temperatures and $n\chi$'s as shown in the figure. Given T_{-1} and T_1 and the $n\chi$'s at the faces, we want to calculate an average $\overline{n\chi}$ between cells -1 and 1. Assumption of a constant heat flux gives, $q_{-1/2} = q_{1/2} = \overline{q}$, i.e., $-(n\chi)_{-1/2}(T_0 - T_{-1})/\Delta x = -(n\chi)_{1/2}(T_1 - T_0)/\Delta x = -\overline{n\chi}(T_1 - T_{-1})/2\Delta x$. This immediately gives a harmonic mean, which is weighted towards the smaller of the two arguments, for the interpolation $\overline{n\chi}$.

5.2.1 Centered asymmetric scheme

The heat flux in the x- direction (in 2-D), using the asymmetric method is given by

$$q_{x,i+1/2,j} = -\overline{n\chi} b_x \left[b_x \frac{\partial T}{\partial x} + \overline{b_y} \overline{\frac{\partial T}{\partial y}} \right], \tag{5.5}$$

where overline represents the variables interpolated to the face at $(i + 1/2, j)$. The variables without an overline are naturally located at the face. The interpolated quantities at the face are given by simple arithmetic averaging,

$$\overline{b_y} = (b_{y,i,j-1/2} + b_{y,i+1,j-1/2} + b_{y,i,j+1/2} + b_{y,i+1,j+1/2})/4, \tag{5.6}$$

$$\overline{\partial T/\partial y} = (T_{i,j+1} + T_{i+1,j+1} - T_{i,j-1} - T_{i+1,j-1})/4\Delta y. \tag{5.7}$$

We use a harmonic mean to interpolate the product of number density and conductivity,

$$\frac{2}{\overline{n\chi}} = \frac{1}{(n\chi)_{i,j}} + \frac{1}{(n\chi)_{i+1,j}}; \tag{5.8}$$

this is second order accurate for smooth regions, but $\overline{n\chi}$ becomes proportional to the minimum of the two $n\chi$'s on either side of the face when the two differ significantly. Figure 5.3 gives the motivation for the use of a harmonic average. Harmonic averaging is also necessary for the method to be stable with the present time step given in Eq. 5.4. Instead, if we use a simple mean, the stable time step condition becomes severe by a factor $\sim \max[n_{i+1,j}, n_{i,j}]/2\min[n_{i+1,j}, n_{i,j}]$, which can result in unacceptably small time steps for initial conditions with large density contrast. Physically, this is because the heat capacity is very small in a low density region, so a small amount of heat flow into that region causes very fast changes in the temperature.

Analogous expressions can be written for the heat fluxes in other directions. This method is used in astrophysical MHD simulations of [148] and [177], who include anisotropic conduction in a cartesian geometry.

5.2.2 Centered symmetric scheme

The notion of symmetric differencing was introduced in [76], where primary heat fluxes are located at the cell corners, with

$$q_{x,i+1/2,j+1/2} = -\overline{n\chi}\,\overline{b_x}\left[\overline{b_x}\overline{\frac{\partial T}{\partial x}} + \overline{b_y}\overline{\frac{\partial T}{\partial y}}\right], \tag{5.9}$$

where overline represents the interpolation of variables at the corner given by a simple arithmetic average

$$\overline{b_x} = (b_{x,i+1/2,j} + b_{x,i+1/2,j+1})/2, \tag{5.10}$$

$$\overline{b_y} = (b_{y,i,j+1/2} + b_{y,i+1,j+1/2})/2, \tag{5.11}$$

$$\overline{\partial T/\partial x} = (T_{i+1,j} + T_{i+1,j+1} - T_{i,j} - T_{i,j+1})/2\Delta x, \tag{5.12}$$

$$\overline{\partial T/\partial y} = (T_{i,j+1} + T_{i+1,j+1} - T_{i,j} - T_{i+1,j})/2\Delta y. \tag{5.13}$$

As before (and for the same reasons), a harmonic average is used for the number density

$$\frac{4}{\overline{n\chi}} = \frac{1}{(n\chi)_{i,j}} + \frac{1}{(n\chi)_{i+1,j}} + \frac{1}{(n\chi)_{i,j+1}} + \frac{1}{(n\chi)_{i+1,j+1}}. \tag{5.14}$$

This is different from [76] who use an arithmetic average for n and χ. Analogous expression can be written for $q_{y,i+1/2,j+1/2}$.

The heat fluxes located at the cell faces, $q_{x,i+1/2,j}$ and $q_{y,i,j+1/2}$, to be used in Eq. (5.3) are given by an arithmetic average,

$$q_{x,i+1/2,j} = (q_{x,i+1/2,j+1/2} + q_{x,i+1/2,j-1/2})/2, \tag{5.15}$$

$$q_{y,i,j+1/2} = (q_{y,i+1/2,j+1/2} + q_{y,i-1/2,j+1/2})/2. \tag{5.16}$$

As demonstrated in [76], the symmetric heat flux satisfies the self adjointness property (equivalent to $\dot{s}^* \equiv -\mathbf{q} \cdot \nabla T \geq 0$ at cell corners) and has the desirable property that the perpendicular numerical diffusion ($\chi_{\perp,num}$) is independent of $\chi_\parallel/\chi_\perp$. But, as we show later, both symmetric and asymmetric schemes do not satisfy the very important local property that heat must flow from higher to lower temperatures; the violation of this at temperature minima can result in negative temperature in regions with large temperature gradients.

As mentioned earlier, the heat flux in the x- direction, q_x, consists of two terms,

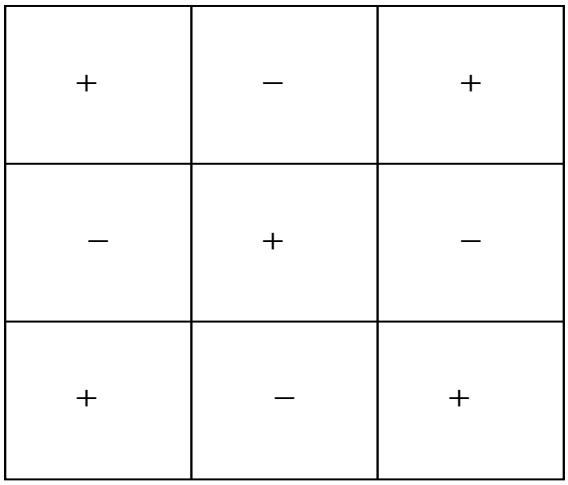

Figure 5.4: The symmetric method is unable to diffuse a temperature distributed in a chess-board pattern. The plus (+) and minus (−) symbols denote two unequal temperatures. Temperature gradients at the cell corners vanish, resulting in a vanishing heat flux independent of the magnetic orientation, e.g., average of $\partial T/\partial x|_{i+1/2,j} = (T_+ - T_-)/\Delta x$ and $\partial T/\partial x|_{i+1/2,j+1} = (T_- - T_+)/\Delta x$ to calculate $\partial T/\partial x|_{i+1/2,j+1/2} = \partial T/\partial x|_{i+1/2,j} + \partial T/\partial x|_{i+1/2,j+1}$ vanishes, similarly $\partial T/\partial y|_{i+1/2,j+1/2} = 0$.

the normal term $q_{xx} = -n\chi b_x^2 \partial T/\partial x$ and the transverse term $q_{xy} = -n\chi b_x b_y \partial T/\partial y$. The asymmetric scheme uses a 2 point stencil to calculate the normal gradient and a 6 point stencil to calculate the transverse gradient, as compared to the symmetric method that uses a 6 point stencil for both (hence the name symmetric). This makes the symmetric method less sensitive to the orientation of coordinate system with respect to the field lines.

A problem with the symmetric method which is immediately apparent is its inability to diffuse away a chess-board temperature pattern, as $\overline{\partial T/\partial x}$ and $\overline{\partial T/\partial y}$, located at the cell corners, vanish for this initial condition (see Figure 5.4). All heat fluxes evaluated with the symmetric method vanish and the temperature pattern is stationary in time. This problem is alleviated if the perpendicular diffusion coefficient, $\chi_\perp$, is large enough to diffuse the temperature gradients at small scales.

5.3 Negative temperature with centered differencing

In this section we present two simple test problems that demonstrate that negative temperatures can arise because of centered differencing, for both asymmetric and symmetric methods.

5.3.1 Asymmetric method

Consider a 2×2 grid with a hot zone ($T = 10$) in the first quadrant and cold temperature ($T = 0.1$) in the rest, as shown in Figure 5.5. Magnetic field is uniform over the box with $b_x = -b_y = 1/\sqrt{2}$. Number density is a constant equal to unity. Reflecting boundary conditions are used. Using the asymmetric scheme for heat fluxes out of the grid point (i, j) (the third quadrant) gives, $q_{x,i-1/2,j} = q_{y,i,j-1/2} = 0$, and $q_{x,i+1/2,j} = q_{y,i,j+1/2} = (9.9/8)n\chi/\Delta x$ (where $\Delta x = \Delta y$ is assumed). Thus, heat flows out of the grid point (i, j), already a temperature minimum. This gives rise to temperature becoming negative. Figure 5.5 shows the temperature in the third quadrant with time for different methods. The asymmetric method gives negative temperature ($T_{i,j} < 0$) for first few time steps, which eventually becomes positive. All other methods (except the one based on entropy limiting) give positive temperatures at all times for this problem. Methods based on limiting temperature gradients will be discussed later. This test demonstrates that the asymmetric method may not be suitable for cases with large temperature gradients because negative temperatures result in numerical instabilities.

5.3.2 Symmetric method

The symmetric method does not give negative temperature with the test problem of the previous section. In fact, the symmetric method gives the correct result for

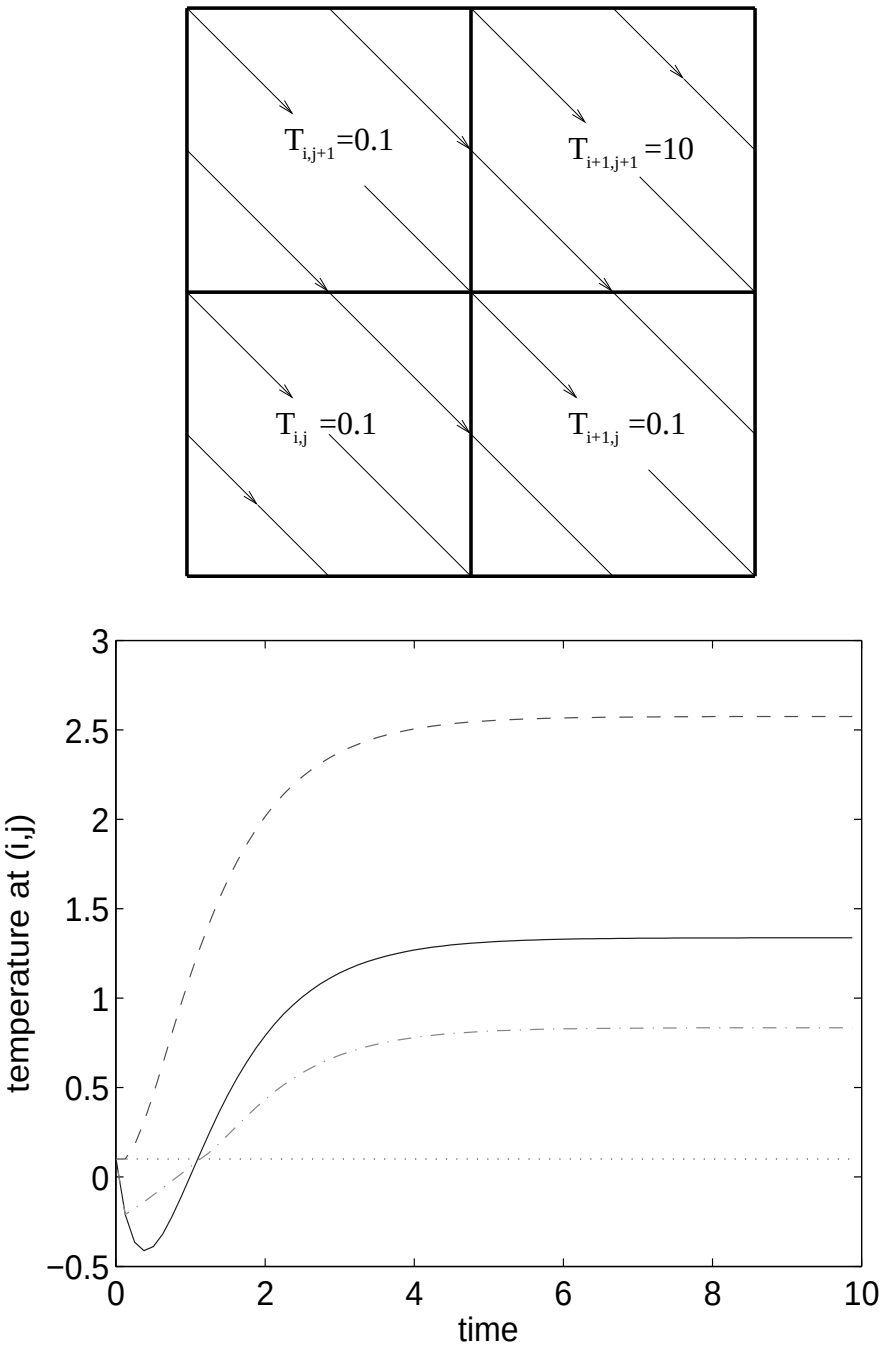

Figure 5.5: Test problem that shows the asymmetric method can give rise to negative temperature. Magnetic field lines are along the diagonal with $b_x = -b_y = 1/\sqrt{2}$. With the asymmetric method, heat flows out of the grid located at southwest corner, resulting in a negative temperature $T_{i,j}$. However, at late times the temperature becomes positive again. The temperature at (i, j) is shown for different methods: asymmetric (solid line), symmetric (dotted line), asymmetric and symmetric with slope limiters (dashed line; both give the same result), and symmetric with entropy limiting (dot dashed line).

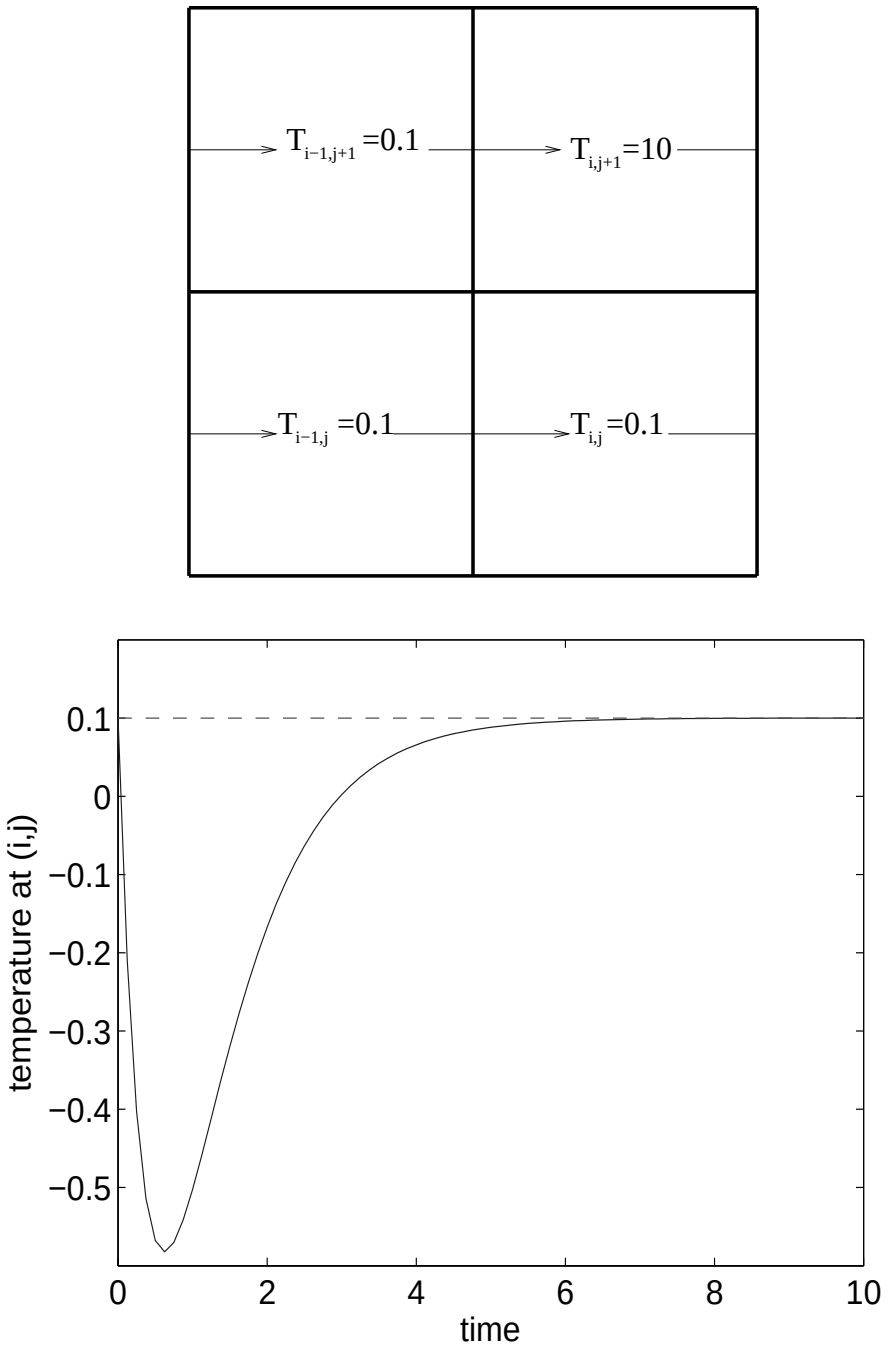

Figure 5.6: The result of the test problem for which the symmetric method gives negative temperature at (i, j). Magnetic field is along the x- direction, $b_x = 1$ and $b_y = 0$. With this initial condition, all heat fluxes into (i, j) should vanish and the temperature $T_{i,j}$ should not evolve. All methods except the symmetric method (asymmetric, and slope and entropy limited methods) give a constant temperature $T_{i,j} = 0.1$ at all times. But with the symmetric method, the temperature at (i, j) becomes negative due to the heat flux out of the corner at $(i - 1/2, j + 1/2)$. The temperature $T_{i,j}$ eventually becomes equal to the initial value of 0.1.

temperature with no numerical diffusion in the perpendicular direction (zero heat flux out of the grid point (i, j), see Figure 5.5). Other methods resulted in a temperature increase at (i, j) because of perpendicular numerical diffusion. Here we consider a case where the symmetric method gives negative temperature.

As before, consider a 2×2 grid with a hot zone ($T = 10$) in the first quadrant and cold temperature ($T = 0.1$) in the rest; the only difference from the previous test problem is that the magnetic field lines are along the x- axis, $b_x = 1$ and $b_y = 0$ (see Figure 5.6). Reflective boundary conditions are used, as before. Since there is no temperature gradient along the field lines for the grid point (i, j), we do not expect the temperature there to change. While all other methods give a stationary temperature in time, the symmetric method results in a heat flux out of the grid (i, j) through the corner at $(i - 1/2, j + 1/2)$. With the initial condition as shown in Figure 5.6, the only non-vanishing symmetric heat flux out of (i, j) is, $q_{x,i-1/2,j+1/2} = -(9.9/2)n\chi\Delta x$. The only non-vanishing face-centered heat flux entering the box through a face is $q_{x,i-1/2,j} = -(9.9/4)n\chi\Delta x < 0$; i.e., heat flows out of (i, j) which is already a temperature minimum. This results in the temperature becoming negative at (i, j), although at late times it becomes equal to the initial temperature at (i, j). This simple test shows that the symmetric method can give negative temperatures (and associated numerical problems) in presence of large temperature gradients.

5.4 Slope limited fluxes

The heat flux q_x is composed of two terms, the normal $q_{xx} = -n\chi b_x^2 \partial T/\partial x$ term, and the transverse $q_{xy} = -n\chi b_x b_y \partial T/\partial y$ term. For the asymmetric method, the discrete form of the term $q_{xx} = -n\chi b_x^2 \partial T/\partial x$ is of the same sign as the x- component of isotropic heat flux ($-n\chi \partial T/\partial x$), and hence it guarantees that heat flows from higher to lower temperatures. However, $q_{xy} = -n\chi b_x b_y \partial T/\partial y$ can have an arbitrary sign,

and can give rise to heat flowing in the "wrong" direction. We use slope limiters, analogous to those used for linear reconstruction of variables in numerical simulation of hyperbolic systems [196, 116], to "limit" the transverse terms. Both asymmetric and symmetric methods can be modified with slope limiters. The slope limited heat fluxes ensure that temperature extrema are not accentuated. Thus, unlike the symmetric and asymmetric methods, slope limited methods can never give negative temperatures.

5.4.1 Limiting the asymmetric method

Since the normal heat flux term, q_{xx}, is naturally located at the face, no interpolation for $\partial T/\partial x$ is required for its evaluation. However, an interpolation at the x- face is required to evaluate $\overline{\partial T/\partial y}$ used in q_{xy} (the term with overlines in Eq. 5.5). The arithmetic average used in Eq. 5.7 for $\overline{\partial T/\partial y}$ to calculate q_{xy} was found to result in heat flowing from lower to higher temperatures (see Figure 5.5). To remedy this problem we have used slope limiters to interpolate temperature gradients in the transverse heat fluxes.

Slope limiters are widely used in numerical simulations of hyperbolic equations (e.g., computational gas dynamics; see [196, 116]). Given the initial values for variables at grid centers, slope limiters (e.g., minmod, van Leer, and Monotonized Central (MC)) are used to calculate the slopes of conservative piecewise linear reconstructions in each grid cell. Limiters use the variable values in the nearest grid cells to come up with slopes which ensure that no new extrema are created for conserved variables, a property of hyperbolic equations. We use slope limiters to interpolate temperature gradients in transverse heat flux terms. Analogous to hyperbolic problems where limiters prevent new unphysical extrema, limiters prevent amplification of temperature extrema; this may result in negative temperatures.

The slope limited asymmetric heat flux in the x- direction is still given by Eq. 5.5,

with the same $\partial T/\partial x$ as in the asymmetric method, but a slope limited interpolation for the transverse temperature gradient, $\overline{\partial T/\partial y}$ is needed,

$$\left.\overline{\frac{\partial T}{\partial y}}\right|_{i+1/2,j} = L\left\{L\left[\left.\frac{\partial T}{\partial y}\right|_{i,j-1/2}, \left.\frac{\partial T}{\partial y}\right|_{i,j+1/2}\right],\ L\left[\left.\frac{\partial T}{\partial y}\right|_{i+1,j-1/2}, \left.\frac{\partial T}{\partial y}\right|_{i+1,j+1/2}\right]\right\}, \tag{5.17}$$

where L is a slope limiter like minmod, van Leer, or Monotonized Central (MC) limiter [116]; e.g., the van Leer limiter is

$$\begin{aligned} L(a,b) &= \frac{2ab}{a+b} \text{ if } ab > 0, \\ &= 0 \text{ otherwise.} \end{aligned} \tag{5.18}$$

Slope limiters weights the interpolation towards the argument smallest in magnitude, and returns a zero if the two arguments are of opposite signs. An analogous expression for the transverse temperature gradient at the y- face, $\overline{\partial T/\partial x}$, is used to evaluate the heat flux q_y. Averaging similar to the asymmetric method is used for all other interpolations (Eqs. 5.6 and 5.8).

5.4.2 Limiting the symmetric method

In the symmetric method, primary heat fluxes in both directions are located at the cell corners (see Eq. 5.9). Temperature gradients in both directions have to be interpolated at the corners. Thus, to ensure that temperature extrema are not amplified with the symmetric method, both $\overline{\partial T/\partial x}$ and $\overline{\partial T/\partial y}$ need to be limited.

The face-centered $q_{xx,i+1/2,j}$ is calculated by averaging q_{xx} from the adjacent cor-

ners, which are given by the following slope-limited expressions:

$$q^N_{xx,i+1/2,j+1/2} = -\overline{n\chi}\,\overline{b_x^2}\,L2\left[\left.\frac{\partial T}{\partial x}\right|_{i+1/2,j}, \left.\frac{\partial T}{\partial x}\right|_{i+1/2,j+1}\right], \tag{5.19}$$

$$q^S_{xx,i+1/2,j-1/2} = -\overline{n\chi}\,\overline{b_x^2}\,L2\left[\left.\frac{\partial T}{\partial x}\right|_{i+1/2,j}, \left.\frac{\partial T}{\partial x}\right|_{i+1/2,j-1}\right], \tag{5.20}$$

where S and N superscripts indicate the south-biased corner heat flux or the north-biased heat flux. The face centered heat flux used in Eq. 5.3 is $q_{xx,i+1/2,j} = (q^N_{xx,i+1/2,j+1/2} + q^S_{xx,i+1/2,j-1/2})/2$; the interpolated quantities (indicated with an overline) are the same as in Eq. 5.9. The limiter $L2$, which is somewhat different from standard slope limiters, is defined as

$$\begin{aligned} L2(a,b) &= (a+b)/2, \text{ if } \min(\alpha a, a/\alpha) < (a+b)/2 < \max(\alpha a, a/\alpha), \\ &= \min(\alpha a, a/\alpha), \text{ if } (a+b)/2 \le \min(\alpha a, a/\alpha), \\ &= \max(\alpha a, a/\alpha), \text{ if } (a+b)/2 \ge \max(\alpha a, a/\alpha), \end{aligned} \tag{5.21}$$

where $0 < \alpha < 1$ is a parameter; this reduces to a simple averaging if the temperature is smooth while restricting the interpolated temperature ($\overline{\partial T/\partial x}$) to not differ too much from $\partial T/\partial x|_{i+1/2,j}$ (and be of the same sign). We choose $\alpha = 3/4$; results are not very sensitive to the exact value of α. The $L2$ limiter is not symmetric with respect to its arguments (and thus the definition of $q^S_{xx,i+1/2,j+1/2}$ is slightly different than the definition of $q^N_{xx,i+1/2,j+1/2}$). It ensures that $q_{xx,i+1/2,j\pm1/2}$ is of the same sign as $-\partial T/\partial x|_{i+1/2,j}$; i.e., the interpolated normal heat flux flows from higher to lower temperatures. If we use a standard slope limiter (e.g., minmod, van Leer, or MC) in Eqs. 5.19 and 5.20, for the chessboard pattern shown in Figure 5.4, all heat fluxes vanish as with the symmetric method. However, the $L2$ limiter gives,

$$q_{xx,i+1/2,j+1/2} = q_{xx,i+1/2,j-1/2} = -\overline{n\chi}\,\overline{b_x}^2\,\alpha\left.\frac{\partial T}{\partial x}\right|_{i+1/2,j},$$

a heat flux from higher to lower temperatures which can diffuse the chessboard pattern.

The transverse temperature gradient is limited in a way similar to the asymmetric method. The temperature gradient $\overline{\partial T/\partial y}$ to be used in Eq. 5.9 is given by

$$\left.\overline{\frac{\partial T}{\partial y}}\right|_{i+1/2,j+1/2} = L\left[\left.\frac{\partial T}{\partial y}\right|_{i+1,j+1/2}, \left.\frac{\partial T}{\partial y}\right|_{i,j+1/2}\right], \tag{5.22}$$

with $q_{xy,i+1/2,j} = L(q_{xy,i+1/2,j+1/2}, q_{xy,i+1/2,j-1/2})$, where L is a standard slope limiter.

5.5 Limiting using the entropy-like source function

If the entropy-like source function, which we define as $\dot{s}^* = -\mathbf{q}\cdot\nabla T$ (see Appendix E to see how this is different from the entropy function), is positive at all spatial locations, heat is guaranteed to flow from higher to lower temperatures. For the symmetric method, $\dot{s}^*$ evaluated at the cell corners is positive definite, but need not be positive definite if evaluated at the cell faces, and thus allows the heat to flow across faces from lower to higher temperatures. This can cause temperature to decrease at a minimum; temperature can also become negative if temperature gradients are large (see Figure 5.6). Thus, $\dot{s}^* \geq 0$ satisfied at all corners on the grid is not sufficient for the heat to flow from higher to lower temperatures. We use the following entropy-like condition, applied at all face-pairs, to limit the transverse heat flux terms (q_{xy} and q_{yx})

$$\dot{s}^* = -q_{x,i+1/2,j}\left.\frac{\partial T}{\partial x}\right|_{i+1/2,j} - q_{y,i,j+1/2}\left.\frac{\partial T}{\partial y}\right|_{i,j+1/2} \geq 0. \tag{5.23}$$

The limiter $L2$ is used to calculate the normal gradients q_{xx} and q_{yy} at the faces, as in the slope limited symmetric method. The use of $L2$ ensures that $-q_{xx,i+1/2,j}\partial T/\partial x|_{i+1/2,j} \geq 0$, and only the transverse terms q_{xy} and q_{yx} need to be reduced to satisfy Eq. 5.23.

That is, if on evaluating $\dot{s}^*$ the entropy-like condition (Eq. 5.23) is violated, the transverse terms are reduced to make $\dot{s}^*$ vanish. The attractive feature of the entropy limited symmetric method is that it reduces to the symmetric method (least diffusive of all the methods; see Figure 5.9) when Eq. 5.23 is satisfied, and the limiting of transverse terms may help with the amplification of temperatures at extrema.

The problem with entropy limiting is that the temperature extrema can still be amplified (see Figures 5.5 and 5.8). For example, when $\partial T/\partial x|_{i+1/2,j} = \partial T/\partial y|_{i,j+1/2} = 0$, Eq. 5.23 is satisfied for arbitrary heat fluxes $q_{x,i+1/2,j}$ and $q_{y,i,j+1/2}$. In such a case, transverse heat fluxes q_{xy} and q_{yx} can cause heat to flow across the zero temperature gradient and result in a new temperature extremum, which may even be a negative. However, this unphysical behavior can only occur for one time step, after which $\nabla T \neq 0$ and Eq. 5.23 becomes a useful limit again. The result is that the overshoots are not as pronounced as in the asymmetric and symmetric methods, as shown in Figures 5.7 and 5.8. With entropy limiting, unlike the symmetric and asymmetric methods, the spurious temperature oscillations (reminiscent of unphysical oscillations near discontinuities in hyperbolic systems) are damped (see Figure 5.8). Although temperature minimum can be accentuated by the entropy limited method, early on one can choose sufficiently small time steps to ensure that temperature does not become negative; this is equivalent to saying that entropy limited method will not give negative temperatures at late times (see Figure 5.8 and Tables 5.1-5.4). This trick will not work for the centered symmetric and asymmetric methods where temperatures can be negative even at late times (see Figure 5.8).

To guarantee that temperature extrema are not amplified, in addition to entropy limiting at all points, one should also use slope limiting of transverse temperature gradients at extrema. This results in a method that does not amplify the extrema, but is more diffusive compared to just entropy limiting (see Figure 5.9). Because of simplicity of slope limited methods and their desirable mathematical properties (dis-

cussed in the next section), they are preferred over the cumbersome entropy limited methods.

5.6 Mathematical properties

In this section we prove that the slope limited fluxes do not amplify the temperature extrema. Also discussed are global and local properties related to the entropy-like condition, $\dot{s}^* = -\mathbf{q} \cdot \nabla T \geq 0$.

5.6.1 Behavior at temperature extrema

Slope limiting of both asymmetric and symmetric methods guarantees that the temperature extrema are not amplified further, i.e., the maximum temperature does not increase and the minimum does not decrease. This ensures that the temperature is always positive and numerical problems because of imaginary sound speed do not arise. The normal heat flux in the asymmetric method ($= -\overline{n\chi} b_x^2 \partial T/\partial x$) and the L2 limited normal heat flux term in the symmetric method (Eqs. 5.19 and 5.20) allows the heat to flow only from higher to lower temperatures. Thus, the terms responsible for unphysical behavior at temperature extrema are the transverse heat fluxes q_{xy} and q_{yx}. Slope limiters ensure that the transverse heat terms vanish at extrema and heat flows down the temperature gradient at those grid points.

The operator $L(L(a,b), L(c,d))$, where L is a slope limiter like minmod, van Leer, or MC, is symmetric with respect to all its arguments, and hence can be written as $L(a,b,c,d)$. For the slope limiters considered here (minmod, van Leer, and MC), $L(a,b,c,d)$ vanishes unless all four arguments a, b, c, d have the same sign.

At a local temperature extremum (say at (i,j)), the x- (and y-) face-centered slopes $\partial T/\partial y|_{i,j+1/2}$ and $\partial T/\partial y|_{i,j-1/2}$ (and $\partial T/\partial x|_{i+1/2,j}$ and $\partial T/\partial x|_{i-1/2,j}$) are of opposite signs or at least one of them is zero. This ensures that the slope lim-

ited transverse temperature gradients ($\overline{\partial T/\partial y}$ and $\overline{\partial T/\partial x}$) vanish (from Eqs. 5.17 and 5.22). The heat fluxes become $q_{x,i\pm1/2,j} = -\overline{n\chi}\,\overline{b_x}^2 \partial T/\partial x|_{i\pm1/2,j}$ and $q_{y,i,j\pm1/2} = -\overline{n\chi}\,\overline{b_y}^2 \partial T/\partial y|_{i,j\pm1/2}$ at the temperature extrema, which are always down the temperature gradient. This ensures that temperature never becomes negative, unlike the methods based on centered differencing.

5.6.2 The entropy-like condition, $\dot{s}^* = -\mathbf{q}\cdot\nabla T \geq 0$

If the number density, n, remains constant in time, then multiplying Eq. 5.1 with T and integrating over all space gives

$$\frac{1}{(\gamma-1)}\frac{\partial}{\partial t}\int nT^2 dV = -\int T\nabla\cdot\mathbf{q}dV = \int \mathbf{q}\cdot\nabla T dV = -\int n\chi|\nabla_\parallel T|^2 dV \leq 0, \tag{5.24}$$

assuming that the surface contributions vanish. This analytic constraint implies that temperature fluctuations cannot increase in time (on an average).

Günter et al. [76] have shown that the symmetric method is self-adjoint and satisfies the entropy-like condition, Eq. 5.24. The local entropy-like source function $\dot{s}^* = -\mathbf{q}\cdot\nabla T$ evaluated at the corner $(i+1/2, j+1/2)$ for the symmetric method is

$$\dot{s}^*_{i+1/2,j+1/2} = -q_{x,i+1/2,j+1/2}\left.\frac{\overline{\partial T}}{\partial x}\right|_{i+1/2,j+1/2} - q_{y,i+1/2,j+1/2}\left.\frac{\overline{\partial T}}{\partial y}\right|_{i+1/2,j+1/2}. \tag{5.25}$$

Using the form for symmetric heat fluxes (Eq. 5.9), the entropy-like function becomes,

$$\begin{aligned}\dot{s}^* &= \overline{n\chi}\,\overline{b_x}^2\overline{\frac{\partial T}{\partial x}}^2 + \overline{n\chi}\,\overline{b_y}^2\overline{\frac{\partial T}{\partial y}}^2 + 2\overline{n\chi}\,\overline{b_x}\;\overline{b_y\frac{\partial T}{\partial x}}\;\overline{\frac{\partial T}{\partial y}},\\ &= \overline{n\chi}\left[\overline{b_x\frac{\partial T}{\partial x}} + \overline{b_y\frac{\partial T}{\partial y}}\right]^2 \geq 0.\end{aligned} \tag{5.26}$$

Thus, $\mathbf{q}\cdot\nabla T \leq 0$, and integration over the whole space implies Eq. 5.24. Although the entropy-like condition is satisfied by the symmetric method at the corners (both

locally and globally), this condition is not sufficient to guarantee local positivity of temperature at cell centers, as we demonstrate in Subsection 5.3.2. Also notice that the modification of the symmetric method to satisfy entropy-like condition at face pairs (see Section 5.5) does not cure the problem of negative temperature. Thus, a method which satisfy the entropy-like condition ($\dot{s}^* = -\mathbf{q} \cdot \nabla T \geq 0$) does not necessarily satisfy the condition that temperature extrema should not be amplified.

With an appropriate interpolation, the asymmetric method and the slope limited asymmetric methods can be shown to satisfy the global entropy-like condition, $\dot{S}^* = -\int \mathbf{q} \cdot \nabla T dV/V \geq 0$. Consider

$$\dot{S}^* = \frac{-1}{N_x N_y} \sum_{i,j} \left[q_{x,i+1/2,j} \left. \frac{\partial T}{\partial x} \right|_{i+1/2,j} + q_{y,i,j+1/2} \left. \frac{\partial T}{\partial y} \right|_{i,j+1/2} \right], \tag{5.27}$$

where N_x and N_y are the number of grid points in each direction. Substituting the form of asymmetric heat fluxes,

$$\begin{aligned} \dot{S}^* &= \frac{1}{N_x N_y} \sum_{i,j} \left[\left(\overline{n\chi} b_x^2 \left| \frac{\partial T}{\partial x} \right|^2 \right)_{i+1/2,j} + \left(\overline{n\chi} b_y^2 \left| \frac{\partial T}{\partial y} \right|^2 \right)_{i,j+1/2} \right. \\ &+ \left. \left(\overline{n\chi b_x b_y \frac{\partial T}{\partial y}} \right)_{i+1/2,j} \left. \frac{\partial T}{\partial x} \right|_{i+1/2,j} + \left(\overline{n\chi b_x b_y \frac{\partial T}{\partial x}} \right)_{i,j+1/2} \left. \frac{\partial T}{\partial y} \right|_{i,j+1/2} \right], \end{aligned} \tag{5.28}$$

where overlines represent appropriate interpolations. We define

$$G_{x,i+1/2,j} = \sqrt{(\overline{n\chi})}_{i+1/2,j} b_{x,i+1/2,j} \left. \frac{\partial T}{\partial x} \right|_{i+1/2,j}, \tag{5.29}$$

$$G_{y,i,j+1/2} = \sqrt{(\overline{n\chi})}_{i,j+1/2} b_{y,i,j+1/2} \left. \frac{\partial T}{\partial y} \right|_{i,j+1/2}, \tag{5.30}$$

$$\overline{G}_{y,i+1/2,j} = \overline{\left. \sqrt{n\chi} b_y \frac{\partial T}{\partial y} \right|_{i+1/2,j}}, \tag{5.31}$$

$$\overline{G}_{x,i,j+1/2} = \overline{\left. \sqrt{n\chi} b_x \frac{\partial T}{\partial x} \right|_{i,j+1/2}}. \tag{5.32}$$

In terms of G's, Eq. 5.28 can be written as

$$\dot{S}^* = \frac{1}{N_x N_y} \sum_{i,j} \left[G^2_{x,i+1/2,j} + G^2_{y,i,j+1/2} + G_{x,i+1/2,j} \overline{G}_{y,i+1/2,j} + \overline{G}_{y,i,j+1/2} G_{y,i,j+1/2} \right]. \tag{5.33}$$

A lower bound on $\dot{S}^*$ is obtained by assuming the cross terms to be negative, i.e.,

$$\dot{S}^* \geq \frac{1}{N_x N_y} \sum_{i,j} \left[G^2_{x,i+1/2,j} + G^2_{y,i,j+1/2} - \left| G_{x,i+1/2,j} \overline{G}_{y,i+1/2,j} \right| - \left| \overline{G}_{y,i,j+1/2} G_{y,i,j+1/2} \right| \right]. \tag{5.34}$$

Now define $\overline{G}_{y,i+1/2,j}$ and $\overline{G}_{x,i,j+1/2}$ as follows (the following interpolation is necessary for the proof to hold):

$$\overline{G}_{y,i+1/2,j} = L(G_{y,i,j+1/2}, G_{y,i,j-1/2}, G_{y,i+1,j+1/2}, G_{y,i+1,j-1/2}), \tag{5.35}$$

$$\overline{G}_{x,i,j+1/2} = L(G_{x,i+1/2,j}, G_{x,i-1/2,j}, G_{x,i+1/1,j+1}, G_{y,i-1/2,j+1}), \tag{5.36}$$

where L is an arithmetic average (as in centered asymmetric method) or a slope limiter (e.g., minmod, van Leer, or MC) which satisfy the property that $|L(a,b,c,d)| \leq (|a| + |b| + |c| + |d|)/4$, to put a lower bound on $\dot{S}^*$. Thus,

$$\begin{aligned} \dot{S}^* \geq & \frac{1}{N_x N_y} \sum_{i,j} G^2_{x,i+1/2,j} + G^2_{y,i,j+1/2} - \frac{1}{4} \left[\left| G_{x,i+1/2,j} G_{y,i,j+1/2} \right| \right. \\ & + \left| G_{x,i+1/2,j} G_{y,i,j-1/2} \right| + \left| G_{x,i+1/2,j} G_{y,i+1,j+1/2} \right| + \left| G_{x,i+1/2,j} G_{y,i+1,j-1/2} \right| \\ & + \left| G_{y,i,j+1/2} G_{x,i+1/2,j} \right| + \left| G_{y,i,j+1/2} G_{x,i-1/2,j} \right| + \left| G_{y,i,j+1/2} G_{x,i+1/2,j+1} \right| \\ & + \left. \left| G_{y,i,j+1/2} G_{x,i-1/2,j+1} \right| \right]. \end{aligned} \tag{5.37}$$

Shifting the dummy indices and combining various terms give,

$$\begin{aligned}
\dot{S}^{*} &\geq \frac{1}{N_x N_y}\sum_{i,j} G_{x,i+1/2,j}^2 + G_{y,i,j+1/2}^2 - \frac{1}{2}\left[\left|G_{x,i+1/2,j}G_{y,i,j+1/2}\right|\right. \\
&+ \left.\left|G_{x,i+1/2,j}G_{y,i,j-1/2}\right| + \left|G_{x,i+1/2,j}G_{y,i+1,j+1/2}\right| + \left|G_{x,i+1/2,j}G_{y,i+1,j-1/2}\right|\right] \\
&= \frac{1}{4N_x N_y}\sum_{i,j}\left[\left(G_{x,i+1/2,j} - G_{y,i,j+1/2}\right)^2 + \left(G_{x,i+1/2,j} - G_{y,i,j-1/2}\right)^2\right. \\
&+ \left.\left(G_{x,i+1/2,j} - G_{y,i+1,j+1/2}\right)^2 + \left(G_{x,i+1/2,j} - G_{y,i+1,j-1/2}\right)^2\right] \geq 0. \qquad (5.38)
\end{aligned}$$

Thus, an appropriate interpolation (for the asymmetric and the slope limited asymmetric methods) can result in a scheme that satisfies the global entropy-like condition just as it does for the non-limited symmetric method. A variation of this proof can be used to prove the global true entropy condition $\dot{S} \geq 0$ by multiplying Eq. 5.1 with $1/T$ instead of T (see Appendix E), although the form of limiting would need to be modified slightly. It is useful to know that introducing a limiter to the asymmetric method does not break the global entropy-like condition, if the right combination of quantities is limited in the interpolation. However, it is important to remember that the entropy-like (or entropy) condition does not guarantee a local heat flow in the correct direction, and hence temperature can still become negative. Thus, to get a robust method for anisotropic diffusion, it is necessary that heat flows in the correct direction at temperature extrema.

5.7 Further tests

We use test problems discussed in [148] and [181] to compare different methods. The first test problem (taken from [148]) initializes a hot patch in circular field lines; ideally the hot patch should diffuse only along the field lines, but perpendicular numerical diffusion can cause some cross-field diffusion. There is a discontinuity in the initial temperature of the hot patch and the background temperature. If the temperature

Table 5.1: Diffusion in circular field lines: 50×50 grid

Method	L1 error	L2 error	L∞ error	T_{max}	T_{min}	$\chi_{\perp,num}/\chi_{\parallel}$
asymmetric	0.0324	0.0459	0.0995	10.0926	9.9744	0.0077
asymmetric minmod	0.0471	0.0627	0.1195	10.0410	10	0.0486
asymmetric MC	0.0358	0.509	0.1051	10.0708	10	0.0127
asymmetric van Leer	0.0426	0.0574	0.1194	10.0519	10	0.0238
symmetric	0.0114	0.0252	0.1425	10.2190	9.9544	0.00028
symmetric entropy	0.03332	0.0477	0.0997	10.0754	10	0.0088
symmetric entropy extrema	0.0341	0.0487	0.1010	10.0751	10	0.0101
symmetric minmod	0.0475	0.0629	0.1322	10.0406	10	0.0490
symmetric MC	0.0289	0.0453	0.0872	10.0888	10	0.0072
symmetric van Leer	0.0438	0.0585	0.1228	10.0519	10	0.0238

Table 5.2: Diffusion in circular field lines: 100×100 grid

Method	L1 error	L2 error	L∞ error	T_{max}	T_{min}	$\chi_{\perp,num}/\chi_{\parallel}$
asymmetric	0.0256	0.0372	0.0962	10.1240	9.9859	0.0030
asymmetric minmod	0.0468	0.0616	0.1267	10.0439	10	0.0306
asymmetric MC	0.0261	0.0405	0.0907	10.1029	10	0.0040
asymmetric van Leer	0.0358	0.0502	0.1002	10.0741	10	0.0971
symmetric	0.0079	0.0173	0.1206	10.2276	9.9499	0.000041
symmetric entropy	0.0285	0.0420	0.0881	10.0961	10	0.0042
symmetric entropy extrema	0.0291	0.0425	0.0933	10.0941	10	0.0041
symmetric minmod	0.0471	0.0618	0.1275	10.0433	10	0.0305
symmetric MC	0.0123	0.0252	0.1133	10.1406	10	0.00084
symmetric van Leer	0.0374	0.0514	0.1038	10.0697	10	0.0104

jump is large temperature can become negative on using centered differencing (asymmetric and symmetric methods). The second test problem includes a source term and an explicit perpendicular perpendicular diffusion coefficient ($\chi_{\perp}$). The steady state temperature gives a measure of the perpendicular numerical diffusion, $\chi_{\perp,num}$.

5.7.1 Circular diffusion of hot patch

The circular diffusion test problem was proposed in [148]. A hot patch surrounded by a cooler background is initialized in circular field lines; the temperature drops

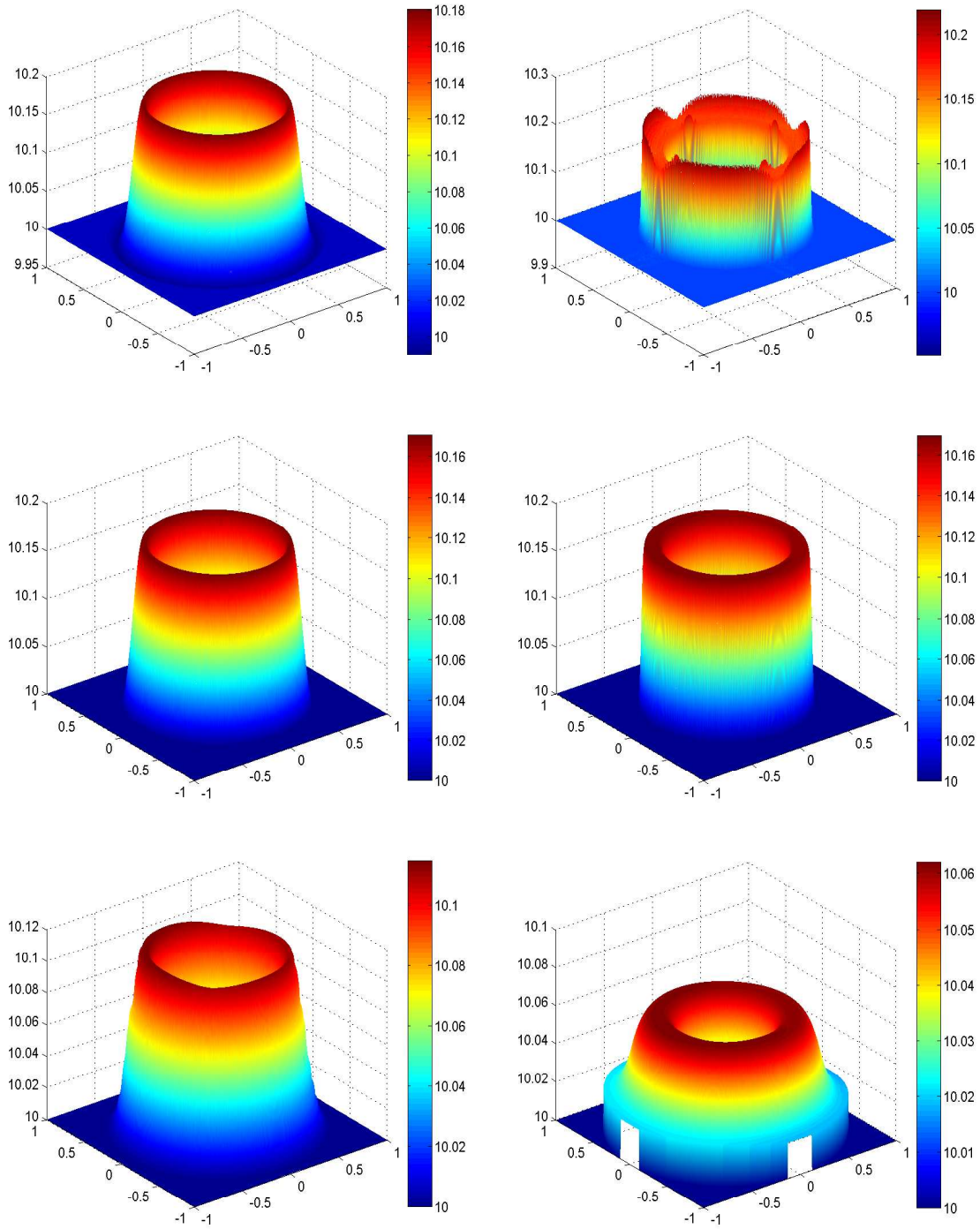

Figure 5.7: The temperature at $t = 200$ for different methods initialized with the ring diffusion problem on a 400×400 grid. Shown from left to right and top to bottom are the temperatures for: asymmetric, symmetric, asymmetric-MC, symmetric-MC, entropy limited symmetric, and minmod methods. Both the asymmetric and symmetric methods give temperatures below 10 (the initial minimum temperature). The result with a minmod limiter is very diffusive. The slope limited symmetric method is less diffusive than the slope limited asymmetric method. Entropy limited method does not show non-monotonic behavior at late times, but is diffusive compared to the better slope limited methods.

Table 5.3: Diffusion in circular field lines: 200×200 grid

Method	L1 error	L2 error	L∞ error	T_{max}	T_{min}	$\chi_{\perp,num}/\chi_{\parallel}$
asymmetric	0.0165	0.0281	0.0949	10.1565	9.9878	0.0012
asymmetric minmod	0.0441	0.0585	0.1214	10.0511	10	0.0191
asymmetric MC	0.0161	0.0289	0.0930	10.1397	10	0.0015
asymmetric van Leer	0.0264	0.0407	0.0928	10.1006	10	0.0035
symmetric	0.0052	0.0132	0.1125	10.2216	9.9509	1.90×10^{-5}
symmetric entropy	0.0256	0.0385	0.0959	10.1103	10	0.0032
symmetric entropy extrema	0.0260	0.0391	0.0954	10.1074	10	0.0032
symmetric minmod	0.0444	0.0588	0.1219	10.0503	10	0.0192
symmetric MC	0.0053	0.0160	0.0895	10.1676	10	0.0002
symmetric van Leer	0.0281	0.0426	0.0901	10.0952	10	0.0038

Table 5.4: Diffusion in circular field lines: 400×400 grid

Method	L1 error	L2 error	L∞ error	T_{max}	T_{min}	$\chi_{\perp,num}/\chi_{\parallel}$
asymmetric	0.0118	0.0234	0.0866	10.1810	9.9898	5.9×10^{-4}
asymmetric minmod	0.0399	0.0539	0.1120	10.0629	10	0.0115
asymmetric MC	0.0102	0.0230	0.0894	10.1708	10	6.8×10^{-4}
asymmetric van Leer	0.0167	0.0290	0.1000	10.1321	10	0.0013
symmetric	0.0033	0.0104	0.1112	10.2196	9.9504	8.37×10^{-6}
symmetric entropy	0.0252	0.0384	0.0969	10.1144	10	0.0027
symmetric entropy extrema	0.0253	0.0383	0.0958	10.1135	10	0.0026
symmetric minmod	0.0401	0.0541	0.1124	10.0622	10	0.0116
symmetric MC	0.0032	0.0122	0.0896	10.1698	10	6.5×10^{-5}
symmetric van Leer	0.0182	0.0307	0.1026	10.1260	10	0.0013

discontinuously across the patch boundary. At late times, we expect the temperature to become uniform (and higher) in a ring along the magnetic field lines. The computational domain is a $[-1,1] \times [-1,1]$ cartesian box, with reflective boundary conditions. The initial temperature distribution is given by

$$\begin{aligned} T &= 12 \quad \text{if } 0.5 < r < 0.7 \text{ and } \frac{11}{12}\pi < \theta < \frac{13}{12}\pi, \\ &= 10 \quad \text{otherwise,} \end{aligned} \tag{5.39}$$

where $r = \sqrt{x^2 + y^2}$ and $\tan\theta = y/x$. A set of circular field lines centered at the origin is initialized. The parallel conduction coefficient χ is chosen to be 0.01; there is no explicit perpendicular diffusion. We evolve the anisotropic conduction equation (5.3) till time = 200, using different methods that we have discussed. By this time we expect the temperature to be almost uniform along the circular ring $0.5 < r < 0.7$. In steady state (at late times), energy conservation implies that the the ring temperature should be 10.1667, while the temperature outside the ring should be maintained at 10.

Figure 5.7 shows the temperature distribution for different methods at time=200. All methods result in a higher temperature in the annulus $r \in [0.5, 0.7]$. The slope limited schemes show larger perpendicular diffusion (Tables 5.1-5.4 and Figure 5.10) compared to the symmetric and asymmetric schemes. The perpendicular numerical diffusion ($\chi_{\perp,num}$) scales with the parallel diffusion coefficient χ for all methods. However, for Sovinec's test problem (discussed in the next subsection) where temperature is always smooth, and an explicit $\chi_\perp$ is present, perpendicular numerical diffusion for the symmetric method does not scale with $\chi_\parallel$.

The minmod limiter is much more diffusive than van Leer and MC limiters. Both symmetric and asymmetric methods give a minimum temperature below the initial minimum of 10, even at late times (see Tables 5.1-5.4). At late times the symmetric method gives a temperature profile full of non-monotonic oscillations (Figure 5.7). Although, the slope limited fluxes are more diffusive than the symmetric and asymmetric methods, they never show undershoots below 10. Although the entropy limited symmetric method gives temperature undershoots at early times, the minimum temperature is still 10 at late times (see Tables 5.1-5.4 and Figure 5.8). Entropy limiting combined with a slope limiter at the extrema behaves similar to the slope limiter based schemes.

Strictly speaking, a hot ring surrounded by a cold background is not a steady

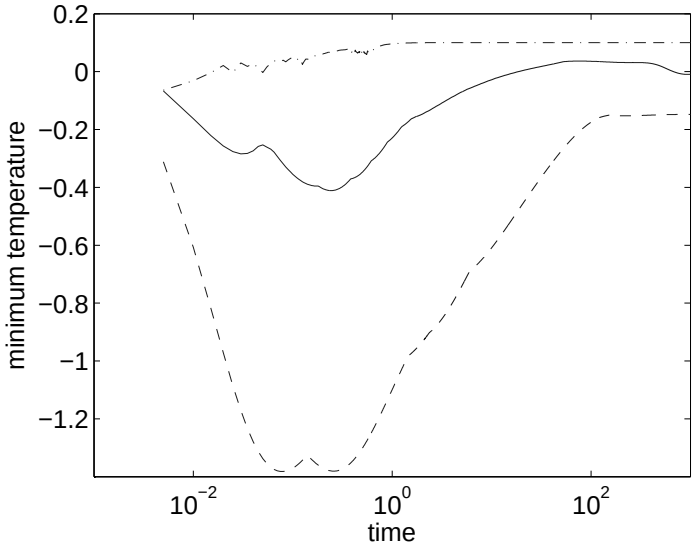

Figure 5.8: The minimum temperature over the whole box for symmetric (dashed line), asymmetric (solid line), and entropy limited symmetric (dot dashed line) methods in presence of circular field lines. Initially the temperature of the hot patch is 10 and the background is at 0.1. Both asymmetric and symmetric result in negative temperature, even at late times. The nonmonotonic behavior with the entropy limited method is considerably less pronounced; the minimum temperature quickly becomes equal to the initial minimum 0.1. The limited heat fluxes keep the minimum at 0.1, as expected physically.

solution for the ring diffusion problem. Temperature in the ring will diffuse in the perpendicular direction (because of perpendicular numerical diffusion, although very slowly) until the whole box is at a constant temperature. A rough estimate for time averaged perpendicular numerical diffusion $\langle \chi_{\perp,num} \rangle$ follows from Eq. 5.1,

$$\langle \chi_{\perp,num} \rangle = \frac{\int (T_f - T_i) dV}{\int dt \left(\int \nabla^2 T dV \right)}, \tag{5.40}$$

where the space integral is taken over the hot ring $0.5 < r < 0.7$, and T_i and T_f are the initial and final temperature distributions in the ring. Figure 5.10 plots the numerical perpendicular diffusion (using Eq. 5.40) for the runs in Tables 5.1-5.4. The estimates for perpendicular diffusion agree roughly with the more accurate calculations using Sovinec's test problem described in the next subsection (compare Figures 5.9 and 5.10). Table 5.6 lists the convergence of $\langle \chi_{\perp,num} \rangle$ for the ring diffusion problem using different methods; as with Sovinec's test, the symmetric method is the least diffusive.

To study the very long time behavior of different methods (in particular to check whether the symmetric and asymmetric methods give negative temperatures even at very late times) we initialize the same problem with the hot patch at 10 and the cooler background at 0.1. Figure 5.8 shows the minimum temperature with time for the symmetric, asymmetric, and entropy limited symmetric methods; slope limited methods give the correct result for the minimum temperature ($T_{\min} = 0.1$) at all times. With a large temperature contrast, both symmetric and asymmetric methods give negative values for the temperature minimum at all times. Such points where temperature becomes negative, when coupled with MHD equations, can give numerical instability because of an imaginary sound speed. The minimum temperature with the entropy limited symmetric method shows small undershoots at early times which are damped quickly and the minimum temperature is equal to the initial minimum (0.1) after time=1.

5.7.2 Convergence studies: measuring $\chi_{\perp,num}$

We have use the steady state test problem described in [181] to measure the perpendicular numerical diffusion coefficient, $\chi_\perp$. The computational domain is a unit square $[-0.5, 0.5] \times [-0.5, 0.5]$, with vanishing temperature at the boundaries. The source term $Q = 2\pi^2 \cos(\pi x)\cos(\pi y)$ that drives the lowest eigenmode of the temperature distribution is added to the anisotropic diffusion equation, Eq. 5.1; the anisotropic diffusion equation with a source term possesses a steady state solution. The equation that we evolve is

$$\frac{\partial e}{\partial t} = -\nabla \cdot \mathbf{q} + Q; \tag{5.41}$$

a forward in time centered in space (FTCS) differencing is used to add the source term.

The magnetic field is derived from the flux function of the form $\psi \sim \cos(\pi x)\cos(\pi y)$; this results in circular field lines centered at the origin. The temperature eigenmode driven by the source function Q is constant along the field lines. The steady state solution for the temperature is $T(x, y) = \chi_\perp^{-1} \cos(\pi x)\cos(\pi y)$, independent of $\chi_\parallel$. The perpendicular diffusion coefficient, $\chi_\perp$, is chosen to be unity, and $T^{-1}(0, 0)$ provides a measure of total perpendicular diffusion, the sum of $\chi_\perp$ (the explicit perpendicular diffusion) and $\chi_{\perp,num}$ (the perpendicular numerical diffusion).

Figure 5.9 shows the perpendicular numerical diffusivity $\chi_{\perp,num} = |T^{-1}(0, 0) - T_{iso}^{-1}(0, 0)|$ for $\chi_\parallel/\chi_\perp = 10$, 100 using different methods (where $T_{iso}^{-1}(0, 0)$ is the temperature at the origin when $\chi_\parallel = \chi_\perp$ is used for the same resolution). Günter et al. [76] and Sovinec et al. [181] use $\chi_{\perp,num} = |T^{-1}(0, 0) - 1|$ to measure perpendicular numerical diffusion; this is not precise and exaggerates the error for the symmetric method.

The perpendicular perpendicular diffusion ($\chi_{\perp,num}$) for all methods except the symmetric method increases linearly with $\chi_\parallel/\chi_\perp$. This property has been emphasized

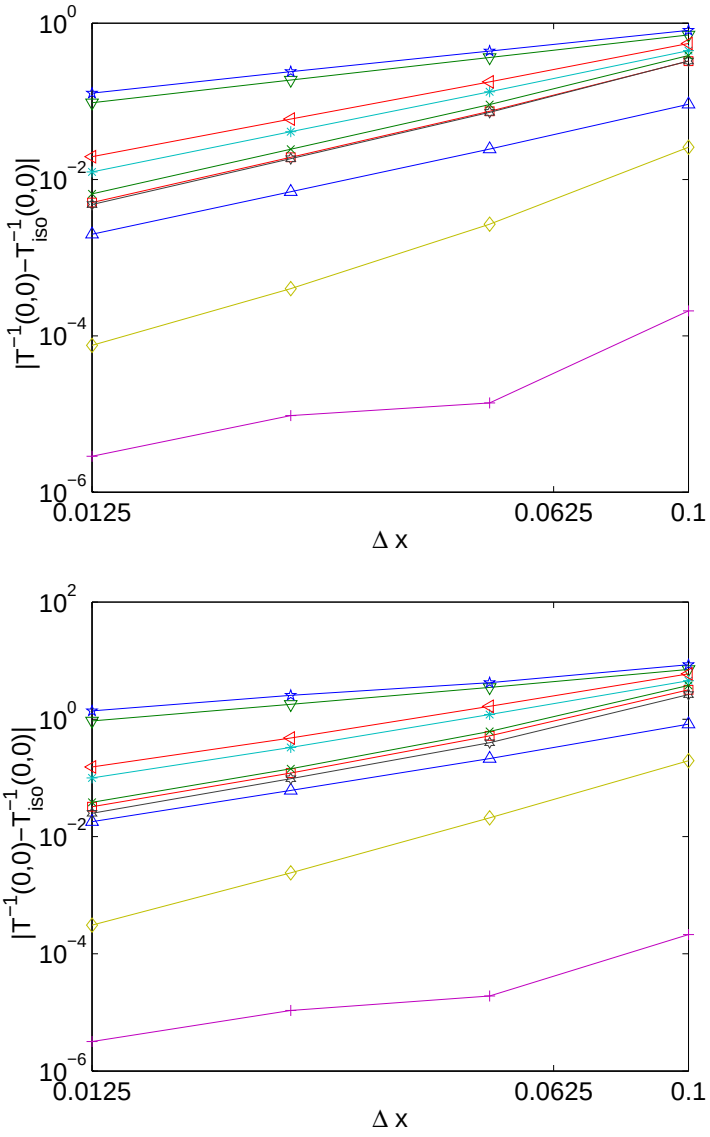

Figure 5.9: A measure of perpendicular numerical diffusion $\chi_{\perp,num} = (T^{-1}(0,0) - T_i^{-1}so)$ for $\chi_\parallel/\chi_\perp = 10$ (top curve) and for $\chi_\parallel/\chi_\perp = 100$ (bottom curve), using different methods for heat conduction. The different schemes are: asymmetric ($\triangle$), asymmetric with minmod ($\triangledown$), asymmetric with MC ($\square$), asymmetric with van Leer ($*$), symmetric ($+$), symmetric with entropy limiting ($\diamond$), symmetric with entropy and extrema limiting ($\triangleright$), symmetric with minmod ($\star$), symmetric with MC ($\times$), and symmetric with van Leer limiter ($\triangleleft$). The numerical diffusion scales with $\chi_\parallel$ for all methods except the symmetric differencing [76]. The slope limited methods using the van Leer and MC limiters show a second order convergence of the L1 error, like the methods based on centered differencing. Limiting both symmetric and asymmetric methods give similar results, but the desirable property of the symmetric method, that the error is independent of $\chi_\parallel/\chi_\perp$, no longer holds.

by [76] to motivate the use of symmetric differencing for fusion applications which require the error (perpendicular numerical diffusion) to be small for $\chi_{\parallel}/\chi_{\perp} \sim 10^9$. Higher order finite elements, which maintain such high anisotropy, have also been used for fusion applications [181].

The slope limited methods (with a reasonable resolution) are not suitable for the applications which require $\chi_{\parallel}/\chi_{\perp} \gg 10^4$; this rules out the fusion applications mentioned in [76, 181]. However, only the slope limited methods give physically appropriate behavior at temperature extrema, thereby avoiding negative temperatures in presence of sharp temperature gradients. The slope limited method with an MC limiter appears to be the most accurate method which does not result in the amplification of temperature extrema.

Table 5.5: Asymptotic slopes for convergence of error $\chi_{\perp,num} = |T^{-1}(0,0) - T_{iso}^{-1}(0,0)|$

Method	$\chi_{\parallel}/\chi_{\perp} = 10$	$\chi_{\parallel}/\chi_{\perp} = 100$
asymmetric	1.802	1.770
asymmetric minmod	0.9674	0.9406
asymmetric MC	1.9185	1.9076
asymmetric van Leer	1.706	1.728
symmetric	1.726	1.762
symmetric entropy	2.407	2.966
symmetric entropy extrema	1.949	1.953
symmetric minmod	0.9155	0.8761
symmetric MC	1.896	1.9049
symmetric van Leer	1.6041	1.6440

The error (perpendicular numerical diffusion, $\chi_{\perp,num} = |T^{-1}(0,0) - T_{iso}^{-1}(0,0)|$) for all methods, except the one which uses a minmod limiter, shows a second order convergence (see Table 5.5). Figures 5.9 and 5.10 show that the perpendicular numerical diffusivity with a van Leer (or an MC) slope limiter is $\sim 10^{-3}$ for ≈ 100 grid points in each direction. This anisotropy is more than sufficient to study qualitatively new effects of anisotropic conduction on dilute astrophysical plasmas [16, 10, 148, 177].

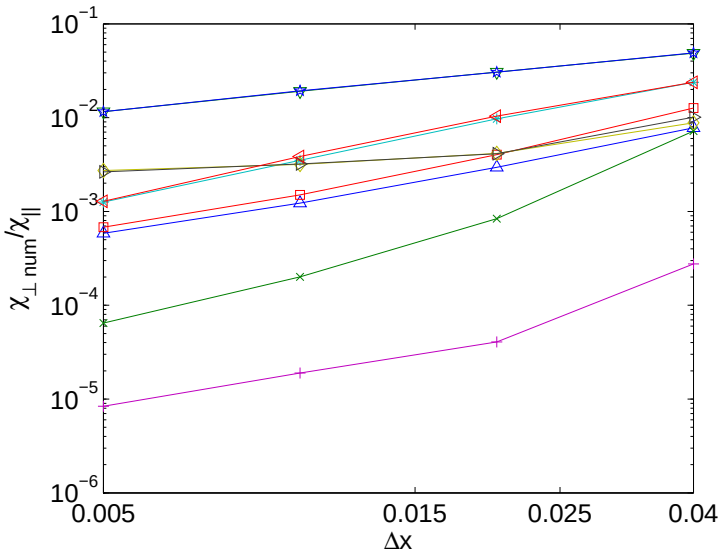

Figure 5.10: Convergence of $\chi_{\perp,num}/\chi_{\|}$ as number of grid points is increased for the ring diffusion problem. The numerical perpendicular diffusion, $\chi_{\perp}$, is calculated numerically, by measuring the heat diffusing out of the circular ring. The different schemes are: asymmetric ($\triangle$), asymmetric with minmod ($\triangledown$), asymmetric with MC ($\square$), asymmetric with van Leer ($*$), symmetric ($+$), symmetric with entropy limiting ($\diamond$), symmetric with entropy and extrema limiting ($\triangleright$), symmetric with minmod ($\star$), symmetric with MC ($\times$), and symmetric with van Leer limiter ($\triangleleft$). The numerical diffusion linearly scales with $\chi_{\|}$ for all methods, even with symmetric differencing for this problem. The slope limited methods using the van Leer and MC limiters show a second order convergence of L1 error, like the methods based on centered differences. The slopes for asymptotic convergence are listed in Table 5.6.

Table 5.6: Asymptotic slopes for convergence of $\chi_{\perp,num}$ in the ring diffusion test

Method	slope
asymmetric	1.066
asymmetric minmod	0.741
asymmetric MC	1.142
asymmetric van Leer	1.479
symmetric	1.181
symmetric entropy	0.220
symmetric entropy extrema	0.282
symmetric minmod	0.735
symmetric MC	1.636
symmetric van Leer	1.587

Among the various limiters discussed, MC is the least diffusive, followed by the van Leer limiter, and minmod is the most diffusive of all.

5.8 Conclusions

It is shown that simple centered differencing of anisotropic conduction can result in negative temperatures in presence of large temperature gradients. We have presented simple test problems where asymmetric and symmetric methods give rise to heat flowing from lower to higher temperatures, leading to negative temperatures at some grid points. Negative temperature results in numerical instabilities, as the sound speed becomes imaginary. Numerical schemes based on slope limiters are proposed to solve this problem.

The methods developed here will be useful in numerical studies of hot, dilute, anisotropic astrophysical plasmas [148, 177], where large temperature gradients may arise. Anisotropic conduction can play a crucial role in determining the global structure of hot, nonradiative accretion flows (e.g., [11, 177, 130]). Therefore, it will be useful to extend ideal MHD codes used in previous global numerical studies (e.g., [188]) to include anisotropic conduction. Because of the huge temperature gradients

that may occur in global disk simulations with a hot, dilute corona and a cold, dense disk, slope limited methods, which guarantee the positivity of temperature, must be used.

Although the slope and entropy limited methods in the present form are not suitable for fusion applications that require accurate resolution of perpendicular diffusion for huge anisotropy ($\chi_\parallel/\chi_\perp \sim 10^9$), they are appropriate for astrophysical applications with large temperature gradients. A relatively small anisotropy of thermal conduction is sufficient to study the effects of anisotropic conduction. The primary advantage of the limited methods is their robustness in presence of large temperature gradients. Apart from the simulations of dilute astrophysical plasmas with large temperature gradients (e.g., solar corona, magnetosphere, and magnetized collisionless shocks), our methods may find a use in diverse fields where anisotropic diffusion is important, e.g., image processing, biological transport, and geological systems.

Chapters 3 and 4 explored local (linear and nonlinear) properties of the MRI in the collisionless regime, but global calculations are required to study the relative roles of conduction, convection, and outflows, which determine the radial profile of different quantities, e.g., density, temperature, and radiation. Anisotropic conduction (and pressure) is crucial to understand the structure of hot, thick, collisionless RIAFs (see Section 1.4), and the slope limited methods are the only option for robust nonlinear simulations because large temperature gradients (e.g., the disk corona interface) arise naturally in global disk simulations.

Chapter 6

Conclusions

The main goal of the thesis was to study plasma kinetic processes operating in radiatively inefficient accretion flows (RIAFs) around compact objects, such as the supermassive black hole in the Galactic center and other nearby galactic centers (see 1.4 for details). Global MHD simulations of hot, thick accretion disks show that very little of the gas initially accreted from the outer regions actually makes it to the last stable orbit; most of the matter is lost as magnetized outflows [188, 84, 83, 95, 149, 155]. Although the reduction of the net mass accretion rate is part of the reason for the low luminosity, it is required by most models that the electrons radiate much less efficiently than the standard 10% efficiency for such low observed luminosities ([156], see 1.4). Some models, e.g., ADAFs, ascribe the low luminosity to low electron temperature compared to ions. To understand whether electrons can be maintained much cooler than ions, one needs to understand the conversion of gravitational energy into internal energy of electrons and ions.

We began by looking into the MRI in the collisionless regime and studied the transition from collisionless to collisional regimes as the collision frequency is increased (see Chapter 3). We show the equivalence of the drift kinetic equation and its moments closed with a Landau fluid closure for parallel heat flux, in both collisional

and collisionless regimes. Unlike MHD, where energy is dissipated (resistively and viscously) only at small scales, the collisionless plasmas have damped modes at all scales which can heat electrons and ions differently (see Figure 3.4). The linear studies were followed by 3-D local unstratified shearing box simulations of magnetized collisionless plasmas, using the kinetic MHD (KMHD) formalism closed with a local form of Landau fluid closure for parallel heat flux (see Chapter 4). Although, both linear studies and nonlinear simulations were carried out in a one fluid plasma with $T_i \gg T_e$, we can roughly estimate the heating rate for both electrons and ions. It is important to investigate what collisionless effects can do to the structure of RIAFs; especially to consider anisotropic thermal conduction, since it has important implications for the convective stability of plasmas [10, 11]. While implementing anisotropic conduction we discovered that the centered finite differencing of anisotropic conduction can give negative temperature in regions with large temperature gradients. To tackle this problem we developed a method where the transverse temperature gradient is obtained, not by simple averaging, but by using slope limiters. The method based on slope limiters guarantees the positivity of temperature (see Chapter 5).

6.1 Summary

To assess the importance of plasma kinetic effects in RIAFs we began with the study of collisionless MRI in the linear regime. The effect of collisions was introduced through a BGK collision operator. We use 3+1 Landau fluid closure for parallel thermal fluxes, which is equivalent to a Padé approximation for the fully kinetic plasma response. The Landau closure gives a good approximation to linear collisionless effects like Landau/Barnes damping.

We verify the equivalence of a fully kinetic analysis and the one based on Landau closure by considering the modes of a magnetized Keplerian disk, in both high and

low collisionality regimes. Heating in a collisionless disk can occur at all scales due to Landau/Barnes damping of the fast and slow modes; whereas, in MHD resistive and viscous heating at small scales is the only source of heating. Since collisionless damping is a resonant phenomenon, it can heat electrons or ions preferentially ($T_p \gg T_e$ is required by some RIAF models; see 1.4). The fastest growing MRI is twice as fast in the collisionless regime as compared to MHD. More importantly, it occurs at much larger length scales compared to MHD. Fast growth at large scales can in principle result in a different nonlinear saturation (for magnetic energy and stress) compared to MHD (though our nonlinear simulations to date find that in practice the final nonlinear spectra are similar). The MRI transitions from the collisionless to the Braginskii regime (when the mean free path becomes short compared to the wavelength, $\nu \gtrsim \Omega\sqrt{\beta}$), and then to the MHD regime (when the parallel viscous damping becomes negligible, $\nu \gtrsim \Omega\beta$), as the collision frequency is increased.

Balbus and Islam (see [12, 96]) have studied collisionless effects on the MRI by adding Braginskii anisotropic stress to the MHD equations, and verified our results; they emphasize the importance of anisotropic stress and call it the "magnetoviscous" instability because the instability occurs at long wavelengths even for an arbitrarily small field strength.

The linear studies were followed by local shearing box simulations of magnetized collisionless disks. The ZEUS MHD code was modified to include the kinetic MHD terms: anisotropic pressure in the equation of motion, and equations evolving $p_\parallel$ and $p_\perp$ closed by a local Landau fluid closure for heat flux along the field lines. Adiabatic invariant ($\mu = p_\perp/B$) is conserved for collisionless plasmas at length scales much larger than the Larmor radius and time scales much larger than the gyroperiod. Pressure anisotropy ($p_\perp > p_\parallel$) is created naturally as magnetic field is amplified by the MRI. Small scale instabilities—mirrror, ion-cyclotron, and firehose—are excited even at at small pressure anisotropies ($\Delta p/p \gtrsim \text{few}/\beta$). Although, mirror and firehose

instabilites are correctly captured in Landau MHD, we have to include a subgrid model for pressure isotropization due to these and ion-cyclotron instabilities because at large pressure anisotropies the fastest growing instabilities occur at the gyroradius scale and violate adiabatic invariance.

The result of pressure anisotropy is that there is a qualitatively new mechanism to transport angular momentum, the anisotropic stress. Apart from appearing in the equation of motion, anisotropic stress also appears in the internal energy equation, resulting in heating. The anisotropic stress is as important as the Maxwell stress, and depends only weakly on k_L (the parameter in the local Landau heat fluxes) and the pitch angle scattering model.

Pitch angle scattering due to microinstabilities limit the pressure anisotropy and results in MHD-like behavior—the reason MHD often provides a good approximation for large scale dynamics of astrophysical systems. What MHD does not tell us is how the energy released from accretion is dissipated—whether it goes into electrons or ions? A fully kinetic simulation with huge resolution can address the issue of plasma heating; but insights can be gained from fluid treatments like kinetic MHD (e.g., anisotropic stress can heat both electrons and ions).

The kinetic MHD simulations also show that the kinetic and magnetic energies are peaked at large scales (as in MHD). The simulations with $B_\phi = B_z$ initially, confirm that the linear growth rate in the kinetic regime is twice faster than in MHD; but the nonlinear saturation is not very different in the two regimes. In fact, somewhat counter-intuitively, the saturated magnetic energy for $B_\phi = B_z$ simulations is smaller compared to simulations with only a vertical field with the same β. Anisotropic stress can be larger than the Maxwell stress for $\beta >$ a few 100. To sum up, the nonlinear saturation of the MRI is quite similar for MHD and kinetic regimes.

Along with the local studies, it is crucial to understand the global structure of hot collisionless accretion flows. Global MHD simulations have shown that very little of

the mass initially accreted from the outer regions actually accreted on to the black hole; most of it is lost in outflows. Anisotropic thermal conduction can be crucial for the structure of hot collisionless accretion flows; collisionless plasmas with long mean free path can transport heat very efficiently along the field lines. When we used finite differencing to implement anisotropic conduction in a global simulation, we discovered that the temperature became negative at the torus-corona interface. This led us to investigate numerical algorithms for anisotropic thermal conduction in presence of large temperature gradients. We devised simple test problems that demonstrated that existing algorithms (both symmetric and asymmetric differencing) can result in heat flux out of a cold region, causing temperature to become negative in regions with high temperature gradient. This problem was solved by using slope limiters to obtain the transverse temperature gradient, instead of using a simple arithmetic average. The limiter-based methods are slightly more diffusive across field lines than the asymmetric method, but still show second order convergence. Although the symmetric method has very small numerical diffusion, it gives rise to high frequency non-monotonic temperature fluctuations with large temperature gradients.

6.2 Future directions

There are several directions for future work, for both local and global studies. Till now we have only done single fluid simulations, assuming the electrons to be cold. We can extended these simulations to include electrons to study comparative heating of electrons and ions. The original ZEUS code did not conserve energy (up to 90% of energy released from accretion was lost numerically), but energy conservation can be restored to a large extent by adding the energy lost while updating velocities and magnetic fields into heating of the plasma [194], or by switching to codes using

conservative algorithms (such as the recently developed ATHENA code [65]). In the absence of explicit resistivity and viscosity, the sources in the internal energy equation are: energy lost in updating magnetic fields (mimics magnetic dissipation), energy lost when updating velocity (represents viscous losses), the $-p\nabla\cdot\mathbf{V}$ heating, and the work done by anisotropic stress.

The energy-conserving one fluid simulations show that the work done by anisotropic stress is comparable to (or even larger than) the energy lost in magnetic field or velocity update; this means that the physical anisotropic heating is not negligible compared to resistive or viscous heating. This has important implications for local two-fluid simulations. The electron pressure will also be anisotropic ($T_{\perp,e} > T_{\parallel,e}$) because of adiabatic invariance, and the anisotropy will be limited by pitch angle scattering due to electron whistler instability with $\Delta p/p \sim$ (a few)$/\beta$ (see [99, 68]). This means that the heating rate due to anisotropic stress, $(1/e)de/dt$, is comparable for electrons and ions, and is comparable to resistive or viscous heating. Thus, local two-fluid simulations which conserve energy can shed some light on electron/ion heating and whether $T_p/T_e \gg 1$ is possible. This approach where both electrons and ions are heated because of the energy released from accretion is different from an approach where one looks for collisionless heat transport from hot ions to cold electrons (e.g., [24]).

Another area of progress is to implement more accurate non-local closures for thermal conduction in nonlinear simulations (see Chapter 2); till now we have used a crude, local approximation with a parameter k_L that exaggerates damping for scales smaller than $2\pi/k_L$ and reduces damping for larger scales. A local approximation may be fine if pitch-angle scattering due to microinstabilities reduces the effective mean free path to be comparable to the fastest growing MRI mode, which reduces the sensitivity to the parameter k_L. However, pitch angle scattering due to microinstabilities is not uniform. This intermittency may lead to a larger effective mean free path than simple

estimates at first suggest. It is important to understand the role of intermittent scattering structures in imposing MHD-like dynamics in collisionless plasmas.

It's important to realize that astrophysical plasmas are very different from fusion plasmas; magnetic fields are strong in fusion devices, with only small perturbation from the equilibrium condition, but in astrophysical plasmas with subthermal fields, strong shear flows can mix the fields and magnetic fields can be chaotic. Chaotic fields reduce thermal conduction as the effective mean free path is reduced to the field correlation length [43], this may mean that results do not sensitively depend on thermal conduction.

Another approach, which is computationally more challenging but feasible for some problems, is to evolve the drift kinetic equation (DKE, Eq. 2.7) to evolve the distribution function in a 5-D phase space and to use its moments for $p_{\parallel}$ and $p_{\perp}$ to close the kinetic MHD moment hierarchy. Many hydrodynamic codes are based on Riemann solvers; given a discontinuity at grid boundaries, Riemann solvers divide the discontinuity into wave families of the system and give the evolution of the variables due to flux through the boundaries [116]. The number of modes of the drift kinetic equation is huge, and it is impossible to solve the Riemann problem exactly. One approach to solve hyperbolic equations that does not require the solution of Riemann problems is based on central methods (alternatively, they can be related to a simple, approximate Riemann solver; see [143, 112]); central methods have also been applied to MHD simulations [9]. The DKE simulations do not require the closure approximation, but like in KMHD with Landau closures, subgrid models for pitch angle scattering to microinstabilities will be required. It is also possible to carry out full Vlasov or particle-in-cell (PIC) simulations where a subgrid model for microinstabilities is not required, but for such simulations to be applicable to RIAFs they will need to resolve both the large MRI scale and the Larmor radius scale (8 orders of magnitudes smaller than the disk height scale).

Recent global MHD simulations were responsible for understanding that only a small fraction of gas accreted in outer region actually make it to the black hole, most of it is lost in outflows. A small accretion rate is one reason for small radiative luminosities of RIAFs. An important direction for future research is to include kinetic MHD effects like anisotropic conduction in global simulations. Since plasma in RIAFs is hot and collisionless, anisotropic thermal conduction is rapid. This can be important in determining the structure of RIAFs. The structure of the self-similar solution for a RIAF changes dramatically if a saturated form of thermal conduction (due to free streaming of particles) is included [130]. Another reason that anisotropic conduction can be important is because the convective stability criterion for anisotropic plasmas is that temperature decreases outwards, $dT/dr < 0$, instead of the usual Schwarzschild condition of entropy increasing outwards, $ds/dr < 0$ [16, 10]. The effect of thermal conduction is subtle because the MRI may generate chaotic fields and suppress thermal conduction and impose more MHD-like behavior, instead of giving a state which is stable to the magnetothermal instability. Thus, it will important to know whether anisotropic thermal conduction will be a small effect due to its suppression because of MHD turbulence, or it will alter the structure of RIAFs.

Appendix A

Accretion models

A.1 Efficiency of black hole accretion

Black holes are different from neutron stars and white dwarfs as they do not have a surface. Although there is no surface, black holes are characterized by an event horizon, a region from which nothing, not even light, can escape. For a non-rotating (Schwarzschild) black hole, Newtonian arguments (speed of light = escape velocity at the event horizon) can be used to calculate the Schwarzschild radius, $r_g = 2GM_*/c^2$, radius of the event horizon for a black hole of mass M_*.

To calculate accretion efficiency one needs to know the form of the effective potential. In Newtonian theory, the energy equation for a mass with specific angular momentum l is

$$\frac{1}{2}\left(\frac{dr}{dt}\right)^2 + \Phi_{\rm eff}(r) = E, \tag{A.1}$$

where E = constant is the total energy per mass, and $\Phi_{\rm eff}(r) = l^2/2r^2 - GM_*/r$ is the effective potential. Newtonian approximation is not valid for a black hole, and a full general relativistic treatment is required. However, Paczynski and Wiita [145] introduced a pseudo-Newtonian potential for a non-rotating black hole, $\Phi_{\rm PW} = GM_*/(r - r_g)$, which gives a good approximation for the effective potential of a

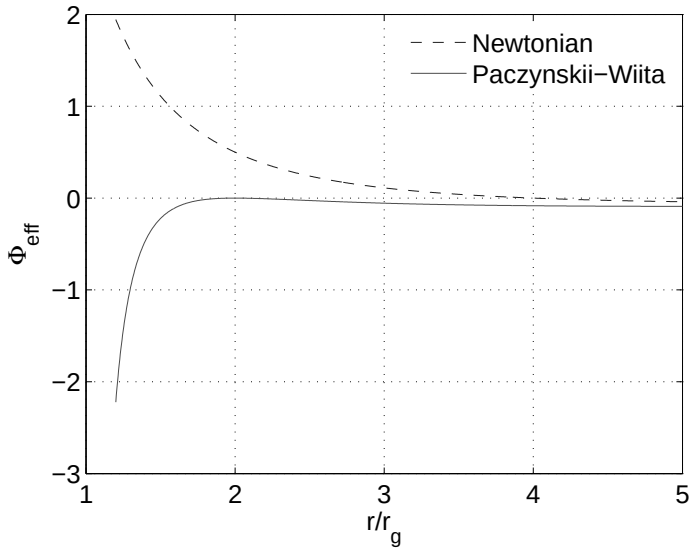

Figure A.1: Comparison of the Newtonian and Paczynski-Wiita potential for $l = 4GM_*/c$, corresponding to a marginally bound orbit in general relativity. Notice that $\Phi \to 0$ as $r \to \infty$.

non-rotating black hole. Using the Paczynski-Wiita potential, the energy equation becomes

$$\frac{1}{2}\left(\frac{dr}{dt}\right)^2 + \frac{l^2}{2r^2} - \frac{GM_*}{r - r_g} = E \tag{A.2}$$

The Paczynski-Wiita potential is useful because the effective potential, as in the case of general relativistic potential, has a minimum and a maximum if the specific angular momentum $l > 2\sqrt{3}GM_*/c$ [172]. In comparison, the Newtonian effective potential has a single minimum (corresponding to the circular Keplerian orbit) for any non-zero angular momentum. The general relativistic consequences are: 1) for any given angular momentum, particles with sufficiently high energy can overcome the centrifugal barrier and fall in, and 2) particles with low (not zero as in the Newtonian case) angular momentum are captured by the hole [61]. The Paczynski-Wiita potential obtains the correct general relativistic result for marginally stable (corresponding to $r = 3r_g$ and $l = 2\sqrt{3}GM_*/c$, within which all orbits are unstable), and

the marginally bound orbit (with $r = 2r_g$ and $l = 4GM_*/c$, particles with $E > 0$ can fall directly on to the hole for specific angular momentum smaller than this). Figure A.1 shows the Newtonian, and the Paczynski-Wiita potential for a marginally bound orbit, with $l = 4GM_*/c$.

The presence of a last stable orbit has important consequences for accretion efficiency; beyond this, matter plunges in the black hole with no time to radiate. Thus, for a Schwarzschild black hole, matter radiates half the released gravitational energy (and retains the other half as the kinetic energy) till the last stable orbit ($3r_g$). This gives a radiative efficiency of $\eta = (GM_*/6r_g)/c^2 = 1/12$. The relativistic relativistic result of 6% is not too far off. For a rotating Kerr hole the last stable orbit moves further in, resulting in a larger efficiency; a maximally rotating black hole has an efficiency of 42.3% (see [133] for detailed introduction to spinning black holes).

A.2 Bondi accretion

Bondi accretion [35], a model for steady, spherical accretion of matter with vanishing angular momentum (e.g., a star accreting from a stationary gas cloud), is commonly used to estimate the accretion rate $\dot{M}$ from the measurement of ambient density and temperature. The following presentation is based on [61].

We will solve the spherically symmetric, hydrodynamic equations in steady state using spherical polar coordinates (r, θ, ϕ) with origin at the center of the star. The fluid variables are independent of θ and ϕ, and the gas has only a radial velocity component $V_r = V$. The equation of continuity

$$\frac{1}{r^2}\frac{d}{dr}\left(r^2 \rho V\right) = 0, \tag{A.3}$$

gives a constant inward flux of matter $\dot{M} = -4\pi r^2 \rho V$ = constant; for accretion

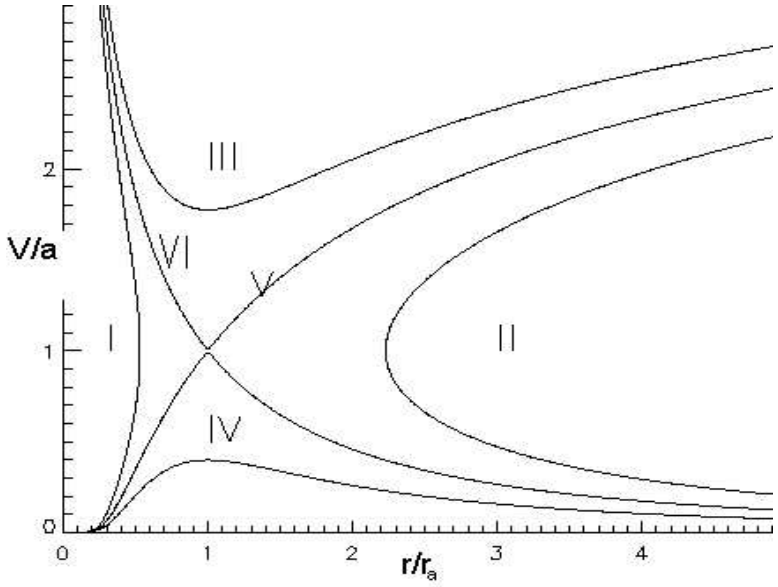

Figure A.2: Mach number (the ratio of fluid velocity and sound speed) as a function of radius for spherical accretion with different inner and outer boundary conditions. Solution VI corresponds to accretion and V to a spherical wind. Taken from Alan Hood's lecture notes, http://www-solar.mcs.st-and.ac.uk/˜alan/sun_course/.

$V < 0$, as matter falls in. The Euler equation becomes

$$V\frac{dV}{dr} + \frac{1}{\rho}\frac{dp}{dr} + \frac{GM_*}{r^2} = 0. \tag{A.4}$$

A polytropic equation of state is used, $p = K\rho^\gamma$, with $1 < \gamma < 5/3$.

Using $dP/dr = a^2 d\rho/dr$, where $a = \sqrt{\gamma p/\rho}$ is the sound speed, the continuity and Euler equations can be combined to give

$$\frac{1}{2}\left(1 - \frac{a^2}{V^2}\right)\frac{d}{dr}V^2 = -\frac{GM_*}{r^2}\left[1 - \left(\frac{2a^2 r}{GM_*}\right)\right]. \tag{A.5}$$

This form is useful to draw inferences about steady, spherically symmetric accretion. At large distances ($r \gg GM_*/2a^2$), the right side of Eq. A.5 is positive, and $dV^2/dr < 0$ at large distances where gas is expected to be at rest. This implies that the gas is subsonic ($V^2 < a^2$) for $r \gg GM_*/2a^2$; this is reasonable because far from the star, the

gas has a non-zero temperature. One need to specify the inner boundary condition in addition to the outer (ambient) boundary conditions to uniquely specify the solution; we choose $V^2 > a^2$ for small r for accretion (see Figure A.2).

At a radius $r_a = GM_*/2a^2$, either $V^2 = a^2$ or $d/dr(V^2) = 0$; latter is true for accretion solution with a supersonic flow for $r < r_a$. The sonic point condition, $r_a = GM_*/2a^2$ leads to the relation between the accretion rate $\dot{M}$ and the ambient conditions. The integral form of Eq. A.4 is the Bernoulli integral:

$$\frac{V^2}{2} + \frac{a^2}{\gamma - 1} - \frac{GM}{r} = \text{Be, a constant.} \tag{A.6}$$

The boundary condition at $r \to \infty$, and the sonic point condition $a^2(r_a) = GM_*/2r_a$ combine to give $a(r_a) = a(\infty)\sqrt{2/(5-3\gamma)}$, which leads to the constant accretion rate in terms of sonic point variables, $\dot{M} = 4\pi r_a^2 \rho(r_a) a(r_a)$. Since $a \propto \rho^{\gamma-1}$,

$$\rho(r_a) = \rho(\infty) \left[\frac{a(r_a)}{a(\infty)}\right]^{2/(\gamma-1)}; \tag{A.7}$$

this combined with $\dot{M}$ in terms of sonic point variables gives the required expression for $\dot{M}$ in terms of conditions at infinity:

$$\dot{M} = \pi G^2 M_*^2 \frac{\rho(\infty)}{a^3(\infty)} \left[\frac{2}{5-3\gamma}\right]^{(5-3\gamma)/2(\gamma-1)}. \tag{A.8}$$

The dependence of $\dot{M}$ on γ is weak. For $\gamma = 1.4$, Eq. A.8 gives

$$\dot{M} \cong 1.4 \times 10^{11} \left(\frac{M}{M_\odot}\right) \left(\frac{\rho(\infty)}{10^{-24}\ \text{g cm}^{-3}}\right) \left(\frac{a(\infty)}{10\ \text{km s}^{-1}}\right)^{-3}\ \text{g s}^{-1}. \tag{A.9}$$

For $r \ll r_a$, matter falls freely, $v^2 \cong 2GM_*/r$; the continuity equation gives $\rho \cong \rho(r_a)(r_a/r)^{3/2}$ for $r < r_a$. One can define an effective accretion radius, beyond which the thermal energy of the gas is larger than the gravitational binding energy.

The ratio of the thermal and gravitational binding energy is $(ma^2(r)/2)/(GM_*m/r) \sim r/r_{acc}$, for $r \gtrsim r_{acc}$, since $a(r) \sim a(\infty)$ for $r > r_{acc} \equiv 2GM_*/a^2(\infty)$ [61]. Hence, for $r \gg r_{acc}$ the gravitational pull of the star has negligible effect on the gas. In terms of the Bondi radius, an approximation for the mass accretion rate is given by $\dot{M} \sim \pi r_{acc}^2 a(\infty)\rho(\infty)$.

Appendix B

Linear closure for high and low collisionality

B.1 Closure for high collisionality: $|\zeta| \gg 1$

For $|\zeta| \gg 1$, $Z(\zeta) \approx -1/\zeta - 1/2\zeta^3 - 3/4\zeta^5$, $R \approx -1/2\zeta^2 - 3/4\zeta^4$, $1 + 2\zeta^2 R \approx -3/2\zeta^2 - 15/4\zeta^4$, $Z - 2\zeta R \approx 1/\zeta^3 + 3/\zeta^5$. Equation (3.26) then becomes

$$\frac{\delta n}{n_0} - \frac{\delta p_\perp}{p_0} = -\frac{\delta B}{B_0}\left(1 + \frac{1}{2\zeta^2}\right) - \frac{\zeta_2}{\zeta}\left(1 + \frac{1}{2\zeta^2}\right)\left(\frac{\delta T}{T_0} - \frac{\delta B}{B_0}\right). \tag{B.1}$$

Assuming $|\zeta_1/\zeta_2| \ll 1$ (a high collisionality limit $\omega \ll \nu$) and using the binomial expansion we get

$$\frac{\delta n}{n_0} - \frac{\delta p_\perp}{p_0} = -\left\{1 - \frac{\zeta_1}{\zeta_2} + \frac{1}{\zeta_2^2}\left(\frac{1}{2} + \zeta_1^2\right) - \frac{\zeta_1}{\zeta_2^3}\left(\frac{1}{2} + \zeta_1^2\right)\right\}\left(\frac{\zeta_1}{\zeta_2}\frac{\delta B}{B_0} + \frac{\delta T}{T_0}\right). \tag{B.2}$$

To the lowest nonvanishing order one gets

$$\frac{\delta n}{n_0}\frac{\zeta_1}{\zeta_2} - \frac{\delta p_\perp}{p_0}\left(\frac{1}{3} + \frac{2}{3}\frac{\zeta_1}{\zeta_2}\right) + \frac{\delta p_\parallel}{p_0}\left(\frac{1}{3} - \frac{\zeta_1}{3\zeta_2}\right) = -\frac{\zeta_1}{\zeta_2}\frac{\delta B}{B_0}. \tag{B.3}$$

Expanding equation (3.27) gives

$$-\frac{\delta n}{n_0}\left(\frac{3}{2\zeta^2}+\frac{15}{4\zeta^4}\right)+\frac{\delta p_\parallel}{p_0}\left(\frac{1}{2\zeta^2}+\frac{3}{4\zeta^4}\right)=-\frac{\delta B}{B_0}\left(\frac{1}{\zeta^2}+\frac{3}{\zeta^4}\right)$$
$$+\left(\frac{\delta B}{B_0}-\frac{\delta n}{n_0}+\frac{\delta T}{2T_0}\right)\zeta_2\left(\frac{1}{\zeta^3}+\frac{3}{\zeta^5}\right). \tag{B.4}$$

Again using the binomial expansion for $|\zeta_1/\zeta_2| \ll 1$ we get

$$\frac{\delta n}{n_0}\left(-\frac{3}{2}\frac{\zeta_1}{\zeta_2}+\frac{9}{2}\left(\frac{\zeta_1}{\zeta_2}\right)^2+\frac{3}{4\zeta_2^2}\right)+\frac{\delta p_\parallel}{p_0}\left(\frac{1}{3}-\frac{1}{2}\frac{\zeta_1}{\zeta_2}+\frac{1}{2}\left(\frac{\zeta_1}{\zeta_2}\right)^2+\frac{1}{4\zeta_2^2}\right)$$
$$+\frac{\delta p_\perp}{p_0}\left(-\frac{1}{3}+\frac{\zeta_1}{\zeta_2}-2\left(\frac{\zeta_1}{\zeta_2}\right)^2-\frac{1}{\zeta_2^2}\right)=\frac{\delta B}{B_0}\left(-\frac{\zeta_1}{\zeta_2}+3\left(\frac{\zeta_1}{\zeta_2}\right)^2\right). \tag{B.5}$$

The lowest order solution is

$$-\frac{3\zeta_1}{2\zeta_2}\frac{\delta n}{n_0}+\left(\frac{1}{3}-\frac{\zeta_1}{2\zeta_2}\right)\frac{\delta p_\parallel}{p_0}+\left(-\frac{1}{3}+\frac{\zeta_1}{\zeta_2}\right)\frac{\delta p_\perp}{p_0}=-\frac{\zeta_1}{\zeta_2}\frac{\delta B}{B_0}. \tag{B.6}$$

We shall expand the parallel and perpendicular pressure perturbations as $\delta p_\perp = \delta^0 p_\perp + \zeta_1/\zeta_2 \delta^1 p_\perp + (\zeta_1/\zeta_2)^2 \delta^2 p_\perp + ...$ and $\delta p_\parallel = \delta^0 p_\parallel + \zeta_1/\zeta_2 \delta^1 p_\parallel + (\zeta_1/\zeta_2)^2 \delta^2 p_\parallel + ...$ From equations (B.2) and (B.5) one gets $\delta^0 p_\parallel/p_0 = \delta^0 p_\perp/p_0 = 5\delta n/3n_0$ for the lowest order, and $(\delta p_\perp - \delta^1 p_\parallel)/p_0 = 3\delta B/B_0 - 2\delta n/n_0$. To the next order we can expand the solution as

$$\frac{\delta p_\parallel}{p_0}=\frac{5\delta n}{3n_0}+\frac{\zeta_1}{\zeta_2}\frac{\delta^1 p_\parallel}{p_0}+\left(\frac{\zeta_1}{\zeta_2}\right)^2\frac{\delta^2 p_\parallel}{p_0}, \tag{B.7}$$
$$\frac{\delta p_\perp}{p_0}=\frac{5\delta n}{3n_0}+\frac{\zeta_1}{\zeta_2}\left(\frac{\delta^1 p_\parallel}{p_0}+3\frac{\delta B}{B_0}-2\frac{\delta n}{n_0}\right)+\left(\frac{\zeta_1}{\zeta_2}\right)^2\frac{\delta^2 p_\perp}{p_0}. \tag{B.8}$$

To the next order in ζ_1/ζ_2 in equation (B.2) one gets

$$-\frac{1}{2\zeta_1^2}\frac{\delta n}{n_0}+\frac{1}{2}\frac{\delta^1 p_\parallel}{p_0}+\frac{1}{3}\left(\frac{\delta^2 p_\parallel}{p_0}-\frac{\delta^2 p_\perp}{p_0}\right)=0. \tag{B.9}$$

To the next order in equation (B.5) we get

$$\left(2+\frac{1}{3\zeta_1^2}\right)\frac{\delta n}{n_0}-\frac{\delta^1 p_\parallel}{p_0}+\frac{1}{3}\left(\frac{\delta^2 p_\parallel}{p_0}-\frac{\delta^2 p_\perp}{p_0}\right)=\frac{3\delta B}{B_0}. \tag{B.10}$$

Equations (3.29) and (3.30) follow from equations (B.9) and (B.10).

B.2 Closure for low collisionality: $|\zeta| \ll 1$

This regime is useful for low collisionality $\nu \ll k_\parallel c_0$ and high β, where the MRI is low frequency as compared to the sound wave frequency. Using the asymptotic expansion for $|\zeta| \ll 1$, $Z(\zeta) \approx i\sqrt{\pi}(1-\zeta^2)-2\zeta$ and $R(\zeta) \approx 1+i\sqrt{\pi}-2\zeta^2$, we simplify equation (3.26) to get

$$\frac{\delta n}{n_0}-\frac{\delta p_\perp}{p_0}=\frac{\delta B}{B_0}\zeta\left(i\sqrt{\pi}-2\zeta\right)+\left(\frac{\delta T}{T_0}-\frac{\delta B}{B_0}\right)\zeta_2\left(i\sqrt{\pi}-2\zeta\right). \tag{B.11}$$

The lowest order term in ζ gives $\delta p_\perp/p_0 = \delta n/n_0$. Let $\delta p_\perp/p_0 \approx \delta n/n_0 + \zeta\delta^1 p_\perp/p_0$. To the next order one gets

$$\zeta\frac{\delta^1 p_\perp}{p_0}=-i\sqrt{\pi}\zeta\frac{\delta B}{B_0}+i\sqrt{\pi}\zeta_2\frac{\delta B}{B_0}=-i\sqrt{\pi}\zeta_1\frac{\delta B}{B_0}. \tag{B.12}$$

Therefore to second order in ζ, $\delta p_\perp/p_0 \approx \delta n/n_0 - i\sqrt{\pi}\zeta_1\delta B/B_0 + \zeta^2\delta^2 p_\perp/p_o$. On using the asymptotic formula for Z and R in equation (3.27), one gets

$$\frac{\delta n}{n_0}-\left(1+i\sqrt{\pi}\zeta\right)\frac{\delta p_\parallel}{p_0}=-i\sqrt{\pi}\zeta\frac{\delta B}{B_0}-\zeta_2\left(i\sqrt{\pi}-4\zeta\right)\left(\frac{\delta n}{n_0}-\frac{\delta T_\parallel}{2T_0}-\frac{\delta B}{B_0}\right). \tag{B.13}$$

To the lowest order one gets $\delta p_\parallel/p_0 = \delta n/n_0$, so let $\delta p_\parallel/p_0 \approx \delta n/n_0 + \zeta\delta^1 p_\parallel/p_0$. To the next order,

$$\zeta\frac{\delta^1 p_\parallel}{p_0}=-i\sqrt{\pi}\zeta_1\frac{\delta n}{n_0}+i\sqrt{\pi}\zeta_1\frac{\delta B}{B_0}. \tag{B.14}$$

Therefore through second order $\delta p_{\parallel}/p_0 \approx \delta n/n_0 + i\sqrt{\pi}\zeta_1 \left(\delta B/B_0 - \delta n/n_0\right) + \zeta^2\delta^2 p_{\parallel}/p_0$. The comparison of the terms of the order ζ^2 in equation (3.26) give

$$\zeta^2 \frac{\delta^2 p_{\perp}}{p_0} = 2\zeta_1\zeta\frac{\delta B}{B_0} - \frac{\pi}{3}\zeta_1\zeta_2\left(\frac{\delta B}{B_0} + \frac{\delta n}{n_0}\right), \tag{B.15}$$

and the terms of the order ζ^2 in equation (3.27) give

$$\zeta^2 \frac{\delta^2 p_{\parallel}}{p_0} = \left(4\zeta_1\zeta_2 - \pi\zeta_1^2 - \frac{7\pi}{6}\zeta_1\zeta_2\right)\frac{\delta n}{n_0} + \left(\sqrt{\pi}\zeta_1\zeta - \frac{\pi}{6}\zeta_1\zeta_2 - 2\zeta^2 - 4\zeta_2\zeta\right)\frac{\delta B}{B_0}. \tag{B.16}$$

From equations (B.15) and (B.16) the asymptotic expansion in equations (3.31) and (3.32) follow.

Appendix C

Kinetic MHD simulations: modifications to ZEUS

C.1 Grid and variables

Figure C.1 shows the location of variables on the grid. Scalars and diagonal components of second rank tensors (ρ, $p_\parallel$, and $p_\perp$) are zone centered. Vectors, representing fluxes out of the box, are located at the cell faces ($\mathbf{V}$, $\mathbf{B}$, and $\mathbf{q}_{\parallel,\perp}$). The inductive electric field ($\mathbf{E}$) is located at cell edges such that the contribution of each edge in calculating $\oint \mathbf{E}\cdot\mathbf{dl}$ over the whole box cancels, and $\nabla\cdot\mathbf{B}=0$ is satisfied to machine precision. The off diagonal part of the pressure tensor in Cartesian coordinates is related to $\mathbf{\Pi} = \hat{\mathbf{b}}\hat{\mathbf{b}}(p_\parallel - p_\perp)$. This is a symmetric tensor whose components Pxy, Pxz, and Pyz are located such that the finite difference formulae for the evolution of velocities due to off diagonal components of stress are given by

$$Vx_{i,j,k}{}^{n+1} = Vx_{i,j,k}{}^{n} - \frac{\delta t}{\delta y}(Pxy^n_{i,j+1,k} - Pxy^n_{i,j,k}) - \frac{\delta t}{\delta z}(Pxz^n_{i,j,k+1} - Pxz^n_{i,j,k}) \quad \text{(C.1)}$$

$$Vy_{i,j,k}{}^{n+1} = Vy_{i,j,k}{}^{n} - \frac{\delta t}{\delta x}(Pxy^n_{i+1,j,k} - Pxy^n_{i,j,k}) - \frac{\delta t}{\delta z}(Pyz^n_{i,j,k+1} - Pyz^n_{i,j,k}) \quad \text{(C.2)}$$

$$Vz_{i,j,k}{}^{n+1} = Vz_{i,j,k}{}^{n} - \frac{\delta t}{\delta x}(Pxz^n_{i+1,j,k} - Pxz^n_{i,j,k}) - \frac{\delta t}{\delta y}(Pyz^n_{i,j+1,k} - Pyz^n_{i,j,k}) \quad \text{(C.3)}$$

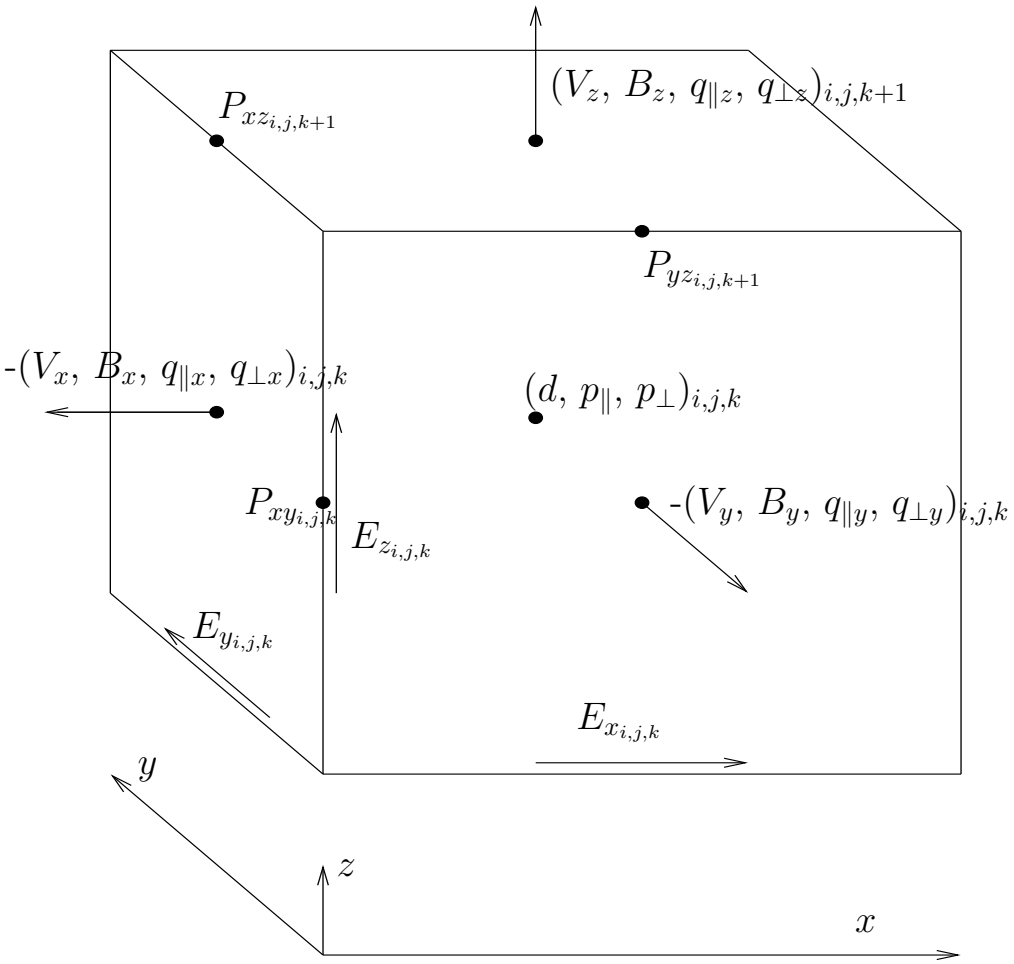

Figure C.1: Location of different variables on a 3-D staggered grid. Vectors $\mathbf{V}$, $\mathbf{B}$, and $\mathbf{q}_{\parallel,\perp}$ are located at the face centers. Density (ρ) and diagonal components of the pressure tensor ($p_\perp$, $p_\parallel$) are located at the zone centers. EMF's (E_x, E_y, E_z), and off diagonal components of the pressure tensor (P_{xy}, P_{xz}, P_{yz}) are located on appropriate edges.

C.1.1 Determination of δt: Stability and positivity

A time explicit algorithm must limit the time step in order to satisfy the Courant-Friedrichs-Levy (CFL) stability condition. Physically, δt must be smaller than the time it takes any signal (via fluid or wave motion) to cross one grid zone. There is also a limit imposed on δt for numerical stability of the diffusive steps. Additionally, since there are quantities which must be positive definite (ρ, $p_\parallel$, $p_\perp$), we also require δt to satisfy positivity. We adopt the following procedure to choose δt:

$$\delta t_{adv} = \frac{\min\{\delta x, \delta y, \delta z\}}{(|V| + |V_A| + |V_s| + |\Omega L_x|)}, \tag{C.4}$$

$$\delta t_\parallel = \frac{\min\{\delta x^2, \delta y^2, \delta z^2\}}{2\kappa_\parallel}, \tag{C.5}$$

$$\delta t_\perp = \frac{\min\{\delta x^2, \delta y^2, \delta z^2\}}{2\kappa_\perp}, \tag{C.6}$$

where $V_A = B/\sqrt{4\pi}$ is the Alfvén speed, and $V_s = \max\{\sqrt{3p_\parallel/\rho}, \sqrt{2p_\perp/\rho}\}$ is the maximum sound speed, taking the anisotropy into account. δt_{adv}, $\delta t_\parallel$, and and $\delta t_\perp$ correspond to limits on the time step for stability to advection, and parallel and perpendicular heat conduction, respectively.

The source steps for $p_\parallel$ and $p_\perp$ are given by

$$\frac{p_\parallel^{n+1} - p_\parallel^n}{\delta t} = \left(-\nabla\cdot\mathbf{q}_\parallel - 2p_\parallel\hat{\mathbf{b}}\cdot\nabla\mathbf{V}\cdot\hat{\mathbf{b}} + 2q_\perp\nabla\cdot\hat{b}\right)^n = A1, \tag{C.7}$$

$$\frac{p_\perp^{n+1} - p_\perp^n}{\delta t} = \left(-\nabla\cdot\mathbf{q}_{\perp\mathbf{T}} - p_\perp\nabla\cdot\mathbf{V} + p_\perp\hat{\mathbf{b}}\cdot\nabla\mathbf{V}\cdot\hat{\mathbf{b}} - q_\perp\nabla\cdot\hat{b}\right)^n = A2, \tag{C.8}$$

where $\mathbf{q}_{\perp\mathbf{T}} = -\kappa_\perp\nabla_\parallel T_\perp$ denotes the temperature gradient part of $\mathbf{q}_\perp$. For positivity of $p_\parallel^{n+1}$ and $p_\perp^{n+1}$ we require that the following conditions are satisfied: whenever $A1$ and $A2$ are negative, $\delta t_{pos} = \min\{-p_\parallel^n/A1, -p_\perp^n/A2\}$; if $A1 > 0$, $A2 < 0$, then $\delta t_{pos} = -p_\perp^n/A2$; if $A1 < 0$, $A2 > 0$, then $\delta t_{pos} = -p_\parallel^n/A1$. Thus, our final constraint

on the timestep δt is given by

$$\delta t = C_0 \times \min\left\{1/[\max\{\delta t_{adv}^{-2} + \delta t_{\parallel}^{-2} + \delta t_{\perp}^{-2}\}]^{1/2}, \min\{\delta t_{pos}\}\right\} \tag{C.9}$$

where the max and min are taken over all zones in the box and C_0 is a safety factor (Courant Number) which we take to be 0.5.

C.2 Implementation of the pressure anisotropy "hard wall"

If the pressure anisotropy is larger than the constraints given in §2 by equations (4.33)-(4.35), then microinstabilities will turn on that will enhance the pitch-angle scattering rate and quickly reduce the pressure anisotropy to near marginal stability. Because this is a numerically stiff problem, we use an implicit approach, following the treatment of [26]. Whenever equation (4.33) is violated, we use the following prescription for pitch angle scattering:

$$p_{\parallel}^{n+1} = p_{\parallel}^{n} - \frac{2}{3}\nu_p \delta t \left(\frac{p_{\parallel}^{n+1}}{2} - p_{\perp}^{n+1} - \frac{B^2}{4\pi}\right), \tag{C.10}$$

$$p_{\perp}^{n+1} = p_{\perp}^{n} + \frac{1}{3}\nu_p \delta t \left(\frac{p_{\parallel}^{n+1}}{2} - p_{\perp}^{n+1} - \frac{B^2}{4\pi}\right), \tag{C.11}$$

where ν_p is a very large ($\gg 1/\delta t$) rate at which marginal stability is approached. This implicit implementation (which can be solved by inverting a 2×2 matrix) with large ν_p ensures that each time step the pressure anisotropy will drop to be very near marginal stability for the firehose instability to break μ invariance. Given this pitch angle scattering, the collisionality parameter ν_{eff} in the thermal conductivity (Eqs. 4.43-4.45) is obtained by comparing equations (C.10) and (C.11) with equations

(4.39) and (4.40):

$$\nu_{eff} = \max\left\{\nu_p \frac{\left(\frac{p_\parallel^{n+1}}{2} - p_\perp^{n+1} - \frac{B^2}{4\pi}\right)}{\left(p_\parallel^{n+1} - p_\perp^{n+1}\right)}, \nu\right\}. \tag{C.12}$$

The effective pitch angle scattering rate ν_{eff} is independent of ν_p (and much smaller than ν_p) in the limit of large ν_p, and is by definition just large enough to balance other terms in equations (4.39-4.40) that are trying to increase the pressure anisotropy beyond marginal stability.

The prescriptions for pitch angle scattering due to mirror modes and ion cyclotron waves are similar. For mirror modes we use

$$p_\parallel^{n+1} = p_\parallel^n - \frac{2}{3}\nu_p \delta t \left(p_\parallel^{n+1} - p_\perp^{n+1} + 2\xi \frac{p_\parallel^{n+1}}{\beta_\perp^{n+1}}\right), \tag{C.13}$$

$$p_\perp^{n+1} = p_\perp^n + \frac{1}{3}\nu_p \delta t \left(p_\parallel^{n+1} - p_\perp^{n+1} + 2\xi \frac{p_\parallel^{n+1}}{\beta_\perp^{n+1}}\right) \tag{C.14}$$

to limit the pressure anisotropy ($\xi = 3.5$ for our fiducial run $Zl4$) and ν_{eff} is given by

$$\nu_{eff} = \max\left\{\nu_p \frac{\left(p_\parallel^{n+1} - p_\perp^{n+1} + 2\xi \frac{p_\parallel^{n+1}}{\beta_\perp^{n+1}}\right)}{\left(p_\parallel^{n+1} - p_\perp^{n+1}\right)}, \nu\right\}. \tag{C.15}$$

For ion cyclotron pitch angle scattering we use

$$p_\parallel^{n+1} = p_\parallel^n - \frac{2}{3}\nu_p \delta t \left(p_\parallel^{n+1} - p_\perp^{n+1} + S \frac{p_\parallel^{n+1}}{\sqrt{\beta_\parallel^{n+1}}}\right), \tag{C.16}$$

$$p_\perp^{n+1} = p_\perp^n + \frac{1}{3}\nu_p \delta t \left(p_\parallel^{n+1} - p_\perp^{n+1} + S \frac{p_\parallel^{n+1}}{\sqrt{\beta_\parallel^{n+1}}}\right), \tag{C.17}$$

and ν_{eff} is given by

$$\nu_{eff} = \max\left\{ \nu_p \frac{\left(p_\parallel^{n+1} - p_\perp^{n+1} + S\frac{p_\parallel^{n+1}}{\sqrt{\beta_\parallel^{n+1}}}\right)}{\left(p_\parallel^{n+1} - p_\perp^{n+1}\right)}, \nu \right\}. \tag{C.18}$$

C.2.1 Implementation of the advective part of $\nabla \cdot \mathbf{q}_\perp$

The flux of $p_\perp$, $\mathbf{q}_\perp = q_\perp \hat{\mathbf{b}}$, is given by

$$q_\perp = -\kappa_\perp \nabla_\parallel \left(\frac{p_\perp}{\rho}\right) + \left[\frac{(p_\parallel - p_\perp)}{\rho\left(\sqrt{\frac{\pi}{2}\frac{p_\parallel}{\rho}}k_L + \nu_{eff}\right)}\frac{\mathbf{B}\cdot\nabla B}{B^2}\right] p_\perp = -\kappa_\perp \nabla_\parallel \left(\frac{p_\perp}{\rho}\right) + V_{mag} p_\perp \tag{C.19}$$

where the quantity in square brackets can be thought of as an advection speed due to parallel magnetic gradients. Because of this term, $\mathbf{q}_\perp$ is not a purely diffusive operator, but also has an advective part characterized by the velocity V_{mag}. If one treats the advective part via a simple central difference method, it does not preserve monotonicity. Instead, to treat the advective part of $\mathbf{q}_\perp$ properly, we include the advective part in the transport step. After including the advective heat flux in the transport step, it takes the form

$$\frac{\partial p_\perp}{\partial t} + \nabla \cdot \left[(\mathbf{V} + V_{mag}\hat{\mathbf{b}})p_\perp\right] = 0. \tag{C.20}$$

Thus, for updating $p_\perp$ in the transport step we calculate fluxes on the cell faces using $\mathbf{V} + V_{mag}\hat{\mathbf{b}}$ instead of just $\mathbf{V}$. The transport step is then directionally split in the three directions. The procedure for monotonicity preserving schemes for calculating fluxes is described in [185].

C.3 Numerical tests

The kinetic modifications to the ZEUS MHD code have been tested for the ability to capture the collisionless effects.

C.3.1 Tests for anisotropic conduction

The kinetic MHD code used for the shearing box simulations of the collisionless MRI uses the asymmetric method for anisotropic thermal conduction [177]. Although, the asymmetric method can result in negative temperature, its fine to use it for local simulations as there are no sharp temperature gradients (see Chapter 5). Anisotropic conduction tests have been discussed extensively in Chapter 5.

C.3.2 Collisionless damping of fast mode in 1-D

We initialize a fast wave eigenmode traveling along the field lines to verify that the Landau closure reproduces the correct damping rate. We choose the following parameters: $\rho_0 = 1.0$, $p_{\parallel 0} = p_{\perp 0} = 10^{-6}$, $kV_{A0} = 10^{-3}$, and $\beta = 10$. A periodic box with the size of two wavelengths is used. Since we initialize a parallel propagating fast mode, there is no magnetic perturbation, and the initial eigenmode is given by

$$\delta\rho = A\cos(kz), \tag{C.21}$$

$$\delta p_{\parallel} = A10^{-6}\left(3p\cos(kz) + 1.36\sin(kz)\right), \tag{C.22}$$

$$\delta p_{\perp} = A10^{-6}\cos(kz), \tag{C.23}$$

$$\delta V_z = A\left(0.0015\cos(kz) + 0.00046\sin(kz)\right), \tag{C.24}$$

where A=0.01 is the amplitude. Figure C.2 shows the results from the ZEUS code modified to include kinetic effects. Simulation recovers the correct phase speed and damping rate. Velocity perturbations are damped and the energy goes to internal

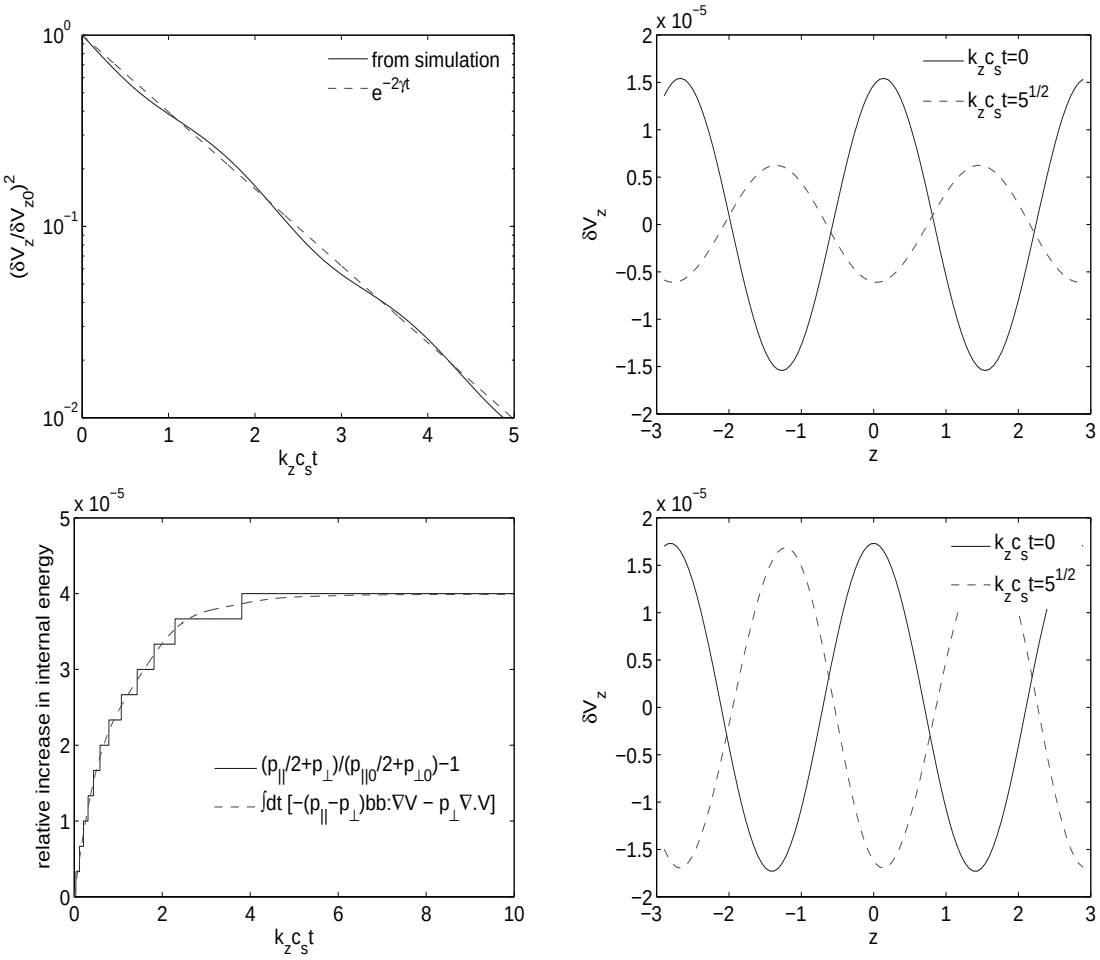

Figure C.2: Figure on top left shows damping of kinetic energy in time; solid line is from the simulation and the dashed line is the result from eigenmode analysis in MATHEMATICA. Top right figure shows the initial eigenmode (solid line) and the damped eigenmode (dashed line) at a later time. Bottom left figure shows the increase in internal energy (solid line) and the result expected from the heating term (dashed line). Bottom right figure shows the initial fast mode eigenmode (solid line) and the eigenmode at a late time (dashed line) with the CGL equation of state, and as expected, there is no damping.

energy. Figure also shows that a fast mode eigenmode in the CGL limit shows no damping.

Since the magnetic perturbation vanishes for this case, there is no $-\mu\nabla_\parallel B$ Barnes damping. This leaves only the parallel $eE_\parallel$ Landau damping. With $eE_\parallel = ik\delta p_\parallel (m_e/m_i)/n$, assuming cold electrons, Landau damping is hidden in pressure terms in the equation of motion and the internal energy equation.

C.3.3 Mirror instability in 1-D

The mirror instability criterion in the CGL limit is $p_\perp/6p_\parallel - 1 - 1/\beta_\perp > 0$ as compared to the criterion in the kinetic regime, $p_\perp/p_\parallel - 1 - 1/\beta_\perp > 0$ [110, 180]. We test Landau closure by initializing an anisotropic pressure ($p_\perp/p_\parallel = 2.5$, $\beta_\parallel = 1$) which is unstable according to the kinetic criterion but stable by the CGL criterion. Landau closure with parameter $k_L = 12\pi/L$ (gives correct kinetic behavior for 6 wavelengths in the box, for larger wavenumber growth rate is faster than the kinetic result, see Figure 2.1). Figure C.3 shows the results of nonlinear simulations initialized with a small amplitude random white noise. Pressure anisotropy is reduced to marginality with time. Particles are trapped in low magnetic field regions due to the mirror force, and density and magnetic field strengths are anticorrelated. Growth rate increases linearly with the resolution, as $\gamma \propto k_\parallel$.

For small pressure anisotropy, adiabatic invariance is obeyed and plasma rearranges itself in the form form of mirrors and becomes marginally stable. These 1-D results are consistent with previous fluid [20] and kinetic [127] studies. Similar 1-D tests for the firehose instability results have shown results consistent with the previous kinetic simulations [162]. Here too, the growth rate is proportional to the grid resolution (as $\gamma \propto k_\parallel$). Fastest growing firehose mode is the one with a parallel wavenumber. The transverse magnetic field disturbances grow until the plasma becomes marginally stable to the firehose instability. A 2-D test for firehose instability

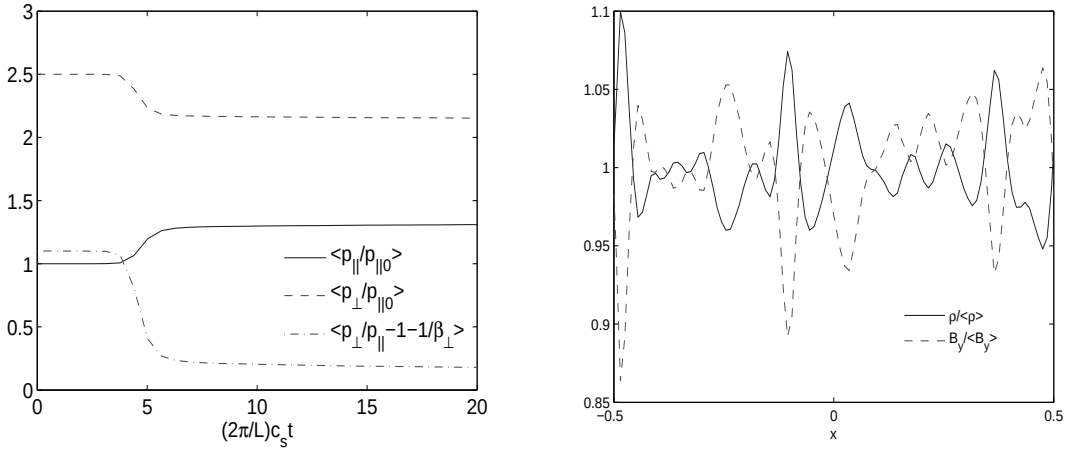

Figure C.3: Figure on left shows normalized parallel and perpendicular pressure (solid and dashed lines respectively), and difference from marginal stability, $p_\perp/p_\parallel - 1 - 1/\beta_\perp$ (dot-dashed line), with time. Pressure anisotropy is reduced towards marginal stability. Right figure shows anticorrelated density (solid line) and magnetic field strength (dashed line), normalized to their mean value, in saturated state ($c_{s\parallel}t/2\pi = 2$).

is discussed in the next section.

C.3.4 Shear generated pressure anisotropy: Firehose instability in 2-D

We have also devised a test problem where the magnetic field strength decreases because of the shear in the box; a decreasing field strength causes pressure to become anisotropic ($p_\parallel > p_\perp$). The firehose instability is excited when the pressure anisotropy increases beyond the firehose instability threshold ($p_\parallel/p_\perp - 1 - 2/\beta_\perp > 0$). The shearing rate is small so that the firehose instability locks the pressure anisotropy to the marginal value.

We use a 50×50 2-D box with $L_x = L_y = 1$, $p_{\parallel 0} = p_{\perp 0} = 0.1$, $\beta = 200$ with $B_{x0} = B_{y0}$, $V_y(-L_x/2) - V_y(L_x/2) = (3/2)\Omega L_x$ with $\Omega = 0.01$, and the collision frequency $\nu = 0.1$. The Landau parameter is $k_L = 0.5/\delta x$; firehose instability is insensitive to the parallel thermal conduction and the CGL equations give the correct

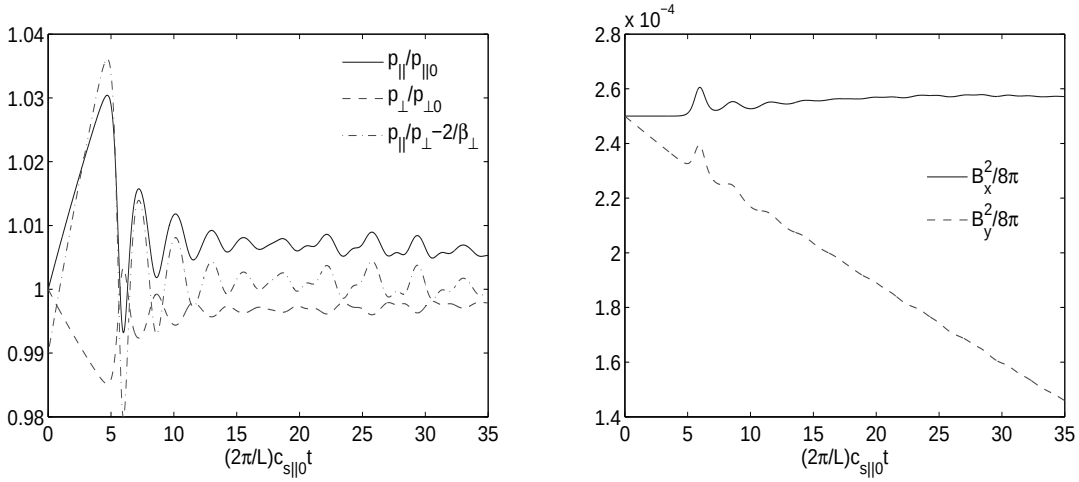

Figure C.4: Figure on the left shows normalized parallel (solid line) and perpendicular (dashed line) pressure, and the firehose marginal stability criterion (dot-dashed line), $p_\parallel/p_\perp - 2/\beta_\perp$. At early times pressure anisotropy is caused by the shear, but as the firehose instability sets in, pressure anisotropy saturates at the marginal state. Right figure shows magnetic field strengths, $B_x^2/8\pi$ (solid line) and $B_y^2/8\pi$ (dashed line). Magnetic strength in the $y-$ direction is reduced by the shear, but at late times there is a bump in field strengths showing the firehose instability.

instability threshold [110, 180]. Parameters are chosen such that the shearing rate is the smallest followed by the collision frequency and the sound crossing frequency, $\Omega \ll \nu \ll (2\pi/L)c_{s\parallel 0}$. In this ordering, plasma is effectively collisionless, and pressure anisotropy is driven slowly by the shear, so that the firehose instability saturates in the marginal state.

Figures C.4 and C.5 show the results: at early times $p_\parallel \propto B^{-2}$ increases and $p_\perp \propto B$ decreases as magnetic field decreases. When pressure anisotropy crosses the firehose threshold, the instability reduces the pressure anisotropy to the marginal state by increasing the transverse (to the mean magnetic field) magnetic perturbations.

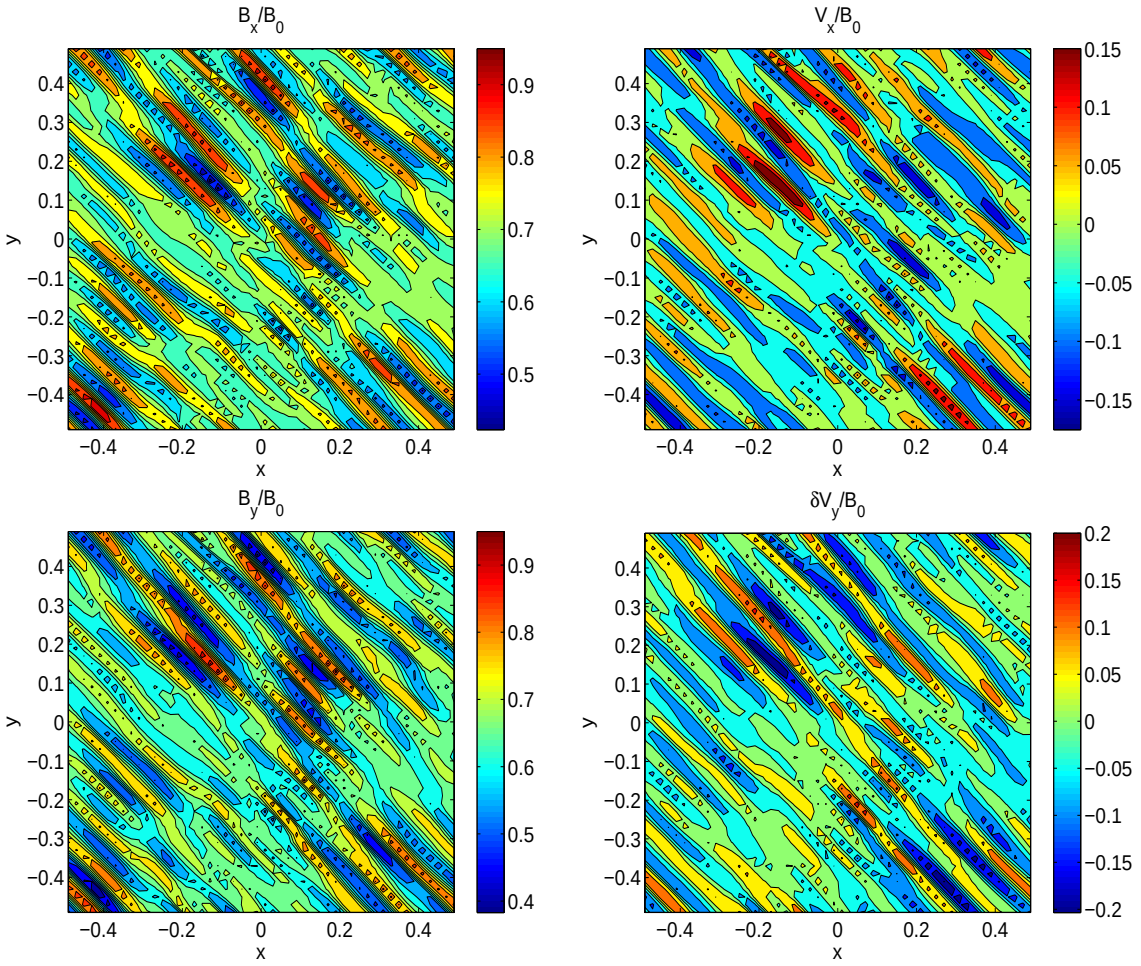

Figure C.5: The 2-D plots of B_x, V_x, B_y, and δV_y, normalized to the initial field strength, at $2\pi c_{s\|0} t \approx 8$. The initially random perturbations give rise to the firehose instability propagating primarily along the field lines.

Appendix D

Error analysis

The standard errors in the time averages reported in Table 4.2 and in Figure 4.7 are estimated by taking into account the finite correlation time for the physical quantities in the simulation, using techniques recommended by [144]. Given a finite time series, we want to calculate the ensemble average and the uncertainty around the ensemble average. The standard deviation of the time series does not represent the error (uncertainty) because the data in the time series are correlated.

For a time series with non-zero correlation time, the standard error for the time average $\langle x \rangle = \int dt\, x(t)/T$ of a signal $x(t)$ is given by $\sigma_{\langle x \rangle} = \sqrt{\mathrm{Var}(x)/N_{eff}}$, where $\mathrm{Var}(x) = \int dt\, (x(t) - \langle x \rangle)^2/T$ is the variance of x, $N_{eff} = T/(2\tau_{int})$ is the effective number of independent measurements, $T = 15$ orbits is the averaging time for the simulations described in Chapter 4, and τ_{int} is an estimate of the integrated autocorrelation time. There are significant subtleties in determining the integrated autocorrelation time from data. To deal with this, we use a windowing technique as recommended by [144], using $\tau_{int} = \int_0^T d\tau\, C(\tau) W(\tau/\tau_w)$, where $C(\tau)$ is the 2-time correlation function from the data, $W(\tau/\tau_w)$ is a smooth window function that cuts off the integral at $\tau \sim \tau_w$, and $\tau_w \sim \sqrt{T\tau_{int}}$ (this gives results insensitive to the choice of window width for $\tau_{int} \ll T$). If windowing is not used, i.e., $W = 1$, then the

integral for τ_{int} vanishes; therefore, an appropriate windowing function is necessary. The two-time autocorrelation function is defined as

$$C(\tau) = \frac{1}{T}\int_0^{T-\tau} dt\tilde{x}(t)\tilde{x}(t+\tau), \tag{D.1}$$

where $\tilde{x} = x - \langle x \rangle$. An example of the windowing function is the Hanning window given by [144]

$$\begin{aligned} H(\xi) &= \frac{1}{2}\left[1+\cos(\pi\xi)\right], |\xi| < 1 & \text{(D.2)} \\ &= 0, |\xi| \geq 1 & \text{(D.3)} \end{aligned}$$

Winters et. al. [200] found from comparing 3 realizations of shearing box MRI simulations that the magnetic stress had a variation of approximately $\pm 6.5\%$ after averaging over 85 orbits. The simulations we show here were averaged over 15 orbits, so extrapolating from [200] one might expect the uncertainties to be larger by a factor of $\approx \sqrt{85/15} \approx 2.4$. This is consistent with the typical error bars we report in Table 4.2 and Figure 4.7.

Appendix E

Entropy condition for an ideal gas

The entropy for an ideal gas is given by $S = nVk\ln(T^{1/(\gamma-1)}/n) + \text{const.}$, where n is the number density, V the volume, T the temperature, and γ the ratio of specific heats (= 5/3 for a 3-D mono-atomic gas). The change in entropy that results from adding an amount of heat dQ to a uniform gas is

$$dS = \frac{nVk}{\gamma - 1}\frac{dT}{T} = \frac{dQ}{T}.$$

We measure temperature in energy units, so $k = 1$ from now on. The rate of change of entropy of a system where number density and temperature can vary in space (density is assumed to be constant in time) is given by

$$\dot{S} \equiv \frac{\partial S}{\partial t} = -\int dV \frac{\nabla \cdot \mathbf{q}}{T} = -\int dV \frac{\mathbf{q} \cdot \nabla T}{T^2} = \int dV n\chi \frac{|\nabla_\parallel T|^2}{T^2} \geq 0, \tag{E.1}$$

where we use an anisotropic heat flux, $\mathbf{q} = -n\chi\hat{\mathbf{b}}\hat{\mathbf{b}}\nabla T$, and the integral is evaluated over the whole space with the boundary contributions assumed to vanish. The local entropy function is defined as $\dot{s} = -\mathbf{q} \cdot \nabla T/T^2$ can be integrated to calculate the rate of change of total entropy of the system.

In Chapter 5 we use a related function (the entropy-like function $\dot{s}^*$) defined as

$\dot{s}^* \equiv -\mathbf{q} \cdot \nabla T$ to limit the symmetric methods using face-pairs, and to prove some properties of different anisotropic diffusion schemes. The condition $-\mathbf{q} \cdot \nabla T \geq 0$ means that heat always flows from higher to lower temperatures.

Bibliography

[1] M. A. Abramowicz, X. Chen, S. Kato, J. P. Lasota, and O. Regev. Thermal equilibria of accretion disks. *Astrophys. J.*, 438(1):L37, 1995.

[2] N. Afshordi, B. Mukhopadhyay, and R. Narayan. Bypass to Turbulence in Hydrodynamic Accretion: Lagrangian Analysis of Energy Growth. *Astrophys. J.*, 629:373, 2005.

[3] E. Agol. Sagittarius A* Polarization: No Advection-dominated Accretion Flow, Low Accretion Rate, and Nonthermal Synchrotron Emission. *Astrophys. J.*, 538:121, 2000.

[4] D. K. Aitken, J. Greaves, A. Chrysostomou, T. Jenness, W. Holland, J. H. Hough, D. Pierce-Price, and J. Richer. Detection of Polarized Millimeter and Submillimeter Emission from Sagittarius A*. *Astrophys. J.*, 534:173, 2000.

[5] P. J. Armitage. Turbulence and Angular Momentum Transport in Global Accretion Disk Simulation. *Astrophys. J.*, 501:L189, 1998.

[6] J. Arons. Photon bubbles — Overstability in a magnetized atmosphere. *Astrophys. J.*, 388:561, 1992.

[7] F. K. Baganoff, M. W. Bautz, W. N. Brandt, G. Chartas, E. D. Feigelson, G. P. Garmire, Y. Maeda, M. Morris, G. R. Ricker, L. K. Townsley, and F. Walter.

Rapid X-ray flaring from the direction of the supermassive black hole at the Galactic Centre. *Nature*, 413(6851):45, 2001.

[8] F. K. Baganoff, Y. Maeda, M. Morris, M. W. Bautz, W. N. Brandt, W. Cui, J. P. Doty, F. D. Feigelson, G. P. Garmire, S. H. Pravdo, G. R. Ricker, and L. K. Townsley. Chandra X-ray Spectroscopic Imaging of Sagittarius A* and the Central Parsec of the Galaxy. *Astrophys. J.*, 591(2):891, 2003.

[9] J. Balbás and E. Tadmor. Non-oscillatory central schemes for one- and two-dimensional MHD equations. II: High-order semi-discrete schemes. *SIAM Journal of Scientific Computation, submitted*, 2006.

[10] S. A. Balbus. Stability, Instability, and "Backward" Transport in Stratified Fluids. *Astrophys. J.*, 534:420, 2000.

[11] S. A. Balbus. Convective and Rotational Stability of a Dilute Plasma. *Astrophys. J.*, 562:909, 2001.

[12] S. A. Balbus. Viscous Shear Instability in Weakly Magnetized, Dilute Plasmas. *Astrophys. J.*, 616:857, 2004.

[13] S. A. Balbus, C. F. Gammie, and J. F. Hawley. Fluctuations, dissipation and turbulence in accretion discs. *Mon. Not. R. Astron. Soc.*, 271:197, 1994.

[14] S. A. Balbus and J. F. Hawley. A powerful local shear instability in weakly magnetized disks. I — Linear analysis. *Astrophys. J.*, 376:214, 1991.

[15] S. A. Balbus and J. F. Hawley. A Powerful Local Shear Instability in Weakly Magnetized Disks. IV. Nonaxisymmetric Perturbations. *Astrophys. J.*, 400:610, 1992.

[16] S. A. Balbus and J. F. Hawley. Instability, turbulence, and enhanced transport in accretion disks. *Rev. Mod. Phys.*, 70:1, 1998.

[17] S. A. Balbus, J. F. Hawley, and J. M. Stone. Nonlinear Stability, Hydrodynamical Turbulence, and Transport in Disks. *Astrophys. J.*, 467:76, 1996.

[18] A. Barnes. Collisionless damping of hydromagnetic waves. *Phys. Fluids*, 9(8):1483, 1966.

[19] P. J. Basser and D. K. Jones. Diffusion-tensor MRI: theory, experimental design, and data analysis – a technical review. *NMR Biomed.*, 15:456, 2002.

[20] K. Baumgartel. Fluid approach to mirror mode structures. *Planetary Space Sc.*, 49:1239, 2001.

[21] B. J. Bayley, S. A. Orszag, and T. Herbert. Instability mechanisms in shear-flow transition. *Ann. Rev. Fluid Mech.*, 20:359, 1988.

[22] M. A. Beer, S. C. Cowley, and G. W. Hammett. Field-aligned Coordinates for Nonlinear Simulations of Tokamak Turbulence. *Phys. Plasmas*, 2:2687, 1995.

[23] M. C. Begelman. Photon Bubbles and the Vertical Structure of Accretion Disks. *Astrophys. J.*, 643:1065, 2006.

[24] M. C. Begelman and T. Chiueh. Thermal coupling of ions and electrons by collective effects in two-temperature accretion flows. *Astrophys. J.*, 332:872, 1988.

[25] P. L. Bhatnagar, E. P. Gross, and M. Krook. A model fo collision processes in gases, 1, small amplitude processes in charged and neutral one-component systems. *Phys. Rev.*, 94(3):511, 1954.

[26] J. Birn and M. Hesse. Geospace environment modeling (GEM) magnetic reconnection challenge: Resistive tearing, anisotropic pressure and hall effects. *J. Geophys. Res.*, 106(A3):3737, 2001.

[27] J. A. Biskamp. *Magnetohydrodynamic Turbulence*. Cambridge Univ. Press, Cambridge, 2003.

[28] E. G. Blackman, R. F. Penna, and P. Varniere. Empirical relation between angular momentum transport and thermal-to-magnetic pressure ratio in shearing box simulations. *astro-ph/0607119, submitted to Mon. Not. R. Astron. Soc.*, 2006.

[29] O. M. Blaes and S. A. Balbus. Local shear instabilities in weakly ionized, weakly magnetized disks. *Astrophys. J.*, 421(1):163, 1994.

[30] O. M. Blaes and A. Socrates. Local Dynamical Instabilities in Magnetized, Radiation Pressure-supported Accretion Disks. *Astrophys. J.*, 553(2):287, 2001.

[31] R. D. Blandford and M. C. Begelman. On the fate of gas accreting at a low rate on to a black hole. *Mon. Not. R. Astron. Soc.*, 303(1):L1, 1999.

[32] R. D. Blandford and M. C. Begelman. Two-dimensional adiabatic flows on to a black hole — I. fluid accretion. *Mon. Not. R. Astron. Soc.*, 349(1):68, 2003.

[33] R. D. Blandford and D. G. Payne. Hydromagnetic flows from accretion discs and the production of radio jets. *Mon. Not. R. Astron. Soc.*, 199:883, 1982.

[34] R. D. Blandford and R. L. Znajek. Electromagnetic extraction of energy from Kerr black holes. *Mon. Not. R. Astron. Soc.*, 179:433, 1977.

[35] H. Bondi. On spherically symmetrical accretion. *Mon. Not. R. Astron. Soc.*, 112:195, 1952.

[36] G. C. Bower, M. C. H. Wright, H. Falcke, and D. C. Backer. Interferometric Detection of Linear Polarization from Sagittarius A* at 230 GHz. *Astrophys. J.*, 588:331, 2003.

[37] S. I. Braginskii. *Reviews of Plasma Physics*, volume 1, page 205. Consultants Bureau, 1965.

[38] A. Brandenburg, A. Nordlund, R. F. Stein, and U. Torkelsson. Dynamo-generated Turbulence and Large-Scale Magnetic Fields in a Keplerian Shear Flow. *Astrophys. J.*, 446:741, 1995.

[39] M. Burin and H. Ji. manuscript in preparation. *private communication*, 2006.

[40] J. Candy and R. E. Waltz. Anomalous Transport in the DIII-D Tokamak Matched by Supercomputer Simulation. *Phys. Rev. Lett.*, 91:045001, 2003.

[41] V. Caselles, J.M. Morel, G. Sapiro, and A. Tannenbaum. Introduction to the special issue on partial differential equations and geometry-driven diffusion in image processing and analysis. *IEEE Trans. on Image Processing*, 7:269, 1998.

[42] G. D. Chagelishvili, J. P. Zahn, A. G. Tevzadze, and J. G. Lominadze. On hydrodynamic shear turbulence in Keplerian disks: Via transient growth to bypass transition. *Astron. Astrophys.*, 402:401, 2003.

[43] B. Chandran and S. C. Cowley. Thermal Conduction in a Tangled Magnetic Field. *Phys. Rev. Lett.*, 80(14):3077, 1998.

[44] S. Chandrasekhar. The stability of non-dissipative Couette flow in hydromagnetics. *Proc. Nat. Acad. Sci.*, 46:253, 1960.

[45] S. Chandrasekhar. *Hydrodynamic and Hydromagnetic Stability*. Oxford Univ. Press, London, 1961.

[46] Z. Chang and J. D. Callen. Unified fluid/kinetic description of plasma microinstabilities. part I: Basic equations in a sheared slab geometry. *Phys. Fluids B*, 4(5):1167, 1992.

[47] S. Chapman and T. G. Cowling. *The Mathematical Theory of Non-Uniform Gases*. Cambridge Univ. Press, Cambridge, 1970.

[48] C. F. Chew, M. L. Goldberger, and F. E. Low. The Boltzmann equation and the one-fluid hydromagnetic equations in the absence of particle collisions. *Proc. R. Soc. London A*, 236:112, 1956.

[49] S. C. Cowley, R. M. Kulsrud, and R. Sudan. Considerations of ion-temperature-gradient-driven turbulence. *Phys. Fluids B*, 3:2767, 1991.

[50] J. A. Crawford and R. P. Craft. An Intrepretation of AE Aquarii. *Astrophys. J.*, 123:44, 1956.

[51] A. M. Dimits. *private communication*, 1994. A.M. Dimits was the first to suggest using Padé approximations for the Landau damping operator, in private communications to G.W. Hammett in the mid 1990's.

[52] A. M. Dimits, G. Bateman, M. A. Beer, B. I. Cohen, W. Dorland, G. W. Hammett, C. Kim, J. E. Kinsey, M. Kotschenreuther, A. H. Kritz, L. L. Lao, J. Mandrekas, W. M. Nevins, S. E. Parker, A. J. Redd, D. E. Shumaker, R. Sydora, and J. Weiland. Comparisons and physics basis of tokamak transport models and turbulence simulations. *Phys. Plasmas*, 7(3):969, 2000.

[53] W. Dorland, F. Jenko, M. Kotschenreuther, and B.N. Rogers. Electron temperature gradient turbulence. *Phys. Rev. Lett.*, 85:5579, 2000.

[54] W. D. Dorland. *Gyrofluid Models of Plasma Turbulence*. PhD thesis, Princeton Univ., 1993.

[55] A. A. Esin, J. E. McClintock, and R. Narayan. Advection-dominated Accretion and the Spectral States of Back Hole X-Ray Binaries: Application to Nova MUSCAE 1991. *Astrophys. J.*, 489:865, 1997.

[56] A. C. Fabian, K. Iwasawa, C. S. Reynolds, and A. J. Young. Broad Iron Lines in Active Galactic Nuclei. *Pub. Astron. Soc. Pacific*, 112(775):1145, 2000.

[57] A. C. Fabian and M. J. Rees. The accretion luminosity of a massive black hole in an elliptical galaxy. *Mon. Not. R. Astron. Soc.*, 277(2):L55, 1995.

[58] L. Ferrarese and D. Merritt. A Fundamental Relation between Supermassive Black Holes and Their Host Galaxies. *Astrophys. J.*, 539(1):L9, 2000.

[59] T. P. Fleming, J. M. Stone, and J. F. Hawley. The Effect of Resistivity on the Nonlinear Stage of the Magnetorotational Instability in Accretion Disks. *Astrophys. J.*, 530:464, 2000.

[60] E. A. Foote and R. M. Kulsrud. Electromagnetic waves in high β plasmas. *Astrophys. J.*, 233:302, 1979.

[61] J. Frank, A. King, and D. Raine. *Accretion Power in Astrophysics*. Cambridge Univ. Press, Cambridge, 2002.

[62] U. Frisch. *Turbulence: The legacy of A. N. Kolmogorov*. Cambridge Univ. Press, Cambridge, 1995.

[63] C. F. Gammie. Layered Accretion in T Tauri Disks. *Astrophys. J.*, 457:355, 1996.

[64] C. F. Gammie. Photon bubbles in accretion discs. *Astrophys. J.*, 297:929, 1998.

[65] T. A. Gardiner and J. M. Stone. An unsplit Godunov method for ideal MHD via constrained transport. *J. Comp. Phys.*, 205(2):509, 2005.

[66] S. P. Gary, B. J. Anderson, R. E. Denton, S. A. Fuselier, M. E. McKean, and D. Winske. Ion anisotropies in the magnetosheath. *Geophys. Res. Lett.*, 20(17):1767, 1993.

[67] S. P. Gary and M. A. Lee. The ion cyclotron anisotropy instability and the inverse correlation between proton anisotropy and proton beta. *J. Geophys. Res.*, 99(A6):11297, 1994.

[68] S. P. Gary and J. Wang. Whistler instability: electron anisotropy upper bound. *J. Geophys. Res.*, 101(A5):10749, 1996.

[69] S. P. Gary, J. Wang, D. Winske, and S. A. Fuselier. Proton temperature anisotropy upper bound. *J. Geophys. Res.*, 102(A12):27159, 1997.

[70] K. Gebhardt and et al. A Relationship between Nuclear Back Hole Mass and Galaxy Velocity Dispersion. *Astrophys. J.*, 539(1):L13, 2000.

[71] A. M. Ghez, G. Duchêne, K. Matthews, S. D. Hornstein, A. Tanner, J. Larkin, M. Morris, E. E. Becklin, S. Salim, T. Kremenek, D. Thompson, B. T. Soifer, G. Neugebauer, and I. McLean. The First Measurement of Spectral Lines in a Short-Period Star Bound to the Galaxy's Central Black Hole: A Paradox of Youth. *Astrophys. J.*, 586(2):L127, 2003.

[72] P. Goldreich, J. Goodman, and R. Narayan. The stability of accretion tori. I — Long-wavelength modes of slender tori. *Mon. Not. R. Astron. Soc.*, 221:339, 1986.

[73] P. Goldreich and S. Sridhar. Toward a theory of interstellar turbulence. 2: Strong Alfvenic turbulence. *Astrophys. J.*, 438(2):763, 1995.

[74] H. Goldstein, C. P. Poole, and J. L. Safko. *Classical Mechanics*. Addison Wesley, 2002.

[75] J. Goodman and G. Xu. Parasitic instabilities in magnetized, differentially rotating disks. *Astrophys. J.*, 432(1):213, 1994.

[76] S. Günter, Q. Yu, J. Krger, and K. Lackner. Modelling of heat transport in magnetised plasmas using non-aligned coordinates. *J. Comp. Phys.*, 209(1):354, 2005.

[77] G. W. Hammett, M. A. Beer, W. Dorland, S. C. Cowley, and S. A. Smith. Developments in the gyrofluid approach to tokamak turbulence simulations. *Plasma Phys. Controlled Fusion*, 35(8):973, 1993.

[78] G. W. Hammett, W. Dorland, and F. W. Perkins. Fluid models of phase mixing, Landau damping, and nonlinear gyrokinetic dynamics. *Phys. Fluids B*, 4(7):2052, 1992.

[79] G. W. Hammett and F. W. Perkins. Fluid Moment Models for Landau Damping with Application to the Ion-Temperature-Gradient Instability. *Phys. Rev. Lett.*, 64(25):3019, 1990.

[80] A. Hasegawa. Drift mirror instability in the magnetosphere. *Phys. Fluids*, 12(12):2642, 1969.

[81] J. F. Hawley. Global Magnetohydrodynamical Smulations of Accretion Tori. *Astrophys. J.*, 528:462, 2000.

[82] J. F. Hawley and S. A. Balbus. A Powerful Local Shear Instability in Weakly Magnetized Disks. II. Nonlinear Evolution. *Astrophys. J.*, 376:223, 1991.

[83] J. F. Hawley and S. A. Balbus. The Dynamical Structure of Nonradiative Black Hole Accretion Flows. *Astrophys. J.*, 573(2):738, 2002.

[84] J. F. Hawley, S. A. Balbus, and J. M. Stone. A Magnetohydrodynamic Nonradiative Accretion Flow in Three Dimensions. *Astrophys. J.*, 554(1):L49, 2001.

[85] J. F. Hawley, S. A. Balbus, and W. F. Winters. Local Hydrodynamic Stability of Accretion Disks. *Astrophys. J.*, 518:394, 1999.

[86] J. F. Hawley, C. F. Gammie, and S. A. Balbus. Local Three-dimensional Magnetohydrodynamic Simulations of Accretion Disks. *Astrophys. J.*, 440:372, 1995.

[87] J. F. Hawley, C. F. Gammie, and S. A. Balbus. Local Three-dimensional Simulations of an Accretion Disk Hydromagnetic Dynamo. *Astrophys. J.*, 464:690, 1995.

[88] J. F. Hawley and J. M. Stone. Nonlinear Evolution of the Magnetorotational Instability in Ion-Neutral Disks. *Astrophys. J.*, 501:758, 1998.

[89] L. C. Ho. The Sectral Energy Distributions of Low-Luminosity Active Galactic Nuclei. *Astrophys. J.*, 516(2):672, 1999.

[90] L. C. Ho, E. D. Feigelson, L. K. Townsley, R. M. Sambruna, G. P. Garmire, W. N. Brandt, A. V. Filippenko, R. E. Griffiths, A. F. Ptak, and W. L. W. Sargent. Detection of Nuclear X-ray Sources in Nearby Galaxies with Chandra. *Astrophys. J.*, 549(1):L51, 2001.

[91] J. D. Huba. *NRL Plasma Formulary*. The Office of Naval Research, 2000.

[92] S. Ichimaru. Bimodal behavior of accretion disks — theory and application to Cygnus X-1 transitions. *Astrophys. J.*, 214:840, 1977.

[93] J. Igea and A. E. Glassgold. X-Ray Ionization of the Disks of Young Stellar Objects. *Astrophys. J.*, 518:848, 1999.

[94] I. V. Igumenshchev and M. A. Abramowicz. Rotating accretion flows around black holes: convection and variability. *Mon. Not. R. Astron. Soc.*, 303(2):309, 1999.

[95] I. V. Igumenshchev, R. Narayan, and M. A. Abramowicz. Three-dimensional Magnetohydrodynamic Simulations of Radiatively Iefficient Accretion Flows. *Astrophys. J.*, 592(2):1042, 2003.

[96] T. Islam and S. A. Balbus. Dynamics of the Mgnetoviscous Istability. *Astrophys. J.*, 633:328, 2005.

[97] F. Jenko, W. Dorland, M. Kotschenreuther, and B.N. Rogers. Electron temperature gradient driven turbulence. *Phys. Plasmas*, 7:1904, 2000.

[98] J. C. Kasper, A. J. Lazarus, and S. P. Gary. Wind/SWE observations of firehose constraint on solar wind proton temperature anisotropy. *Geophys. Res. Lett.*, 29(17):20–1, 2002.

[99] C. F. Kennel and H. E. Petchek. Limit on stably trapped particle fluxes. *J. Geophys. Res.*, 71:1, 1966.

[100] C. F. Kennel and R. Z. Sagdeev. Collisionless shock waves in high β plasmas, 1. *J. Geophys. Res.*, 72(13):3303, 1967.

[101] M. G. Kivelson and D. J. Southwood. Mirror instability II: The mechanism of nonlinear saturation. *J. Geophys. Res.*, 101(A8):17365, 1996.

[102] S. S. Komissarov. Observations of the Blandford-Znajek process and the magnetohydrodynamic Penrose process in computer simulations of black hole magnetospheres. *Mon. Not. R. Astron. Soc.*, 359(3):801, 2005.

[103] A. Koratkar and O. Blaes. The Ultraviolet and Optical Continuum Emission in Active Galactic Nuclei: The Status of Accretion Disks. *Pub. Astron. Soc. Pacific*, 111(755):1, 1999.

[104] N. A. Krall and A. W. Trivelpiece. *Principles of Plasma Physics*. San Francisco Press, San Francisco, 1986.

[105] J. H. Krolik and J. F. Hawley. Magnetically Driven Jets in the Kerr Metric. *Astrophys. J.*, 641:103, 2006.

[106] J. H. Krolik and E. G. Zweibel. The weak-field limit of the magnetorotational instability. *Astrophys. J.*, 644:651, 2006.

[107] M. D. Kruskal and C. R. Oberman. On the stability of plasma in static equilibrium. *Phys. Fluids*, 1(4):275, 1958.

[108] G. P. Kuiper. On the Interpretation of β Lyrae and Other Close Binaries. *Astrophys. J.*, 93:133, 1941.

[109] R. M. Kulsrud. General stability theory in plasma physics. In M. N. Rosenbluth, editor, *Proceedings of the international school of Physics, Enrico Fermi, Course XXV, Advanced Plasma Theory*. North Holland, 1962.

[110] R. M. Kulsrud. *Handbook of Plasma Physics*, volume 1, page 115. North Holland, 1983.

[111] R. M. Kulsrud. *Plasma Physics for Astrophysics*. Princeton Univ. Press, Princeton, 2005.

[112] A. Kurganov and E. Tadmor. New high-resolution central schemes for nonlinear conservation laws and convection-diffusion equations. *Astrophys. J.*, 93:133, 1941.

[113] L. D. Landau. On the vibrations of the electronic plasma. *J. Phys. USSR*, 10:26, 1946.

[114] J. P. Lasota, M. A. Abramowicz, X. Chen, J. Krolik, R. Narayan, and I. Yi. Is the Accretion Flow in NGC 4258 Advection Dominated? *Astrophys. J.*, 462:142, 1996.

[115] G. Lesur and P. Y. Longaretti. On the relevance of subcritical hydrodynamic turbulence to accretion disk transport. *Astron. Astrophys.*, 444(1):25, 2005.

[116] R. J. Leveque. *Finite Volume Methods for Hyperbolic Problems*. Cambridge Univ. Press, Cambridge, 2002.

[117] C. D. Levermore and G. C. Pomraning. A flux-limited diffusion theory. *Astrophys. J.*, 248(1):321, 1981.

[118] D. N. C. Lin and J. Papaloizou. On the structure and evolution of the primordial solar nebula. *Mon. Not. R. Astron. Soc.*, 191:37, 1980.

[119] M. Loewenstein, R. F. Mushotzky, L. Angelini, K. A. Arnaud, and E. Quataert. Chandra Limits on X-Ray Emission Associated with the Supermassive Black Holes in Three Giant Elliptical Galaxies. *Astrophys. J.*, 555:21L, 2001.

[120] D. Lynden-Bell. Galactic Nuclei as Collapsed Old Quasars. *Nature*, 223:690, August 1969.

[121] D. Lynden-Bell and J. E. Pringle. The evolution of viscous discs and the origin of the nebular variables. *Mon. Not. R. Astron. Soc.*, 168:603, 1974.

[122] J. Magorrian, S. Tremaine, D. Richstone, R. Bender, G. Bower, A. Dressler, S. M. Faber, K. Gebhardt, R. Green, C. Grillmair, J. Kormendy, and T. Lauer. The Demography of Massive Dark Objects in Galaxy Centers. *Astron. J.*, 115(6):2285, 1998.

[123] E. Marsch, R. Schwenn, H. Rosenbauer, K. H. Muehlhaeuser, W. Pilipp, and F. M. Neubauer. Solar wind protons — Three-dimensional velocity distributions and derived plasma parameters measured between 0.3 and 1 AU. *J. Geophys. Res.*, 87:52, 1982.

[124] R. Matsumoto and T. Tajima. Magnetic viscosity by localized shear flow instability in magnetized accretion disks. *Astrophys. J.*, 445:767, 1995.

[125] T. Di Matteo, R. M. Johnstone, S. W. Allen, and A. C. Fabian. Accretion onto Nearby Supermassive Black Holes: Chandra Constraints on the Dominant Cluster Galaxy NGC 6166. *Astrophys. J.*, 550(1):L19, 2001.

[126] N. Mattor. Can Landau-fluid models describe nonlinear Landau damping. *Phys. Fluids B*, 4(12):3952, 1992.

[127] M. E. McKean, S. P. Gary, and D. Winske. Kinetic physics of the mirror instability. *J. Geophys. Res.*, 98(A12):21313, 1993.

[128] J. C. McKinney and C. F. Gammie. A Measurement of the Electromagnetic Luminosity of a Kerr Black Hole. *Astrophys. J.*, 611(2):977, 2004.

[129] F. Melia. An accreting black hole model for Sagittarius A. *Astrophys. J.*, 387:L25, 1992.

[130] K. Menou. Hot Accretion With Saturated Conduction. *astro-ph/0507189*, 2005.

[131] D. Mihalas and B. W. Mihalas. *Foundations of Radiation Hydrodynamics*. Oxford Univ. Press, 1985.

[132] K. A. Miller and J. M. Stone. The Formation and Structure of a Strongly Magnetized Corona above a Weakly Magnetized Accretion Disk. *Astrophys. J.*, 534(1):398, 2000.

[133] C. W. Misner, K. S. Thorne, and J. A. Wheeler. *Gravitation*. Freeman, 1973.

[134] M. Miyoshi, J. Moran, J. Herrnstein, L. Greenhill, N. Nakai, P. Diamond, and M. Inoue. Evidence for a Black-Hole from High Rotation Velocities in a Sub-Parsec Region of NGC4258. *Nature*, 373(6510):127, 1995.

[135] D. C. Montgomery and D. A. Tidman. *Plasma Kinetic Theory*. Mc-Graw Hill, 1964.

[136] P. Mrázek and M. Navara. Consistent positive directional splitting of anisotropic diffusion. In *Proc. of Computer Vision Winter Workshop*, page 37, Bled, Slovenia, 2001. http://www.mia.uni-saarland.de/mrazek/Publications/Mrazek-cvww01.pdf.

[137] F. Najarro, A. Krabbe, R. Genzel, D. Lutz, R. P. Kudritzki, and D. J. Hillier. Quantitative spectroscopy of the HeI cluster in the Galactic center. *Astron. Astrophys.*, 325:700, 1997.

[138] R. Narayan. *Unsolved Problems in Astrophysics*, page 301. Princeton Univ. Press, Princeton, 1997.

[139] R. Narayan. Black holes: Sparks of interest. *Nature*, 425(6961):908, 2003.

[140] R. Narayan, R. Mahadevan, and E. Quataert. *Theory of Black Hole Accretion Disks*, page 148. Cambridge Univ. Press, 1998.

[141] R. Narayan and I. Yi. Advection-dominated accretion: A self-similar solution. *Astrophys. J.*, 428(1):L13, 1994.

[142] R. Narayan and I. Yi. Advection-dominated accretion: Self-similarity and bipolar outflow. *Astrophys. J.*, 444(1):231, 1995.

[143] H. Nessyahu and E. Tadmor. Non-oscillatory central differencing for hyperbolic conservation laws. *J. Comp. Phys.*, 87:408, 1990.

[144] W. Nevins. A Statistical Analysis of ITG Turbulence. *manuscript in preparation*, 2005.

[145] B. Paczynski and P. J. Wiita. Thick accretion disks and supercritical luminosities. *Astron. Astrophys.*, 88:23, 1980.

[146] J. C. B. Papaloizou and J. E. Pringle. The dynamical stability of differentially rotating discs with constant specific angular momentum. *Mon. Not. R. Astron. Soc.*, 208:721, 1984.

[147] S. E. Parker, W. Dorland, R. A. Santoro, M. A. Beer, Q. P. Liu, W. W. Lee, and G. W. Hammett. Comparisons of gyrofluid and gyrokinetic simulations. *Phys. Plasmas*, 1(5):1461, 1994.

[148] I. J. Parrish and J. M. Stone. Nonlinear Evolution of the Magnetothermal Instability in Two Dimensions. *Astrophys. J.*, 633:334, 2005.

[149] U. Pen, C. D. Matzner, and S. Wong. The Fate of Nonradiative Magnetized Accretion Flows: Magnetically Frustrated Convection. *Astrophys. J.*, 596(2):L207, 2003.

[150] M. E. Pessah, C. Chan, and D. Psaltis. The signature of the magnetorotational instability in the Reynolds and Maxwell stress tensors in accretion discs. *astro-ph/0603178, submitted to Mon. Not. R. Astron. Soc.*, 2006.

[151] R. A. Piontek and E. C. Ostriker. Saturated-State Turbulence and Structure from Thermal and Magnetorotational Instability in the ISM: Three-dimensional Numerical Simulations. *Astrophys. J.*, 629:849, 2005.

[152] K. H. Prendergast and G. R. Burbidge. On the Nature of Some Galactic X-Ray Sources. *Astrophys. J.*, 151:L83, 1968.

[153] J. E. Pringle. Accretion disks in astrophysics. *Ann. Rev. Astron. Astrophys.*, 19:137, 1981.

[154] D. Proga and M. C. Begelman. Accretion of Low Angular Momentum Material onto Black Holes: Two-dimensional Hydrodynamical Inviscid Case. *Astrophys. J.*, 582(1):69, 2003.

[155] D. Proga and M. C. Begelman. Accretion of Low Angular Momentum Material onto Black Holes: Two-dimensional Magnetohydrodynamic Case. *Astrophys. J.*, 592(2):767, 2003.

[156] E. Quataert. Radiatively Inefficient Accretion Flow Models of Sgr A*. *Astronom. Nachr.*, 324:435, 2003.

[157] E. Quataert. A Dynamical Model for Hot Gas in the Galactic Center. *Astrophys. J.*, 613(1):322, 2004.

[158] E. Quataert, W. Dorland, and G. W. Hammett. The Magnetorotational Instability in a Collisionless Plasma. *Astrophys. J.*, 577(1):524, 2002.

[159] E. Quataert and A. Gruzinov. Constraining the Accretion Rate onto Sagittarius A* Using Linear Polarization. *Astrophys. J.*, 545:842, 2000.

[160] E. Quataert and A. Gruzinov. Convection-dominated Accretion Flows. *Astrophys. J.*, 539(2):809, 2000.

[161] E. Quataert and R. Narayan. Spectral Models of Advection-dominated Accretion Flows with Winds. *Astrophys. J.*, 520(1):298, 1999.

[162] K. B. Quest and V. D. Shapiro. Evolution of the fire-hose instability: Linear theory and wave-wave coupling. *J. Geophys. Res.*, 101(A11):24457, 1996.

[163] M. J. Rees, E. S. Phinney, M. C. Begelman, and R. D. Blandford. Ion-supported tori and the origin of radio jets. *Nature*, 295:17, 1982.

[164] D. Richard and J. P. Zahn. Turbulence in differentially rotating flows. What can be learned from the Couette-Taylor experiment. *Astron. Astrophys.*, 347:734, 1999.

[165] M. N. Rosenbluth and N. Rostoker. Theoretical structure of plasma equations. *Phys. Fluids*, 2(1):23, 1959.

[166] D. Ryu and J. Goodman. Convective instability in differentially rotating disks. *Astrophys. J.*, 388:438, 1992.

[167] T. Sano, S. Inutsuka, N. J. Turner, and J. M. Stone. Angular Momentum Transport by Magnetohydrodynamic Turbulence in Accretion Disks: Gas Pressure Dependence of the Saturation Level of the Magnetorotational Instability. *Astrophys. J.*, 605(1):321, 2004.

[168] T. Sano, S. M. Miyama, T. Umebayashi, and T. Nakano. Magnetorotational Instability in Protoplanetary Disks. II. Ionization State and Unstable Regions. *Astrophys. J.*, 543:486, 2000.

[169] T. Sano and J. M. Stone. The Effect of the Hall Term on the Nonlinear Evolution of the Magnetorotational Instability. I. Local Axisymmetric Simulations. *Astrophys. J.*, 570(1):314, 2002.

[170] A. A. Schekochihin, S. C. Cowley, R. M. Kulsrud, G. W. Hammett, and P. Sharma. Plasma Instabilities and Magnetic Field Growth in Clusters of Galaxies. *Astrophys. J.*, 629(1):139, 2005.

[171] R. Schödel, T. Ott, R. Genzel, R. Hofmann, M. Lehnert, A. Eckart, N. Mouawad, T. Alexander, M. J. Reid, R. Lenzen, M. Hartung, F. Lacombe, D. Rouan, E. Gendron, G. Rousset, A.-M. Lagrange, W. Brandner, N. Ageorges, C. Lidman, A. F. M. Moorwood, J. Spyromilio, N. Hubin, and K. M. Menten. A star in a 15.2-year orbit around the supermassive black hole at the centre of the milky way. *Nature*, 419(6908):694, 2002.

[172] B. F. Schutz. *A First Course in General Relativity.* Cambridge Univ. Press, Cambridge, 1985.

[173] B. D. Scott. Free-energy conservation in local gyrofluid models. *Phys. Plasmas*, 12(10):102307, 2005.

[174] N. I. Shakura and R. A. Sunyaev. Black holes in binary systems. Observational appearance. *Astron. Astrophys.*, 24:337, 1973.

[175] P. Sharma and G. W. Hammett. Anisotropic conduction with large temperature gradients. *to be submitted to J. Comp. Phys.*, 2006.

[176] P. Sharma, G. W. Hammett, and E. Quataert. Transition from Collisionless to Collisional Magnetorotational Instability. *Astrophys. J.*, 596:1121, 2003.

[177] P. Sharma, G. W. Hammett, E. Quataert, and J. M. Stone. Shearing Box Simulations of the MRI in a Collisionless Plasma. *Astrophys. J.*, 637:952, 2006.

[178] K. Shibata and Y. Uchida. A magnetodynamic mechanism for the formation of astrophysical jets. ii - dynamical processes in the accretion of magnetized mass in rotation. *Pub. Astron. Soc. Japan*, 38:631, 1986.

[179] S. A. Smith. *Dissipative Closures for Statistical Moments, Fluid Moments, & Subgrid Scales in Plasma Turbulence*. PhD thesis, Princeton Univ., 1997.

[180] P. B. Snyder, G. W. Hammett, and W. Dorland. Landau fluid models of collisionless magnetohydrodynamics. *Phys. Plasmas*, 4(11):3974, 1997.

[181] C. R. Sovinec, A. H. Glasser, T. A. Gianakon, D. C. Barnes, R. A. Nebel, S. E. Kruger, D. D. Schnack, S. J. Plimpton, A. Tarditi, and M. S. Chu. Nonlinear magnetohydrodynamics simulation using high-order finite elements. *J. Comp. Phys.*, 195(1):355, 2004.

[182] T. H. Stix. *Waves in Plasmas*. AIP Press, New York, 1992.

[183] J. M. Stone and S. A. Balbus. Angular Momentum Transport in Accretion Disks via Convection. *Astrophys. J.*, 464:364, 1996.

[184] J. M. Stone, J. F. Hawley, C. F. Gammie, and S. A. Balbus. Three-dimensional magnetohydrodynamical simulations of vertically stratified accretion disks. *Astrophys. J.*, 463:656, 1996.

[185] J. M. Stone and M. L. Norman. ZEUS-2D: A radiation magnetohydrodynamics code for astrophysical flows in two space dimensions. I. The hydrodynamic algorithms and tests. *Astrophys. J. Suppl.*, 80(2):753, 1992.

[186] J. M. Stone and M. L. Norman. ZEUS-2D: A radiation magnetohydrodynamics code for astrophysical flows in two space dimensions. II. The magnetohydrodynamic algorithms and tests. *Astrophys. J. Suppl.*, 80(2):791, 1992.

[187] J. M. Stone and M. L. Norman. Numerical simulations of magnetic accretion disks. *Astrophys. J.*, 433:946, 1994.

[188] J. M. Stone and J. E. Pringle. Magnetohydrodynamical non-radiative accretion flows in two dimensions. *Mon. Not. R. Astron. Soc.*, 528:462, 2001.

[189] J. M. Stone, J. E. Pringle, and M. C. Begelman. Hydrodynamical non-radiative accretion flows in two dimensions. *Mon. Not. R. Astron. Soc.*, 310:1002, 1999.

[190] T. Tanaka and K. Menou. Hot Accretion Hot Accretion With Conduction: Spontaneous Thermal Outflows With Saturated Conduction. *astro-ph/0604509*, 2006.

[191] H. Tennekes and J. L. Lumley. *A First Course in Turbulence*. The MIT Press, Cambridge, 1972.

[192] B. T. Tsurutani, E. J. Smith, R. R. Anderson, K. W. Ogilvie, J. D. Scudder, D. N. Baker, and S. J. Bame. Lion roars and nonoscillatory drift mirror waves in the magnetosheath. *J. Geophys. Res,*, 87:6060, 1982.

[193] N. J. Turner, O. M. Blaes, A. Socrates, M. C. Begelman, and S. W. Davis. The Effects of Photon Bubble Instability in Radiation-dominated Accretion Disks. *Astrophys. J.*, 624:267, 2005.

[194] N. J. Turner, J. M. Stone, J. H. Krolik, and T. Sano. Local Three-dimensional Simulations of Magnetorotational Instability in Radiation-dominated Accretion Disks. *Astrophys. J.*, 593:992, 2003.

[195] O. M. Umurhan and O. Regev. Hydrodynamic stability of rotationally supported flows: Linear and nonlinear 2D shearing box results. *Astron. Astrophys.*, 427:855, 2004.

[196] B. van Leer. Towards the Ultimate Conservative Difference Scheme V, A Second Order Sequel to Gudonov's Method. *J. Comp. Phys.*, 32:101, 1979.

[197] E. P. Velikhov. Stability of an ideally conducting liquid flowing between cylinders rotating in a magnetic field. *Soviet Phys.-JETP*, 36:1398, 1959.

[198] J. P. De Villiers. Accretion Disks in Large-scale Magnetic Fields. *astro-ph/0605744*, 2006.

[199] J. P. De Villiers, J. F. Hawley, and J. H. Krolik. Magnetically Driven Accretion Flows in the Kerr Metric. I. Models and Overall Structure. *Astrophys. J.*, 599(2):1238, 2003.

[200] W. F. Winters, S. A. Balbus, and J. F. Hawley. Chaos in turbulence driven by the magnetorotational instability. *Mon. Not. R. Astron. Soc.*, 340(2):519, 1992.